Anisotropic Nanoparticles— Synthesis, Characterization and Applications

Symposium held November 27–29, 2000, Boston, Massachusetts, U.S.A.

EDITORS:

L. Andrew Lyon
Georgia Institute of Technology
Atlanta, Georgia, U.S.A.

Stephan J. Stranick
National Institute of Standards and Technology
Gaithersburg, Maryland, U.S.A.

Christine Dolan Keating
The Pennsylvania State University
University Park, Pennsylvania, U.S.A.

Peter C. Searson
Johns Hopkins University
Baltimore, Maryland, U.S.A.

MⓇS

2001 0824 058

Anisotropic Nanoparticles—
Synthesis, Characterization
and Applications

CONTENTS

METALLIC NANOPARTICLES AND CLUSTERS I

METALLIC NANOPARTICLES AND CLUSTERS II

METALLIC NANOWIRES

*Invited Paper

POSTER SESSION

NANOWIRES AND NANOTUBES

NANOPARTICLES IN BIOLOGY

SEMICONDUCTOR NANOPARTICLES

*Invited Paper

PREFACE

This volume contains a series of papers originally presented at Symposium C, "Anisotropic Nanoparticles—Synthesis, Characterization and Applications," at the 2000 MRS Fall Meeting in Boston, Massachusetts. In addition to support from the Materials Research Society, this symposium was co-sponsored by NIST, NSF-DMR, and ONR, with corporate support from SurroMed, Inc. and Digital Instruments.

The purpose of this symposium was to review the broad multidisciplinary activities in this rapidly growing area. The properties of nanoscale materials are derived from the additional dimensional and compositional degrees of freedom that arise when the physical dimensions of the system are smaller than a characteristic length scale of interest. Anisotropic particles can exhibit novel and enhanced properties compared to isotropic spherical particles. This symposium focused on all aspects of anisotropy on the nanoscale, including anisotropy resulting from shape (e.g. rods, nanowires, biomolecules), juxtaposition of different materials (e.g. nanoparticle heterodimers), compositional heterogeneity (e.g. core-shell particles, multilayer nanowires) or the intrinsic directionality of a probe (e.g. electromagnetism).

In addition to the synthesis of new anisotropic materials, the ability to address individual nanostructures (e.g. electrically, magnetically, or optically) is important for technological applications such as nanoelectronics and biomedical engineering. Furthermore, the assembly of ordered 1D, 2D, and 3D arrays of anisotropic nanoparticles presents new challenges not encountered with isotropic particles. Chemical interactions (e.g. self-assembly) and electric fields (e.g. electrostatic trapping) can be used to assemble ordered arrays from colloidal suspensions. The ability to address isolated anisotropic particles (e.g. nanowires, DNA strands) allows fundamental measurements of properties such as electrical transport and tunneling. By assembling an extremely multidisciplinary group of scientists, this symposium attempted to address all of these issues in some way. This volume presents a subset of the presentations in this symposium and attempts to provide the scientific community with a progress report in nanoscale anisotropy and its applications in a variety of fields.

<div style="text-align: right">

L. Andrew Lyon
Stephan J. Stranick
Christine Dolan Keating
Peter C. Searson

April 2001

</div>

MATERIALS RESEARCH SOCIETY SYMPOSIUM PROCEEDINGS

MATERIALS RESEARCH SOCIETY SYMPOSIUM PROCEEDINGS

Prior Materials Research Society Symposium Proceedings available by contacting Materials Research Society

Metallic Nanoparticles
and Clusters I

Structure and Electrical Properties of an Assembly of Au Nanoclusters

G. Muralidharan, L. Maya and T. Thundat
Oak Ridge National Laboratory
Oak Ridge, TN-37831-6123.

ABSTRACT

Conduction through an assembly of nanosized clusters coupled by tunneling barriers is of significant interest both for understanding the fundamental physics involved and for potential applications. In this study, we describe a technique for preparing relatively large (dimensions of a few 100 μm to a few mm in size) monolayer films consisting of 3 nm diameter Au clusters coated with mercaptododecanoic acid, using low molecular weight-polymers as coupling agents. Electrical measurements of the assembly show non-linear characteristics. Below a certain threshold voltage, the current does not vary with an increase in voltage. Above this threshold voltage, current increases with voltage and can be described by a power-law relationship with an exponent close to unity. These characteristics of the I-V curve are discussed with specific reference to theoretical studies on conduction through an array of capacitance-coupled metallic islands and previous experimental results in similar systems.

INTRODUCTION

Recently, there has been significant interest in observing Coulomb blockade effects at room temperature in systems containing multiple tunnel junctions comprising of small, metallic clusters separated by tunnel barriers due to potential applications in nanoscale electronics [1-5]. Two criteria have to be satisfied for observing Coulomb blockade in such systems. Firstly, the Coulomb charging energy of the cluster or island ($E_c = e^2/2C$) where e is the electron charge and C is the capacitance of the island, has to be larger than the ambient thermal energy kT. The second criterion to be satisfied is that the tunnel barrier between islands must have a tunnel resistance greater than the quantum resistance h/e^2, where h is the Planck's constant. Ligand-stabilized metal particles offer an attractive method for synthesizing two-dimensional arrays of multiple tunnel junctions, since the ligand shells not only facilitate coupling amongst the metallic clusters but they also serve as tunnel barriers [6].

Various methods have been used to synthesize two-dimensional assemblies consisting of nm sized metallic clusters separated by ligand shells. Spin casting has been used to prepare ordered assemblies of size 450 nm consisting of 3.7 nm Au clusters [2, 7]. Biopolymer templates have been used to prepare two-dimensional assemblies consisting of 0.7 nm Au nanoparticles between electrodes separated by distances of 15 μm [3-5]. Room temperature electrical conductance of such an assembly showed evidence of Coulomb gap. In the current study, we present a methodology to prepare relatively large assemblies (100 μm – 2 mm in size) consisting of Au clusters coated with mercaptododecanoic acid. We also present room temperature electrical properties of such assemblies, which show evidence of a Coulomb gap.

EXPERIMENTAL METHOD

Au clusters coated with mercaptododecanoic acid were obtained by a modification of the given by Zhao and Crooks [8] which involves the use of polyamido dendrimers and electroless

displacement of a copper metal colloid by Au (III) ions. The reaction was conducted in 30mL of a 2:1 mixture of water and tetrahydrofuran. The insoluble product was extracted with toluene and centrifuged to obtain reddish gold colloids. Films were observed to form at the liquid-vapor interface after reaction mixtures containing the carboxylic acid-coated gold colloids and equivalent amounts of polyethyleneimine were stirred for a few minutes. The films were seen clearly as a reflective coating on the surface and could be isolated as platelets of sizes ranging from a few hundred microns to as large as 1-2 mm on each side. In some instances, peptide linkages between the acid and the polymer were made through the intervention of EDC by itself or through an intermediate step involving the use of N-Hydroxysuccinimide, NHS, to modify the carboxylic acid into an amine reactive NHS ester. Further details of the preparation of the clusters and the films may be obtained from [9].

Au clusters were characterized by x-ray diffraction (XRD) to confirm crystallinity and to derive an average crystallite size. After washing them thoroughly to remove the reaction medium, infrared spectra were obtained from the colloids to assess the local molecular environment that enabled the association of the colloidal clusters. Gold cluster sizes and spatial organization of the clusters within the films were characterized using transmission electron microscopy (TEM) of the films placed directly on coated copper grids. Atomic force microscopy was also performed on both the individual Au clusters and the films. For the AFM study, individual Au clusters were suspended in water or methanol and a drop of the solution was dispensed and spin-coated on mica. The free-standing films were characterized by allowing them to settle on a sapphire substrate. For electrical property measurements, the films were collected on a pyrex or a sapphire substrate and electrical contacts were made to the films using silver paint. I-V characteristics were measured in an electrically isolated Faraday cage under controlled low-humidity conditions.

RESULTS

Figure 1 shows an XRD pattern from the clusters coated with mercaptododecanoic acid. The x-ray diffraction pattern shows that the particles are crystalline with the presence of Au (111), (200) and (220) lines. Note that, as expected, the peaks show significant broadening due to the size of the particles. Scherrer analysis of the peaks results in particle sizes of about 3 nm. Figure 2 shows the TEM image obtained by evaporating a droplet of the liquid containing the Au colloids mixed with polyethyleneimine and carbodiimide on a carbon-coated Cu grid. The sizes of the clusters observed in the TEM are consistent with the results of the XRD analysis. Note that there is a significant tendency for the clusters to associate into small assemblies with the overall shape of the assembly being circular. From the figure, it should also be observed that there is very little overlap in the images of the clusters within a group indicating that these prefer to form monolayers (2-D structures) rather than to associate to form a three-dimensional assembly.

Figure 3 shows an AFM image obtained from a mica surface on which the Au clusters were dispersed by spin coating a suspension consisting only of the clusters in water and without any coupling agents. The images were obtained using the tapping mode with very low tapping force. As observed from the figure, there is decreased tendency for the particles to associate under these conditions, clearly illustrating the role of the coupling agents in inducing the assembly of the clusters shown in figure 2. Figure 4 shows the variation in height obtained along the specified line shown in the figure. AFM imaging shows a typical height of 1.7 nm for the clusters, which is smaller than that predicted by both analyses of the x-ray data and electron
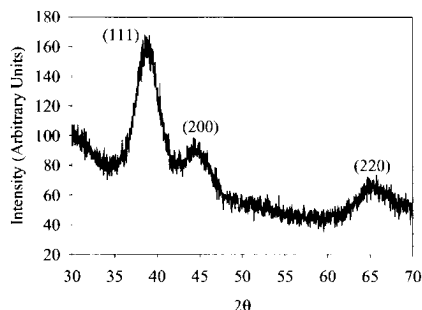
Figure 1. X-ray diffraction pattern from the Au clusters coated with mercaptododecanoic acid.

Figure 2. TEM micrograph of evaporation residue from liquid containing Au clusters mixed with polyethyleneimine and reaction promoted with carbodiimide.

microscopy. It is possible that the AFM image shows a smaller particle size due to tip-induced deformation of the clusters. Further experiments are underway to confirm this hypothesis.

Figure 5 shows a TEM image of a film collected on a carbon-coated TEM grid. Note the presence of a space-filling arrangement of the Au clusters. Although no defects are observed in the film over the scale of a few hundred nm, small regions devoid of clusters have been observed when imaging is performed over the scale of a few microns. An important feature to note from this image is that the inter-cluster spacing is not always uniform and the structure does not seem
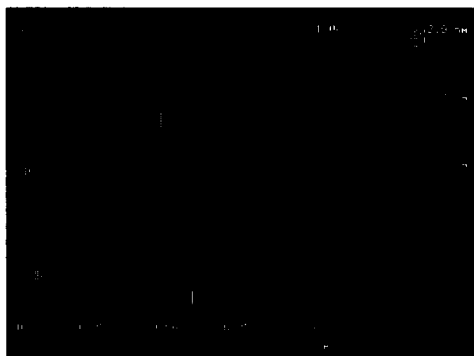
Figure 3. Tapping mode AFM image of the Au clusters dispersed on mica.

Figure 4. Variation in height obtained from the AFM image shown in figure 3 and along the trace shown in the figure.

C1.2.3

to show any long-range order in the organization of the individual clusters.

Figure 6 shows an optical microscope image of a film that was collected on the surface of a sapphire substrate. Electrical connections were made to the film using Ag paint. Also shown in the figure are the two electrical contacts with the distance of separation measured to be 220 μm. Figures 7 and 8 show the I-V characteristics of the film shown in figure 6 for two different ranges of voltages. Figure 7 shows the measured I-V characteristics (linear scale), both in the presence and in the absence of the film, for the voltage range of 0.01 to 1 volt with an incremental voltage of 10 mV. To measure the I-V characteristics in the absence of the film, the film was mechanically removed from the substrate without disturbing the two Ag contacts. Clearly, in the presence of the film, the observed current for a particular voltage is larger than that observed in the absence of the film. This confirms the role of the film in the electrical conduction between the two contacts. Also note that the minimum measurable current between the two contacts is of the order of a few fA. Figure 8 shows the current-voltage response (log-log scale) of the film over the voltage range of 0.01 to 30 V. An important feature of the curve shown in figure 8 is that it is not linear. It should be noted that in the voltage range 0.01 to 0.1 V, the current does not increase significantly with an increase in voltage. This can be seen in both figures 7 and 8, although more dramatically in figure 8. Note further that for voltages greater than about 1.0 volt, the log (I) – log (V) curve is linear with a slope close to unity. The non-linearity in the I-V characteristics of the film indicates that the presence of the tunnel junctions has a significant impact on the conductance through this film [10].

DISCUSSION

Electrical transport through the disordered array of Au clusters used in this study shows some of the characteristics predicted by the theoretical models and is consistent with previous experimental work. Middleton and Wingreen [10] studied conduction through a one and a two-dimensional array of small capacitance-coupled metal dots with charges allowed to tunnel between neighboring dots. Based on this model, they predicted that onset of conduction through
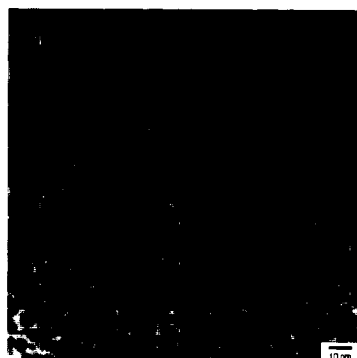
Figure 5. TEM image of the film formed by the assembly of the Au clusters.
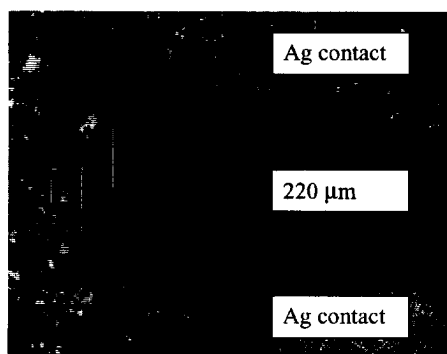
Figure 6. Optical micrograph of a film used for electrical measurements. The film was collected on a sapphire substrate.
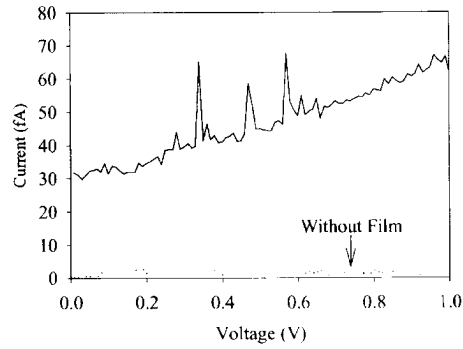
Figure 7. I-V characteristics obtained from the film shown in figure 6 for the voltage range 0.01 to 1.0 V. Also shown in the figure is the current observed between the contacts in the absence of the film.
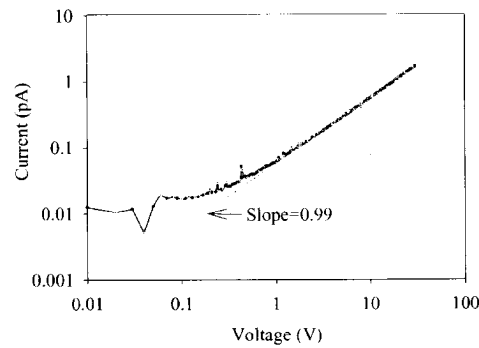
Figure 8. I-V characteristics obtained from the same film over the voltage range of 0.01 to 30V (log-log scale).

the array would occur at a threshold voltage V_T which is proportional to its linear size. Further, they predicted that above the threshold voltage, the current through the linear and square array would vary as

$$I \sim \left(\frac{V}{V_T} - 1 \right)^\zeta \qquad (1)$$

where $\zeta = 1$ and $5/3$ in dimensions $d = 1$ and 2 respectively. In the present experimental study, a threshold voltage (estimated as 100 mV) has been observed, a voltage above which the current increases rapidly. Further, for voltages $V \gg V_T$ ($V/V_T \gg 1$) the current follows the relationship predicted by equation (1) with the exponent being close to unity. Note that this value is closer to the value predicted for a one-dimensional array rather than the two-dimensional array used in the current study. Such an observation has also been reported in other studies on conduction through Au clusters linked by a biomolecular template [5]. Further work is underway to carry out such measurements at lower temperatures for obtaining a better understanding of charge transport in this system.

CONCLUSIONS

Monolayer asssemblies of size ranging from 100 μm to 2 mm have been prepared from nm sized Au clusters coated with mercaptododecanoic acid. I-V curves obtained from such films show non-linear characteristics. Results obtained from the study have been compared with theoretical predictions and results of other experimental work in similar systems.

ACKNOWLEDGMENTS

REFERENCES

1. U. Simon, Adv. Mater., **10**, 1487 (1998).
2. R. P. Andres, T. Bein, M. Dorogi, S. Feng, J. I. Henderson, C. P. Kubiak, W. Mahoney, R. G. Oshifchin and R. Reifenberger, Science, **272**, 1323 (1996).
3. L. Clarke, M. N. Wybourne, Mingdi Yan, S. X. Cai, L. O. Brown, J. Hutchison and J. F. Keana, J. Vac. Sci. Technol. B, **15**, 2925 (1997).
4. M. N. Wybourne, L. Clarke, M. Yan, S. X. Cai, L. O. Brown, J. Hutchison and J. F. W. Keana, Jpn. J. Appl. Phys., **36**, 7796 (1997).
5. C. A. Berven, M. N. Wybourne, L. Clarke, J. E. Hutchison, L. O. Brown, J. L. Mooster and M. E. Schmidt, Superlattices and Microstructures, **27**, 489 (2000).
6. S. Peschel and G. Schmid, Angew. Chem. Int. Ed. Engl., **34**, 1442 (1995).
7. R. P. Andres, J. D. Bielefeld, J. I. Henderson, D. B. Janes, V. R. Kolagunta, C. F. Kubiak, W. J. Mahoney, R. G. Osifchin, Science, **273**, 1690 (1996).
8. M. Zhao and R. M. Crooks, Chem. Mater., **11**, 3379 (1999).
9. L. Maya, G. Muralidharan, T. Thundat and E. A. Kenik, Langmuir, **16**, 9151 (2000).
10. A. A. Middleton and N. S. Wingreen, Phys. Rev. Lett., **71**, 3198 (1993).

Nanoparticles and Polymers. 'Bricks and Mortar' Self-Assembly of Nanostructures

Andrew Boal, Faysal Ilhan, Vincent Rotello,* Thomas Russell[1]
Dept. of Chemistry,[1] Dept. of Polymer Science and Engineering,
University of Massachusetts, Amherst, MA 01003 USA

ABSTRACT

Polymers provide a useful tool for the controlled assembly of colloidal nanoparticles. We have developed a "bricks and mortar" strategy in which colloidal gold particles functionalized with recognition elements serve as the bricks and polymers bearing complementary functionality serve as mortar to hold together the nanoparticles. In this methodology, the conformational flexibility of the polymer compensates for irregularities in the size and shape of the aggregate structure. We have used this method to create discrete micrometer-scale spherical assemblies based on 2 nm gold nanoparticles. Both the size and shape of these assemblies can be controlled, providing spherical assemblies ranging from 50 nm to 1500 nm, as well as network structures.

DISCUSSION

To provide a general means for the controlled self-assembly of nanoparticles, we have developed a "bricks and mortar" approach. In this strategy, colloidal gold particles functionalized with recognition elements serve as the bricks, while polymers bearing complementary functionality serve as mortar, holding together the colloidal particles. Using this strategy, the conformational flexibility of the polymer compensates for irregularities in the size and shape of the aggregate structure, allowing the efficient propagation of order during the self-assembly process.[1]

Complementarity between colloid and polymer was achieved using diaminotriazine-thymine three-point hydrogen bonding interaction (Figure 1a). For the polymer component, diaminotriazine-functionalized polystyrene 1 was employed (Figure 1b).[2] The required thymine-functionalized colloids were synthesized starting with ~2 nm gold particles covered with an octanethiol self-assembled monolayer (SAM). Thiol place-exchange with thymine-functionalized alkanethiol 5 then provided the derivatized colloid **Thy-Au** (Figure 2). To provide a control system which cannot participate in hydrogen bonding, the highly analogous **MeThy-Au** was prepared in a similar fashion.
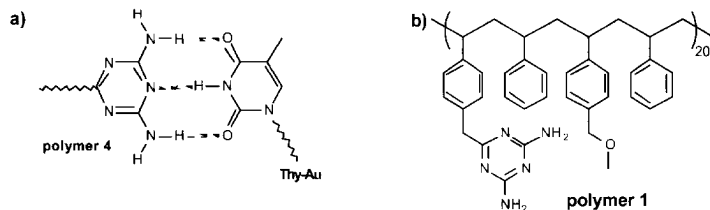
Figure 1. Recognition motif and polymer 'mortar'. a) Diaminotriazine-thymine recognition b) Triazine-functionalized random copolymer **1**.

Figure 2. Preparation of **Thy-Au** and **MeThy-Au**.

Addition of polymer **1** to concentrated solutions of **Thy-Au** in non-competitive solvents such as dichloromethane and chloroform resulted in rapid formation of a black solid. In contrast, no precipitation was observed upon addition of **1** to the control colloid **MeThy-Au**. The lack of aggregation observed in the control system demonstrates that the precipitation observed upon the addition of **1** to **Thy-Au** was the result of specific hydrogen bond interactions between the colloid thymines and the polymer triazines.

To provide control of the aggregation process, polymer **1** and **Thy-Au** were mixed in dilute dichloromethane solution, with precipitation proceeding over a 96 h period. The resulting solid was insoluble in non-polar solvents, but >80% could be dissolved in polar media such as methanol and tetrahydrofuran (THF). Small angle x-ray scattering (SAXS) was used to characterize the Au particles *in situ* before and after this aggregation using Ni-filtered Cu Kα radiation. After polymer **4**-induced aggregation, the SAXS plot of the precipitates exhibited a distinct maximum at $Q = 0.94 \ nm^{-1}$ characteristic of a defined separation distance between neighboring Au particles. After background subtraction, the center-to-center distance of Au particles was determined to be 6.4±0.3 nm in the polymer **1**-**Thy-Au** aggregate, corresponding to a 4.4 nm interparticle distance. Significantly, a sharp increase in the scattering was observed at small Q, suggesting the presence of larger scale structure (>20 nm) beyond instrumental resolution.

A model for the self-assembly observed in the aggregated structure is shown in Figure 3a. In non-polar solvents, polymer **1** folds into a highly compact structure due to intramolecular hydrogen bonds between the triazines. Multivalent interactions of polymer **1** with **Thy-Au** induce the unfolding of the compact structure of **1**, exposing further triazine recognition units. This allows polymer **1** to interact with further **Thy-Au** units, propagating the assembly process.
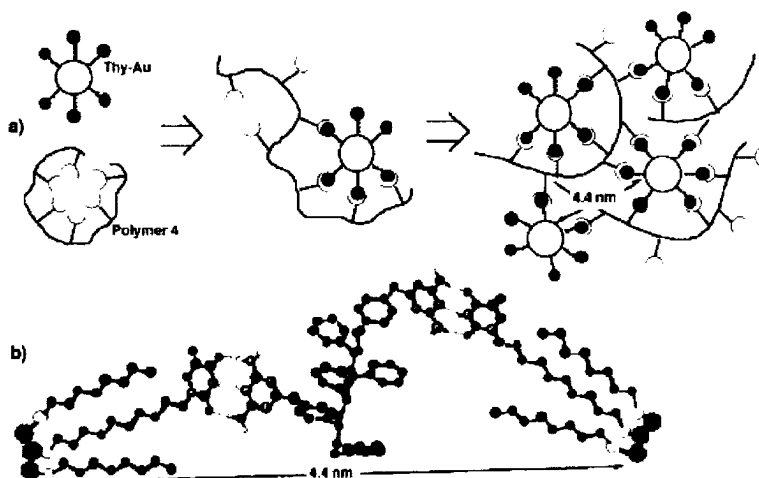
Figure 3. Proposed mechanism for **Thy-Au**-polymer **1** aggregation. a) Polymer mediated self-assembly of **Thy-Au**. with experimentally determined interparticle distance shown. b) Proposed polymer **1-Thy**-Au self-assembled structure (AMBER forcefield), with computationally predicted interparticle distance shown.

Insight into the structure of the polymer **4-Thy-Au** aggregate was obtained through molecular modeling (Figure 3b). Using a configuration of the polymer chain that spans the gold particles, a particle-particle distance of 4.4 nm is obtained, agreeing very well with the distance of 4.4±0.3 nm determined by SAXS. This provides a working model for the polymer conformation between the Au-Au particles. The influence of polymer molecular weight, polymer functionalization, particles size, and particle functionalization on the self-assembly process is currently under investigation.

Proof of the large-scale ordering suggested by SAXS was obtained using transmission electron microscopy (TEM). Micrographs of the THF-soluble fraction of the polymer **4-Thy-Au** precipitate reveal the formation of large highly regular, spherical clusters with diameters of 97 nm ± 17 nm in diameter. These clusters are comprised of 3000-7000 individual nanoparticles per microsphere. Significantly, the self-assembled microspheres are stable in polar solvents known to disrupt hydrogen bond interactions, providing further evidence that the macrostructure is stabilized by polyvalent polymer-colloid interactions. Roughly spherical aggregates of similar dimensions (~60 nm) were obtained from 6 nm analogs of **Thy-Au** and polymer **1**, demonstrating the applicability of our polymer-mediated approach to the assembly of different size nanoparticle subunits.

Self-assembly processes are governed by a balance of entropic and enthalpic effects, making them highly temperature dependent. This temperature dependence is manifested by more efficient recognition processes at lower temperatures,[21] a modification that would be expected to yield larger aggregate structures. Investigations of temperature effects on the preparation of the aggregates yielded intriguing results consistent with this prediction. TEM micrographs of the precipitate formed at –20°C revealed the formation of *microscale* (0.5-1 μm) discrete spherical

particles, comprised of $6x10^5$-$5x10^6$ individual Thy-Au units. These microscale particles are among the most complex synthetic self-assembled structures known, demonstrating the thermal control of aggregate size using the 'bricks and mortar' methodology.

In addition to controlling the size of the aggregates, temperature dramatically affects the morphology of the resulting ensembles. At 10°C, networks were formed, as opposed to the discrete structures observed at higher and lower temperatures. This suggests that network formation is an intermediate process in the formation of the giant assemblies at –20 °C. the individual assemblies within these networks remained spherical, although their sizes are more highly dispersed. We are currently investigating methods aimed at achieving control over the size and the geometry of these networks, which would allow the fabrication of rod- and wire-like structures for incorporation in nanoscale constructs.

ACKNOWLEDGEMENTS

1) Boal, A. K.; Ilhan, F.; DeRouchey, J. E.; Thurn-Albrecht, T.; Russell, T. P.; Rotello, V. M. "Self-assembly of nanoparticles into structured spherical and network aggregates" *Nature* **2000**, *404*, 746-748.
2) Deans, R.; Ilhan, F.; Rotello, V. M. "Recognition-mediated unfolding of a self-assembled polymeric globule" *Macromolecules* **1999**, *32*, 4956-4960.

Structural and Optical Properties of Gold In MgO:
Effects of Shape And The Interface

Elana M. Bryant, Akira Ueda, Richard R. Mu, Marvin H. Wu, Alkiviathes Meldrum[1] and Don O. Henderson
Chemical Physics Laboratory, Department of Physics, Fisk University, Nashville, TN 37208, USA
[1] Department of Physics, University of Alberta, Edmonton, Alberta, Canada

ABSTRACT

The fundamental studies of metallic nanoparticles embedded in various host materials have been made. The host-guest interaction causes the shapes of embedded nanoparticles, and the surface plasmon resonances of the metallic nanoparticles are affected by the host materials. The control of the surface plasmon resonance condition is a challenging question. We will discuss the interface effect of the systems where gold nanoparticles were fabricated between materials of MgO and SiO_2.

INTRODUCTION

Surface plasmon resonance (SPR) of small metallic particles has been studied since Mie's idea of 1908 about the study [1] of optical properties of gold particles, and in the past three decades the new field of cluster science has been developed with many potential applications. Although many studies have been published, there are still new interesting systems and there are fundamental questions to be answered. In our laboratory, we have studied the systems of several insulating materials implanted with gold ions (Al_2O_3:Au, CaF_2:Au, Silica SiO_2:Au, MgO:Au, Muscovite Mica:Au, and Vycor Glass:Au) and of the porous materials impregnated with gold (Vycor Glass: Au)[2-5].

In the systems of SiO_2:Au and MgO:Au fabricated by ion implantation, we have previously seen the growth of gold nanocrystals and found the SPR positions to be 530 nm and 560 nm, respectively, after a suitable thermal annealing in $5\%O_2+95\%Ar$ atmosphere. These SPR positions agree with the Mie's theory using a dipole approximation for spherical particles, that satisfies the following equation [6]:

$$\varepsilon\left(\omega_{SP}\right)+2\varepsilon_m = 0,\qquad(1)$$

where $\varepsilon(\omega)$ is the dielectric function of gold, ε_m is the dielectric function of host material, and ω_{SP} is the surface plasmon frequency.

As shown in figure 1, from our previous experiments, the gold nanocrystals in MgO have cubic shape, that aligns along the crystal axis of MgO (100), while the gold nanocrystals in SiO_2 are spherical. (The detail of this result will be discussed elsewhere.) If only the surface energy of gold particles plays the

Figure 1 TEM image of Gold nanocrystals fabricated in MgO single crystal by ion implantation with a post annealing. The shape of the gold nanocrystals is cubic and they align along the crystal axis of host MgO (100).

dominant role for the nanocrystal growth, the shape should be spherical. The host MgO crystal, therefore, must contribute to this result of cubic gold particles because MgO single crystal has a cubic crystal structure.

In this paper, we will discuss the interfacial interaction between gold nanocrystals and the dielectric hosts, in terms of dielectric constants and the crystal-amorphous character of host, by observing the SPR band of the system. In order to see the matrix dependence, we fabricated the following four systems: (1)Au deposited on MgO substrate with a MgO overcoat [MAM] , (2)Au deposited on SiO_2 substrate with a MgO overcoat [SAM], (3)Au deposited on MgO substrate with a SiO_2 overcoat [MAS], and (4)Au deposited on SiO_2 substrate with a SiO_2 overcoat [SAS]. Hereafter, the abbreviations for the systems MAM, SAM, MAS, and SAS will be used for simplicity: the each letter in the abbreviations from left to right represents the substrate material, gold deposition, and the overcoat materials, respectively.

EXPERIMENTAL

MgO substrates were single crystal plates (1" x 1" x 0.5 mm) with polished (100) surface obtained from Princeton Scientific Corporation. SiO_2 substrates were Corning 7940 optical grade Fused silica glass windows. Gold was deposited onto the substrates in a vacuum with the pressure of ~ 10^{-7} torr by the pulsed laser deposition method with a pico-second Nd:YAG laser. The used wavelength was 532 nm, which was the second harmonic of Nd:YAG laser. The laser beam energy was controlled with a cross polarizer. The used energy was 100 µJ per pulse with 10 Hz repetition rate for 60 min. Overcoating was carried out by electron beam evaporation with thickness of 100 nm and a deposition rate of 1.5 Å/sec for both SiO_2 and MgO in a vacuum of ~10^{-7} torr. UV-Visible spectra of the samples were taken before and after every thermal annealing with a Hitachi spectrophotometer. Thermal annealing was made with a tube furnace with Ar gas (99.995%) flow.

RESULTS AND DISCUSSIONS

Figure 2 shows the annealing temperature dependence of the UV-V absorbance spectra for four systems. Each spectrum was taken from a different sample annealed isothermally at a certain temperature as indicated. Since each sample may have a variance in gold density and in the thickness of overcoat materials, there should exist some fluctuation among spectra. However, according to these spectra, there are obvious differences and tendency among spectra for four types of systems. In general, at low annealing temperatures, there are SPR absorption bands tailing into longer wavelength because the prepared sample consists of an island-type gold film and the gold film may not be ruptured at low temperatures. The SPR bands became sharper as the annealing temperature increased, which indicates that the gold film had been ruptured and formed nano-meter size gold particles in the system. For the system with MgO overcoat (MAM and SAM), the SPR band dramatically decreased at the temperature greater than 1000°C, which indicated gold atoms escaped from the system through the thin overcoat with a thickness of 100 nm.

In Figure 3, the annealing temperature dependence of SPR peak position is shown, abstracted from the spectra in figure 2. For the system with MgO overcoat (MAM and SAM), SPR bands shifted to longer wavelength side at 400°C, while SPR positions for the system with SiO_2 overcoat (MAS and SAS) stayed up to the temperature below 700°C. At 600°C, for the system with MgO overcoat (MAM and SAM), SPR bands shifted to shorter wavelength side up to the temperature of 1000°C in the similar way, although the SPR positions themselves were different. Since gold atoms in MAM and SAM may have escaped above 1000°C, it is difficult to compare these four type systems. For the system with SiO_2 overcoat, SAS and MAS, above 900°C, the SPR

for MAS shifted to longer wavelength, while SPR for SAS shifted to shorter wavelength. The final SPR position for SAS (536 nm) is close to the SPR position 531-535 nm for the system of SiO_2 implanted with gold with post annealing. On the other hand, the SPR positions for the systems related to MgO substrate (MAM and MAS) were both longer wavelength side than the SPR position 560 nm for the system of MgO implanted with gold with post annealing. For the system of MAM, before the SPR band became weak at $900^\circ C$, the SPR peak was located at 583 nm. This result indicates that the SPR position dose not depends only on the dielectric function of the surrounding material.

Figure 2   Overview of UV-Vis spectra for four kinds of systems: (a) MgO|sub|/Au/SiO₂|coat|, (b) MgO|sub|/Au/MgO|coat|, (c) SiO₂|sub|/Au/SiO₂|coat|, and (d) SiO₂|sub|/Au/MgO|coat|.

Figure 3 The aneealing temperature dependence of SPR for four-types of system

Since there is a possibility to have anisotropic gold particles in the system, especially system MAM, we have measured transmission spectra of MAM using polarized light in two different geometry as shown in Figure 4. The first configuration (a) is for the absorption measurement of anisotropic gold particles by rotating the polarization plane relative to the crystal axis of MgO with normal incident. The second configuration (b) is for the absorption measurement of anisotropic gold particles by changing the incident angle with p-polarized light. The results are shown in Figure 5: Figure 5(a) shows transmission spectra in which there are no significant changes while the polarization plane rotates relative to crystal axis. Figure 5(b) shows the some effect of change in the incident angle on the SPR position, which suggests that there exists some anisotropy in the system although the reflection loss depends on incident angle and wavelength, which may cause shift of the SPR position.
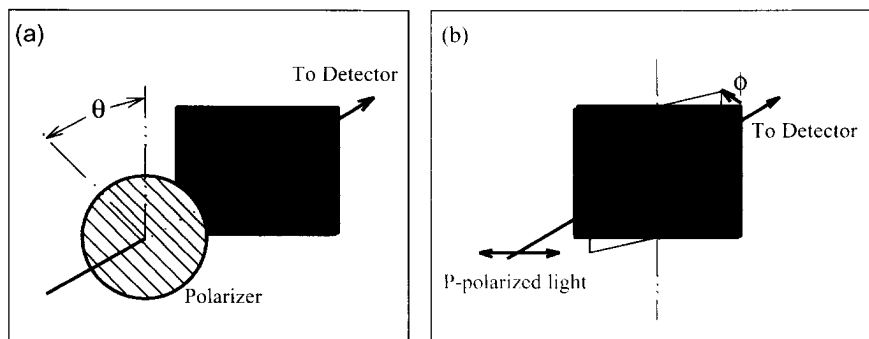
Figure 4 Two configurations for transmission measurements using polarized light
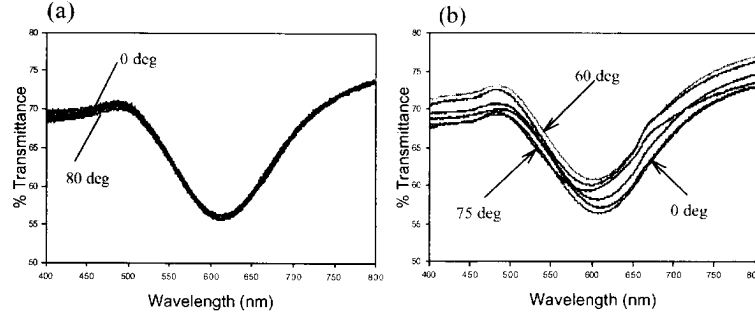
Figure 5 The transmission spectra for two types of configuration as shown in Figure 4 (a) and (b), respectively.

Figure 5(a) suggests that the gold particles have spherical symmetry around the axis normal to the interface and Figure 5(b) suggests that the gold particles have oblate spheroid shape (pancake shape) with a minor axis normal to the interface. Although the spectra in Figure 5(a) did not show the change due to the rotation of polarization, this does not mean that the gold particles do not have anisotropic shapes within the interface plane. The absorption cross-section due to a prolate spheroid (cigar shape) lying in the interface is given by [Warmack]

$$\sigma(\theta) = \frac{2\pi}{\lambda} \operatorname{Im}\left(\alpha_x \cos^2\theta + \alpha_y \sin^2\theta\right) \quad , \tag{2}$$

where the polarizability α_i's and depolarization factors n_i are given by, with the assumption that the major axis of prolate spheroid is y-component and the minor axis is x-component with the eccentricity of e,

$$\operatorname{Im}\alpha_i = \frac{\varepsilon_2 \varepsilon_m n_i}{\left[\varepsilon_m + (\varepsilon_1 - \varepsilon_m)n_i\right]^2 + (\varepsilon_2 n_i)^2} V \tag{3}$$

$$n_y = \frac{1-e^2}{2e^3}\left(Ln\frac{1+e}{1-e} - 2e\right) \text{ and } n_x = \frac{1}{2}(1 - n_y). \tag{4}$$

Here the angle θ is taken between the major axis of spheroid and the polarization of the incident light, and V is the volume of the gold particle. If 50% of prolate spheroids distribute in (100) direction and the other 50% distribute in (010) direction, then the total absorption cross-section becomes

$$\bar{\sigma}(\theta) = \frac{2\pi}{\lambda} \operatorname{Im}\left[\frac{1}{2}\left(\alpha_x \cos^2\theta + \alpha_y \sin^2\theta\right) + \frac{1}{2}\left(\alpha_x \sin^2\theta + \alpha_y \cos^2\theta\right)\right] = \frac{\pi}{\lambda}\operatorname{Im}\left[\alpha_x + \alpha_y\right]. \tag{5}$$

This does not effectively depend on the angle θ, so that we may not have seen the polarization dependence. In order to see the particle shapes, the direct measurement of the particle shape is necessary with TEM, and TEM measurements are in the process.

According to the comparison among the four-type systems (MAM, MAS, SAM, and SAS), SAS system probably has spherical gold because we saw SPR around 530 nm, while the other systems may have anisotropic gold particles. For SAS, the coated SiO_2 fuses to the substrate SiO_2 during the annealing, and then gold particles could relax to form spherically shaped particles. For the hetero-system, MAS and SAM, the coated material would not fuse to the substrate material, and then the shape of gold particle remains anisotropic, which is most likely oblate spheroid shape. For homo-system, MAM, we may have prolate spheroid as well as oblate spheroid.

There may have other possibilities to explain the spectra, one of which is the aggregation of gold particles. Before annealing, an imperfect gold film was formed by laser ablation, which consists of many small gold particles. A particle can interact with the other particles through the induced dipole moments as long as the distance between particles is short enough. This interaction causes other modes locating at longer wavelengths.

Conclusion

We have proposed a fabrication method to produce a system of anisotropic gold nanoparticles, which may control the SPR position. For the fundamental point of view, it is interesting to see the effect of materials that contact gold particles in these systems.

Reference

[1]G. Mie, Ann, Physik **25**, 377(1908). (German)

[2]D.O. Henderson, Y.-S. Tung, A. Ueda, R. Mu, Y. Xue, C. Hall, W.E. Collins, C.W. White, R.A. Zuhr, Jane G. Zhu, and P.W. Wang, J. of Vacuum Science and Technology **A 14**(3), 1199(1996); D.O. Henderson, Y.-S. Tung, R. Mu, A. Ueda, J. Chen, R. Gu, C.W. White, Jane G. Zhu, M. McKay, and O. Scott., International Conference of Defects in Insulating Materials, Wake Forest University, Winston-Salem, NC, USA, 1996. Materials Science Forum **239-241**, 695(1997).

[3]Z. Gu, R. Mu, A. Ueda, Y.-S. Tung, M.H. Wu, D.O. Henderson, A. Meldrum, C.W. White, and R.A. Zuhr, JVST **A16**(3), 1409(1998).

[4]A. Ueda, D.O. Henderson, R. Mu, Y.-S. Tung, C.W. White, Jane G. Zhu, International Conference of Defects in Insulating Materials, Wake Forest University, Winston-Salem, NC, USA, 1996. Materials Science Forum **239-241**, 675(1997); A. Ueda, R. Mu, Y.-S. Tung, M. H. Wu, W.E. Collins, D.O. Henderson, C.W. White, R.A. Zuhr, J.D. Budai, A. Meldrum, P.W. Wang, and Xi Li, Nucl. Instru. Mater. Method in Phys. Res. **B 141** 261(1998).

[5]D.O. Henderson, R. Mu, A. Ueda, Y.-S. Tung, C.W. White, R.A. Zuhr, and Jane G. Zhu, J. of Non-Crystalline Solids, **205/207**, 788(1996). The Ninth International Conference on Liquid and Amorphous Metal, Chicago, IL October 8-13, 1995, Proceedings; Y.-S. Tung, R. Mu, D.O. Henderson, A. Ueda, C.W. White, Jane G. Zhu, International Conference of Defects in Insulating Materials, Wake Forest University, Winston-Salem, NC, USA, 1996. Materials Science Forum **239-241**, 691(1997).

[6]U. Kreibig and M. Vollmer, "Optical Properties of Metal Clusters," Springer Series in Materials Science **25** (Springer, New York, 1995).

[7]P. Clippe, R. Evrard, and A.A. Lucas, Phys. Rev. B14, 1715(1976); M. Ausloos and P. Clippe, Phys. Rev. **B18**, 7176(1978).

**Metallic Nanoparticles
and Clusters II**

Optical Properties of Nanoparticle Pair Structures

Marie L. Sandrock, Mahnaz El-Kouedi, Maryann Gluodenis and Colby A. Foss, Jr.[1]
Department of Chemistry, Georgetown University, Washington, District of Columbia 20057.
[1]Current address: Trex Enterprises Corporation, 3038 Aukele Street, Lihue, Hawaii, 96766.

ABSTRACT

The synthesis of nanoparticle pair structures via porous host electrochemical template synthesis reviewed. Electrochemical template synthesis offers two advantages over solution methods, namely: 1) control over particle pair structure and orientation; and 2) control over geometry, size and composition of each member of the particle pair. These features of electrochemical template synthesis allow for straightforward comparison of experimental and theoretical spectra. Orientation control allows for the evaluation of second order nonlinear optical properties of centrosymmetric and non-centrosymmetric nanoparticle pair systems. The dependence of Second Harmonic Generation intensity on particle pair shape size and orientation is discussed. The synthesis and linear spectra of metal-semiconductor nanoparticle pair structures are also discussed, with emphasis on interparticle physical and electromagnetic interactions.

INTRODUCTION

There are numerous methods for synthesizing nanoscopic metal particles, such as bulk solution reduction of metal salts [1,2], electric discharge [3], vacuum deposition [4], and template synthesis [5,6]. Template synthesis involves the use of a host material whose pores define the geometry of the structures grown within it, for example via electrochemical deposition of metals. In the last decade, there has been an increasing interest in the optical properties of nanoscopic metal particle structures, with a keen emphasis on how optical properties depend on particle size, shape, composition, and orientation in the incident field. Electrochemical template synthesis is well-suited for fundamental optical studies on nanoparticle structures because it allows for the control of particle size, shape and orientation. A common porous host material is anodic aluminum oxide, which possesses not only well-defined parallel arrays of cylindrical pores, but is also transparent through most of the visible and near-infrared spectrum.

A number of previous studies have focused on the optical properties of metal spheres and rods grown in porous aluminum oxide [5-9]. In our laboratories, we have extended the electrochemical template synthesis method to metal nanoparticle pair structures, where both members of the pair are spheres or rods of equivalent dimensions, or where the pair structure is non-centrosymmetric (e.g., composed of a sphere and a rod, or two rods of different dimensions). We have been able to examine the linear spectra as a function of particle shape and interparticle spacing [10], and compare the second harmonic generation (SHG) signals produced by centrosymmetric and non-centrosymmetric structures [11]. We have also extended the template synthesis method to pair structures where one member is a metal and the other is a semiconductor [12,13].

In this paper, we review the synthesis of nanoparticle pair structures, and present some of our recent results on the SHG of gold nanoparticle pairs, and the linear spectra of gold/silver iodide nanoparticle pair structures.

A Pore wall • Pore •
Silver Sputter Deposition

B

C Au electroplating

D After nitric acid etch of Ag
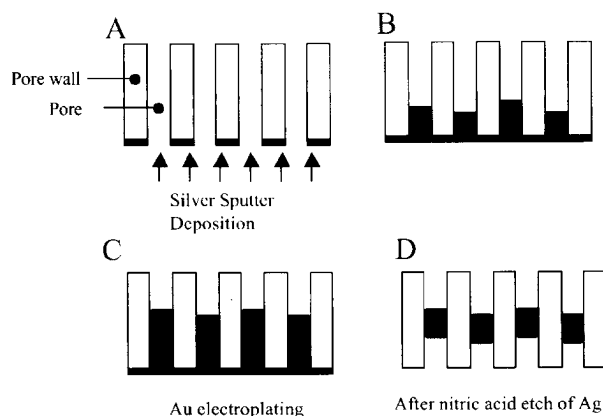
Figure 1. Schematic of the electrochemical template synthesis for single particle structures. A. Porous template host is coated with silver to provide a conductive layer. B. With the silver coat as the working electrode, additional silver is deposited electrochemically to form a foundation of silver rods. C. Gold is deposited onto the silver foundation to form gold nanorods. The aspect ratio is controlled by the pore diameter and the amount of gold deposited. D. The silver foundation is removed via nitric acid etching, leaving isolated gold structures within the pores.

EXPERIMENTAL DETAILS

Figure 1 shows a schematic of the electrochemical template synthesis method for preparing single rods. One face of the porous film is coated with silver using a plasma deposition device (Anatech Hummer 10). The coated film is then placed in an electrochemical cell such that only the uncoated face is exposed to silver plating solution [14]. Additional silver metal is deposited potentiostatically until the coated face is sealed and silver rods grow part way into the film. The silver plating solution is then removed, the cell rinsed with distilled water, and then filled with Au(I) cyanide plating solution (Orotemp 24, Technic, Inc.). The deposition current is integrated to provide a continuous indication of the progress of the gold deposition. The length of the gold rods can be controlled by halting the deposition after a certain number of coulombs has passed [7]. Once the gold deposition is complete, the metal/host film composite is immersed in concentrated nitric acid to remove the silver foundation. In the majority of our studies, the host film was porous anodic aluminum oxide, which we prepare from ultrapure aluminum. Details of the aluminum anodization are given elsewhere [6,8].

Figure 2A shows the electrochemical template synthesis scheme for metal nanoparticle pair structures. Following step C in figure 1, instead of proceeding to the Ag etch step, additional silver is deposited onto the gold layer. Gold is then deposited onto the second silver layer. The spacing between the two gold structures is determined by the thickness of the silver spacer layer. Finally, the silver foundation and spacer layers are removed via nitric acid etch.

In figure 2B, we summarize the electrochemical template synthesis of gold/silver iodide nanoparticle pair structures. Again following step C in figure 1, additional silver is deposited onto the gold layer. This second silver layer is then oxidized in the presence of an aqueous potassium iodide solution (1 M). This results in the precipitation of AgI in the vicinity of the gold layer. If the entire second layer of Ag is converted to AgI, the resulting AgI semiconductor phase is in intimate contact with the gold metal layer. However, if some of the Ag layer is left

2A: Metal Pair Synthesis

Deposit
second Ag
layer

Deposit
second Au
layer

After nitric acid
etch of Ag
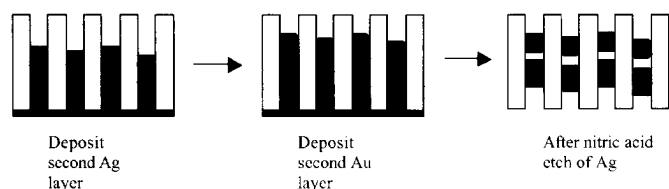
2B: Metal/Semiconductor Pair Synthesis

Deposit
second Ag
layer

Convert
Second Ag
Layer to AgI

After nitric
acid etch of
Ag
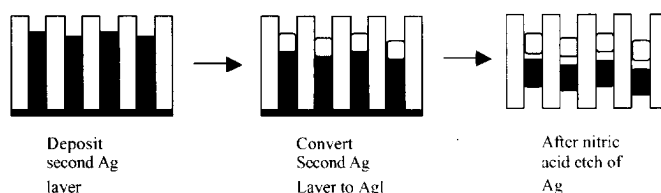
Figure 2. *A. Electrochemical template synthesis of gold nanoparticle pair structures. B. Electrochemical template synthesis of gold/silver iodide nanoparticle pair structures.*

unoxidized, its subsequent removal in the nitric acid etch step results in Au and AgI particles which are, on average, separated by certain distance within each pore.

In our laboratory, all electrochemical deposition and oxidation steps were performed potentiostatically using an EG&G Princeton Applied Research Model 273 potentiostat. The exposed plating area of each film was ca. 3.14 cm^2. The reference electrode in all cases was a silver chloride coated silver wire immersed in 4M KCl, and separated from the plating solution by a Vycor® porous glass junction. The counter electrode was platinum mesh (ca. 1 cm^2).

Structural characterization of the particles involved imbedding the aluminum oxide composites in resin, and microtoming sections thin enough for transmission electron microscopic (TEM) imaging. A JEOL 1200 EX TEM was used for all characterizations.

Linear optical characterization was performed using a Hitachi U3501 UV/Visible/Near-IR spectrometer, equipped with a model 210-2130 polarizer accessory. SHG measurements were performed using a mode locked titanium:sapphire laser pumped with an argon ion laser. The details of the laser setup are described elsewhere [11,15]. The basic optical setup is shown in figure 3. The thin aluminum oxide film (typically 40-50 μm in thickness) is mounted in a
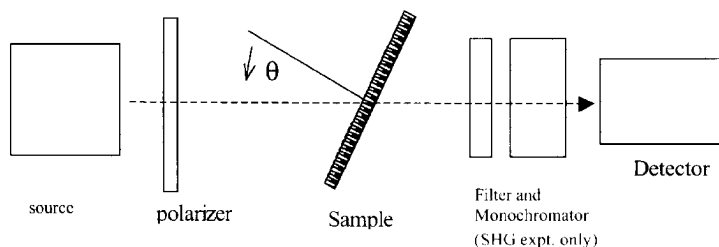
Figure 3. *Schematic of the optical sample configuration for linear and nonlinear optical studies. In the figure above, the incident light is defined as p-polarized (φ⁻ 0°) when the electric field is polarized in the plane of incidence (also plane of the page). s-polarization (φ= 90°) corresponds to the electric field polarized in the plane of the sample (perpendicular to the plane of the page).*

sample holder which affords control over the incidence angle (θ, measured versus the surface normal) of the source beam. The polarizer defines the polarization angle ϕ. In the case of the SHG measurements, the incident wavelength is ca. 800 nm. A cut-off filter between the sample and detector removes the incident wavelength, and a monochromator isolates the SHG signal at ca. 400 nm [11,15].

RESULTS

Some examples of the gold nanoparticle pair structures that we have prepared via electrochemical template synthesis are shown in figure 4. These TEM images are cross sections through the template host aluminum oxide films. The template synthesis method allows for the control of metal nanoparticle dimensions and pair spacing, but only in an average sense. The standard deviation of most parameters (length, diameter, and spacing) is 10% or greater, which is certainly a lower precision than modern optical and electron beam lithographic methods can achieve. However, electrochemical template synthesis is inexpensive, and low tech enough to be executed in even modestly equipped laboratories. In spite of the shortcoming in terms of dimensional precision, the method has allowed us to perform some basic optical investigations and gain important insights into nanostructure-optical property relationships.
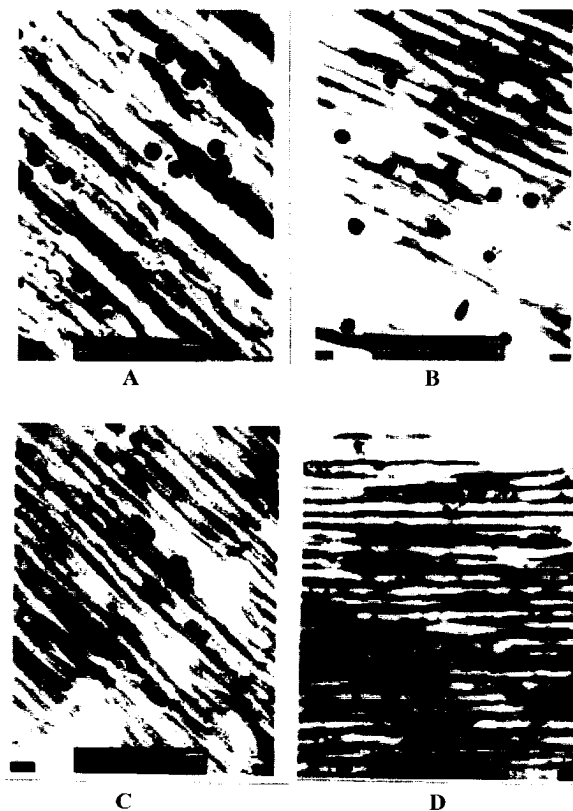
Figure 4. *Gold nanoparticle pair structures prepared in porous anodic aluminum oxide via the electrochemical template synthesis method. A. 32 nm diameter sphere pairs, edge-edge spacing ca. 20 nm. B. 32 nm sphere pairs, edge-edge spacing ca. 80 nm. C. Centrosymmetric rod pairs (diameters = 30 ± 3 nm, lengths = 70 ± 10 nm, edge-edge spacing 70 ± 20 nm). D. Non-centrosymmetric rod-sphere pairs (rod dimensions: length= 100 ± 10 nm, diameter ~ 33 ± 4 nm; sphere-like segment length ~ 34 ± 5 nm, diameter = 33±4 nm). Scale bar (white bar in image caption box) 50 nm in all images.*

To examine the effects of interparticle spacing on the optical spectra of metal nano-particles, we conducted polarization spectroscopy measurements on the samples corresponding to the TEM images in figures 4a and 4b. The plasmon resonance bands of the gold nanoparticle pairs were measured under p-polarization as a function of incidence angle θ. Table I summarizes the results.

Table I. Effect of Interparticle Spacing on Plasmon Resonance Maximum

Sample	λ_{max}(nm) $\theta = 0°$	λ_{max}(nm) $\theta = 20°$	λ_{max}(nm) $\theta = 30°$	λ_{max}(nm) $\theta = 45°$
32 nm diameter Au spheres, Separation distance 20 nm	539	543	549	558
32 nm diameter Au spheres, Separation distance 80 nm	548	548	548	548

It is clear that when the average spacing between the two spheres is small, their plasmon resonance maximum is incidence angle dependent. As θ increases, and increasing component of the incident electric field is parallel to the particle pair axis. If the induced electric field of one particle is sensed by its partner, the plasmon resonance maximum will be red-shifted. At large separations, the particles are not electromagnetically coupled, and thus their spectral maxima are independent of the incidence angle. These observations are in qualitative accord with simple quasistatic model predictions [10,15]. However, the experimental spectral bands are considerably broader than those predicted by theory.

In the case of molecular materials, second order nonlinear optical behavior is expected only when the crystalline solid (or local ensemble subject to measurement) lacks inversion symmetry [16]. One of our primary motivations for extending the template synthesis to particle pair structures was to prepare nanoscale structures that lack inversion symmetry, and then investigate their second order nonlinear optical properties. Using the optical configuration shown in figure 3, we measured the SHG signal from two sample types, centrosymmetric gold rods and non-centrosymmetric gold rod-sphere pairs. The dimensions of each system were chosen such that their linear optical properties were similar, both in terms of the position the spectral maxima, and also the absolute optical density. This was done so that local field enhancements would be similar in both systems, and thus allow us to focus specifically on nanostructure symmetry.

Figure 5 summarizes the results of the first SHG study, which involved particles of moderate aspect ratio (length/diameter), which we shall refer to as Group I. It is clear that in p-polarization, the SHG counts for the non-centrosymmetric system are significantly higher than in the case of the centrosymmetric rods. In figure 5B, the increase in SHG counts with θ are expected, as an increasing incidence angle implies a larger component of the electric field along the asymmetry axis of the pair. Neither sample showed significant SHG counts in s-polarization. In figure 6, we show an analogous set of plots for higher aspect ratio particles (which we refer to as Group II). It is interesting that in p-polarization, the SHG counts for the centrosymmetric and non-centrosymmetric systems are similar. Furthermore, both samples in Group II give significantly higher SHG counts than the samples of Group I.

While a more detailed interpretation will be given elsewhere [17], the comparison of the Group I and Group II studies suggests the following: for second order nonlinear optical behavior in nanoparticle systems, symmetry is more important when the particles are small. As the particles increase in size, second order effects such as SHG become less sensitive to symmetry. This preliminary interpretation would indicate that the well-known electric dipole approximation [16] which is the context in which the second order nonlinear optical properties of molecular systems is discussed, is not generally applicable to nanoparticle systems. This is consistent with the fact that other electromagnetic induction modes become significant as the particle dimensions
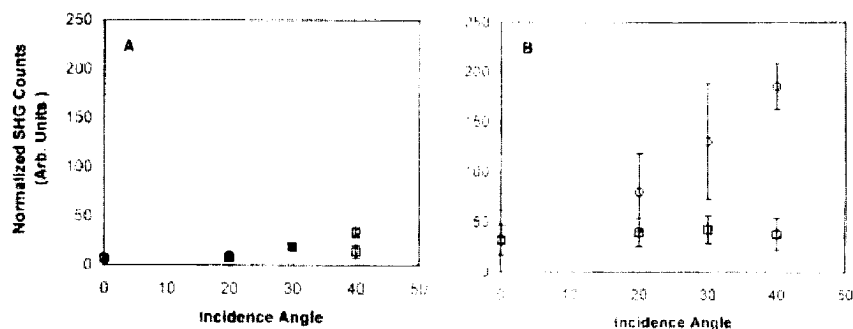
Figure 5. SHG counts for centrosymmetric and noncentrosymmetric gold nanoparticle structures (Group I) versus incidence angle θ. Open circles correspond to p-polarization. Open squares are counts obtained in s-polarization. Error bars based on standard deviation of measurements on three different locations on film samples. All counts normalized to signal from a slurry of potassium dihydrogen phosphate crystals in decahydronaphthalene. A. Centrosymmetric rods, length = 54 ± 7 nm, diameter = 30 ± 4 nm. **B.** Non-centrosymmetric rod-sphere pairs. Rods: length – 37 ± 6 nm, diameter – 26 ± 3 nm. Spheroids: length – 27 ± 5 nm, diameter – 26 ± 3 nm. Edge-edge spacing = 22 ± 8 nm.
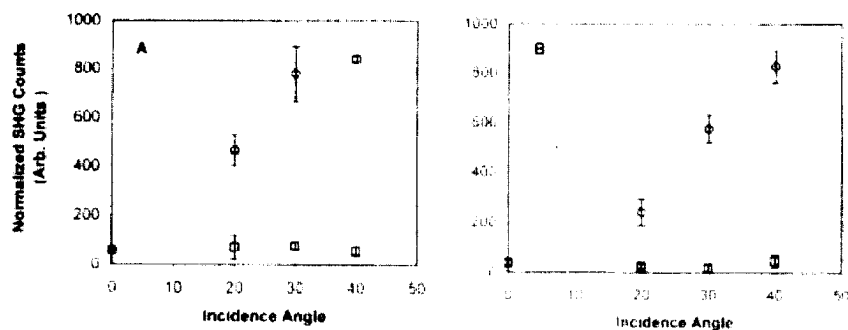
Figure 6. SHG counts for centrosymmetric and noncentrosymmetric gold nanoparticle structures (Group II) versus incidence angle θ. Open circles correspond to p-polarization. Open squares are counts obtained in s-polarization. Error bars based on standard deviation of measurements on three different locations on film samples. All counts normalized to signal from a slurry of potassium dihydrogen phosphate crystals in decahydronaphthalene. A. . Non-centrosymmetric rod-sphere pairs. Rods: length = 100 ± 10 nm, diameter = 33 ± 4 nm. Spheroids: length =34 ± 5 nm, diameter = 33 ± 4 nm Edge-edge spacing = 57 ± 13 nm. **B.** Centrosymmetric rods, length = 133 ± 20 nm, diameter = 31 ± 4 nm.

increase. For example, the magnetic dipole and electric quadrupole oscillations can produce a second harmonic signal even from centrosymmetric particles [18]. We should note that because

the increased aspect ratio of the Group II particles caused their long axis plasmon resonance to coincide more closely with the incident laser wavelength, we considered the possibility that huge local fields may be enhancing weak magnetic dipole and electric quadrupole modes (hence, the important difference between Group I and Group II is not overall particle size, but the aspect ratio). While this remains a distinct possibility, our local field calculations, which take into account particle shape and size [19] suggest that local field enhancements are negligible.

Another approach to achieving non-centrosymmetric pair structures is for the two pair members to be composed of different materials. We originally prepared the gold/silver iodide pair structures according to the scheme in figure 2B with the intention of investigating their potential for SHG. While these systems proved too photochemically fragile for laser work, their linear optical spectra revealed other issues which are quite relevant to nanoparticle technology.

As we seek to prepare nanoparticle structures of increasing geometric and compositional complexity, two key issues are 1) the nature of the electromagnetic interaction between particles composed of different materials, and 2) in the case where the two particles are in contact, the nature of the interface between two dissimilar materials. When we first prepared gold/silver iodide particle systems, we expected the linear optical spectra to reflect a weighted sum of the two materials; the gold particle component should exhibit a plasmon resonance band near 520 nm, and the silver iodide should show a band edge and sharp exciton feature at 425 nm. However, the first spectral studies, which considered gold and silver iodide phases in intimate contact, showed gold plasmon resonance bands that were red-shifted and severely broadened. Furthermore, the silver iodide exciton peak was absent [12]. When we synthesized the particle pair such that there was a space between the metal and semiconductor phases, the gold plasmon resonance band narrowed and shifted back to its expected λ_{max} [13] (See the spectral curves in figure 7 which pertain to contacting and spaced particles).

As we were unable to model the experimental spectra assuming bulk optical properties for gold and silver iodide, and thus concluded that material cross-contamination was likely occurring. Using effective medium type theories and a modified Drude free electron model for the metal phase, we simulated both atomic level mixing and gross aggregate formation of large domains of semiconductor in the metal phase, and vice versa [13]. The simulated spectra showed red-shifting and broadening of the gold plasmon resonance similar to the experimental results.

The cross-contamination hypothesis led us to modify slightly the template synthesis scheme shown in figure 2B. After the gold layer is deposited, the gold plating solution is removed and replaced with an aqueous potassium sulfide solution. A potential sufficiently positive to cause oxidation of the gold is applied briefly, resulting in the formation of a thin layer of gold sulfide (Au_2S). Silver is then deposited onto the sulfide coated gold surface, and subsequently converted to silver iodide. The middle curve of figure 7 shows the consequences of adding a gold sulfide layer: the gold plasmon resonance band recovers its position and shape (it is nearly identical to the band corresponding to gold particles separated from the silver iodide by an air gap), but the exciton peak is still absent. Our preliminary interpretation is that the gold sulfide layer prevents contamination of the gold phase by silver or iodine atoms of the AgI phase. The persistent absence to the AgI exciton may be due to the close proximity of the metal phase (the high concentration of free electrons in the gold may promote image charges which destabilize electron-hole interactions in the semiconductor phase.
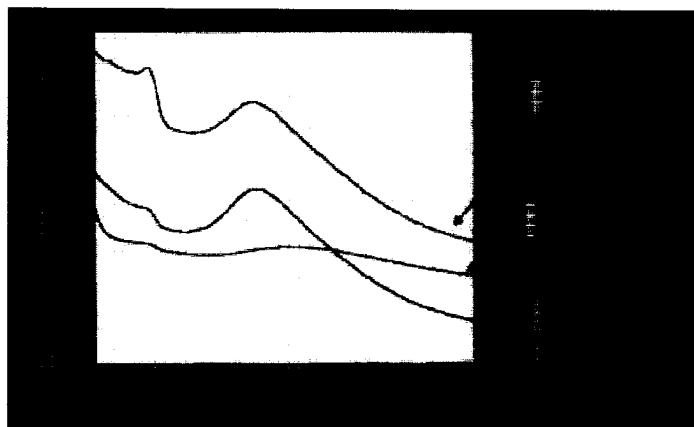
Figure 7. *Linear optical spectra of gold/silver iodide nanoparticle pair structures. All spectra were obtained at normal incidence (See figure 3). Spectral curves are on same relative absorbance scale, but displaced vertically and arbitrarily for clarity.*

CONCLUSIONS

The electrochemical template synthesis method offers a straightforward and inexpensive means for preparing nanoparticle pair structures. The variety of structures includes both centro- and noncentro- symmetric metal pairs, and metal-semiconductor pairs. While the method does not currently afford precise control over particle dimensions (at least compared to modern lithographic techniques), it has allowed us to gain insight into nanostructure-optical property relationships. Second order nonlinear optical properties can be achieved in nanomaterials, but the absence of inversion symmetry may be a strict requirement only when the nanoparticles are small and amenable to the dipole approximation. Complex nanostructures that involve particles composed of different materials may engender the risk of cross contamination, especially if the two phases are placed in physical contact. As we seek to prepare nanostructures with increased geometric and compositional complexity, we will need to develop synthetic strategies for controlling the interface between particles.

ACKNOWLEDGMENTS

REFERENCES

1. M.A. Hayat, *Colloidal Gold: Principles, Methods and Applications*, (Academic Press, 1989).
2. J.E. Beesley, *Proc. Royal Microscop. Soc.*, **20**, 187 (1985).
3. Faraday, M., *Philos. Trans.*, **147**, 145 (1857).
4. J.C. Hulteen and R.P. van Duyne *J. Vac. Sci. Tech.*, **13**, 1553 (1995).
5. M.J. Tierney and C.R. Martin, *J. Phys. Chem.*, **93**, 2878 (1989).
6. C.K. Preston and M. Moskovits *J. Phys. Chem.*, **92**, 2957 (1988).
7. C.A. Foss, Jr., M.J. Tierney, and C.R. Martin, *J. Phys. Chem.*, **96**, 9001 (1992).
8. C.A. Foss, Jr., G.L. Hornyak, J.A.Stockert, and C.R. Martin, *J. Phys. Chem.*, **98**, 2963 (1994).
9. N.A.R. Al-Rawashdeh, M.L. Sandrock, C.J. Seugling, and C.A. Foss, Jr., *J. Phys. Chem. B*, **102**, 361 (1998).
10. M.L. Sandrock and C.A. Foss, Jr. *J. Phys. Chem. B*, **103**, 11398 (1999).
11. M.L. Sandrock, C.D. Pibel, F.M. Geiger, and C.A. Foss, Jr., *J. Phys. Chem. B*, **103**, 2668 (1999).
12. M. El-Kouedi, M.L. Sandrock, C.J. Seugling, and C.A. Foss, Jr. *Chem. Mater.* **10**, 3287 (1998).
13. M. El-Kouedi and C.A. Foss, Jr. *J. Phys. Chem. B*, **104**, 4031 (2000).
14. N.A. Shumilova and G.V. Zutaeva, in *Encyclopedia of Electrochemistry of the Elements*, ed. A.J. Bard (Marcel Dekker, 1978).
15. M.L. Sandrock, PhD Dissertation, Georgetown University, 2000.
16. R.W. Boyd, *Nonlinear Optics*, (Academic Press, 1992).
17. M.L. Sandrock and C.A. Foss, Jr., manuscript in preparation.
18. X.M. Hua and J. I. Gersten, *Phys. Rev. B*, **33**, 3756 (1983).
19. M. Meier and A. Wokaun, *Optics Lett.*, **8**, 851 (1983).

Strain Anisotropies in Core/Shell Magnetic Nanostructures

Georgia C. Papaefthymiou
Department of Physics, Villanova University, Villanova, PA 19085

ABSTRACT

The magnetic properties of nanosized iron-oxo molecular clusters have been investigated via Mössbauer spectroscopy and compared to those of silica coated iron-oxide nanoparticles. The clusters, prepared by controlled hydrolytic iron polymerization reactions, contain a ~ 1.2 nm diameter magnetic core of spin-coupled iron ions surrounded by a shell of benzoate ligands. The nanoparticles, prepared via sol-gel synthesis, contain a ~ 4.0 nm average diameter γ-Fe_2O_3 core coated by a shell of SiO_2. Both systems exhibit magnetic bistability at low temperatures with estimated magnetic anisotropy constants of $K_{eff} = 0.63 \times 10^5$ J/m^3 for the clusters and $K_{eff} = 0.55 \times 10^5$ J/m^3 for the particles. The similar values of K_{eff} indicate that these two systems experience similar degrees of strain at the core/shell interface. This is further supported by the values of the quadrupole splitting, $\Delta E_Q = 0.77$ mm/s for the clusters and $\Delta E_Q = 0.75$ mm/s for the particles, pointing to same degree of distortion from pure octahedral or tetrahedral symmetry at the iron coordination sites for either system. Implications of these observations for the surface atomic structure of γ-Fe_2O_3 nanoparticles are discussed.

INTRODUCTION

It has been widely observed that values of magnetic anisotropies in small particles exceed by two orders of magnitude those of their corresponding bulk magnetocrystalline anisotropies [1]. This has been attributed to the dominating effect of surface strain anisotropies in small particles. In this respect, core/shell magnetic nanostructures are of special interest as surface strain anisotropy on the magnetic core can be altered through core/shell interface microstructure manipulation. Given the important technological applications of small magnetic particles in magnetic memory storage [2] and biotechnology [3], better understanding and greater control of surface strain at the atomic level is desired.

Small core/shell particles, of ~3-10 nm diameter, are produced in finite particle size distributions leading to broad X-ray diffraction patterns. This makes detailed structural characterization of the particle core/shell interface difficult. In contrast, nanosize core/shell molecular complexes, of ~ 1-2 nm diameter, can be synthesized as monodispersed, identical, chemical structures which are amenable to X-ray structural characterization [4]. Such clusters lie at the molecular/solid boundary and exhibit collective magnetic phenomena [5]. Comparative studies of related systems may shed light at core/shell interface structural characteristics in small particles.

We have examined the electronic and magnetic properties of two iron based, nanoscale core/shell structures derived by self-assembly, co-precipitation techniques. The first structure is a nanosized iron-oxo molecular complex of the form $Fe_{16}MnO_{10}(OH)_{10}/(O_2CPh)_{20}$ [1], and the second is γ-Fe_2O_3/SiO_2 [2] nanoparticles. A comparative Mössbauer spectroscopic study of their micromagnetic properties is presented. Implications on the degree of coordination distortion of iron sites at the core/shell interface needed to produce the observed strain anisotropies of small iron-oxide magnetic particles are discussed.

MATERIALS

Iron polymerization in aqueous solutions results in the uncontrollable formation of mixtures of high molecular weight polymers. The generation of monodispersed iron-oxo nanoclusters requires competitive reaction chemistry between core cluster growth to form bulk material and cluster encapsulation by terminal ligation to arrest further core growth [5]. By using aprotic solvents as the reaction medium and adding water, needed for hydrolysis, and an organic base in limited quantities, a certain degree of control of the extent of polymerization and resulting size of the cluster can be achieved. Structurally characterized iron-oxo clusters of nuclearity Fe_3, Fe_4, Fe_6, Fe_{11} and Fe_{17} (and heterometal $Fe_{16}Mn$, $Fe_{16}Co$) have been reported [6]. Herewith, we revisit the structural and magnetic characteristics of the heterometal cluster $Fe_{16}MnO_{10}(OH)_{10}/(O_2CPh)_{20}$ [1] [7]. Sixteen Fe^{3+} (S=5/2) and one Mn^{2+}(S=5/2) ions superexchange-coupled through oxygen bridging ligands form a magnetic core of $ca.$ 1.2 nm diameter. A surrounding shell of 20 benzoate ligands stabilizes and disperses the magnetic cores. The structure is centrosymmetric with eight unique iron crystallographic sites. See Figures 1a and b. This is a neutral molecule forming crystals through van der Waals forces.
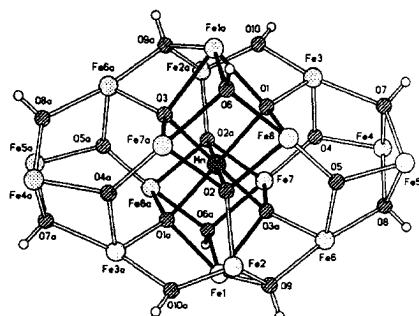
Figure 1(a). Perspective view of the metal atoms in $Fe_{16}MnO_{10}(OH)_{10}/(O_2CPh)_{20}$ [1] cluster's magnetic core. Atoms are shown as spheres of arbitrary radius for clarity. Adapted from ref. [6].
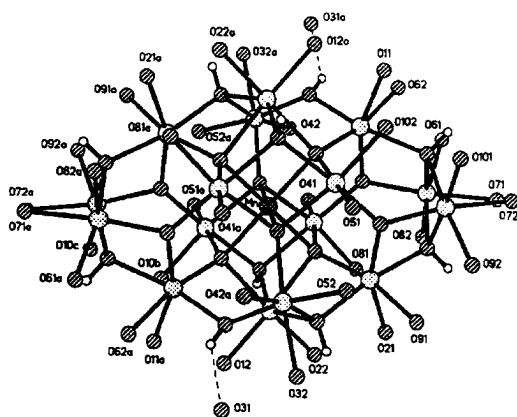
Figure 1(b). Perspective view of metal atoms in cluster [1] including the iron coordinated benzoate oxygen atoms of the shell. Atoms are shown as spheres of arbitrary radius for clarity. Adapted from ref. [6].

C2.4.2

Bulk γ-Fe_2O_3 has a spinel structure with Fe^{3+} (S=5/2) ions situated in octahedral and tetrahedral sites. Herewith, we report on γ-Fe_2O_3 nanoparticles prepared by a sol-gel co-precipitation method, previously reported [7]. A mixture of $FeCl_2$ and $FeCl_3$ was used as starting material in order to promote crystallization of the ferrimagnetic γ-Fe_2O_3 spinel structure over the antiferromagnetic α-Fe_2O_3 structure. An inert SiO_2 coating stabilized and dispersed the particles. The γ-Fe_2O_3/SiO_2 nanocomposites were obtained as a reddish brown powder. The morphology of the magnetic particles was studied with transmission electron microscopy. TEM micrographs (Fig. 2(a), ref. [7]) indicate well-dispersed γ-Fe_2O_3 particles of average size *ca.* 4-nm diameter.

EXPERIMENTAL RESULTS

We have used Mössbauer spectroscopic methods to study the microstructural and micromagnetic properties of the [$Fe_{16}Mn$] cluster [1] and the γ-Fe_2O_3/SiO_2 particles [2]. A conventional constant acceleration Mössbauer spectrometer was used with a $^{57}Co(Rh)$ source maintained at room temperature. Sample temperatures were varied using a Lakeshore temperature controller and a Janis supervaritemp cryogenic dewar.

Mössbauer spectra of [1], cluster complex $Fe_{16}MnO_{10}(OH)_{10}/(O_2CPh)_{20}$, are shown in Figure 2. At 10 K, and higher temperatures, the spectrum is paramagnetic, with a quadrupole splitting ΔE_Q=0.77 mm/s and isomer shift δ = 0.51 mm/sec measured at 80 K, consistent with high spin S=5/2 ferric ions. At low temperatures the spectra are superparamagnetic. At 1.8 K a well defined magnetic, six-line absorption spectrum is obtained indicating that the complex has passed from fast to slow spin relaxation on the Mössbauer time scale ($\tau = 10^{-8}$ sec). A blocking temperature T_B = 4 K is estimated. The overall splitting of the magnetic spectra indicates an internal magnetic field at the iron nucleus of H_{hf} = 400 kOe.

Mössbauer spectra of structure [2], γ-Fe_2O_3 /SiO_2 nanoparticles are shown in Figure 3. At high temperatures the spectra are paramagnetic with ΔE_Q= 0.75 mm/s and δ = 0.43 mm/sec measured at 130 K. Below 30 K superparamagnetism is observed. Broader and noisier spectra compared to [1] are seen due to the existence of a distribution in particle-size and competing electronic absorption of the γ-ray by Si present in the sample. The saturation hyperfine field H_{hf} = 487 kOe and the estimated blocking temperature T_B = 23 K [7].

The observed superparamagnetism, characteristic of small magnetically ordered particles, is due to spontaneous spin reversals above their respective blocking temperatures. For magnetically isolated particles, as is the case here, the spin relaxation time is related to the average volume, V, and effective magnetic anisotropy density, K_{eff}, according to equation (1)

$$\tau_s = \tau_0 \exp (K_{eff}V/k_BT) \tag{1}$$

where τ_0 is a constant characteristic of the material, k_B is Boltzmann's constant and T is the temperature [8]. With the Mössbauer effect, the nuclear Zeeman splitting caused by the internal magnetic field at the site of the iron nucleus is observed. However, the magnetic quantum numbers are well defined only if the Larmor precession time, τ_L, of the nuclear spin around the internal magnetic field of the particle is shorter than τ_s. The temperature at which $\tau_s = \tau_L$ defines T_B. Thus, solving for the anisotropy constant K_{eff}, equation (1) gives $K_{eff} = \ln (\tau_L/\tau_0) (k_B/V) T_B$.

K_{eff} is proportional to T_B and inversely proportional to V, the volume of the particle (or cluster). It also depends on the value of τ_0. Magnetically isolated small iron and iron-oxide particles have been measured to posses $\tau_0 \sim 10^{-9}$ to 10^{-12} sec [7,9,10,11].
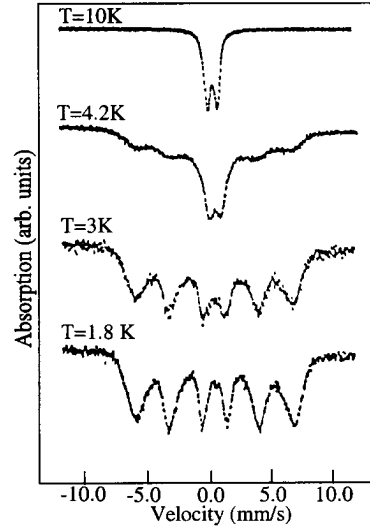
Figure 2. *Mössbauer spectra of Fe₁₆MnO₁₀(OH)₁₀/(O₂CPh)₂₀ at various temperatures.*
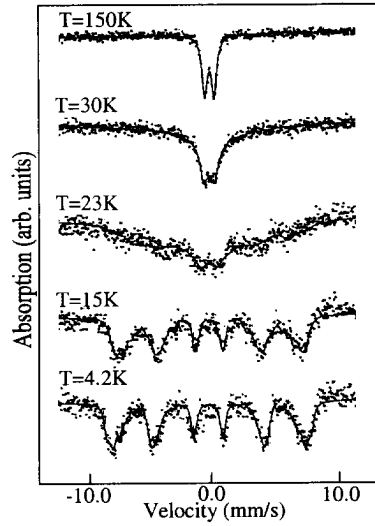
Figure 3. *Mössbauer spectra of γ-Fe₂O₃/SiO₂ nanoparticles at various temperatures.*

Alternatively, collective magnetic excitations [12] below T_B, if observable, may be used to obtain the value of K_{eff} independently of τ_0. The manifestation of collective magnetic excitations is a temperature dependent magnetic hyperfine field below the blocking temperature which, to a first order approximation, can be described by equation (2),

$$H_{hf} = H_{hf0} (1 - k_B T/2 K_{eff} V)$$ (2)

where H_{hf0} is the saturation magnetic hyperfine field at T = 0 K [12]. Detailed analysis of the temperature profile of the Mössbauer spectra for the cluster [**1**] and the particles [**2**] indicates that the iron oxide particles exhibit collective magnetic excitations below their blocking temperature, while those of the cluster do not.

Analysis of collective magnetic excitation processes below T_B for the γ-Fe₂O₃/SiO₂ nanoparticles determined K_{eff} and τ_0 to be: $K_{eff} = 0.55 \times 10^5$ J/m³ and $\tau_0 = 3.3 \times 10^{-11}$ sec [7]. The anisotropy constant for the cluster was determined from its blocking temperature to be: $K_{eff} = 0.66 \times 10^5$ J/m³, assuming $\tau_0 \sim 10^{-9}$ sec [13]. The observed values of K_{eff} are two orders of magnitude larger than the magnetocrystalline anisotropy of epitaxial single-crystal films and polycrystalline powders of γ-Fe₂O₃ ($K_{mc} = 4.7 \times 10^3$ J/m³) [14,15].

The effective anisotropy constant is given by $K_{eff} = K_{mc} + K_{sh} + K_s + K_\sigma$, where K_{mc} is the magnetocrystalline anisotropy of the material, K_{sh} is the shape anisotropy of the particle, K_s the surface anisotropy, and K_σ the strain anisotropy [16]. For spherical core/shell nanostructures the strain at the interface is the most significant contribution, making the K_σ term the most dominant.

In bulk γ-Fe_2O_3, Fe^{3+} ions occupy octahedral or tetrahedral sites of a spinel structure, and exhibit no quadrupole splitting. The observed non-vanishing ΔE_Q in small particles of γ-Fe_2O_3 is associated with crystallographic distortions away from perfect octahedral or tetrahedral iron coordination symmetry, due to lattice strain at the particle core/shell interface. The degree of distortion must correlate with the magnitude of strain contributions to K_{eff}. No structural characterization of the core/shell interface is possible, however, in small particles, due to size distributions rendering broadened X-ray absorption spectra.

In contrast, detailed X-ray structural information of cluster [1] is possible, and has been obtained (Figures 1a and b). All iron ions are octahedrally coordinated to oxygen atoms. Iron-oxygen bonds pointing either into the interior of the core, along its surface or outwardly towards the benzoate ligands of the shell are clearly discernible. Selected O-Fe-O bond angles have been tabulated in Table I. Due to space limitations only the angles along the x, y and z coordinates of local octahedra are tabulated. The complete set of bond angles and bond lengths is available in the supplementary material of ref. [6].

Table I. Selected O-Fe-O bond angles in degrees for the [$Fe_{16}Mn$] cluster of Figure 1(a) and (b). The structure is centrosymmetric with only eight unique iron crystallographic sites. Corresponding O-Mn-O angles are also included for comparison. Complete set of bond angles and bond lengths are given in the supplementary materials of ref. [6].

O(9)-Fe(1)-O(6a)	145.2	O(7)-Fe(4)-O(82)	170.4	O(41)-Fe(7)-O(3a)	173.8
O(22)-Fe(1)-O(1a)	169.5	O(4)-Fe(4)-O(71)	169.8	O(5)-Fe(8)-O(6)	169.1
O(12)-Fe(1)-O(3a)	175.8	O(8)-Fe(5)-O(101)	171.1	O(2)-Fe(8)-O(102)	168.6
O(2)-Fe(2)-O(32)	173.8	O(5)-Fe(5)-O(72)	167.7	O(1)-Fe(8)-O(51)	173.8
O(52)-Fe(2)-O(10a)	170.5	O(7)-Fe(5)-O(92)	170.4	O(3)-Mn-O(3a)	180.0
O(9)-Fe(2)-O(42a)	169.2	O(5)-Fe(6)-O(21)	159.0	O(1)-Mn-O(3)	180.0
O(1)-Fe(3)-O(62a)	169.2	O(8)-Fe(6)-O(9)	170.9	O(2)-Mn-O(2a)	180.0
O(7)-Fe(3)-O(10)	166.3	O(91)-Fe(6)-O(3a)	164.8		
O(4)-Fe(3)-O(11)	159.4	O(4)-Fe(7)-O(6a)	170.1		
O(8)-Fe(4)-O(61)	165.0	O(81)-Fe(7)-O(2a)	168.2		

The greatest distortion is associated with Fe (1) with 9.16% deviation from 180 degrees, expected for perfect octahedral coordination. The smallest distortion is exhibited by Fe (2) with 4.91% deviation. The average deviation for all 8 unique iron crystallographic sites is 6.67%. The central Mn ion possesses perfect octahedral oxygen coordination. The observed distortions produce unresolved, non-vanishing quadrupole splittings at the iron sites of an average value $\Delta E_Q = 0.77$ mm/sec measured at 80 K, and create shear stress at the surface of the magnetic core resulting in the observed $K_{eff} = 0.63 \times 10^5$ J/m^3.

The comparable values of ΔE_Q and K_{eff} measured for structures [1] and [2], would indicate that bond angles at the core/shell interface of the γ-Fe$_2$O$_3$ particles must be similarly distorted relative to the bulk spinel structure (ignoring, for simplicity, contributions of bond-length distortions). Thus, large strains of the order of 6% to 7% may be structurally imposed at the core/shell interface resulting in magnetic surface reconstruction, spin canting [17,18], high shear stresses and a value of K_{eff} of the order of 10^5 J/m^3 for the γ-Fe$_2$O$_3$ /SiO$_2$ nanoparticles. It is noteworthy that this observed strain is two to three orders of magnitude larger than the magnetostriction constant of bulk polycrystalline γ-Fe$_2$O$_3$ ($\lambda = 2.2 \times 10^{-5}$) [19].

CONCLUSION

It is well established that nanosized particles of iron-oxide and iron-hydroxide phases exhibit non-vanishing quadrupole splittings and magnetic anisotropy constants of the order of 10^5 J/m^3. It is also well established that the magnetic anisotropies are sensitive to surface modifications. Lacking detailed structural information of the core/shell interface in most nanoparticulate systems, the degree of surface strain structurally imposed is unknown. We have proposed that nanosized, structurally characterized iron-oxo molecular clusters exhibiting comparable K_{eff} and ΔE_Q values model the microstructure of the core/shell interface in small iron oxide magnetic particles. This has led to the proposition that structurally imposed strains at the surface of *ca.* 4nm diameter silica-coated iron-oxide particles may be of the order of several percent.

ACKNOWLEDGMENTS

REFERENCES

1. *Magnetic Properties of Fine Particles,* J. Dorman and D. Fiorani Eds. (North-Holland 1991).
2. A.E. Berkowitz, F.T. Parker, F.E. Spada and D. Margulies, *ibid,* p.309.
3. *Scientific and Clinical Applications of Magnetic Carriers,* ed. by U. Häfeli, W. Schütt, J. Teller and Zborowski (Plenum, New York, 1997).
4. G. C. Papaefthymiou, *Hyperfine Interactions,* **113,** 357, (1998) and references there in.
5. G. C. Papaefthymiou, *Phys. Rev. B,* **46,** 10366 (1992).
6. W. Micklitz, V. Mckee, R. Lyn Rardin, L. E. Pence, G.C. Papaefthymiou, S.G. Bott and S.J. Lippard, *J. Am. Chem. Soc.* **116,** 8061 (1994).
7. L. Zhang, G.C. Papaefthymiou and J.Y. Ying, *J. Appl. Phys.* **81,** 6892 (1997).
8. W.F. Brown Jr., *Phys. Rev.,* **130,** 1677 (1963).
9. B.H. Sohn, R.E. Cohen and G.C. Papaefthymiou, *J. Mag. Mag. Mat.* **182,** 216 (1998).
10. C.L. Chien, in: *Science and Technology of Nanostructured Magnetic Materials,* G.C. Hadjipanayis, G.A. Prinz Eds., NATO ASI Series B, **259** (Plenum Press, N.Y. 1991) p. 4772
11. D.P.E. Dickson, N.M.Reid, C. Hunt, H.D. Williams, M.E. Hilo and K. O' Grandy, *J. Mag. Mag. Mat.,* **125,** 345 (1993).
12. S. Mørup and H. Topsøe, *J. Appl. Phys.* **11,** 63 (1976).
13. G.C. Papaefthymiou, *Mat. Res. Soc. Symp. Proc.* **286,** (1993) p. 67.
14. H. Takei and S. Shiba, *J. Phys. Soc. Jpn.,* **21,** 1255 (1966).
15. A.H. Morrish and E.P. Valstyn, *J. Phys. Soc. Jpn.,* **17 B-1,** 392 (1962).
16. A.H. Morrish, *The Physical Principles of Magnetism* (John Wiley & Sons, New York, 1965).
17. J.M.D. Coey, *Phys. Rev. Lett.,* **17,** 1140 (1971).
18. R.H. Kadama, A.E. Berkowitz, E.J. McNiff, Jr. and S. Foner, *Phys. Rev. Lett.,* **77,** 394 (1996)
19. V.A.M. Brabers in: *Handbook of Magnetic Materials,* K.H.J. Buschow Ed. (Elsevier, Amsterdam, 1995), vol. **8,** p. 189.

Metallic Nanowires

Matrix-Assisted Synthesis of Palladium Nanocage and Nanowires

Jinwoo Cheon*, Kyung-Bok Lee, Hongkyu Kang, S. J. Oh[1] and H.-C. Ri[1]
Department of Chemistry and School of Molecular Science-BK21,
Korea Advanced Institute of Science and Technology (KAIST), Taejon, 305-701, Korea.
[1]Korea Basic Science Institute (KBSI), Taejon, 305-333, Korea.

ABSTRACT

Our study describes the synthesis of novel nanoscale Pd cage and wires whose sizes and shapes are templated by mesoporous matrices. The templates used are cubic phase MCM-48 and hexagonal phase C_nMCM-41 (n = 16, and 22), SBA-15, which have pore diameters of ~3, ~3.8, ~4.7, and ~9 nm, respectively. For Pd@MCM-48, the Pd metal forms spherical domains (~38 nm) consisting of three dimensionally interconnected into Pd arrays; for Pd@SBA-15 and Pd@MCM-41, the Pd metal forms of one-dimensional wires. Etching out the matrix produces porous Pd cages (pore sizes of ~1.5 - 2.0 nm) with retaining original domain sizes of ~38 nm; similarly Pd@SBA-15 and Pd@MCM-41 afford freestanding Pd nanowires. All the materials are examined by TEM, XRD, BET, and EDAX analysis. Furthermore, the thermal behavior of Pd nanowire is briefly described.

INTRODUCTION

Recently, interest has grown in the synthesis of nanosized materials due to their novel electronic, optical, and catalytic properties [1]. Of the various methods available to prepare these materials, one is the templated synthesis where the desired nanomaterial is encapsulated into the channels and pores of a host [2]. Mesoporous solids with pore size tunability ranging from ~2 to ~30 nm have been the focus of special attention as hosts for quantum dots and wires [3]. One of the studies used the two step nanocasting process where mesoporous organic networks were grown by polymerization of monomers and subsequent removal of silicate matrix [4]. Excellent carbon-based mesoporous materials were also obtained from a MCM-48 template [5]. The fabrication of stable metallic structures with ordered nanopores of less than 10 nm are rare and have recently been reported for Ag, Pt, and Sn [6]. Using the mesoporous silica template, it is potentially feasible to have various 1 to 3 dimensional shapes of nanostructured materials depending on the architecture of the silicate host. For example, recently, Stucky and coworkers reported the preparation of Au, Ag, and Pt nanowires using hexagonal mesoporous silica (SBA-

15) via a solution phase infiltration process [7]. Ordered porous gold nanostructures with larger pore dimensions (~150 nm – 1 μm) have been synthesized by using latex spherical templates [8]. We present in this report matrix free palladium based porous nanoballs and nanowires as well as palladium superlattices and wires inside of cubic MCM-48 and hexagonal MCM-41 and SBA-15 matrices. Pd was chosen as the case study material because of its catalytic activity and its potential applications in H_2 storage and advanced electronics [9].

EXPERIMENTAL DETAILS

Matrix materials such as MCM-48 (pore size of ~3 nm), C_{16}MCM-41, C_{22}MCM-41, and SBA-15 (pore size of ~3.7, ~4.6, and ~9 nm) particles are dried at 400 °C for 8 h under dynamic vacuum (~10^{-2} Torr) [10], prior to introduction of the Pd metal-organic precursor, Pd(hfac)$_2$ (hfac=1,1,1,5,5,5-hexafluoroacetylacetonate) via chemical vapor infiltration (CVI) [11]. The precursor is sublimed into the empty pores of the mesoporous materials under vacuum (~10^{-2} Torr) at 55 °C; during this time the samples exhibit a color change from white to the yellow color indicative of the precursor [12]. The resulting Pd(hfac)$_2$@MCM-48, Pd(hfac)$_2$@C$_{16}$MCM-41, Pd(hfac)$_2$@C$_{22}$MCM-41, and Pd(hfac)$_2$@SBA-15 composites are then pyrolyzed at 150 °C under a 10 % H_2/N_2 flow to produce black powders of Pd@MCM-48, Pd@C$_{16}$MCM-41, Pd@C$_{22}$MCM-41, and Pd@SBA-15. To obtain unsupported freestanding Pd nanocage and nanowires, the Pd containing silicate composites were carefully treated with a solution of HF/H_2O, affording a black powder suspension, which can be obtained as a black powder after centrifugation. To study the thermal behavior of the Pd nanowires, they were mounted on transmission electron microscope (TEM) grids and thermally treated under an argon atmosphere where the temperature was slowly increased at the rate of 2 ℃/min and maintained at the designated temperature (150, 200, and 300 ℃) for 1 hr and finally cooled to R. T. The sample containing grids were then transferred to TEM for analysis.

DISCUSSION

The Pd nanowires appear as dark rod-like objects inside host matrix C_{16}MCM-41, C_{22}MCM-41, and SBA-15, respectively, and range in length from 50 to a few hundred nanometers. The thickness of each Pd nanowire appears to be confined by the channel diameter of the pure mesoporous silicate samples and one of the TEM image of the Pd@C$_{22}$MCM-41 sample is show in Figure 1. This observation indicates that the silicate host frameworks were
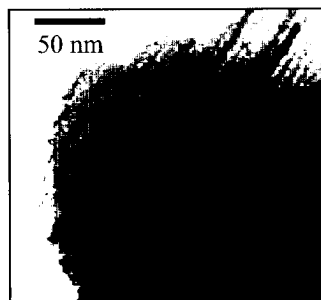
Figure 1. TEM images of the supported Pd nanowires within the mesoporous silicate channels: Pd@C₂₂MCM-41.

neither deformed nor affected by the loading of Pd inside the channels by our CVI filling method. For Pd@MCM-48, the TEM images show that the Pd aggregates into ball shaped domains of 8.2 nm ($\sigma = 3.3$); these domains consist of a three dimensionally interconnected network of Pd filled pores in the MCM-48 matrix. Some pore filled Pd nanoballs are clearly shown in the (111) crystallographic direction of the MCM-48 matrix. The formation of spherical ball type domains can possibly be attributed to the mesoscale stress field of periodic mesoporous structures as similarly seen in the other metal system [13]. Energy dispersive X-ray analysis (EDAX) data show Si, O, and Pd peaks and the presence of Pd as ~5 - 6 weight percent of mesoporous silicate templates.
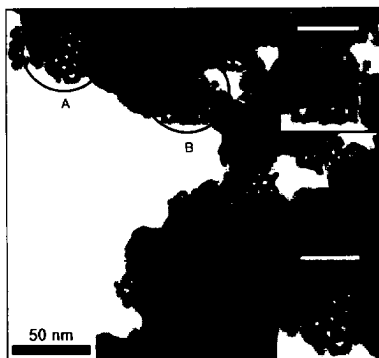
Figure 2. TEM image of the porous Pd superlattice nanoballs.
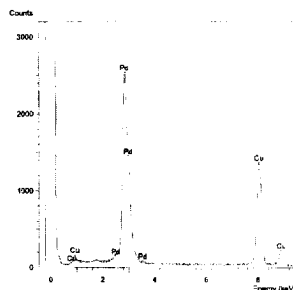
Figure 3. *EDAX analysis of the Pd nanoball. Cu is from TEM grid.*

To obtain freestanding Pd nanocage and wires, the silicate matrices were removed by slowly adding HF solution and the resulting black powder suspension was centrifuged to obtain the nanowires in powder form. TEM examination of the powder shows that it consists of agglomerated and randomly stacked Pd nanoballs of ~37.6 nm (σ = 3.9) in diameter. Each ball shaped domain consists of an interconnected network of Pd whose shapes and pores are obtained as the replication of the MCM-48 template (Figure 2). Some Pd nanoballs are clearly observed in the (111) and (100) crystallographic directions (Figure 2 inset). The structures of the Pd superlattices remain unchanged during the silicate dissolution process. Energy dispersive X-ray emission analysis confirms that Pd is the major product without any significant contaminants (Figure 3).

The TEM images of the freestanding Pd nanowires are shown in Figure 4a, 4b, and 4c. It was found that the diameters of the nanowires remain ~3.7, ~4.6, and ~8.8 nm which is consistent with the diameter of the nanowires encapsulated inside the matrix and remain unchanged after etching.
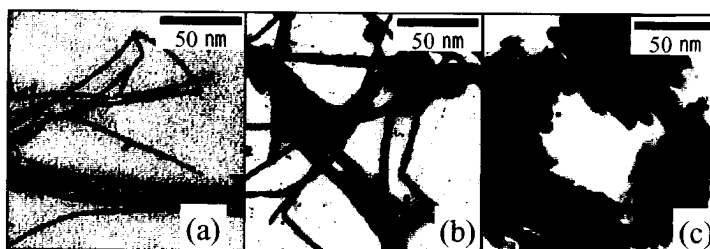
Figure 4. *TEM images of the freestanding Pd nanowires after removal of the silica matrices: obtained from (a) C_{16}MCM-41 template, (b) C_{22}MCM-41 template, (c) SBA-15 template.*

The lengths of the matrix free Pd nanowires also vary from 50 to a few hundred nanometers as they did inside the matrix channels. Selected-area electron diffraction patterns of the Pd nanowires exhibit the (111), (220), and (311) directions and confirms the cubic structure of polycrystalline Pd.

Figure 5 shows the thermal behavior of the 4.6 nm Pd nanowires. From room temperature to 150 ℃, the nanowires are stable and essentially no changes is observed. However, the shape of the nanowires begin to deteriorate in certain areas of the wire at 200 ℃. Finally, a large deformation and eventual collapse of the Pd nanowires in both width and shape is observed at 300 ℃. Observed thermal behavior of the 4.6 nm Pd nanowires at 300 ℃ represents huge melting point depression of more than 1100 ℃ as compared to the bulk melting point of Pd at 1445 ℃.
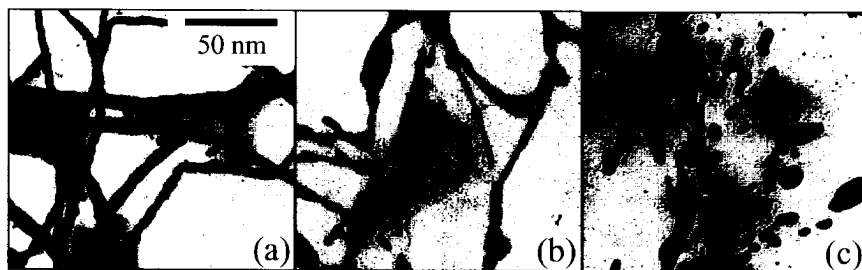
Figure 5. Temperature dependent shape change of the ~4.6 nm Pd nanowires: (a) 150 ℃, (b) 200 ℃, (c) 300 ℃.

CONCLUSION

In summary, this article demonstrates the size and shape-tuned synthesis of Pd nanowires and cages using hexagonal or cubic phased mesoporous silicate materials as templates via a CVI method. Combined results of XRD, TEM, EDAX, and XPS show that loaded Pd metal inside the silicate host materials do not affect the mesoporous silica framework, and uniquely structured Pd nanowires and cages without chemical contaminations and deformations are obtained after removal of the silica matrix HF. Our study indicates that mesoporous silica are good templates for the synthesis Pd nanostructured materials. A significantly depressed melting point of the Pd nanowires is observed around 300 ℃ due to large surface to volume ratio which is characteristic of nanomaterials. In addition, the low temperature CVI approach is of particular interest since the process conditions are mild enough to avoid any disruption of both the desired material and the template structure in the thermally sensitive nanoscale regime.

REFERENCE

1. A. P. Alivisatos, *Science,* **271**, 933 (1996).
2. a) C. Wu and T. Bein, *Science,* **264**, 1757 (1994). b) C. Wu and T. Bein, *Science,* **266**, 1013 (1994). c) C. R. Martin, *Chem. Mater.,* **8**, 1739 (1996).
3. J. Y. Ying, C. D. Mehnert and M. S. Wong, *Angew. Chem., Int. Ed. Engl.,* **38**, 56 (1999).
4. S. A. Johnson, P. J. Ollovier and T. E. Mallouk, *Science,* **283**, 963 (1999).
5. R. Ryoo, S. H. Joo and S. Jun, *J. Phys. Chem. B,* **103**, 7743 (1999).
6. G. S. Attard, P. N. Bartlett, R. B. Coleman, J. M. Elliott, J. R. Owen and J. H. Wang, *Science,* **278**, 838 (1997).
7. a) Y. J. Han, J. Kim and G. D. Stucky, *Chem. Mater.,* **12**, 2068 (2000). b) M. H. Huang, A. Choudrey and P. Yang, *Chem. Commun.* 1063 (2000). c) H. Kang, Y. Jun, J.-I. Park, K.-B. Lee, and J. Cheon, *Chem. Mater.,* **12**, 3530 (2000).
8. O. D. Velev, P. M. Tessier, A. M. Lenhoff and E. W. Kaler, *Nature,* **401**, 548 (1999).
9. *McGraw-Hill Concise Encyclopedia of Science and Technology,* ed. S. P. Parker (McGraw-Hill: New York, 1989) pp.1343.
10. The cubic MCM-48 and hexagonal SBA-15 hosts were prepared by a literature method. See: D. Zhao, J. Feng, Q. Huo, N. Melosh, G. H. Fredrickson, B. F. Chmelka and G. D. Stucky, *Science,* **279**, 548 (1998).
11. Pd(hfac)$_2$ was synthesized following a literature method. See: A. R. Siedle, R. A. Newmark, A. A. Kruger, L. H. Pignolet, *Inorg. Chem.,* **20**, 3399 (1981).
12. Pd(hfac)$_2$ is known to adsorb readily on silica surfaces by means of strong Lewis acid-base interactions between the Pd center and surface hydroxyl groups. See: A. R. Siedle and R. A. Newmark, *J. Am. Chem. Soc.,* **103**, 1240 (1981).
13. L. Conners, T. Hollis, D. A. Johnson and G. Blyholder, *J. Phys. Chem. B,* **102**, 10112 (1998).

Poster Session

Site-Specific Attachment of Gold Nanoparticles to DNA Templates

Karen A. Stevenson, Govindarajan Muralidharan, Leon Maya[1], Jack C. Wells[2], Jacob Barhen[2],
Thomas Thundat
Life Sciences Division,
[1]Chemical and Analytical Sciences Division,
[2]Computer Science and Mathematics Division,
Oak Ridge National Laboratory, Oak Ridge, TN 37831

ABSTRACT

DNA was used as a scaffold for the binding of gold nanoparticles using a standard chemical technique. A DNA template was designed with amino-modified thymines located every 3.7 nm, which would allow the attachment of the carboxylic acid functionalized gold nanoparticles. The gold particles were covalently bound to the amino groups on the DNA using standard 1-ethyl-3-(3-dimethylaminopropyl) carbodiimide hydrochloride (EDC) chemistry in the presence of a competitor to block excess gold binding sites. The products were analyzed by transmission electron microscopy (TEM) and atomic force microscopy (AFM).

INTRODUCTION

The need to produce regular arrangements of nanoparticles led to the idea of using DNA as a scaffold or template for assembly of nanoscale arrays. Beginning in the 1980s Seeman et al. experimented with combining DNA fragments to produce geometrical shapes, including cubes [1], triangles [2], two-dimensional arrays [3-5] and various forms of DNA knots [6,7].

Using DNA as a structural molecule has many advantages. It can be easily synthesized in lengths from 5 to over 100 nucleotides. It can be joined end to end to produce longer linear molecules or more complex shapes, and it can be modified at predetermined sites to allow for the attachment of other molecules in a specific manner.

The precise arrangement of nanoparticles to form an array is a difficult task. DNA has been used by others as a template for the attachment of particles. Mirkin et al. [8-10] and Alivisatos et al. [11,12] have successfully attached oligonucleotide derivatized nanoparticles to DNA using hybridization techniques. Niemeyer and coworkers have assembled biotinylated gold clusters on streptavidin-DNA oligonucleotides and subsequently hybridized the clusters to a complementary RNA template [13]. Cassell et al. assembled fullerene derivatives along the DNA backbone using cation exchange [14].

The present study was an attempt to use DNA as a scaffold for placement of gold nanoparticles at specific sites using a chemical reaction. Gold nanoparticles with an average diameter of 1.5 nm were synthesized with a mercaptosuccinic acid coating. Oligonucleotides were designed with amino-modified bases for attachment to carboxylic acid functionalized gold particles. The modified bases were separated by 10 base pairs (approximately 3.7 nm). The reaction between the amino group on the DNA and the carboxyl group on the gold particle was facilitated by 1-ethyl-3-(3-dimethylaminopropyl) carbodiimide hydrochloride (EDC) and N-hydroxysuccinimide (NHS). Analysis of the products by transmission electron microscopy

(TEM), and atomic force microscopy (AFM) showed that the gold particles are bound to the DNA.

EXPERIMENTAL DETAILS

Oligonucleotides were purchased from Oligos Etc. They were designed with C6-amino-modified thymines (X) separated by 10 base pairs and with compatible overhangs to permit ligation reactions to easily occur:

GATCTAXCAACGGCTCAXCCAA $X=T-(CH_2)_6-NH_2$
       TAGTTGCCGAGTAGGTTCTAGA

The 5' ends of the double-stranded oligonucleotide were phosphorylated and then the DNA was ligated. Enzymes were purchased from Promega.

Gold nanoparticles coated with mercaptosuccinic acid were synthesized as described elsewhere [15]. The gold was dissolved in water and the pH adjusted to ~3.8. Final concentration of the gold solution was 4.7 mg/ml. Approximately 50μg gold nanoparticles were incubated at room temperature with ~1.5mg 1-ethyl-3-(3-dimethylaminopropyl) carbodiimide hydrochloride (Pierce) and ~2.0mg N-hydroxysuccinimide (Pierce) for 30-60 minutes.

Methylamine (Sigma) concentrations were calculated as multiples of gold binding sites on the DNA. Typical amounts used were 1X (equal to the concentration of modified thymines), 2X, 5X, 10X, and no methylamine. The methylamine was added to 2-10 μg DNA and then this mixture was added to the gold particles. Incubation was typically 2-4 hours at room temperature.

For AFM imaging, reaction mixtures were diluted 1:10,000 to 1:20,000 in 20mM Tris, 5mM KCl, 5mM MgCl$_2$, and 3mM ZnCl$_2$. Five μl of this solution was deposited on freshly cleaved mica. The samples were allowed to dry for 10-30 minutes, then washed first with water, then 50% ethanol, and finally ethanol. After drying overnight in a vacuum desiccator, imaging was carried out on a Nanoscope III AFM system (Digital Instruments).

For transmission electron microscope (TEM) imaging, reaction samples were typically diluted 1:60. The TEM grid was dipped into the solution and allowed to dry overnight before imaging on a Hitachi H-600 system.

RESULTS

Figure 1 shows an AFM image of the mercaptosuccinic acid coated gold particles used in the binding reaction with the DNA. The average diameter of the particles was 1.5 nm as measured by X-ray diffraction [15]. Each particle has multiple reactive carboxyl groups on its surface. In order to decrease the chances of one particle binding to many amino groups on the DNA, an agent was used to block some of the carboxyl groups on the gold. Methylamine was chosen because of its small size and similarity to the methylene side chain containing the amino group on the DNA.
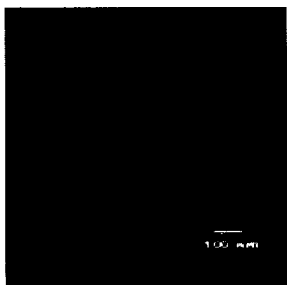
Figure 1. AFM image of mercaptosuccinic acid coated gold nanoparticles.

Figure 2. TEM image of DNA bound to gold nanoparticles at magnification of 250,000.

Figure 2 shows a transmission electron micrograph of DNA bound to the gold nanoparticles without the methylamine blocker. The gold particles are bound to the DNA but multiple strands of DNA are held together because of the many reactive sites on each gold particle. The particles cause cross-linking between different DNA strands and possibly between different sites on the same DNA strand, leading to an aggregate of DNA and gold.

AFM images of DNA bound to gold in the presence of methylamine are shown in Figure 3. The methlyamine concentration in the reaction was equal to the concentration of amino-modified thymines on the DNA. Figure 3A shows linear double-stranded DNA bound to the gold nanoparticles. The looping seen in the image may be the result of sample deposition on the mica substrate, or there may still be some cross-linking between DNA strands due to the multiple binding sites on the gold particles. However, if cross-linking is occurring, it is greatly reduced by the addition of the methylamine (compare with Figure 2). Figure 3B shows a close-up view of the upper right quadrant of 3A. Analysis of the interparticle distance reveals that the closest resolvable particles are about 12.3 nm apart, a separation of 3-4 binding sites on the DNA. It is not clear at this time why all the binding sites are not occupied. Further studies are underway to address this issue.
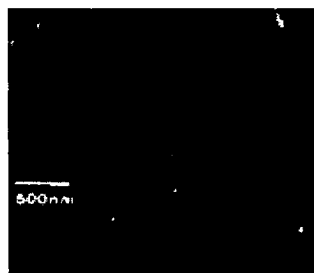
A
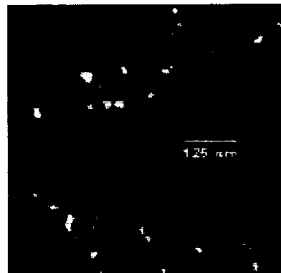
B

Figure 3. AFM images of gold nanoparticles bound to DNA. **A.** Carboxylic acid functionalized gold particles bound to amino-modified thymines on the DNA using EDC and methylamine. **B.** Close-up view of upper right quadrant of **A.** An analysis of the spacing between particles indicates that the closest resolvable particles are separated by 3-4 binding sites on the DNA.

CONCLUSIONS

Gold nanoparticles functionalized with carboxylic acid groups have been chemically bound to amino-modified thymine bases on double-stranded DNA. The blocking agent methylamine was used to inactivate excess reactive groups on the gold particles, minimizing cross-linking between strands of DNA.

The advantages to this method are that particles can potentially be placed wherever a modified base is inserted during synthesis of the DNA. Therefore, arrangement of the particles would be dependent only on design of the DNA template and the size of the particle. A variety of functional groups can be used to modify DNA during synthesis and any particle that can be functionalized with a complementary reactive group can be bound to the DNA. The DNA product is double-stranded thus retaining the regularity of structure that makes DNA an attractive building block.

ACKNOWLEDGMENTS

REFERENCES

1. Chen, J., Seeman, N. C. *Nature*, **350,** 631 (1991).
2. Qi, J., Li, X., Yang, X., Seeman, N. C. *J. Am. Chem. Soc.*, **118,** 6121 (1996).
3. Zhang, Y., Seeman, N.C. *J. Am. Chem. Soc.*, **116,** 1661 (1994).
4. Li, X., Yang, X., Qi, J., Seeman, N. C. *J. Am. Chem. Soc.*, **118,** 6131 (1996).
5. Winfree, E., Liu, F., Wenzler, L. A., Seeman, N. C. *Nature*, **394,** 539 (1998).
6. Mueller, J. E., Du, S. M., Seeman, N. C. *J. Am. Chem. Soc.*, **113,** 6306 (1991).
7. Du, S. M., Seeman, N. C. *Biopolymers*, **34,** 31 (1994).
8. Mirkin, C. A., Letsinger, R. L., Mucic, R. C., Storhoff, J. J. *Nature*, **382,** 607 (1996).
9. Mitchell, G. P., Mirkin, C. A., Letsinger, R. L. *J. Am. Chem. Soc.*, **121,** 8122 (1999).
10. Mirkin, C. A. *Inorg. Chem.*, **39,** 2258 (2000).
11. Loweth, C. J., Caldwell, W. B., Peng, X., Alivisatos, A. P., Schultz, P. G. *Angew. Chem. Int. Ed.*, **38,** 1808 (1999).
12. Alivisatos, A. P., Johnsson, K. P., Peng, X., Wilson, T. E., Loweth, C. J., Bruchez, M. P., Jr., Schultz, P. G. *Nature*, **382,** 609 (1996).
13. Niemeyer, C. M., Burger, W., Peplies, J. *Angew. Chem. Int. Ed.*, **37,** 2265 (1998).
14. Cassell, A. M., Scrivens, W. A., Tour, J. M. *Angew. Chem. Int. Ed.*, **37,** 1528 (1998).
15. Maya, L., Muralidharan, G., Thundat, T. G., Kenik, E. A. *Langmuir*, **16,** 9151 (2000).

Nanoparticle Assembly via Hydrogen-Bonding: IRS, TEM and AFM Characterizations

Li Han, Mathew M. Maye, Chuan-Jian Zhong
Department of Chemistry, State University of New York at Binghamton, Binghamton, New York 13902.

ABSTRACT

This paper reports results of the characterizations of nanoparticle assembly formed via spontaneous core-shell and shell-shell reactivities at thiolate-capped gold nanoparticles. Gold nanoparticles of two different core sizes and thiols with carboxylic acid terminals are exploited as a model system. The reactivities involve covalent Au-thiolate bonding and non-covalent hydrogen-bonding with anisotropic linking character. We employed infrared reflection spectroscopy (IRS), atomic force microscopy (AFM) and transmission electron microscopy (TEM) for the characterizations. While IRS provides structural assessment, TEM and AFM imaging measurements probe the morphological properties.

INTRODUCTION

The study of nanostructured materials is emerging as a research area of tremendous interest, largely because of their potential functional properties in molecular recognition, chemical and biological sensors, microelectronics, optic devices, magnetic materials and catalysis [1]. Nanoconstruction via molecular linking strategies [1b] using metallic nanocrystal cores with organic shell encapsulation as building blocks has recently been demonstrated. Excellent examples include stepwise layer-by-layer assembling [2-4] and DNA-based linking [5]. Because hydrogen-bonding is one of the common non-covalent interactions in chemical and biological systems, we view it as an ideal model towards building biomimetic functional nanomaterials from the core-shell nanoparticles [6-7]. We have recently demonstrated [7] that hydrogen-bonding of carboxylic acid functionalized shells at gold nanocrystals of different size and shape exhibits intriguing anisotropic reactivity in terms of cis- or trans-configuration. (Scheme 1). An understanding of how structures and morphologies of such core-shell architecture correlate with size and shape has important implications to the ultimate exploration of nanostructured molecular recognition. We have employed IRS, TEM, and AFM to address relevant issues.
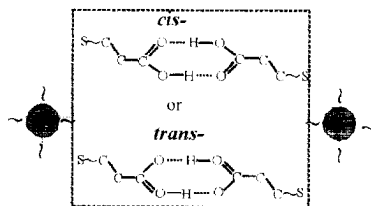
Scheme 1. Schematic illustration of two possible shell-shell linking via cis- and trans-configurations of the head-to-head hydrogen-bonding at carboxylic acid groups. The C_α-C_β bond is in the same side of the C=O group for cis configuration, whereas the C_α-C_β bond is in the opposite side of the C=O group for trans configuration.

EXPERIMENT

Synthesis. Gold nanoparticles of ~2 nm core size (Au_{2-nm}, 1.9 ±0.7 nm) encapsulated with decanethiolate (DT) monolayer shells were synthesized by standard two-phase method [8-9]. Particles of ~5 nm core size (Au_{5-nm}, 5.2 ±0.3 nm) were derived from the Au_{2-nm} by thermally-activated processing route [10].

Preparation. As detailed in a previous report [7], DT-encapsulated Au_{2-nm} and Au_{5-nm} particles and COOH-terminated thiol, i.e., 11-mercaptoundecanoic acid (MUA), were used as the networking building blocks. The thin films were prepared via "exchanging-crosslinking-precipitation" route [6-7], which involved an exchange of the MUA with the gold-bound thiolates followed by crosslinking and precipitation via hydrogen bonding at the terminals. The reaction was in a toluene solvent with a controlled thiol-to-Au ratio. The thickness of the resulting thin films was controlled by immersion time.

Instrumentation. IRS spectra were acquired with a Nicolet 760 FTIR spectrometer that was purged with boil-off from liquid N_2. It was in an external reflection mode using *p*-polarized light. A gold slide coated with octadecanethiolate-d_{37} monolayer was used as the reference. TEM was performed on Hitachi H-7000 Electron Microscope. Carbon-coated copper grid sample holder with thin films deposited on it was used for transmission measurements. AFM images were acquired using Digital Instrument's Nanoscope IIIa. The nanoparticle films were deposited on gold film on glass substrate for IRS and on glassy carbon substrate for AFM measurement.

RESULTS AND DISCUSSION

Both MUA-Au_{5-nm} and MUA-Au_{2-nm} films are first examined using IRS. As we have recently demonstrated [7], the carboxylic acid groups provide a diagnostic handle for probing the shell linking structure and reactivity. Figure 1 presents a set of IRS spectra for the two films (a and b). The spectrum (c) for MUA monolayer on planar gold substrate is included for comparison.
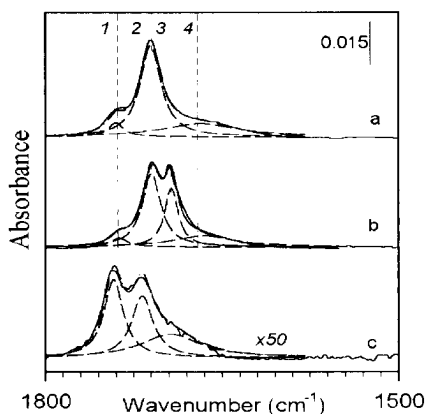
Figure 1. IRS spectra for MUA-Au_{5-nm} (a), MUA-Au_{2-nm} (b), and MUA monolayer (c). The dashed lines represent spectral deconvolution of the $v_{C=O}(CO_2H)$ spectral envelope.

The ν(COOH) vibration envelope in the 1740-1650 cm^{-1} region differ significantly between these films. The spectra of the nanoparticle films (a and b) have an overall absorbance of ~50 times larger than that for the monolayer (c), presumably due to a combination of the nanoparticle multilayer (~10 equivalent) and surface enhancement effects [6-7]. Each spectrum exhibits an envelope of multiple band components, as represented by the dashed curves based on spectral deconvolution (numerically numbered as *1, 2, 3, 4*). The two nanoparticle films (*a* and *b*) show remarkable distinctions from the MUA monolayer (c) in terms of band position and relative intensity. For the MUA monolayer, the three ν(C=O) bands were previously assigned [11] to -COOH groups of free or non-hydrogen-bonded mode (1741 cm^{-1}), side-by-side dimeric hydrogen-bonded mode (1718 cm^{-1}), and polymeric hydrogen-bonded (~1690 cm^{-1}) modes, respectively. In comparison, the three bands identified for the MUA-Au$_{5-nm}$ network film are displayed at 1740 cm^{-1} (*1*), 1710 cm^{-1} (*2*) and ~1670 cm^{-1} (*4*). While the free acid band (*1*) remains basically unchanged, the shifts in the hydrogen-bonded modes (*2, 4*) are remarkable. We attribute these bands to the formation of head-to-head hydrogen-bonding of the -COOH groups in the nanostructure. In fact, the wavenumber of band *2* is identical to the band position observed for the head-to-head hydrogen-bonding dimer with cis-configuration in condensed phases of alkanoic acids [12]. The trans-configuration is basically absent in the MUA-Au$_{5-nm}$ film. The broad band *4* is mostly due to polymeric hydrogen-bonding. Its difference from the MUA monolayer in band position reflects the difference of the hydrogen-bonding properties between head-to-head and side-by-side configurations. The head-to-head binding modes are impossible in the 2D MUA monolayers. While the 2D monolayer exhibits ~40% free acid component, the MUA-Au$_{5-nm}$ film shows only a level of <10%. The results therefore support the formation of predominant head-to-head hydrogen-bonding linkages in the MUA-Au$_{5-nm}$ network. Interestingly, the MUA-Au$_{2-nm}$ film (*b*) exhibits a striking distinction from the MUA-Au$_{5-nm}$ film by displaying a new peak component at 1694 cm^{-1} (*3*). The relative absorbance of the free acid band (~1738 cm^{-1} (*1*)) remains a small fraction. We attribute the band at 1708 cm^{-1} (*2*) and the new band at ~1694 cm^{-1} (*3*) to cis- and trans-modes of the head-to-head hydrogen-bonded dimers [34a] (Scheme 1), in sharp contrast to the MUA-Au$_{5-nm}$ film. It is known that the trans-configuration of alkanoic acid dimer in solids is more stable than cis-configuration [34]. The different configurations in the two films are intriguing because it demonstrates that fine structures of the hydrogen-bonding linkages are strongly dependent on particle sizes.

In the C-H region, our IRS detection of predominant methylene stretching bands at 2918 & 2848 cm^{-1} for the two network films further support that the network structure is primarily composed of MUA chains. The slight different from those for the MUA monolayer (2920 & 2850 cm^{-1}) is indicative of largely comparable chain-chain packing properties between these films. The methyl stretching bands are nearly absent for the Au$_{2-nm}$ film, consistent with a significant replacement of the original capping thiolates by MUA, which is almost 100% for the MUA-Au$_{2-nm}$ network film.

The core-shell nanocrystals and the hydrogen-bounded nanostructure are further examined using TEM and AFM to characterize their morphological properties. Figure 2 shows two representative TEM images and corresponding electron diffraction (ED) data for nanoparticles of Au$_{5-nm}$ (A) and Au$_{2-nm}$ (B) cast on carbon-coated TEM grid.
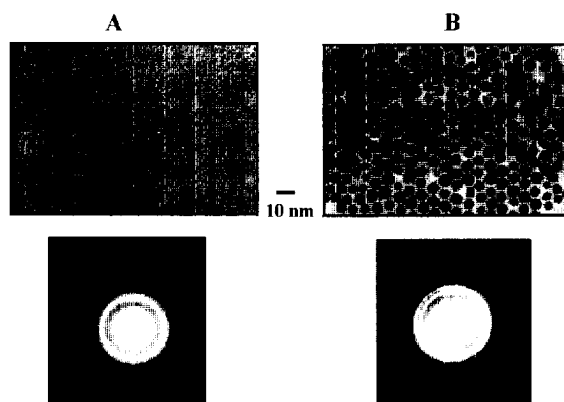
Figure 2. TEM images and corresponding ED images for Au_{5-nm} (A) and Au_{2-nm} (B).

In comparison with the two-phase synthesized nanoparticles (1.9 ±0.7 nm, Au_{2-nm}), the thermally-processed nanoparticles (5.2 ±0.3 nm, Au_{5-nm}) exhibit monodispersing core size and uniform shape with hexagonal outlines. These Au_{5-nm} nanocrystals also exhibit a remarkable long-range ordering feature, as reflected by the two-dimensional ordered arrays with a hexagon-type arrangement. In an agreement with the notion that the encapsulating chains are likely interdigitated between opposing alkyl shells [1b], the determined average core-core (edge-to-edge) distance, ~1.5 nm, is close to the chain length expected for DT. Effects from both van der Waals attractions of the encapsulating shells and the core shape are believed to be responsible for the formation of ordered arrays. The control of nanoparticle size and shape is currently an area of great interest [1a,10,13]. We are presently refining our thermally-activated nanoparticle processing route for processing nanoparticles towards defined size and shape. Sizes up to ~20 nm and shapes with triangle and rectangular features have been observed in our recent work.

The electron diffraction data (Figure 2) provide further information on the nanocrystalline properties of the two different sized particles. Crystalline features of the particles were confirmed by the ring patterns. In the ED pattern, all diffraction rings can be assigned to fcc gold. The difference in line width and intensity for all prominent diffraction lines between the two core sizes is expected based on d spacing parameters for gold and are qualitatively consistent with the dependence of electron diffraction on particle size. The relative intensities of the diffraction lines are also consistent with the results of our previous x-ray diffraction study [10a]. The ED patterns for these two sized particles consisted of continuous rings (rather than discrete spot pattern) of the diffracted electrons because the cast particles do not have a particular orientation on the surface.

Figure 3 shows the TEM images for both MUA-Au_{5-nm} and MUA-Au_{2-nm} films. These thin films were prepared by immersing carbon film-coated TEM grids in the preparation solution for a short time (1~3 hrs) so that a monolayer or submonolayer coverage could be produced for TEM imaging.

(B)   (A)
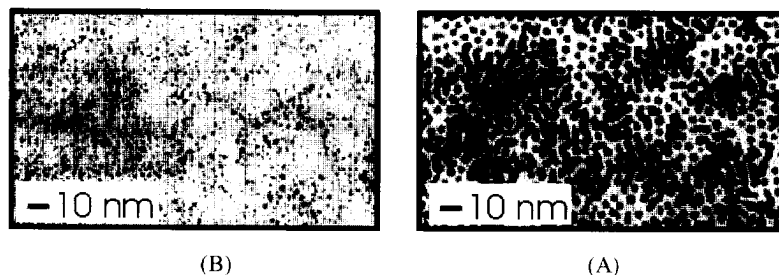
Figure 3. TEM images of submonolayer-coverage films of MUA-Au$_{5\text{-nm}}$ (A) and MUA-Au$_{2\text{-nm}}$ (B).

In contrast to largely evenly-spaced features observed for DT-Au nanoparticles evaporated on the grid, the images, especially for the MUA-Au$_{5\text{-nm}}$ film (A), display regions of collectively-connected particles forming partially-continuous network, and domains including parallel lines, rings, and other type of patterns. As the film grows, these domains or patterns extend through the film. We are conducting further investigation to delineate possible chain length correlation of these features. The TEM data obtained at the submonolayer coverage provide a comparison of core-shell crosslinking or networking morphologies of the two films at the initial formation stage.

Two of the limitation of TEM imaging of the nanoparticle assembly is the special requirement of grid holder and monolayer or submonolayer coverage of the particles. AFM imaging overcomes these limitations. The capability of TappingMode(TM)-AFM allows imaging at minimum disruption of the nanostructures. A typical TM-AFM image is shown in the Figure 4 for MUA-Au$_{5\text{-nm}}$ film assembled on a polished glassy carbon substrate. The film thickness is equivalent to 3~5 layers of nanoparticles based on an estimate from quartz-crystal microbalance data of the thin film mass loading.

1 x 1 μm
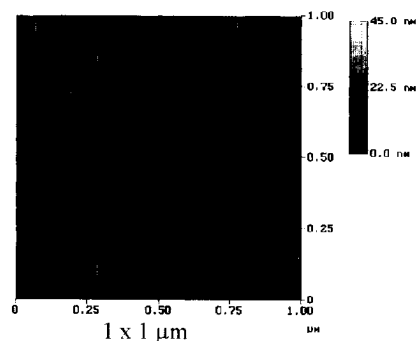
Figure 4. TM-AFM image of a MUA-Au$_{5\text{-nm}}$ film.

The assembled nanoparticles appear to be spatially-isolated or individually-isolated. The apparent inhomogeneity feature of the overall surface morphology is probably due to the surface roughness effect of glassy carbon substrate. The particles appear somewhat larger than the core-shell particle size due to tip-sample convolution, but a cross-section view reveals an average height as expected for the particle size. Similar surface morphology has also been observed for MUA-Au_{2-nm} film.

CONCLUSION

In conclusion, the IRS results have unraveled that the molecular shell-shell linkage structure via hydrogen-bonding at carboxylic acid shell groups are dependent on the nanoparticle core size. The dependence is reflected by the detection of fine structures of cis- and trans- carboxylic hydrogen-binding linkages. The imaging studies using TEM, ED and AFM techniques have provided the morphological assessment of the core-shell nanoparticles and the hydrogen-bonding nanostructures. A further study of the fine tuning of the core-shell nanostructures is underway, which should serve as a model system of chemical manipulation at interparticle linkages for designing molecular recognition elements.

ACKNOWLEDGEMENTS

REFERENCES

1. (a) S. Link, MA. El-Sayed, Int. Rev. Phys. Chem. **19**, 409 (2000). (b) A. C. Templeton, W. P. Wuelfing and R. W. Murray, Acc. Chem. Res. **33**, 27 (2000). and references therein. (c) C. J. Kiely, J. Fink, M. Brust, D. Bethell, and D. J. Schiffrin, Nature **396**, 444.(1998)
2. (a) M. Brust, D. Bethell, C .J. Kiely and D. J. Schiffrin, Langmuir. **14**, 5425 (1998). (b) D. Bethell, M. Brust, D. J. Schiffrin and C. J. Kiely, J. Electroanal. Chem. **409**, 137 (1996).
3. (a) M. D. Musick, C. D. Keating, L. A. Lyon, S. L. Botsko, D. J. Pena, W. D. Holliway, T. M. McEvoy, J. N. Richardson, and M. J. Natan, Chem. Mater **12**, 2869 (2000). (b) K. C. Grabar, K. R. Brown, C. D. Keating, S. J. Stranick, S. L. Tang and M. J. Natan, Anal. Chem. **69**, 471 (1997).
4. (a) F. P. Zamborini, J. F. Hicks and R. M. Murray, J.; Am. Chem. Soc. **122**, 4514 (2000). (b) A. N. Shipway, M. Lahav, R. Blonder and I. Willner. Chem. Mater. **11**, 13.(1999).
5. C. Mirkin, R. L. Letsinger, R. C. Mucic and J. J. Storhoff, Nature. **382**, 607 (1996).
6. F.L Leibowitz, W. X. Zheng, M. M. Maye and C. J. Zhong, Anal. Chem. **71**, 5076 (1999).
7. W.X. Zheng, M.M. Maye, F.L. Leibowitz and C.J. Zhong, Anal. Chem. **72**, 2190 (2000).
8. M. Brust, M. Walker, D. Bethell, D. J. Schiffrin and R. Whyman, J. Chem. Soc., Chem. Commun., 801 (1994).
9. M. J. Hoetetler, J .E. Wingate, C. J. Zhong, J. E. Harris,R. W. Vachet, M. R. Clark, J. D. Londono, S. J. Green, J. J. Stokes, G. D. Wignall, G. L. Glish, M. D. Porter, N. D. Evans and R. W. Murray, Langmuir **14**, 17 (1998).
10. (a) M. M. Maye, W. X. Zheng, F. L. Leibowitz, N. K. Ly and C. J. Zhong, Langmuir **16**, 490 (2000). (b) M. M. Maye and C. J. Zhong, J. Mater. Chem. **10**, 1895 (2000).
11. Y.-T. Tao, W.-L. Lin, G. D. Hietpas and D. L. Allara, J. Phys. Chem. B **101**, 9732 (1997).
12. S. Hayashi and J. Umemura, J. Chem. Phys. **63**, 1732 (1975).
13. R. L. Whetten, J. T. Khoury, M. M. Alvarez, S. Murthy, L. Vezmar, Z. L. Wang,P. W. Stephens, C. L. Cleveland, W. D. Luedtke and U. Landman, Adv. Mater. **8**, 428 (1996).

Nanoparticles and Nanocomposites in RF Plasma

Jin Cao and Themis Matsoukas
Department of Chemical Engineering, The Pennsylvania State University
University Park, PA 16802, U.S.A.

ABSTRACT

The use of low pressure radio-frequency (rf) plasma for nanoparticle formation and the deposition of thin film on particulate substrates are reported. Plasma polymer particles are synthesized in a capacitively-coupled Ar/monomer discharge at rf power of 15-30 W. A variety of particle structures are observed, including monodispersed nanospheres and liquid-like viscous nano-droplets. Styrene in particular is observed to produce hollow nanospheres. By manipulating the process parameters, films of plasma polymers can be deposited onto suspended submicron particles. We take advantage of the electrostatic trapping of "dusty plasma" to suspend small particles in plasma for extended periods of time until the desired coating thickness is achieved. Sub-micron silica particles introduced into a low pressure rf Ar/monomer plasma are coated with film of thickness ranging from 2 to 70 nm.

INTRODUCTION

Most efforts in gas phase thin film deposition have been directed towards flat substrates. While it is very difficult to apply a homogeneous and low-thickness coating to particles by physico-chemical or purely chemical approaches such as spraying, dipping, or fluidization [1], polymer films as thin as several tens of angstroms can be deposited in plasmas [2]. High molecular weight solid deposits formed in plasma are termed "plasma polymers." High energy electrons in plasma sever chemical bonds and ionize neutral species, making the polymerization process atomic in nature. The final product can be controlled via process parameters [3], and materials with many unique and useful features have been obtained [4-11]. Almost any compound that can be brought into the plasma can undergo polymerization. This leads to a wide variety of products not observed from thermally activated reactions. Plasma polymers are generally highly cross-linked and can therefore deposit as pinhole free film. Plasma polymers also deposit in the form of particles depending on the monomer and reaction conditions [12, 13], giving even more varieties in plasma polymer coating. However, only film deposition of plasma polymerization has been extensively studied thus far. This work reports our study of the particle formation during plasma polymerization, since these particles may be used as substrates for the coated nanocomposites of our interest.

The key to thin film deposition on particles in plasma is a controlled manner of fluidization of the substrates. The present work demonstrates the new concept of fluidizing particles using "dusty plasma," i.e., plasma with trapped particles, for surface coating. We have successfully fabricated nanocomposites with a silica core and plasma polymer coating using this method. There have been only very few efforts of thin film deposition on particles in plasma to date[1, 14, 15]. In those cases, either a tumbling device was used to keep the particles separated or a flow system was used where it was difficult to control the residence time of the particles entrained. In our system, these problems are easily solved using particle trapping.

EXPERIMENTAL

The reactions are carried out in a capacitively-coupled rf plasma at 13.56 MHz. The operating pressure is between 10 mTorr and 1 Torr. In such a "cold plasma," electrons and ions are not in thermal equilibrium, with electron temperature typically at about 2-3 eV and ions slightly above room temperature, and an ionization fraction under 1% [16]. Figure 1 is a schematic representation of the reactor used in our work. The parallel-plate electrodes, separated at 1-2 cm, are different in size—the grounded upper electrode 8 cm in diameter and the powered lower electrode 4 cm—to produce an asymmetric plasma with a large negative dc bias across the lower sheath where most particles are trapped. Small particles introduced into plasma quickly charge up, and the equilibrium charge is negative due to the large difference in electron and ion mobility. These particles experience a variety of forces [17]. Electric and ion drag forces dominate for submicron particles, and electric and gravitational forces dominate for above-micron particles [18]. The particles become trapped at parts of the plasma where the net force vanishes. For smaller particles, this occurs in the bulk plasma, while larger ones are suspended near the sheath/plasma boundary or inside the sheath, as seen in figure 2, a snapshot of the particle trapping phenomenon in our reactor. The lower electrode has a slightly depressed center of 2 cm in diameter to provide horizontal confinement of the trapped particles. A laser is used to illuminate the particle clouds for visualization with a CCD camera.

Upon opening the reservoir, particles to be coated fall directly into the interelectrode plasma region through the hollow upper electrode. A fine mesh at the entry point eliminates large agglomerates. The particle substrates used in this work are spherical silica particles in the size range of 0.5-1.5 μm. The particles remain suspended in the plasma throughout the reaction, and fall onto the lower electrode as the discharge is extinguished. Ar is used as the carrier gas, and monomers studied are styrene, isopropanol, and ethylene. A carrier gas is needed in most cases because the pulsation of a pure monomer plasma resulting from the polymerization process easily disturbs the trapped particles.
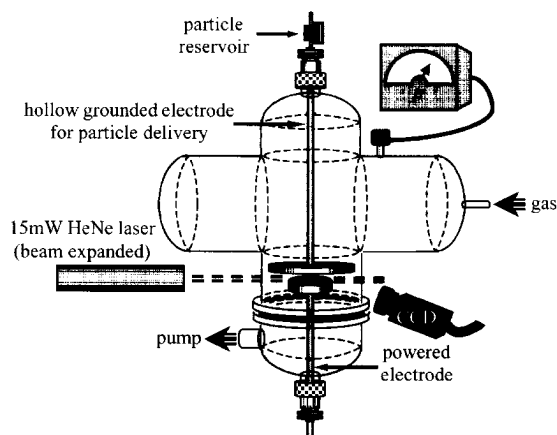
Figure 1. A schematic representation of the glass plasma reactor used in our work.

RESULTS AND DISCUSSIONS

Particle formation of plasma polymer

Plasma polymer can deposit either as film or particles. The three monomers studied have different tendency to form particles. Styrene plasma polymer mostly deposits as particles. Isopropanol polymerizes into particles and film with comparable ease. Film is almost the exclusive product of the plasma polymerization of ethylene. A wide variety of interesting particle morphologies are observed in the reaction products.

The plasma polymer of styrene readily deposits as spherical particles at 15W of rf power, 400 mTorr of system pressure, and 4:1 Ar:styrene flow rate. TEM images like figure 3a suggest that the particles have an empty core. Figure 3b is a micrograph of a 30nm- section of the resin dispersed with these hollow particles, providing better core and shell contrast. The particles are mostly hollow and spherical, and range from 50-300 nm in diameter. The size of core is about a quarter to a third of the particle diameter. These particles are amorphous as determined by electron diffraction.

The TEM image of one particle in figure 3a is analyzed by plotting the pixel intensity vs. the distance from the center of the particle as shown in figure 4. The intensity is directly proportional to the incident electron flux. It is evident from figure 4 that the mass thickness of the particle center is much smaller than would be expected of a solid sphere. The significance of this result is that if the particle consists of a spherical core and shell, the minimum intensity corresponds to the boundary of the two layers. As shown in figure 4, the experimental data can

(a)   (b)   (c)   (d)
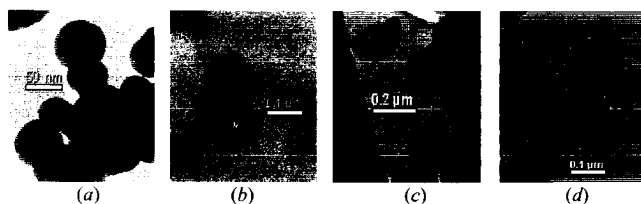
Figure 3. TEM micrograph of (a)hollow particles of styrene plasma polymer made at 400 mTorr; (b)a 30nm-section of the resin dispersed with the hollow particles in (a); (c)broken shells of styrene plasma polymer made at 40 mTorr; (d)monodispersed nanospheres of styrene plasma polymer made at 28mTorr.
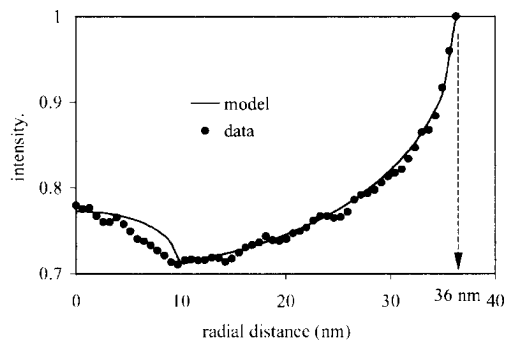
Figure 4. *Radial intensity profile of a hollow styrene plasma polymer particle (intensity normalized to background). The particle radius is 36 nm with a core radius of 10 nm. The Beer-Bouguer model assumes an empty core but constant absorption coefficients.*

be described by a simple Beer-Bouguer type of model

$$\Phi = \Phi_0 e^{(-\alpha_s x_s - \alpha_c x_c)} \tag{1}$$

where Φ is the electron flux that go through the sample, Φ_0 the initial electron flux, α the absorption coefficient of the sample, x the thickness of the sample, and the subscripts s and c stand for shell and core. In this case, the particle radius is 36 nm, the core radius is 10 nm, $\alpha_s = 0.00485$, and $\alpha_c = 0$, meaning an empty core. The mechanism of hollow particle formation is under investigation. The morphology is not restricted to hollow spheres only. Under similar reaction conditions but a lower system pressure, broken shells are observed (figure 3c). Monodispersed spheres of about 40nm (figure 3d) are also observed at styrene pressure of 28 mTorr and no Ar flow.

Isopropanol does not form hollow plasma polymer particles. Instead, monodispersed spheres of about 35nm are found at 30W rf power, 600 mTorr total system pressure, and 3:1 Ar:isopropanol flow rate. Also obtained under the same conditions are structures that resemble highly viscous droplets in the high nanometer range (figure 5).

Plasma polymer thin film deposition on particulate substrates

Spherical silica particles in the high nm and low μm size range have been successfully coated with plasma polymer of all three monomers. Film as thin as 2nm has been deposited on

Figure 5. *TEM micrograph of plasma polymer beads of isopropanol made at 30W, 600mTorr, 3:1 Ar:monomer flow*

the substrates. The nanocomposite is observed under TEM where the plasma polymer film and the bulk silica particle have different contrasts. The micrographs in figure 6 show comparisons of uncoated and coated silica particles. Energy dispersive spectroscopy (EDS) verifies that they are silica particles.

Although the film thickness varies among particles and sometimes is even non-uniform on the same particle, the trend can be observed that a longer deposition time leads to thicker film, as illustrated in figures 6c and 6d of silica particles coated with the plasma polymer film of isopropanol for different lengths of time. The estimated power deposition per unit pressure of monomer for figure 6d is four times greater than that for figure 6b. Thicker film is deposited in the former case in just half of the reaction time. Therefore, qualitatively, higher power density absorbed by the monomer leads to greater deposition rate.

Ethylene plasma polymer deposits as film as well on silica particles (figure 7a), while styrene plasma polymer deposits as both film and particulates on the silica particle surface (figures 7b-d). Film deposition of styrene plasma polymer is observed to increase at lower pressures. This is also seen in the particle coating experiments with styrene. The pressure for figure 7b is much lower than for that for figure 7c. The particle in figure 7b is coated with a film, whereas the particle in figure 7c is coated with both film and particulates. This is most likely due to the decreased monomer concentration in the gas phase at lower pressures which facilitates film formation [11].

CONCLUSIONS

We have successfully proved the concept of plasma polymer coating of nano/micro-particles using the principle of "dusty plasma." Film as thin as 2nm has been observed on the particles

(c)   (d)

Figure 6. TEM micrographs of (a)an uncoated silica particle; (b) silica particles coated with plasma polymer film of isopropanol for 20 min. at 30W of rf power, 800 mTorr of system pressure, and 1:1 Ar:isopropanol flow rate; (c)a silica particle coated with plasma polymer film of isopropanol for 5 min. at 30W of rf power, 200 mTorr of system pressure, and 1:1 Ar:isopropanol flow rate; (d)same conditions as (c) for 10 min.

(a)	(b)	(c)
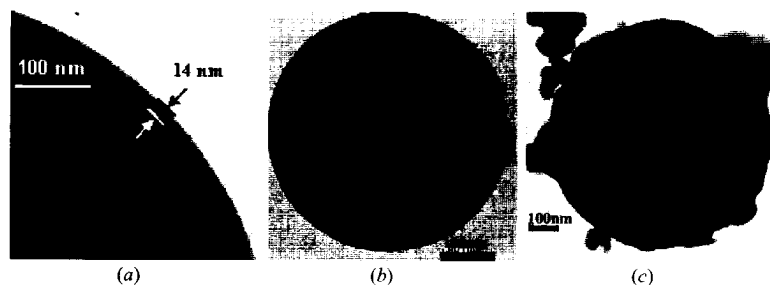
Figure 7. *TEM micrographs of silica particles coated with (a)ethylene plasma polymer at 20W, 100 mTorr, and 1:1 Ar:ethylene flow rate; (b)styrene plasma polymer at 15W, 28 mTorr, and no Ar flow; (c)styrene plasma polymer at 15W, 470 mTorr, and 6:1 Ar:styrene flow rate.*

under TEM. The coating thickness can be controlled through deposition time. The film, however, is not always uniform among the particles or on the same particle. It has been shown that styrene plasma polymer readily deposits as hollow nanoparticles. Other morphologies are also observed in the plasma polymer of styrene as well as isopropanol and ethylene.

REFERENCES

1. PROGIL, *U. K. Patent*, GB 1,269,018 (1972).
2. A. Grill, *Cold Plasma in Materials Fabrication*, (IEEE Press, 1994) pp.180.
3. Y. Matsuda and H. Yasuda, *Thin Solid Films*, **118**, 211 (1984).
4. H. Biederman and Y. Osada, *Adv. Polym. Sci.*, **95**, 57 (1990).
5. R. Liepins and H. Yasuda, *J Appl. Polym. Sci.*, **15**, 2957 (1971).
6. H. Nomura, P. W. Kramer, and H. Yasuda, *Thin Solid Films*, **118**, 187 (1984).
7. R. K. Sadhir, W. J. James, and R. A. Auerbach, *Thin Solid Films*, **97**, 17 (1982).
8. H. P. Schreiber, M. R. Wertheimer, and A. M. Wrobel, *Thin Solid Films*, **72**, 487 (1980).
9. C. M. Weikart, M. Miyama, and H. K. Yasuda, *J. Colloid Interface Sci.*, **211**, 18 (1999).
10. C. M. Weikart, M. Miyama, and H. K. Yasuda, *J. Colloid Interface Sci.*, **211**, 28 (1999).
11. H. Yasuda, *Plasma Polymerization*, (Academic, 1985) pp.277-333, pp.238-250.
12. R. Liepins and K. Sakaoku, *J. Appl. Polym. Sci.*, **16**, 2633 (1972).
13. H. Kobayashi, A. T. Bell, and M. Shen, *J. Appl. Polym. Sci.*, **17**, 885 (1973).
14. M. Nakayama, H. Morita, and Y. Kubota, *U.S. patent*, US 4,810,524 (1989).
15. D. Vollath, B. Seith, and V. Szabó, *German patent*, DE 19,638,601 (1998).
16. M. A. Lieberman and A. J. Lichtenberg, *Principles of Plasma Discharges and Materials Processing*, (Wiley, 1994) pp.16.
17. J. –P. Bœuf and C. Punset, Physics and modeling of dusty plasmas, *Dusty Plasmas*, ed. A. Bouchoule (Wiley, 1999) pp.27-39.
18. T. Nitter, *Plasma Sources Sci. Technol.*, **5**, 93 (1996).

HIGH SPIN Mn MOLECULAR CLUSTERS: SPIN STATE EFFECTS ON THE OUTER CORE-LEVEL MULTIPLET STRUCTURES

A. J. NELSON[*], J. G. REYNOLDS[*] and GEORGE CHRISTOU[**]

[*]Lawrence Livermore National Laboratory, Livermore, CA 94550
[**]Indiana University, Department of Chemistry, Bloomington, IN 47405

ABSTRACT

Oxo-bridged manganese polynuclear complexes have applications in a variety of technologies, such as single-molecule nanomagnets, catalysis and photosynthetic redox chemistry. The reason that these types of compounds are capable of such important and varied technologies is thought to be because they possess ground states with large spin values. However, the electronic, structural and magnetochemical relationships are not well understood and need to be thoroughly investigated to adequately explain why Mn is such an integral part of so many useful processes. X-ray photoemission spectroscopy was used to study the Mn 3p, 3s and valence band electronic behavior as a function of Mn cluster structural properties, where the cluster size and nuclearity are systematically varied. Results show a chemical shift of the Mn $3p_{3/2,1/2}$ spin-orbit pair related to the cluster size and nuclearity. Also, the Mn 3s ^{7}S and ^{5}S final state multiplet components shift since it involves the binding energy of a ligand valence electron. In addition, the branching ratio of the ^{7}S:^{5}S states is related to the 3s-3d electron correlation. Specifically, in the ^{7}S state, the remaining 3s electron is well correlated with 3d electrons of parallel spin, while in the ^{5}S state the two spins are antiparallel. Changes in this electron correlation are clearly observed in the ^{7}S:^{5}S branching ratio as a function of cluster size and ligand electronegativity.

INTRODUCTION

Oxo-bridged manganese polynuclear complexes have proved useful in the development of single-molecule nanomagnets. [1,2] These molecules have a large ground state spin S and a large magnetic hysteresis comparable to that observed in hard magnets. This provides the possibility of molecular bistability, opening the way to store information at the molecular level.

Spin state effects can be examined by x-ray photoemission spectroscopy of outer core-level multiplet structures. Previous photoemission studies on transition metal compounds reveal core-level multiplet structures that are best understood in terms of configuration-interaction (CI) calculations including intrashell electron correlation, charge-transfer and final-state screening.[3-5] In addition, these multiplet structures are also strongly influenced by covalency and ligand coordination.[6,7]

The neutral Mn atom has a $1s^2 2s^2 2p^6 3s^2 3p^6 3d^6$ configuration and a high-spin $[3d^5 4s^2]$ configuration. In solids the (empty) 4s band lies 2 to 4 eV above the top of the $3d^N$ band, depending on the ion. Photoelectron transitions are allowed between the initial state $2p^6 3s^2 3p^6 3d^N$ (N = 3,4,5 for Mn^{+4}, Mn^{+3}, Mn^{+2}, respectively) and a series of final states ($2p^5 3d^{N+1}$).

It has been shown that for Mn dihalides, the outer Mn 3s core-level final state configuration can be either $\underline{3s}3d^5$ or $\underline{3s}3d^6\underline{L}$ depending on final state screening effects due to the ligand ($\underline{3s}$ and $\underline{L}$ indicate that there is one electron missing in the Mn 3s and the ligand valence state, respectively). Also, the 3s final state has ^{7}S and ^{5}S symmetry, e.g. the Mn^{2+} initial state $(3s^2 3p^6 3d^5)^6$S has two possible final states, $(3s^1 3p^6 3d^5)^7$S or $(3s^1 3p^6 3d^5)^5$S. In the ^{7}S state, the remaining 3s electron is well correlated with 3d electrons of parallel spin, while in the ^{5}S state

the two spins are antiparallel. This electron correlation reduces the branching ratio of the ^7S:^5S states. In addition, as the ligand electronegativity decreases, charge-transfer satellites become important and the spin state purity is lost in the 3s spectra. The spectra become representative of mixed unscreened ($3d^N$) and locally screened ($3d^{N+1}$) final states. Thus, we see that the 3s core-level is polarized by the $3d^5$ shell.

This paper presents the results of a systematic study of the 3s and 3p core-level photoemission, and satellite structures for Mn oxo-bridged compounds. Outer core-level multiplet splitting was characterized as a function of Mn cluster size, nuclearity and ligand type. Interpretation of the 3p and 3s spectra is consistent with the configuration-interaction (CI) model including intrashell electron correlation, charge-transfer and final-state screening.

EXPERIMENTAL

The manganese polynuclear complexes are characterized as having trapped-valence oxidation-state Mn cores bridged to various ligands. The Mn cores analyzed are Mn^{3+}, $[Mn_3O]^{6+}$, $[Mn_4O_3]^{7+}$, $[Mn_4O_2]^{8+}$, and $[Mn_{12}O_{12}]^{16+}$. The ligands are dibenzoylmethane (dbm), 2-hydroxymethyl pyridine (hmp), picolinic acid (pic), pyridine (py), and 2-hydroxy-2,4,6-cycloheptatrienone (tropolone or TROP). Note that the ligands dbm, hmp and pic usually bind as anions while pyridine usually forms a neutral complex. The cation tetra-n-butylammonium (TBA) is used as a counter ion. These structures have high ground state spins as determined by oxidation state and topology of the polynuclear transition metal core.[8-10]

ESCA experiments were performed on a Physical Electronics 5400 ESCA system using Mg Kα radiation (1253.6 eV) and a hemispherical analyzer pass energy of 17.90 eV giving an overall energy resolution of 1.1 eV. All binding energies are referenced to the Fermi level of the analytical instrument as calibrated to the Au 4f peaks. Binding energies were further referenced to the C 1s photoelectron line arising from adventitious carbon at 284.6 eV to account for charging effects.

RESULTS AND DISCUSSION

Figure 1 shows the Mn 3s and 3p spectral regions for the manganese polynuclear complexes. As previously stated, the excitation energy was 1253.6 eV, and thus the positions and relative intensities of the Mn 3s and Mn 3p multiplets can be considered to be in the sudden limit approximation [1,2] with little coupling between the ion and the photoelectron. The figure shows a chemical shift of the Mn $3p_{3/2,1/2}$ spin-orbit pair associated with the trapped-valence oxidation states. The unresolved 3p peaks are somewhat broadened, but a direct correspondence can be made between observed features in these spectra and those in the literature.[3] Specifically, the main 3p line represents the ^7P ionic final state and the higher binding energy shoulder represents the spin-orbit component $^5P(1)$. Final state screening effects in the core level spectra depends strongly on the electronegativity of the anions (dbm$^-$, hmp$^-$, and pic$^-$) and will affect the final state branching ratio. Specifically, note the variation of the quintet:septet (^7P:^5P) final state branching ratio as the Mn core size increases and becomes a $[Mn_{12}O_{12}]^{16+}$ $Mn^{II}Mn^{III}Mn^{IV}$ trapped-valence oxidation-state. In addition, the covalency of the larger complexes increases manifesting itself as a drastically reduced 3p branching ratio.
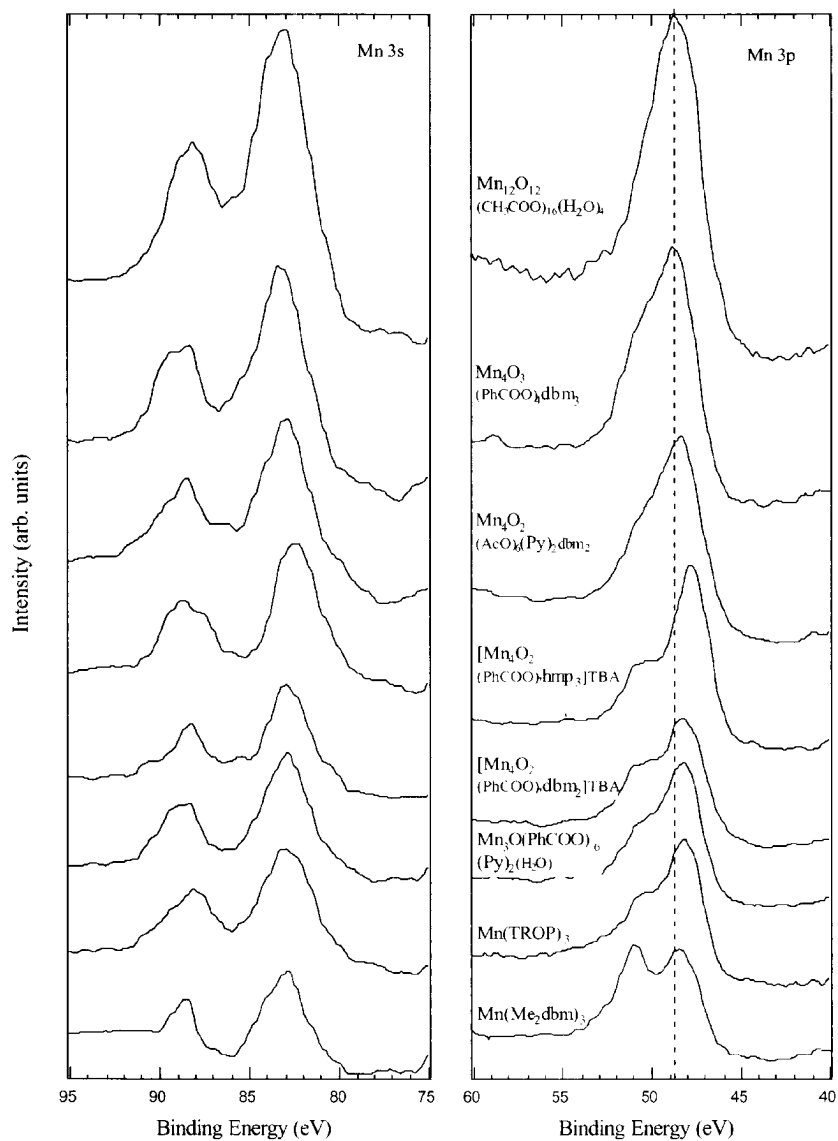
Figure 1. High-resolution XPS spectra of Mn 3p and 3s core levels for the Mn polynuclear complexes.

The binding energy positions for the Mn 3s ^7S and ^5S multiplet components are summarized in Table I. Note that the Mn 3s multiplet splitting (ΔMn 3s) becomes smaller as the Mn trapped-valence oxidation state increases, consistent with published data.[3-5] Also note that the ^7S and ^5S multiplet components shift accordingly since they are correlated with charge transfer between the Mn d-states and ligand p-states. In addition, note that the FWHM of the ^5S multiplet component is affected by ligand chemistry consequently affecting the Mn 3s branching ratio. Specifically, as the ligand electronegativity decreases, charge-transfer from the ligand p-state to the Mn d-state causes the spin state purity to be lost in the 3s spectra. Thus, the branching ratio corresponding to S − 1/2 and S + 1/2 final states that principally reside on the p orbitals of the [ligand]- and the d orbitals of the [MnO]+ core, decreases. Note that the branching ratios for complexes with the dbm ligand are larger since the ^5S component is diminished indicating that the s and d electrons spins are mostly parallel.

Table I. Summary of the Mn 3p and 3s Photoelectron Results for Manganese Polynuclear Complexes.

Sample [Mn oxidation state]	Mn 3p (eV)		Mn 3s (eV)		FWHM[a]		ΔMn 3s (eV)	Mn 3s Branching Ratio[b]
	^7P	^5P	^7S	^5S	^7S	^5S		
Mn(Me$_2$dbm)$_3$ [Mn^{III}]	48.4	50.9 Δ=2.5	82.7	88.4	3.0	1.5	5.7	4.4
Mn(TROP)$_3$ [Mn^{III}]	48.2	50.2 Δ=2.0	82.7	88.0	3.5	3.2	5.3	1.8
[Mn$_3$O(PhCOO)$_6$ (Py)$_2$(H$_2$O)] [Mn^{II}, 2Mn^{III}]	48.2	50.5 Δ=2.3	82.8	88.6	3.2	2.8	5.8	2.2
[Mn$_4$O$_2$(PhCOO)$_7$db m$_2$]TBA [Mn^{III}]	48.2	50.4 Δ=2.2	82.9	88.2	2.8	2.0	5.3	2.4
[Mn$_4$O$_2$(PhCOO)$_7$hm p$_3$]TBA [Mn^{III}]	47.7	50.2 Δ=2.5	82.4	88.4	3.0	3.2	6.0	1.8
[Mn$_4$O$_2$(AcO)$_6$ (Py)$_2$dbm$_2$] [Mn^{III}]	48.3	50.6 Δ=2.3	82.8	88.4	3.5	3.0	5.6	2.2
[Mn$_4$O$_3$(PhCOO)$_4$db m$_3$] [3Mn^{III}, Mn^{IV}]	48.7	50.8 Δ=2.1	83.2	88.5	3.2	3.0	5.3	2.1
[Mn$_{12}$O$_{12}$ (CH$_3$COO)$_{16}$ (H$_2$O)$_4$] [Mn^{II}, Mn^{III}, Mn^{IV}]	48.7	−	83.1	88.2	3.8	4.8	5.1	1.4

a) Full width half-maximum of Mn 3s peaks in eV.
b) The branching ratio of the Mn 3s peaks are based the area ratio of the ^7S:^5S states.

Figure 2 graphically summarizes the Mn cluster oxidation state versus Mn 3s multiplet splitting for the Mn polynuclear complexes. The multiplet splitting for these ligands is an

indication of the 3s polarization by the 3d final states. Also, polarization of the ligand can delocalize mobile π electrons and thus affect multiplet splitting.
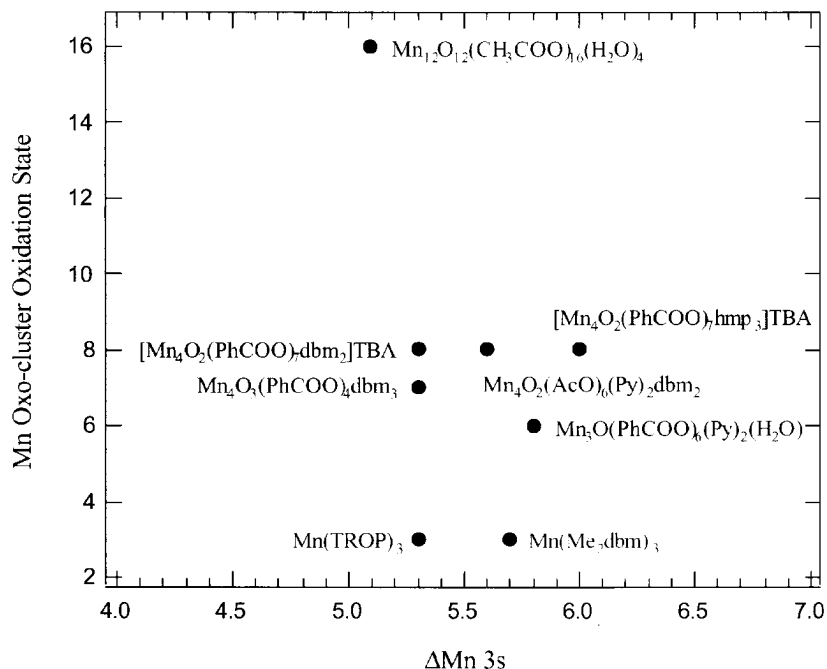
Figure 2. Mn cluster oxidation state versus Mn 3s multiplet splitting for the Mn polynuclear complexes.

CONCLUSIONS

We have presented the results of a systematic study of the 3s and 3p outer core-level multiplet splitting as a function of Mn cluster size, nuclearity and ligand type. Results show that the Mn 3p final state branching ratio changes as the Mn core size and trapped-valence oxidation-state increases. In addition, as the covalency of the larger complexes increases the 3p branching ratio is reduced. Results also show that the Mn 3s multiplet splitting became smaller as the Mn trapped-valence oxidation state increased. The observed multiplet splitting provides further understanding of these single-molecule nanomagnet materials.

Acknowledgments

REFERENCES

1. D. Ruiz-Molina, G. Christou, D.N. Hendrickson, Mol. Cryst. Liq. Cryst. **343**, 335 (2000).

2. J. Yoo, E.K. Brechin, A. Yamaguchi, M. Nakano, J.C. Huffman, A.L. Maniero, L.C. Brunel, K. Awaga, H. Ishimoto, G. Christou, and D.N. Hendrickson, Inorg. Chem. **39**, 3615 (2000).

3. P.S. Bagus, A.J. Freeman and F. Sasaki, Phys. Rev. Lett. **30**, 850 (1973).

4. C.S. Fadley, in *Electron Spectroscopy: Theory, Techniques, and Applications*, edited by C.R. Brundle and A.D. Baker (Academic, London, 1978) Vol. II, Chap. 1.

5. B. Hermsmeier, C.S. Fadley, B. Sinkovic, M.O. Krause, J. Jimenez-Mier, P. Gerard, T.A. Carlson, S.T. Manson and S.K. Bhattacharya, Phys. Rev. **B48**, 12425 (1993).

6. M. Fujiwara, T. Matsushita and S. Ikeda, J. Electron Spectroscopy Rel. Phenom. **74**, 201 (1995).

7. A. J. Nelson, John G. Reynolds and Joseph W. Roos, J. Vac. Sci. Technol. **A18(4)**, 1072 (2000).

8. Michael W. Wemple, H.-L. Tsai, S. Wang, Juan Pablo Cluade, W.E. Streib, J.C. Huffman, D.N. Hendrikson and George Christou, Inorg. Chem. **35**, 6437 (1996).

9. S. Wang, H.-L. Tsai, Eduardo Libby, K. Folting, W.E. Streib, D.N. Hendrikson and George Christou, Inorg. Chem. **35**, 7578 (1996).

10. Sheyi Wang, Michael S. Wemple, Jae Yoo, Kirsten Folting, John C. Huffman, Karl S. Hagen, David N. Hendrickson, and George Christou, Inorg. Chem. **39**, 1501 (2000).

Intra-Monolayer Hydrogen-Bonding in Monolayer Protected Gold Clusters

Andrew K. Boal and Vincent M. Rotello*
Department of Chemistry
University of Massachusetts, Amherst
Amherst M.A. 01003

ABSTRACT

Unlike the highly ordered Self-Assembled Monolayers (SAMs) formed on flat gold surfaces, those on gold nanoparticles radiate from a roughly spherical center and are amorphous in structure. One result of this structural motif is that the strength of *intra*-monolayer non-covalent interactions, such as π-stacking and hydrogen bonding, are a function of the distance of the recognition element from the colloidal core. We present here an exploration of these phenomena in amide functionalized thiols in MPCs where the amide functionality position was varied in the alkane chain. [1]

INTRODUCTION

Self-Assembled Monolayers (SAM) of organic molecules on flat surfaces are well known to form highly-ordered, semi-crystalline phases.[2] SAMs on nanoparticles, or Monolayer Protected Clusters (MPCs) [3] are less ordered as they radiate from a highly faceted, roughly spherical surface. Here, order is decreased as a function of distance from the nanoparticle core (Figure 1).[4] This variable degree of order will have a strong impact on the design and fabrication of nanoscale devices based on functional organic components in the monolayer.[5] To explore this phenomena, we have prepared a series of amide functionalized MPCs (Figure 2) and investigated the nature of both *intra-* and *inter*-monolayer hydrogen bonding in the solid and solution phases.
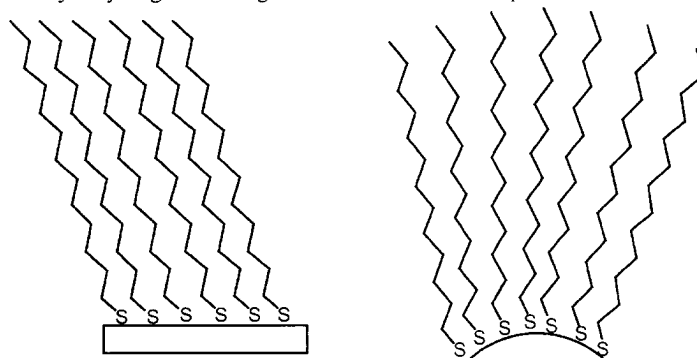
Figure 1. Monolayer structure on (left) flat and (right) colloidal surfaces.
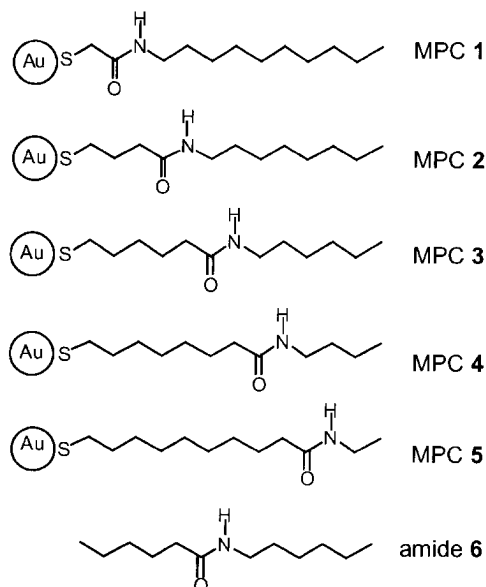
Figure 2. MPCs 1 - 5 and amide 6.

EXPERIMENTAL DETAILS

Synthesis of amide functionalized thiols, which typically involved acylation various alkyl amines with ω-haloacid chlorides followed by halogen displacement with potassium thiol acetate and acyl protection group removal with methoxide, was described fully earlier.[1] These thiols were then used in the standard two-phase Brust reaction to yield the desired MPCs.[6] All MPCs behaved in a manor typical for alkane monolayers, except MPC 5 which precipitated out during its synthesis, likely due to the high polarity of the near-terminal amide groups. Finally, amide 6 was also prepared to provide a non-monolayer reference compound.

IR spectra were recorded either as thin films cast on NaCl plates from CH_2Cl_2 or as CH_2Cl_2 solutions in a CaF_2 solution IR cell. 1H NMR spectra were recorded in K_2CO_3 neutralized $CDCl_3$ and referenced to TMS ($\delta = 0.0$ ppm) as an internal standard. TEM samples were prepared by placing one drop of the desired MPC solutions (1 mg/mL in CH_2Cl_2) on a 300 mesh Cu grid with a carbon film. Samples were then analyzed on a JEOL 100CX TEM using an acceleration voltage of 100 keV.

DISCUSSION

Hydrogen bonding was initially investigated in films of MPCs. (Figure **3**) Here, a general trend in decreased hydrogen bonding efficiency is observed for the series of MPCs **2** to **5**, with a gradual increase in the NH stretching frequency from 3290 cm⁻¹ to 3294 cm⁻¹. In sharp contrast, a significant decrease in hydrogen bonding is exhibited by MPC **1**, with a NH stretching frequency of 3300 cm⁻¹. Amide thiols on flat gold surfaces, by comparisons, typically exhibit NH stretching frequencies of *ca.* 3293 cm⁻¹.[7] Further comparison can be made to films of amide **6**, known to be hydrogen bonded in the solid state, where the NH stretch occurs at 3286 cm⁻¹. The amide II region of the IR also provides insight into hydrogen bonding.[8] Non-hydrogen bound amides typically exhibit a peak at 1510 cm⁻¹, and a substantial shift to lower wave-numbers for MPC **1** is again indicative of decreased hydrogen bonding relative to the other MPCs. (Figure **3**)
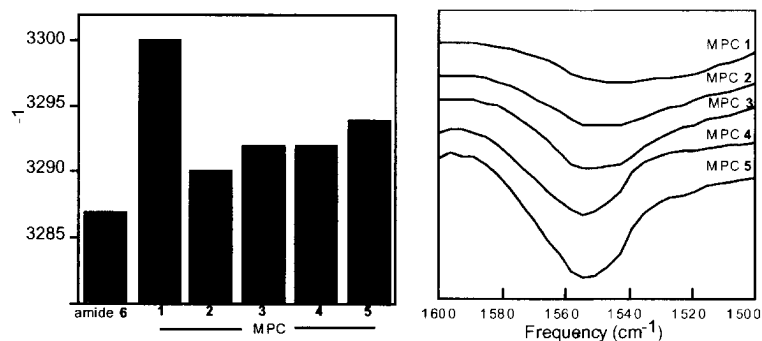
Figure 3. Left: NH stretching frequency of amide **6** and MPCs **1** - **5** as thin films. Right: IR spectra of the Amide II region for the same compounds.

Since MPC monolayers are well known to interdigitate in the solid state,[9] hydrogen bonding was also investigated in solution to confirm that *intra*-monolayer interactions predominate. In CH₂Cl₂ solutions, a similar trend of NH bond stretching was observed: MPC **1** was found to be the least hydrogen-bound ($v_{NH} = 3302$ cm⁻¹), followed by an initial increase then gradual decrease in the hydrogen bonding in MPCs **2** to **5**. In solution, the NH stretch of amide **6** occurred at 3446 cm⁻¹, and is indicative of negligible hydrogen bonding. Further, ¹H NMR confirmed this result in that the chemical shift of the amide NH proton moved upfield from 8.15 ppm (MPC **2**) to 7.7 ppm (MPC **5**), again indicating a decrease in hydrogen bonding when the distance from the core surface is increased.[10] These results are readily compared to amide **6**, where the amide NH proton is observed at 5.6 ppm. Neither the NH stretching frequency or chemical shift was significantly effected by a 10-fold dilution, indicating a low chance that the spectral shifts are a result of *inter*-monolayer hydrogen bonding (Figure **4**). Further, these experiments point out a more significant distance dependence trend in hydrogen bonding as a function of surface distance.
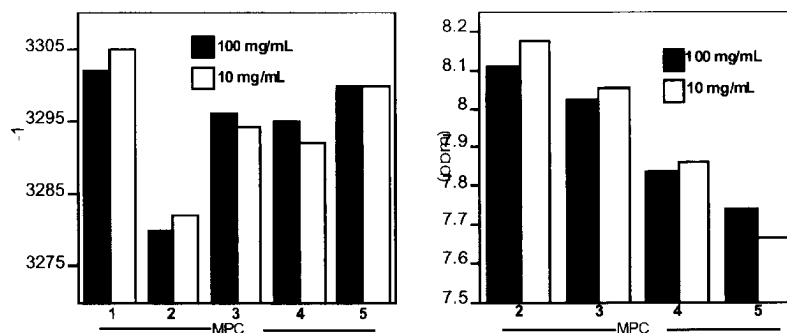
Figure 4. Left: NH stretching frequency of MPCs **1 - 5** as CH_2Cl_2 solutions at concentrations of 100 and 10 mg/mL. Right: NH chemical shift from the ^{1}H NMR spectra of MPCs **2 - 5** as $CDCl_3$ solutions at concentrations of 100 and 10 mg/mL.

These results can be rectified upon consideration of the radial nature of the monolayer structure. Close to the surface, as for MPC **1**, there is a high amount of steric congestion, and this likely leads to the inability of the amide groups to adopt an ideal configuration. Close packing is overcome for MPC **2**, where the strongest hydrogen bonding is observed. As the amide group is moved further from the inorganic core, MPCs **3 - 5**, an increase in monolayer disorder makes hydrogen bonding entropically unfavorable.

Transmission Electron Microscopy (TEM) can provide insight to *inter*-monolayer hydrogen bonding interactions as this should lead to the formation of nanoparticle aggregates. In the case of MPCs **1 - 4**, no aggregation is observed (Figure **5**). TEMs of MPC **5**, however, reveal the presence of several large (hundreds of nanometers in size) aggregates. These structures are likely a result of strengthened interdigitation as a result of *inter*-monolayer amide hydrogen bonding (Figure **6**).
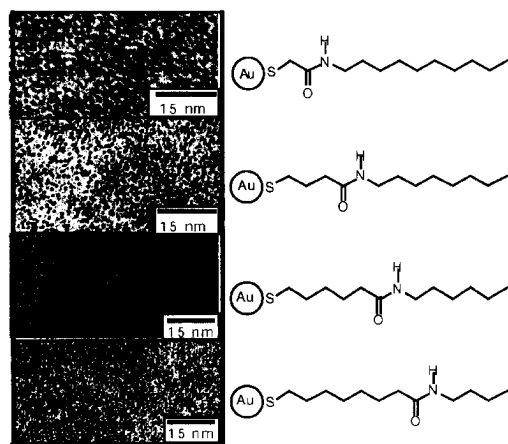
Figure 5. TEM micrographs of MPCs **1** - **4**.
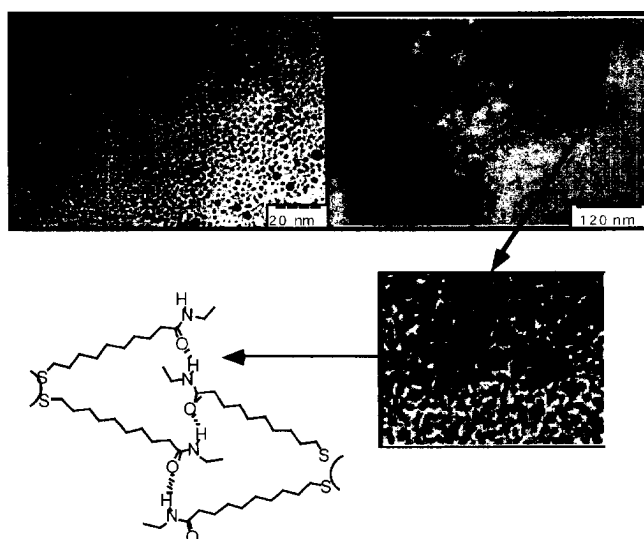
Figure 6. TEM micrographs of MPCs **5**. Top left: an unaggregated region showing particles of both *ca.* 2 and *ca.* 6 nm diameter. Top right: a low magnification view of an aggregated region and, bottom right, a magnification of the region indicated by the box. Bottom left: depiction of the proposed *inter*-monolayer hydrogen bonding responsible for aggregation.

CONCLUSIONS

In summary, a series of MPCs bearing amide containing monolayers has been prepared. In this series, the amide linkage was systematically moved along the alkane chain to provide the ability to study the strength of *inter-* and *intra*-monolayer hydrogen bonding interactions as a function of distance from the gold core. It was found that when the amide group was in extreme proximity to the core surface, steric crowding prohibited extensive hydrogen bonding interactions. This was followed by an increase in interactions when steric congestion could be overcome, and a slow decline in hydrogen bonding as the amide was moved further away from the surface. Near terminal amide groups were also found to participate in *inter*-monolayer interactions in the solid state, as evidenced by aggregation observed in TEM. These findings are consistent with the radial nature of monolayer structure in MPCs.

ACKNOWLEDGMENTS

REFERENCES

1. The majority of this work has appeared in print previously, see: A. K. Boal, V. M. Rotello, *Langmuir* **16**, 9527 (2000).
2. (a) C. D. Bain, E. B. Troughton, Y.-T. Tao, J. Evall, G. M. Whitesides, R. G. Nuzzo, *J. Am. Chem. Soc.* **111**, 321 (1989). (b) Ulman, A. *An Introduction to Ultrathin Organic Films,* (Academic Press, Boston, M. A., 1991).
3. A. C. Templeton, W. P. Wuelfing, R. W. Murray, R. W. *Acc. Chem. Res.* **33**, 27 (2000).
4. (a) W. D. Luedtke, U. Landman, *J. Phys. Chem.* **100**, 13323, (1996). (b) M. J. Hostetler, J. J. Stokes, R. W. Murray, *Langmuir* **12**, 3604 (1996).
5. (a) A. K. Boal, V. M. Rotello, *J. Am. Chem. Soc.* **121**, 4914 (1999). (b) A. K. Boal, V. M. Rotello, *J. Am. Chem. Soc.* **122**, 734 (2000).
6. M. Brust, M. Walker, D. Bethell, D. J. Schiffrin, R. Whyman, *Chem. Comm.* 801 (1994).
7. R. S. Clegg, J. E. Hutchison *Langmuir* **12**, 5239 (1996).
8. S.-W. Tam-Chang, H. A. Biebuych, G. M. Whitesides, N. Jeon, R. G. Nuzzo, *Langmuir* **11**, 4371 (1995).
9. A. Badia, S. Singh, L. Demers, L. Cuccia, G. R. Brown, R. B. Lennox, *Chem. Eur. J.* **2**, 359 (1996).

Planar Synthesis of Anisotropic Nanoparticles

Gennady B. Khomutov, Radmir V. Gaynutdinov[1], Sergey P. Gubin[2], Alexander Yu. Obydenov, Eugene S. Soldatov, Alla L. Tolstikhina[1], Artem S. Trifonov
Faculty of Physics, Moscow State University, Moscow 119899, Russia, GBK@phys.msu.su
[1]Institute of Crystallography RAS, Moscow 119899, Russia
[2]Institute of General and Inorganic Chemistry RAS, Moscow 119899, Russia

ABSTRACT

A novel method of two-dimensional (2-D) synthesis of anisotropic nanoparticles have been developed in which nanoparticle growth is an example of 2-D process where true 2-D diffusion of precursor molecules and active intermediates, metal atoms and its complexes, nucleus and growing nanoparticles, surfactants and additives occurs only in the plain of a monolayer at the gas/liquid interface. Nanoparticles were generated via ultraviolet decomposition of a volatile insoluble metal-organic precursor compound (iron pentacarbonyl) and by chemical reduction of palladium from $Pd_3(CH_3COO)_6$ molecules in a mixed Langmuir monolayer with stearic acid, arachidic acid or octadecyl amine on the aqueous subphase surface. The properties of such surfactants to form Langmuir monolayer and to prevent aggregation of nanoparticles were here combined successfully. Atomic force microscopy, scanning tunneling microscopy and transmission electron microscopy techniques were used to study morphology of deposited nanoparticulate monolayers. The size and shape of nanoparticles were dependent substantially on the monolayer composition and state during the synthesis process. We demonstrate that planar synthesis in a monolayer at the gas/liquid interface allows to produce anisotropic extremely flat nanoparticles with very high surface to volume ratio and unique morphologies such as iron-containing magnetic nano-rings.

INTRODUCTION

Synthesis of nanosize metal-containing particles (metallic, oxidic and semiconductor) has recently drawn great attention because of their unique physicochemical properties and potentially wide applications in diverse devices and processes exploiting nanophase and nanostructured materials [1-3]. Anisotropic nanoparticles are of particular interest for basic and applied studies due to the anisotropy of size-dependent properties and substantial surface effects which can result in much more rich and enhanced physical and chemical properties compared to the conventional isotropic spherical particles. Therefore, development of novel methods for effective shape and size control of nanoparticles is of principal importance for nanoparticles research. The method of nanoparticles synthesis often influences the properties of the product, particularly the shape, size, crystal morphology and degree of crystallinity [4-11]. A novel approach to the synthesis of anisotropic nanoparticles was introduced recently in which nanoparticles were fabricated in a mixed Langmuir monolayer at the gas/liquid interface [12]. In the present study, nanoparticles were generated by the ultraviolet (UV) decomposition of $Fe(CO)_5$, and by chemical reduction of palladium from $Pd_3(CH_3COO)_6$ in mixed monolayers with stearic acid, arachidic acid or octadecyl amine onto the aqueous subphase surface. Atomic force microscopy (AFM), scanning tunneling microscopy (STM) and transmission electron microscopy (TEM) were used to image grown nanoparticles.

EXPERIMENTAL DETAILS

Stearic acid (SA), arachidic acid (AA) and octadecyl amine (ODA) were obtained

from Aldrich/Sigma. Iron pentacarbonyl was obtained from Alfa Inorganic. $Pd_3(CH_3COO)_6$ was obtained and purified by Prof. S.P. Gubin using known procedures. A MilliQ water purification system was used to produce clean water with an average resistivity of 18 MΩ-cm. Iron-containing nanoparticles were fabricated by the UV decomposition (UV irradiation from 300 mW conventional UV source, $\lambda \cong 300$ nm) of iron pentacarbonyl, a volatile water-insoluble metal-organic compound, in a mixed Langmuir monolayer formed by spreading an appropriate amount of the chloroform solution of $Fe(CO)_5$ with SA on the surface of purified water (pH=5.6). To synthesize Pd nanoparticles, the mixed solution of $Pd_3(CH_3COO)_6$ (water-insoluble precursor) with AA or ODA in chlorophorm was spread onto the surface of aqueous phase containing $NaBH_4$ as reducing agent. Nanoparticles then were synthesized in the mixed Langmuir monolayer formed after fast solvent evaporation on the surface of aqueous phase (incubation time 30 min, 21 °C). Langmuir monolayer formation, surface pressure (π) - monolayer area isotherm measurements and nanoparticulate monolayer transfer to solid substrates were carried out on a full automatic conventional Teflon trough as described elsewhere [12, 13]. Mica (for AFM study) and graphite (for STM study) substrates were freshly cleaved immediately before use. Samples for TEM measurements were prepared by direct collection of the nanoparticulate monolayer material from the aqueous subphase surface onto the Formvar film supported by the copper grid (diameter = 3 mm), then samples were dried and subjected to TEM analyses with the use of Jeol JEM-100B microscope. AFM measurements were performed with the use of Solver P47-SPM-MDT scanning probe microscope (NT MDT Ltd., Moscow, Russia) in a tapping mode. Images were measured in air at ambient temperature (21 °C) and were stable and reproducible. STM topographic images were obtained by recording the tip height at a constant tunnel current in a modified Nanoscop I microscope (Digital Instruments, U.S.A.) at ambient temperature. Tunnel current I = 0.3 nA, and a bias voltage V_{bias} = 200 mV.

RESULTS AND DISCUSSION

Typical STM image of the ultraflat iron-containing nanoparticle photochemically generated in a mixed iron pentacarbonyl/SA monolayer is shown in figure 1. In a sence, such system where 2-D arranged precursor molecules are photochemically decomposed with initiation of 2-D reactions of nanoparticles growth represents an ultimately thin photosensitive
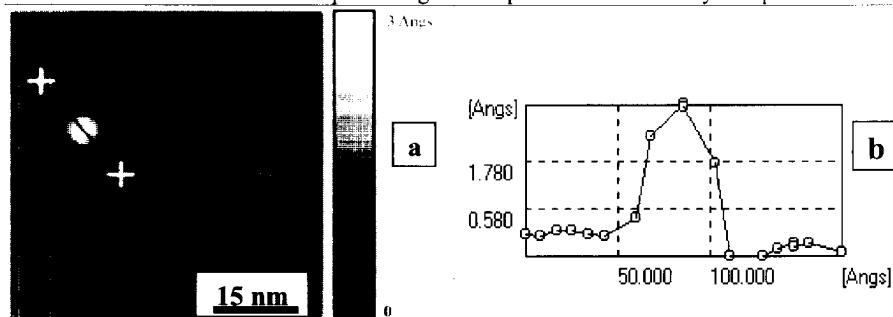
Figure 1. a): *STM topographic image (top view) of individual iron-containing nanoparticle synthesized in a mixed Langmuir monolayer and deposited by horizontal lifting method onto the surface of high oriented pyrolytic graphite substrate. Reaction conditions: initial* $Fe(CO)_5/SA$ *ratio in monolayer was 10:1, UV exposure time 3 min, T = 294 K, subphase pH = 5.6, uncompressed monolayer ($\pi = 0$). The white crosses and black line mark the position of cross-section.* **b):** *Cross-section profile of the nanoparticle shown on figure 1a).*

structure. Figure 2 shows corresponding AFM images of the nanoparticulate monolayer deposited onto the surface of mica substrate. Figure 2b) demonstrates AFM phase contrast regime image corresponding to the image 2a) revealing the difference in material of circular objects and surrounding SA matrix, thus indicating grown nanoparticles. Figure 1c) shows the typical height cross section profile of the image 1a) and indicates an overall film roughness of ~ 4 nm with clearly observable nanoparticles of the volkano-like morphology with obvious cavity in the central part. Nanoparticles are very flat (height about 1 nm) with very high surface-to-volume ratio (diameter/height ratio ~ 100). Nanoparticles grown in the compressed mixed monolayer (figure 2d) are characterized by significantly larger diameter (~ 200 nm and more), noncircular shape, but also by extremely small height (~ 2 nm). Some nanoparticles possessed ledges of ~ 5 nm height and formed aligned aggregates clearly seen in figure 2d). Such differences in morphologies of nanoparticles indicate that kinetic factors (anisotropic 2-D diffusion and surface concentration of reagents and active intermediates) and complex
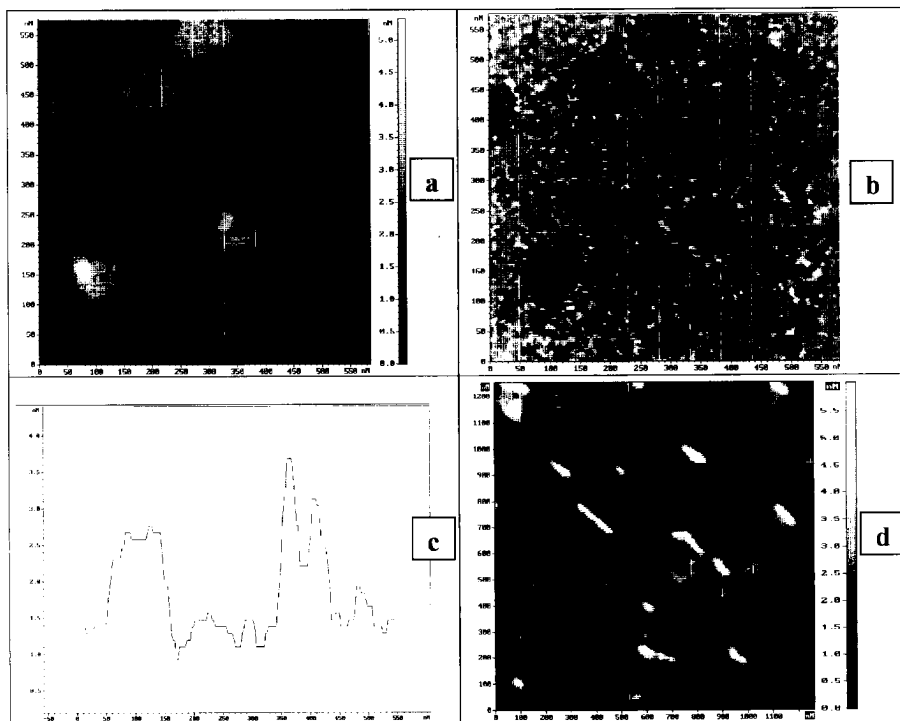
Figure 2. AFM tapping mode topographic images of iron-containig nanoparticles synthesized in the mixed floating monolayer (initial $Fe(CO)_5$/SA ratio was 10:1, UV exposure time 4 min, T = 294 K, subphase pH = 5.6) and deposited onto the mica substrate at π = 25 mN/m using vertical substrate lifting method. **a)**: nanoparticles were sinthesized at π = 0, top view image, 580×580 nm^2 scan area, the black-to-white color height scale is 0 -5 nm. **b)**: AFM phase contrast mode top view image corresponding to the image 2a). **c)**: Typical height cross-section profile of image 2a). **d)**: top view image of nanoparticles synthesized in a compressed monolayer (surface pressure during the synthesis of nanoparticles was $\pi \cong 2$ mN/m) 1.25×1.25 μm^2 scan area, the black-to-white color height scale is 0 – 6 nm.

structure of mixed compressed monolayer can play important role in the determination of nanoparticle morphology in the 2-D synthesis method.

Figure 3 illustrates the possibilities of 2-D synthesis approach to control the shape of noble metal, in particularly, Pd nanoparticles. In this embodiment the reduction of palladium in a mixed precursor plus surfactant monolayer floating on the surface of the aqueous subphase with sodium borohydride can be considered as an ultimate version of a two-phase reducing system in which precursor phase represents a monomolecular structure. It follows from figure 3 that the morphology of grown Pd nanoparticles is dependent on the presence of surfactant in the monolayer and on the nature of surfactant used. The homogeneous flat morphology of nanoparticles is clearly illustrated by figure 3c) where height histogram of the image 3a) is presented with two broad peaks corresponding to the most frequently present structure heights with main height difference about 2.4 nm demonstrating the terrace structure of the particulate monolayer with probable main Pd nanoparticle height about 2.4 nm.

Figure 4 shows TEM micrographs obtained from corresponding nanoparticulate
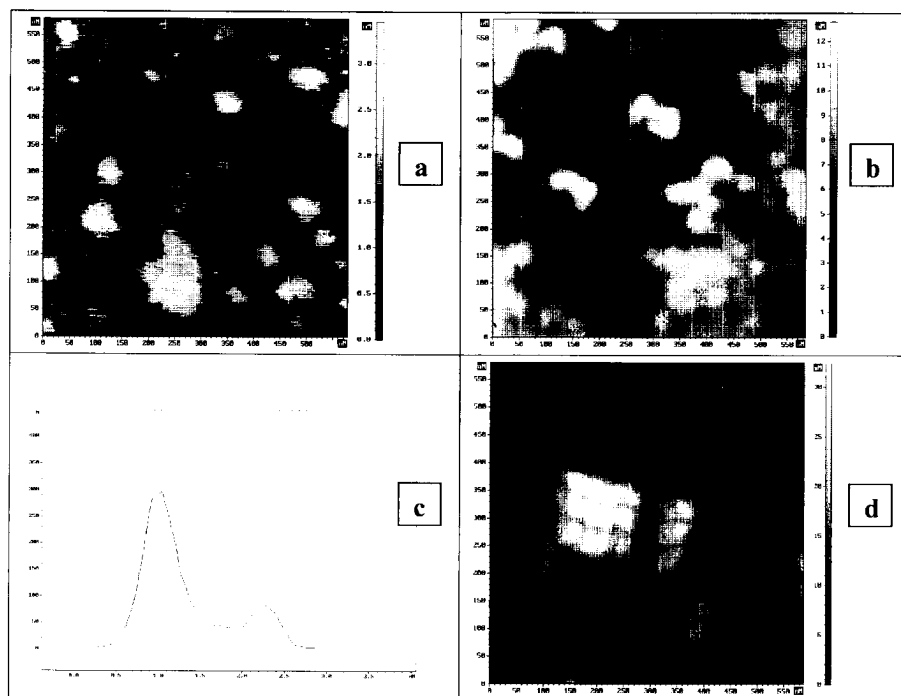
Figure 3. AFM tapping mode topographic images of Pd nanoparticles synthesized in a monolayer at the gas/NaBH$_4$ solution (5×10^{-3} M) interface at π = 0, T = 294 K, and deposited onto the mica substrate. **a):** top view image, 580×580 nm^2 scan area, the black-to-white color height scale is 0 - 3 nm, spreading solution of Pd$_3$(CH$_3$COO)$_6$/ODA with 1:1 ratio in chlorophorm (10^{-4} M ODA) was used. **b):** top view image, 580×580 nm^2 scan area, the black-to-white color height scale is 0 - 12.5 nm, spreading solution of Pd$_3$(CH$_3$COO)$_6$/AA with 1:1 ratio in chlorophorm (10^{-4} M AA) was used. **c):** height histogram of the image 3a). **d):** top view image, 580×580 nm^2 scan area, the black-to-white color height scale is 0 - 35 nm, spreading solution of Pd$_3$(CH$_3$COO)$_6$ in chlorophorm (10^{-4} M) without surfactant was used.

samples giving evidence for amorphous character of iron-containing nanoparticles and polycrystalline metallic Pd nanoparticles with morphology being in good agreement with STM and AFM data. Earlier we have observed ferromagnetic resonance and superparamagnetic signals in the material with iron-containing nanoparticles, indicating magnetic moments of the grown particles [14]. It was also found that the size and shape anisotropy of iron-containing nanoparticles grown under applied external fields were strongly dependent on the applied field orientation relatively to the monolayer surface [14, 15].
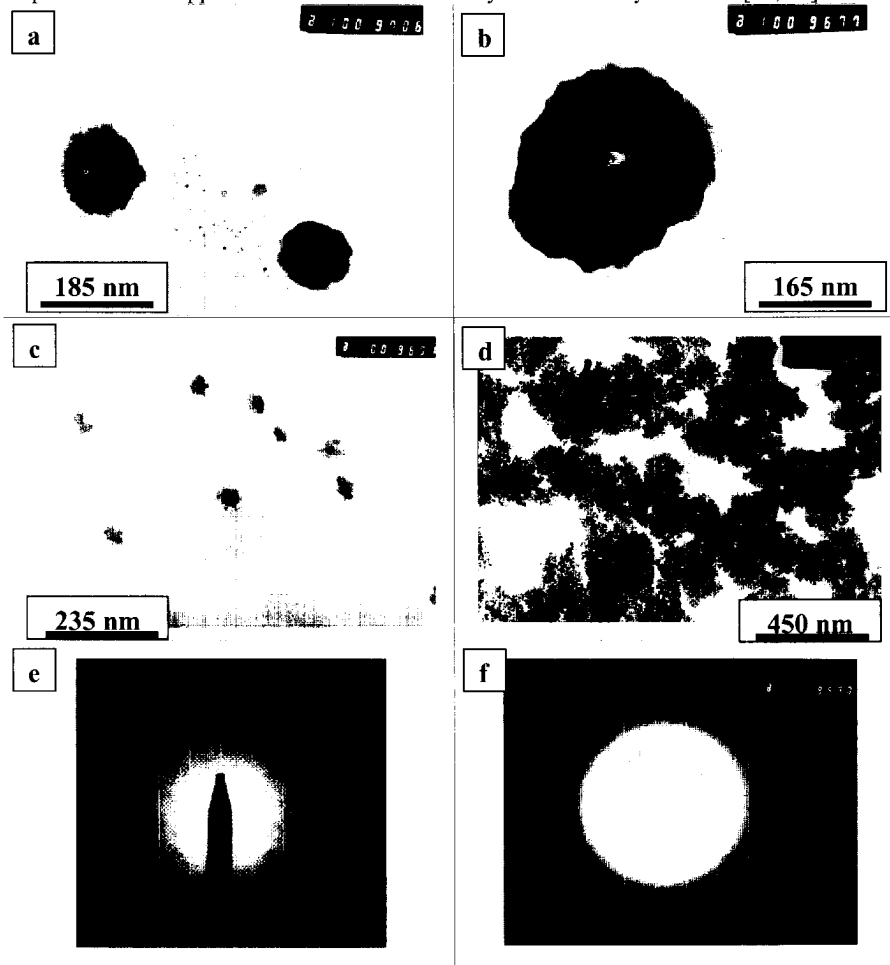
Figure 4. Transmission electron micrographs showing nanoparticles grown in Langmuir monolayer and deposited onto the copper grid with Formvar coating. Conditions for nanoparticle synthesis: for images **a)** and **b)** the same as in figure 2a), for image **c)** the same as in figure 3a), for image **d)** the same as in figure 3b). Image **e)** – selected area electron diffractogramm obtained from amorphous iron-containing nanoparticles (images 4a) and 4b)). Image f) – selected area electron diffraction pattern obtained from nanoparticles shown on images 4c) and 4d) indicating polycrystalline Pd.

CONCLUSIONS

A novel approach to the synthesis of anisotropic nanoparticles is developed in which nanoparticles are fabricated via decomposition of an insoluble metal-organic precursor compound in a mixed surfactant monolayer at the gas/liquid interface accompanied by 2-D reactions of nanoparticles growth. It is demonstrated that such 2-D synthesis method allows to produce anisotropic extremely flat inorganic nanoparticles including noble metal nanoparticles with very high surface to volume ratio and unique morphologies such as iron-containing magnetic nanoparticles with characteristic nano-ring shape. Controlling the morphology of nanoparticles via planar synthesis in a monolayer at the gas/liquid interface and/or under applied external fields opens new possibilities for regulation of the nanoparticles growth processes to obtain anisotropic inorganic nanostructures with different predetermined morphologies what could prove to be a promising approach for nanotechnology, nanophase engineering and creation of new nanostructured bulk materials and ultrathin films (down to monolayer thickness) with advanced, in particularly, highly anisotropic physical and chemical properties perspective for applications.

ACKNOWLEDGMENTS

REFERENCES

1. A.P. Alivisatos, *Science*, **271**, 933 (1996).
2. C.P. Collier, R.J. Saykally, J.J. Shiang, S.E. Henrichs and J.R. Heath, *Science*, **277**, 1978 (1997).
3. I. Pastoriza-Santos, D.S. Koktysh, A.A. Mamedov, M. Giersig, N.A. Kotov and L.M. Liz-Marzan, *Langmuir*, **16**, 2731 (2000).
4. *Nanoparticles in solids and solutions*, ed. J.H. Fendler and I. Dekany (Kluwer Academic Publishers, 1996).
5. T.S. Ahmadi, Z.L. Wang, T.C. Green, A. Henglein and M.A. El-Sayed, *Science*, **272**, 1924 (1996).
6. J. Zhu, S. Liu, O. Palchik, Yu. Koltypin and A. Gedanken, *Langmuir*, **16**, 6396 (2000).
7. C.K. Preston and M. Moskovits, *J. Phys. Chem*, **97**, 8495 (1993).
8. Y.Y. Yu, S.S. Chang, C.L. Lee and C.R.C. Wang, *J. Phys. Chem. B*, **101**, 6661 (1997).
9. S. Ravaine, G.E. Fanucci, C.T. Seip, J.H. Adair, D.R. Talham, *Langmuir*, **14**, 708 (1998).
10. E.S. Smotkin, C. Lee, A.J. Bard, A. Campion, M.A. Fox, T.E. Mallouk, S.E. Webber and J.M. White, *Chem. Phys. Lett.*, **152**, 265 (1988).
11. A.V. Nabok, A.K. Ray, A.K. Hassan, J.M. Titchmarsh, F. Davis, T. Richardson, A. Starovoitov and S. Bayliss, *Mat. Sci. Eng. C*, **8-9**, 171 (1999).
12. G.B. Khomutov, A.Yu. Obydenov, S.A. Yakovenko, E.S. Soldatov, A.S. Trifonov, V.V. Khanin, S.P. Gubin, *Mat. Sci. Eng. C*, **8-9**, 309 (1999).
13. G.B. Khomutov, E.S. Soldatov, S.P. Gubin, S.A. Yakovenko, A.S. Trifonov, A.Yu. Obydenov, V.V. Khanin, *Thin Solid Films*, **327-329**, 550 (1998).
14. G.B. Khomutov, S.P. Gubin, Yu.A. Koksharov, V.V. Khanin, A.Yu. Obidenov, E.S. Soldatov, A.S. Trifonov, *Mat. Res. Soc. Symp. Proc.*, **577**, 427 (1999).
15. S.P. Gubin, A.Yu. Obydenov, E.S. Soldatov, A.S. Trifonov, V.V. Khanin and G.B. Khomutov, *PCT International Patent* WO 00/15545, Application RU99/00091, Filed 30.03.1999., Published 23.03.2000, Priority date 11.09.98.

Polymeric Surfactants Based on Oleic Acid— Lamellar Liquid Crystal Polymerization of Sodium Oleate/Water/Hexadecane/4-Allyl-1, 6-Heptadiene-4-ol System And Sodium Oleate/ Water/ Hexadecane/Pentaerythritol Triarylate System

Qinghong Fu
Institute of Materials Science, University of Connecticut,
Storrs, CT06269, U.S.A.

ABSTRACT

The lamellar liquid crystalline (LLC) regions of sodium oleate (NaOL)/ water/ hexadecane/4-allyl-1,6-heptadiene-4-ol (AHD-ol) system and sodium oleate (NaOL) /water/ hexadecane/pentaerythritol triacrylate (PETA) system were determined when the weight ratio of NaOL to hexadecane was kept at 90:10. Copolymerization was accomplished in the LLC phases of the above systems. AHD-ol and PETA acted as the cross-linking agents between the double bonds on NaOL backbones in their systems respectively. Interlayer spacing determinations showed that the cross-linking agents, AHD-ol and PETA, were solubilized in the middle of the NaOL hydrocarbon chains in each LLC system. As a result, the copolymerization reactions were confined within each monolayer of the amphiphilic bilayer. The systems after the copolymerization were a mixture of water and LLC phase for the former system and a mixture of LLC phase and solid particles for the latter one. The aqueous solutions of copolymers exhibited surface activity, but with both higher CMC and surface tension values than NaOL aqueous solutions.

INTRODUCTION

In the two lamellar liquid crystalline (LLC) polymeric systems studied previously[1,2], all the cross-linkers used had two reactive double bonds in each molecule. The cross-linker DVG, which was dissolved in the middle of NaOL hydrocarbon chains, was used to confine the copolymerization within each monolayer of amphiphilic bilayer although the copolymerization itself would somewhat disrupt the original ordered LLC structure. It showed that the copolymers formed still kept the surface activity in each system studied.

$$CH_2= CH-\overset{\overset{O}{\|}}{C}-O-CH_2-\overset{\overset{OH}{|}}{\underset{\underset{CH_2}{|}}{\overset{|}{C}}}-CH_2-O-\overset{\overset{O}{\|}}{C}-CH=CH_2$$

CH₂= CH—C—O—CH₂—C—CH₂—O—C—CH=CH₂

$$CH_2= CH-\overset{\overset{OH}{|}}{\underset{\underset{\underset{CH_2}{\|}}{CH}}{C}}-CH= CH_2$$
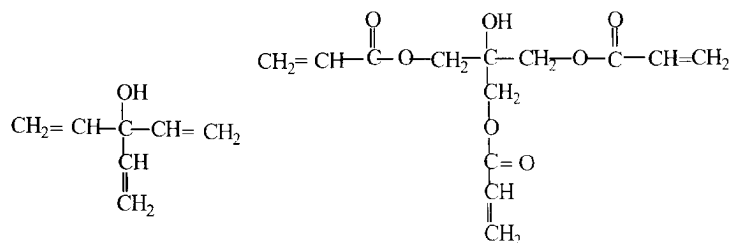
AHD-ol   **PETA**

4 – Allyl -1, 6 – heptadiene – 4 - ol (AHD-ol) and pentaerythritol triacrylate (PETA), which have three double bonds in one molecule respectively (as shown above), were selected as crosslinkers in this study. Both of the cross-linkers could be dissolved only in the middle of the hydrocarbon

chains in the LLC phase of NaOL/ water/ hexadecane system. Moreover, these crosslinkers have polar groups substituted next to the double bonds to promote their reactivity, which would facilitate the complete copolymerization. As a result, the copolymerization was confined only within each monolayer of the bilayer in the LLC phases of both NaOL/ water/ hexadecane/ AHD-ol and NaOL/ water/ hexadecane/ PETA systems.

EXPERIMENT

Lamellar liquid crystalline phases of NaOL/ water/ hexadecane/ AHD-ol and NaOL/ water/ hexadecane/ PETA systems were polymerized with the initiation of BPO by heating at 72 ^{0}C for 48hrs under the protection of pure nitrogen. The molar ratios of double bonds between AHD-ol (or PETA) and (NaOL + OLA) were kept at 1:1.

The IR spectra were recorded on a Mattson Galaxy 202 Fourier Transform Infrared Spectrometer, casting the chloroform solutions of the systems after polymerization onto CaF_2 disks and letting the solvent evaporate. The solid sample of NaOL was determined in the form of a KBr pellet. Liquid samples of AHD-ol and PETA were measured by placing several drops between the two CaF_2 crystal windows. The partial phase diagrams of both the four-component systems containing NaOL/ water/ hexadecane/ AHD-ol and NaOL/ water/ hexadecane/ PETA were determined by optical observation of the samples both visually and with the aid of polarized optical microscopy. In these four-component systems, the weight ratio of hexadecane to NaOL was always kept at 10:90. The boundary of the liquid crystalline phase was confirmed by the results from small-angle X-ray diffraction. The surface tension of the aqueous solutions of NaOL and copolymers was measured by means of Fisher Surface Tensionmat Model 21. Liquid crystalline samples were observed with Olympus Polarized Optical Microscope (Model BHA-P) and microphotos were obtained with a Polaroid microcamera

RESULTS AND DISCUSSION

LLC structure of NaOL/ water/ hexadecane/ AHD-ol system and NaOL/ water/hexadecane/ PETA system

Figure 1(a) is the partial phase diagram for NaOL/ water/ hexadecane/ AHD-ol system. AHD-ol was solubilized into the LLC phase of NaOL/ water/ hexadecane system with its maximum solubility at 16(wt.)% when the weight ratio of water to (NaOL + OLA) was 56:28. Figure 1(b) is the partial phase diagram for the NaOL/ water/ hexadecane/ PETA system. PETA was also solubilized into the LLC phase of the NaOL/ water/ hexadecane system, but with its maximum solubility at 12(wt.)% when the weight ratio of water to (NaOL + OLA) was equal to 61:27.

Figure 2 shows the relationship of interlayer spacing with the volume ratio of water in the systems NaOL/ water/ hexadecane, NaOL/ water/ hexadecane/ AHD-ol, and NaOL/ water/ hexadecane/ PETA. In all three systems, the weight ratio of NaOL to hexadecane was kept constantly at 90:10. It was shown in Figure 4 that the addition of cross-linkers to the LLC phase of NaOL/water/hexadecane system did not affect the interlayer spacing, with or without water, of the LLC phase. Thus both of the cross-linkers used here, similar to DVG reported previously[2], were solubilized in the middle of the hydrocarbon chains of the NaOL molecules.

The bilayer structure of lamellar liquid crystalline system NaOL/ hexadecane/ water/ crosslinkers is shown in Figure 3.
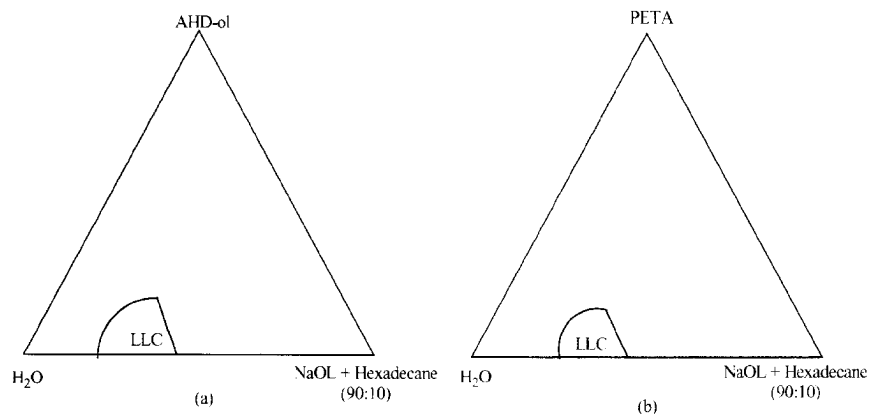
Figure 1. *Partial phase of (a) NaOL/ water/ hexadecane/ AHD-ol system and (b) NaOL/ water/ hexadecane/ PETA system*
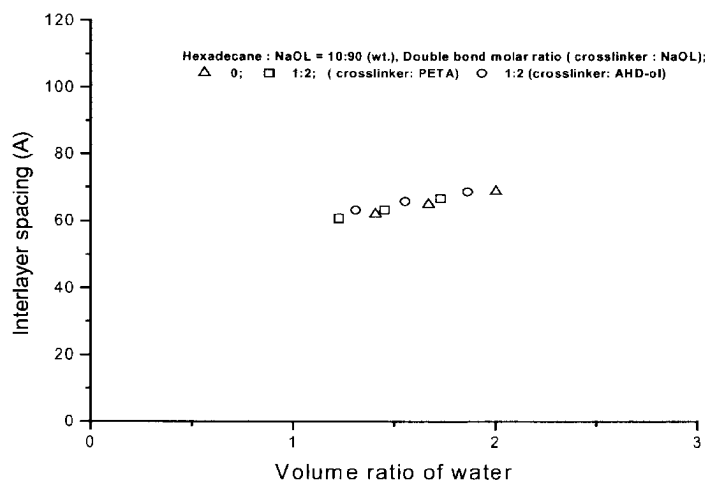
Figure 2. *The change of the interlayer spacings with volume ratio of water in NaOL / water/ hexadecane, NaOL/ water/ hexadecane/ AHD-ol, and NaOL /water/ hexadecane/ PETA systems.*
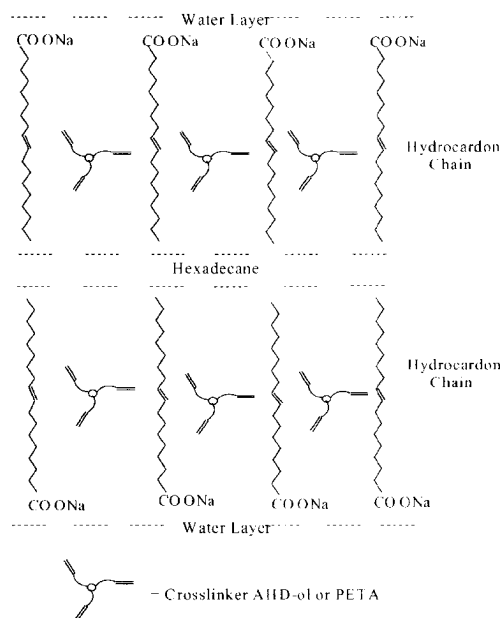
Figure 3. *The bilayer structure of lamellar liquid crystalline system NaOL/ hexadecane/ water/ crosslinker*

LLC phase polymerization of NaOL/ water/ hexadecane/ AHD-ol and NaOL/ water/ hexadecane/ PETA system

Both of the systems changed from transparent to milky-white opaque during copolymerization between NaOL and cross-linkers, because of phase separation, as reported in the similar system[3-4]. There was water, about ten percent of the total polymerization system, precipitated from NaOL/ water/ hexadecane/ AHD-ol system when the copolymerization finished. After the water was removed from the system through centrifugation, the phase remained was lamellar liquid crystalline state. The copolymer synthesized from this system could be dissolved into water again. However, there was no water precipitated from NaOL/ water/ hexadecane/ PETA system when copolymerization completed. The phase after the polymerization was the mixture of LLC phase and solid particles in this system. The solid particles precipitated from polymerization system became not dissolvable in water.

IR spectra of NaOL, AHD-ol, and the copolymer formed from the LLC phase of NaOL/water/hexadecane/AHD-ol system showed that the C-H stretch of the double bonds in AHD-ol presented IR absorptions mainly at 3077cm^{-1} and 3007cm^{-1}. The C-H stretch of the double bonds in NaOL also presented absorption at 3007cm^{-1}. These absorption bands decreased greatly after the copolymerization. IR spectra of NaOL, PETA, and the copolymer formed from

the LLC phase of NaOL/water/ hexadecane/PETA system also showed that the C-H stretch of the double bonds in PETA exhibited its IR absorptions mainly at $3107cm^{-1}$ and $3040cm^{-1}$, which were higher in wavenumber than that of AHD-ol. This is because in PETA the double bonds connected directly to the carboxyl groups and could form a conjugation structure with them. These absorption bands, as well as the C-H stretch absorption in the double bonds of NaOL, decreased greatly after copolymerization. The carboxyl absorption for the cross-linker PETA appears at $1726cm^{-1}$ while that for its copolymer at $1736cm^{-1}$, which was caused by the loss of the conjugation with the double bonds after copolymerization. The carboxyl absorption of NaOL appears at $1560cm^{-1}$ because the carboxyl group in NaOL exists in the form of a $-COO^{-1}$ ion. In the IR spectra of the copolymers, the absorption strength and area for these two kinds of carboxyl groups were almost the same. It means that there was same amount of the comonomer units existed in the copolymer. Thus all the solid particles precipitated from NaOL/water/ hexadecane/PETA system were the copolymer of NaOL and PETA since it is almost impossible for NaOL to execute homogeneous polymerization because of the steric hindrance in this kind of 1,2-disubstituted ethylene monomer structures. The alternative copolymer structure between PETA and NaOL was favored because there is big polarity difference between the two comonomers, which also helped to overcome the steric hindrance in NaOL molecule and to promote the copolymerization happened. There exist electron-drawing groups connected directly to the double bonds in the PETA molecules, which made its double bonds much more polar than those of NaOL. When the copolymer backbone propagated too long, it began to precipitate from the original LLC phase, which caused the whole system to be opaque. The IR spectra for these two systems showed that almost all of the three double bonds in these two cross-linker molecules polymerized with the double bonds in NaOL molecules, which proved the proposed copolymer structure. The IR spectra of copolymers also exhibited the carbonyl group absorptions in both monomers, which also proved the copolymerization between crosslinkers and NaOL molecule.

The small-angle x-ray diffraction determination of the LLC phase obtained from the polymerization of NaOL (33.0%)/water (62.5%)/ hexadecane (1.7%)/AHD-ol (2.8%) system gave the interlayer spacing as equal to 39.0Å. Compared with the interlayer spacing, 62.6 Å, of the above system before polymerization, the value after polymerization decreased greatly. Increasing the amount of cross-linker, AHD-ol, used in the polymerization system would decrease the interlayer spacing of the polymer's LLC phase, as seen in Table I, but not significantly. The same things occurred in the NaOL/water/ hexadecane/ PETA system, as shown in Table II. Wide-angle x-ray diffraction determination of the two systems after polymerization also showed that there were only LLC structures formed from polymerization.

Table I. The interlayer spacing of the LLC phase of NaOL/water/ hexadecane/AHD-ol system before and after polymerization (NaOL: hexadecane = 90: 10 wt.; NaOL 0.35g; water 0.65g)

Molar ratio of AHD-ol to NaOL AHD-ol : NaOL	Interlayer spacing (Å) before	Interlayer spacing (Å) after
4 : 12	63.7	39.1
5 : 12	63.2	38.7
6 : 12	62.5	37.8
7 : 12	62.3	37.2
8 : 12	61.7	36.2

Table II. The interlayer spacing of the LLC phase of NaOL/water/ hexadecane/PETA system before and after polymerization (NaOL: hexadecane = 90: 10 wt.; NaOL 0.35g; water 0.65g)

Molar ratio of PETA to NaOL PETA : NaOL	Interlayer spacing (Å) before	Interlayer spacing (Å) after
1 : 12	64.3	40.8
2 : 12	63.3	40.4
3 : 12	62.3	39.7
4 : 12	61.9	39.2
5 : 12	61.4	39.0

The ordered and stiff arrangements of the hydrocarbon chains in the amphiphilic bilayer of NaOL/water/hexadecane system were distorted greatly by the polymerization with such branched cross-linkers as AHD-ol and PETA. Thus it can be expected that the interlayer spacing of LLC system after polymerization decreased greatly compared with that before polymerization.

Surface activity of the polymeric surfactants

The polymeric surfactant synthesized from NaOL/water/hexadecane/AHD-ol was dissolved into water. Thus the relationship between the surface tension and concentration was determined. The CMC of the polymeric surfactant aqueous solution was higher than that of NaOL aqueous solutions, and also the surface tension. Since the polymeric surfactant, synthesized from NaOL/water/hexadecane/PETA, was not able to completely dissolvable in water, the data were determined after dispersing the polymer by ultrasonic method. The surface tension of the aqueous solutions of this polymer changed quickly with time at first and then leveled off during the determination.

SUMMARY

Polymeric surfactants were synthesized from the LLC phase polymerization of NaOL/ water/ hexadecane/ AHD-ol and NaOL/ water/ hexadecane/ PETA systems. AHD-ol and PETA acted as cross-linkers of the double bonds in NaOL molecules during polymerization.

REFERENCES

1. Q.H. Fu, S. E. Friberg, Z. Q. Zhang, and P. Aikens, *J. Dispersion. Sci & Tech.*, **2000**, *21*(7), 1007-1021
2. Q.H. Fu, Z. Q. Zhang, S. E. Friberg, *J. Dispersion Sci &Tech.*, **2000**, submitted.
3. Kayali, Ibrahim; Li, Fang; Zhang, Zhiqiang; Sandburg, Joel D.; Friberg, Stig E.. *J. Dispersion Sci. Technol.* **1999**, *20(7)*, 1789-1807.
4. Li, Fang; Zhang, Zhiqiang; Friberg, Stig E.; Aikens, Patricia A. *J. Polym. Sci., Part A: Polym. Chem.* **1999**, *37(15)*, 2863-2872.

Fabrication and Characterization of Chromium Oxide Nanoparticles/Thin Films

Zhenchen Zhong
Institute for Micromanufacturing (IfM) and Physics Program, Louisiana Tech University,
Ruston, LA 71272; U.S.A.
and Department of Physics, Grambling State University, Grambling, LA 71245, U.S.A.
Ruihua Cheng
Department of Physics and Astronomy and the Center for Materials Research and Analysis
(CMRA), Behlen Laboratory of Physics, University of Nebraska-Lincoln, NE 68588-0111,
U.S.A.

ABSTRACT

Well-dispersed nanoscale textured chromium oxide particles/thin films can be fabricated under certain conditions by laser-induced solution deposition (LISD) from organic solutions and by using selective organometallic chemical vapor deposition (OMCVD). The fabricated nanoparticles/thin films are characterized by scanning electron microscope (SEM), EDX, X-ray diffraction, and magnetic measurements. We have successfully demonstrated that the LISD and OMCVD are unique techniques for fabricating uniformly-distributed thin films but anistropic chromium oxide particles, which can be used in electro-magnetic devices. The magnetization measurements show that both types of chromium oxides are presented and that the Curie temperature T_c and the saturation magnetization field may be adjustable by controlling the stoichiometry.

INTRODUCTION

Spin-tunnel junctions, spin-vlaves [1] and other magnetoresistive devices [2,3] have aroused wide interests because of their importance in science and technology. These so-called spin-dependent devices, i.e., spintronics depend upon spin-polarized electrons rather than bias voltages or currents. They are new generation microelectronics, in other words, nanoelectronics. Chromium oxides are promising candidates because of their half-metallic properties and high spin-polarization. The insulating antiferromagnetic chromium oxide Cr_2O_3 has a Neél temperature T_N (i.e., the similar Curie temperature for the antiferromagnetic case) 307 K and is suitable for tunnel junction barrier [3] both below and above the Neél temperature. The ferromagnetic chromium oxide CrO_2 with T_c 397 K [4] has been predicted to be half-metallic (metallic for one spin direction while insulating for the other spin direction) by band structure calculations [5-9], though Kulatov and Mazin found CrO_2 to be insulating in both spin-directions [10]. Evidence of 80 to 100% polarization, consistent with the half metallic character of CrO_2, were observed in many experimental measurements such as spin-polarized photoemission [11], vacuum tunneling [12], and Andreev scattering [13,14]. The high electron polarization, in addition to the half metallic character of the surface [9] makes CrO_2 an attractive material for spin-polarized electron tunneling. Very large spin-dependent tunneling (junction) magnetoresistance (TMR) made of CrO_2 is expected.

Therefore CrO_2 is a material of interest for spin-polarized electronics (i.e., spintronics) because of the spin-polarization in this material approaching unity. Another reason for using CrO_2 in spintronics is that it is possible to make all magnetic oxide spin-dependent tunnel

junctions. In this case the tunnel barrier is likely to be a native Cr_2O_3 layer sandwiched in-between the two CrO_2 layers. The research for making $CrO_2/Cr_2O_3/CrO_2$ tunnel junctions is in progress, which will be reported elsewhere.

It is difficult to fabricate CrO_2 ultrathin films/nanoparticles using conventional methods because CrO_2 is metastable. However, it is good thing in some cases because the two phases CrO_2/Cr_2O_3 system exhibits higher magnetoresistance than the pure material [3]. The oxidation of the organometallic complex hexacarbonyl $Cr(CO)_6$ has the potential for selective deposition of CrO_2 [15-17]. These studies have established that chromium oxides are the thermodynamic sinks of chromium hexacarbonyl decomposition [17] and the oxidation is further aided by the presence of an ambient oxygen background [15,16]. By modifying this organometallic chemical vapor deposition (OMCVD) procedure, we have been able to fabricate the ferromagnetic and antiferromagnetic chromium oxides. Meanwhile we have used a counterpart laser-induced deposition in solution (LISD) to fabricate magnetic nanoparticle oxides. However, the precursor $Cr(CO)_6$ did not work in solution deposition as we expected. By error and try, we found that $CrCl_2$ was a choice as the solute of the deposition solution. In this paper we describe both the formation and the magnetic properties of these ultrathin films/nanoparticles by both vapor and solution deposition induced by laser.

EXPERIMENTAL DETAILS

The growth of the chromium oxide films/nanoparticles by OMCVD were carried out on Si(111) substrates in an ultra high vacuum chamber, maintained at a base pressure at 1.0^{-9} torr or less. This chamber was designed for laser initiated chemical vapor deposition as described elsewhere [18,19]. The photolytic decomposition and oxidation of $Cr(CO)_6$ was performed by a commercial nitrogen laser with the main emission line at 337 nm (corresponding to 3.69 eV). The ambient oxygen (O_2) atmosphere was varied from 1×10^{-7} to 1×10^{-5} torr relative to the $Cr(CO)_6$ partial pressure of 1×10^{-5} torr, uncorrected for ionization gauge cross-section and monitored with a quadruple mass spectrometer operated in pulse counting mode.

The deposition of chromium oxides by laser-induced solution deposition (LISD) (the experimental system of LISD is described elsewhere [20]) were carried out by an argon ion-laser (the Coherent Innova 90 Series Ion Laser). The deposition solution was $CrCl_2$ dissolved in solvents containing various mixtures of methanol, cyclohexane, tetrohydrofuran (THF), and diethlether. The deposition time in this experiment varies from 0.5 hour to 24 hours. Both visible (laser power: 5-7 W and wavelength : 514 nm (457 – 528 nm) and UV radiation (laser power: 5-7 W and wavelength : 351 nm) were used in the experiment. The substrates for deposition were Si (111) wafers and sodium-glasses in all the experiments.

RESULTS AND DISCUSSION

The SEM microscope of the thin film/nanoparticles, fabricated with 1×10^{-6} torr O_2 partial pressure and 1×10^{-5} torr $Cr(CO)_6$ partial pressure, is shown in Figure 1. The topology of the film is relatively uniform, with only a fine microstructure visible on the scale of 800 nm.

Figure 1. The scanning electron microscope image of a chromium oxide thin film/nanoparticles fabricated on Si (111) substrate through laser-initiated decomposition of $Cr(CO)_6$ (pressure 1×10^{-5} torr) in an ambient atmosphere of O_2 (1×10^{-6} torr) as background.

The EDX spectra of the same thin film/nanoparticles in different areas provide evidence for the desirable oxygen and chromium signal in addition to the strong Si signal coming from the Si (111) substrate. We have done many spectra for the deposited thin films/nanoparticles. The results are quite similar, showing both peaks of chromium and oxygen.

Figure 2 shows the magnetization versus temperature obtained from superconducting quantum interference devices (SQUID) magnetometer. The inserted figures are Auger electron spectroscopy (AES). The critical temperature clearly depends upon the experimental conditions, especially the oxygen partial pressure at the time of thin film/nanoparticle fabrication. At 2×10^{-7} torr oxygen partial pressure relative to the $Cr(CO)_6$ partial pressure of 1×10^{-5} torr the Curie temperature was 345 ± 10 K. At the higher 1×10^{-6} torr oxygen partial pressure (relative to the $Cr(CO)_6$ partial pressure of 1×10^{-5} torr) the Curie temperature was about 390 ± 10 K. The absence of a sharp T_c and the presence of a long tail in the magnetization curves (Figure 2), near the critical temperature, indicate positively a two phases system. The amount of CrO_2 phase increases with the O_2 partial pressure and the critical temperature approaches finally the expected T_c of CrO_2 [4]. The samples characterized by Auger electron spectroscopy (AES), as shown in the insets of Figure 2, (A) presents the Auger spectrum characteristic to a Cr_2O_3 rich sample, and

(B) for a CrO_2 rich sample. The spectra show clearly that the Cr signal increases relative to the overlapping oxygen signal for the Cr_2O_3 samples as compared to the CrO_2 samples.
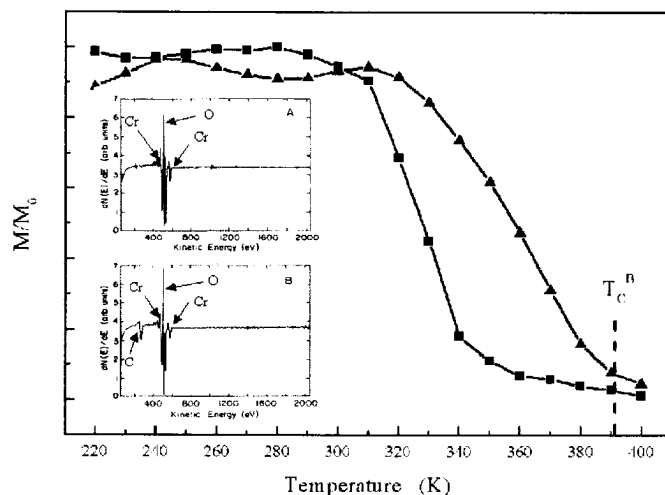
Figures 2. The magnetization (M) versus temperature (T) at an applied field of H=500 Oe. Data are shown for two thin films/nanoparticles: the data (∇) were taken from the film fabricated in an O_2 pressure of 2×10^{-7} torr relative to the $Cr(CO)_6$ partial pressure of 1×10^{-5} torr, while the data ( ) were taken from the film fabricated in an O_2 pressure of 1×10^{-6} torr relative to the $Cr(CO)_6$ partial pressure of 1×10^{-5} torr. Auger electron spectra of the photolytic oxidative chemical vapor deposition of Cr_2O_3 and CrO_2 (for high and low O_2 partial pressure respectively) are shown as insets A and B respectively.

As contrast, the growth of chromium oxides in the laser-induced solution deposition is usually islands growth mode rather than that of layer-by-layer growth (usually into films) in vapor deposition. The precursor $Cr(CO)_6$ worked fine in vapor deposition did not appear to be effective in solution deposition. Figure 3 shows the scanning electron microscope of the textured CrO_x nanoparticles obtained by laser-induced deposition in solution (LISD) and the distribution of nanoparticles in the center of 230 nm in diameter. The experimental conditions for this sample are laser wavelength was at 514 nm in visible regime; laser beam exposure area was about 10 mm; solute was $CrCl_2$ (2.0 mg) dissolved in solvents of 1.5 ml THF and 1.5 ml cyclohexane; and the deposition time was twelve hours. The dominant particle size (CrO_x) was about 230 nm in diameter and there are also those bi-grains and triple-grains with 350 nm and 400 nm in diameter. The distribution shows uniform and appears textured.
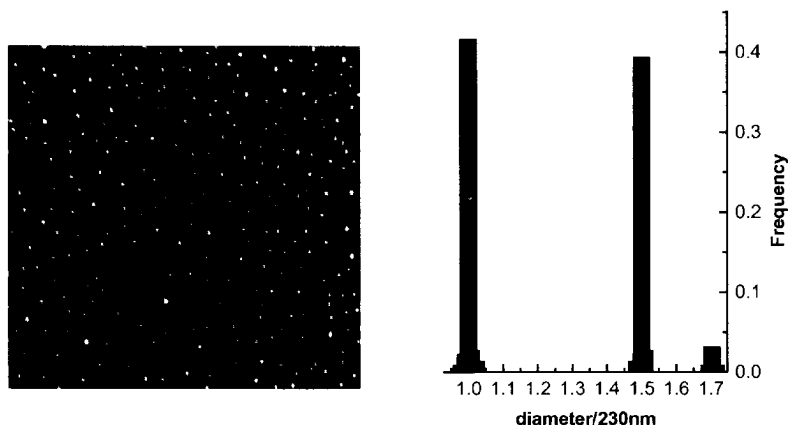
Figure 3. Scanning electron spectroscope of CrO_2 (major) and Cr_2O_3 (minor) nanoparticles deposited on soda-glass by laser-induced deposition in solution (LISD) (left) and the distribution diagram from the SEM image (right)

We did not know the exact nucleation and growth mechanisms in the laser-induced vapor and solution depositions yet. However, it is worthwhile to be further investigated. The preliminary AES and magnetic measurements of LISD deposited samples show similar results of these counterparts of OMCVD deposits – showing two phases rather than pure CrO_2 or Cr_2O_3. We will publish these results elsewhere due to the limitation to the length of this paper.

CONCLUSIONS

We conclude in this presentation that we have used laser-initiated chemical vapor deposition and laser-induced solution deposition to successfully fabricate chromium oxide thin films and nanoparticles. The advantages of these techniques are selectively area deposition and strong texture growth as well as uniform deposits. Phase control of this system, at the surface or boundary layers, appears to be far more likely than the potential half metallic systems $La_{0.65}Sr_{0.35}MnO_3$ [21] and NiMnSb [22] where surface segregation readily occurs. The magnetization measurements show that the relative weight of both Cr_2O_3 and CrO_2 phases depends on and can be controlled by the oxygen partial pressure in the vapor deposition and by the selection of appropriate solute and solvents in the solution deposition.

ACKNOWLEDGEMENTS

REFERENCES

1. A.M. Bratkovsky, Phys. Rev. **B56**, 2344 (1997).
2. S.S. Manoharan, D. Elefant, G. Reiss and J.B. Goodenough, Appl. Phys. Lett. 72, 984 (1998); X.W. Li, A. Gupta, T.R. McGuire, P.R. Duncombe, and Gang Xiao, J. Appl. Phys. **85**, 5585 (1999); K. Suzuki and P.M. Tedrow, Phys. Rev. **B58**, 11597 (1998).
3. J.D.M. Coey, A.E. Berkowitz, Ll Balcells, F.F. Putris and A. Barry, Phys. Rev. Lett. **80**, 3815 (1998).
4. J. S. Kouvel, D. S. Rodbell, J. Appl. Phys. **38**, 979 (1967).
5. K. Schwarz, J. Phys. **F 16**, L211 (1986).
6. S. Matar, G. Demazeau, J. Sticht, V. Eyert, and J. Kübler, J. de Physique **I 2**, 315 (1992).
7. M.A. Korotin, V.I. Anisimov, D.I. Khomskii and G.A. Sawatzky, Phys. Rev. Lett. **80**, 4305 (1998).
8. S. P. Lewis, P.B. Allen, and T. Sasaki, Phy. Rew. **B55**, 10 253 (1997).
9. H. van Lueken and R.A. de Groot, Phys. Rev. **B51**, 7176 (1995).
10. E. Kulatov and I.I. Mazin, J. Phys. Condens. Matter. **2**, 343 (1990).
11. K.P. Kämper, W. Schmitt, G. Güntherodt, R.J. Gambino, and R. Ruf. Phys. Rev. Lett. **59**, 2788 (1987).
12. R. Weisendanger, H.-J. Güntherodt, G. Güntherodt, R.J. Gambino, and R. Ruf, Phys. Rev. Lett. **65**, 247 (1990).
13. R.J. Soulen, et al., Science **282**, 85 (1998); R.J. Soulen, et al., J. Appl. Phys. **85**, 4589 (1999).
14. W.J. DeSisto et al., Appl. Phys. Lett. **70**, 3789 (2000)
15. P. A. Dowben, et al., J. Appl. Phys. **67**, 5658 (1990).
16. K. Perkins, C. Hwang, M. Onellion, Yoon–Gi Kim, and P.A. Dowben, *Thin Solid Films* **198** (1991) 317–329
17. Derrick C. Mancini, et al., *J. Vac. Sci. Technol.* **B8**, 1804 (1990).
18. D. Welipitiya, et al., Mat. Res. Soc. Symp. Proc. **475**, 257 (1997).
19. C. N. Borca, D. Welipitiya, S. Adenwalla, P. A. Dowben, Phys. Low-Dim. Struct. **11/12**, 173 (1997)
20. Z.C. Zhong, P.A. Dowben and D. J. Sellmyer, Materials Letters **37**, 320 (1998); Z.C. Zhong, V. Holmes, P.A. Dowben and D.J. Sellmyer, Mat. Res. Soc. Symp. Proc. (2000) pp 231; P.A. Dowben, Z.C. Zhong and D.J. Sellmyer, U.S. Patent No. 6,025,038, (15 February 2000).
21. H. Dulli, E. W. Plummer, P. A. Dowben, J. Choi and S-H, Liou, Appl. Phys. Lett. **77**, 88 (2000).
22. D. Riotoiu, J. P. Nozieres, C. N. Borca, B. Borca and P. A. Dowben, Appl. Phys. Lett. **76**, 2349 (2000).

Multi-Layer Coating of Ultrathin Polymer Films on Nanoparticles of Alumina by a Plasma Treatment

Donglu Shi, Zhou Yu, S. X. Wang[1], Wim J. van Ooij, L. M. Wang[1], and J. G. Zhao
Department of Materials Science and Engineering, University of Cincinnati
Cincinnati, OH 45221-0012
[1]Dept. of Nuclear Engineering and Radiological Science, University of Michigan
Ann Arbor, MI 48109

ABSTRACT

Multi-layer ultrathin polymer films have been deposited on the surfaces of nanoparticles of alumina using a plasma polymerization treatment. The nanoparticles ranged from 10-150 nm in spherical shapes. High-resolution transmission electron microscopy (HRTEM) experiments showed that an extremely thin film of the pyrrole layer (10-20 Å) was uniformly deposited on the surfaces of the nanoparticles. In particular, the particles of all sizes (10-150 nm) exhibited equally uniform ultrathin films indicating well-dispersed nanoparticles in the fluidized bed during the plasma treatment. After single layer coating, hexamethyldisiloxane (HMDSO) was coated again as a second layer onto the surface of pyrrole. Subsequently, a third layer of pyrrole was coated on the top of HMDSO film completing the multi-layer coating process. Time-of-Flight Secondary ion mass spectroscopy (TOFSIMS) experiments confirmed the deposition of these multi-layer thin films on the nanoparticles. The deposition mechanisms and the effects of plasma treatment parameters are discussed.

INTRODUCTION

Surface coating of nanoparticles is an important area in nanomaterials synthesis. Because of their special composition, these coatings possess a unique combination of properties of the inorganic and organic components, for instance hydrophobic, hydrophilic, anti-fogging, anti-fouling, anti-adhesive and/or teflon-like properties in combination with hardness and scratch and abrasive resistance. The combination of mutually chemically interconnected organic and inorganic networks results in coatings with a very low permeability for gases and liquids. Hybrid materials are very suitable for application as coatings on a highly diverse spectrum of substrates including glasses, ceramics, plastic, wood, and metal. Before curing, the coating materials consist of a clear alcoholic solution that can easily be processed by classical application techniques such as dipping, spraying, or spin coating. However, in these previous coating processes, the coatings are quite thick up to the order of microns.

The current trend of developing nanophase materials has motivated an increased need for nanometer-scale structures in a variety of applications. Indeed, it is clear that, in order to achieve unique mechanical, physical, chemical, and biomedical properties, it is necessary to develop novel synthesis routes by which new nanostructures can be developed. In the past, great efforts have been focused on nanoparticle synthesis, assembly, interfaces, dispersions, and functional devices (1-5). Although high volume

(~80 vol.%) polymer coating of nanoparticles has been reported (6), no studies so far have shown uniform deposition of ultrathin films of the order of 10-20 Å on the surface of the nanoparticles, which is, in this letter, referred to as "nanocoating." The deposited film can also be tailored to multi-layers on a nanoparticle. Nanocoating is of particular importance in electronics, functional devices, new materials synthesis, nanobiomolecular applications, tissue engineering, and drug delivery. Using nanocoating, it is possible to alter the intrinsic properties of materials that cannot be achieved by conventional methods and materials.

For nanoscale ceramics particles, under a well-dispersed condition, it is possible to deposit a thin film of foreign species uniformly on the nanoparticle surfaces and thereby reduce their surface energies. In this study we will address these issues and report experimental data on the deposition of multiple layers of polymer ultrathin films on the surfaces of nanoscale alumina particles by a plasma polymerization process. The deposited thin films are plasma-polymerized pyrrole and hexamethyldidiloxane (HMDSO).

EXPERIMENTAL DETAILS

In this experiment, a RF-plasma reactor was used for the nanoparticle coating. In this experiment, we have selected nanoscale alumina particles ranging from a few nanometers to 150 nm. This large distribution of particles is particularly useful for the study of deposition experimental conditions for different sizes. The schematic diagram of the plasma reactor for thin film deposition of nanoparticles is shown in Figure 1. The vacuum chamber of plasma reactor consists of a long Pyrex glass column about 80 cm in height and 6 cm in internal diameter (7,8).
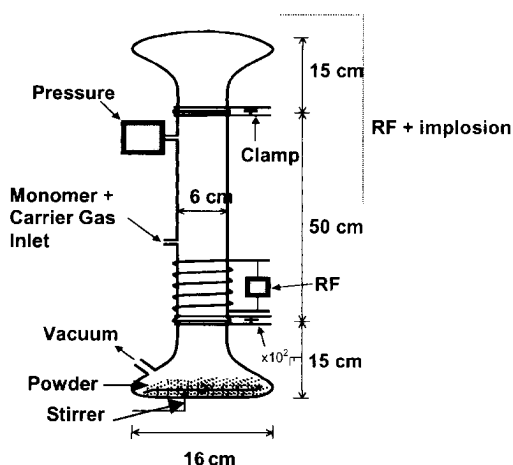
Figure 1. Schematic diagram of the plasma reactor for thin polymer film coating of the nano-particles.

The nanoparticles of alumina are vigorously stirred at the bottom of the tube and thus the surfaces of nanoparticles can be continuously renewed and exposed to the plasma for thin film deposition during the plasma polymerization process. A magnetic bar was used to stir the powders. The gases and monomers were introduced from the gas inlet during the plasma cleaning treatment or plasma polymerization. The system pressure was measured by a pressure gauge. A discharge by RF power of 13.56 MHz was used for the plasma film deposition. Before the plasma treatment, the basic pressure was pumped down to less than 200 mTorr and then the plasma gases or monomer vapors were introduced into the reactor chamber. The operating pressure was adjusted by the gas/monomer mass flow rate. The base pressure was less than 200 mTorr. Pyrrole and HMDSO were used as monomers for plasma polymerization. During the plasma polymerization process, the input power was 20 W and the system pressure was 450 mTorr. The plasma treatment time was 240 min. Per batch 40 grams of powder were treated.

For the single layer coating, pyrrole was used as the monomer. Double and triple layers coatings were done after the single layer coating batch. For the double layer coating, pyrrole was coated for 240 min followed by another 240 min of HMDSO coating under the same condition. For the triple layer coating, the same procedure for double layer coating was employed followed by a second pyrrole coating for 240 min.

After the plasma treatment, the nanoparticles of alumina were examined by using transmission electron microscopy (TEM), scanning electron microscopy (SEM), x-ray diffraction (XRD), and Time-of-Flight secondary ion mass spectroscopy (TOFSIMS). The high-resolution TEM (HRTEM) experiments were performed on a JEOL JEM 4000EX TEM; the TOFSIMS analyses were performed on an ION-TOF Model IV instrument.

In transmission electron microscopy, the original and coated Al_2O_3 nanoparticles were dispersed onto the holy-carbon film supported by Cu-grids for the TEM operated at 400 kV. Figure 2 shows the high-resolution transmission electron microscopy (HRTEM) image of the original, uncoated alumina nanoparticles. As can be seen in this figure, the particle size ranges between 10 nm and 150 nm. The particles are also spherical in shape for all sizes.
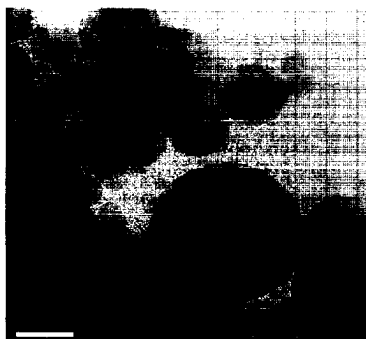
Figure 2 TEM image showing the uncoated alumina nanoparticles. The scale bar is 50 nm.

Figure 3a is the HRTEM image of the coated particles. Compare to Figure 2, one can see a bright ring on the particle surfaces, which is the result of the polymer coating. Figure 3b is a high magnification image showing a uniform coating on the particle surfaces. In this figure one can see not only that the large particle (d ~ 100 nm) in the photograph is well coated, but also the two smaller ones with a diameter of 15 nm. The coating thickness is approximately 2 nm all the way surrounding the particle surfaces. Particularly interesting, although these particles have different diameters, the coating remains the same thickness indicating the uniform distribution of polymer atoms in the plasma chamber. The coating layer is amorphous based on the HREMs of different particles. In contrast, the images of the original particles (Figure 2) do not show the amorphous layer. Thus, we are certain that the observed layer is due to coating rather than an artifact in TEM observation. For multiple-layer-coated nanoparticles, however, we did not observe any distinguishable layers of pyrrole and HMDSO. The coated layers exhibit amorphous-like structures similar to the TEM images shown in Figure 3. More detailed HRTEM work is currently under way for the double- and triple- layer coatings.
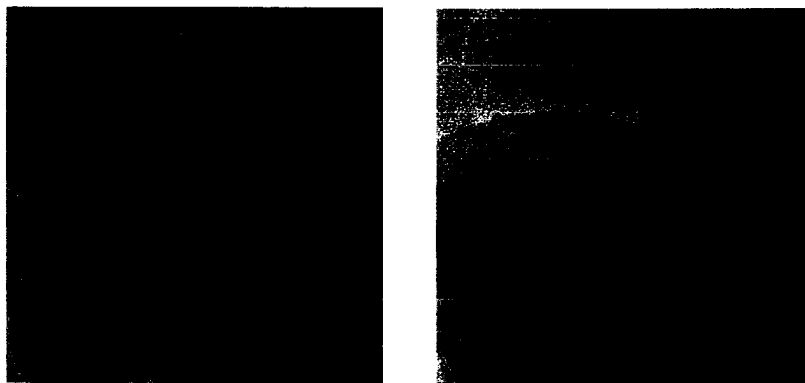
Figure 3. TEM images showing coated nano alumina particles. The scale bar is 50 nm in Fig. 3a and 10 nm in Fig. 3b. The arrows in Fig. 3b indicate the polymer coatings.

Figure 4 shows the SIMS spectrum of pyrrole-coated nanoparticles of alumina. As can be seen in this figure, the strong pyrrole peaks indicate the surface coating of the nanoparticles and are consistent with the HRTEM data presented in Figure 3. The spectrum of the untreated powder shows an appreciable intensity of magnesium in the surface layers. There are also traces of sulfur, iodine and organic material. The treated aluminum oxide shows the characteristic cluster pattern of plasma-polymerized pyrrole (9). The intense peak at -26 m/z (CN) is typical of all nitrogen-containing functionalities. The intense peak of Al[1] at +27 m/z is *not* the result of an incomplete coverage of the particles by the plasma polymer, but is caused by the intense sputtering of aluminum atoms from the particle surface during the initial phase of the plasma film deposition (10). Consistent with this view is the absence of magnesium in the spectrum of the treated powder. The aluminum atoms or ions are incorporated in the first 5 nm of the plasma polymer film (11).
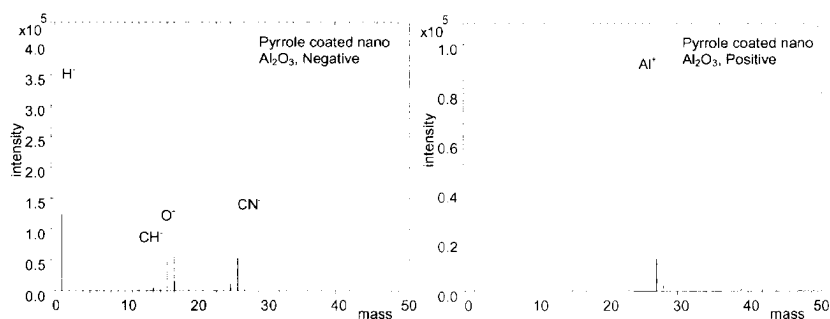
Figure 4. *SIMS data of single-layer, pyrrole-coated alumina nanoparticles.*

For the double layer coatings of pyrrole (first layer) and HMDSO (second layer), peaks at -75 m/z and -89 m/z in Figure 5 indicate siloxane on the sample surface. The peak at -60 m/z is believed to be the SiO_2^- in this figure. However, in the HREM images of the doubly coated samples, we cannot find a distinctive interface between the first and the second polymer layers. The reason is that these two polymers did not crystallize during the plasma synthesis and HREM cannot distinguish these two different amorphous layers.

For the triple layer coating, pyrrole was again used to deposit on the surface of second layer of HMDSO. The typical intensity peak at -26 m/z (CN^-) can be found in Figure 6 that confirms the existence of nitrogen-containing molecules. Also the typical patterns of polymerized pyrrole re-appear in Figure 6, and the siloxane peaks have vanished due to the third layer coating. The pattern of pyrrole peaks is similar to that in Figure 4. This indicates that the pyrrole film as the third coating has completely covered the second layer of the nanoparticles.
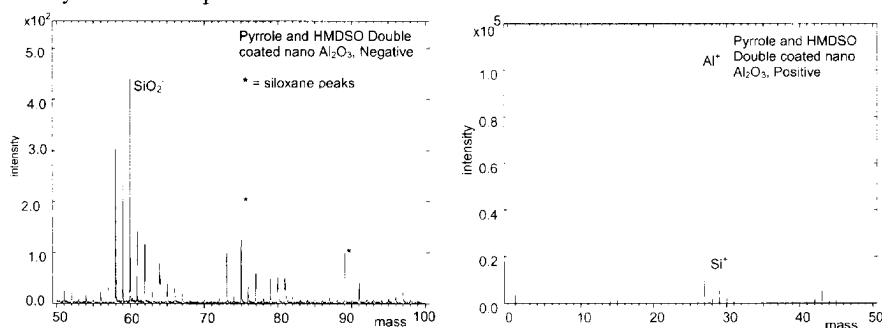
Figure 5. *SIMS data of second-layer, HMDSO-coated alumina nanoparticles.*

During coating, the polymer is introduced as a vapor and the collision frequency increases with the gas pressure. The rate of polymer condensation on the nanoparticle surfaces may be influenced by many parameters such as electron density, temperature,

and energy density. To achieve a thin and uniform coating on such small nanoparticles, all these synthesis parameters must be optimized. Although a systematic study on the optimization of synthesis parameters has not yet been carried out, the preliminary experimental data have indicated that the coating polymer must be stable and not reactive with the substrate during coating. The gas pressure must be moderate for a low collision rate on the nanoparticle surfaces. In addition, polymerization should take place relatively fast after the condensation on the particle surfaces. These will ensure a uniform coating on the order of 1-2 nm for all particle sizes.
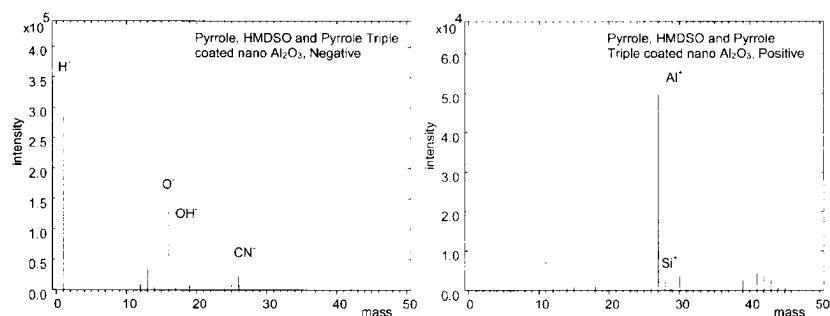
Figure 6. *SIMS data of third-layer, pyrrole-coated alumina nanoparticles.*

In summary, we have coated alumina nanoparticles with multi-layers of pyrrole HMDSO by means of a plasma polymerization treatment. The coating is not only uniform on all particle sizes, but also deposited in an extremely thin thickness of 1-2 nm. Such coating characteristics are essential in establishing multi-layer nanostructures, tailoring unique physical properties, and pioneering novel synthesis route.

REFERENCES

1. R. W. Siegel, Nanostructured Materials, **3**, 1-18, (1993).
2. G. C. Hadjipanayis and R. W. Siegel, "Nanophase Materials: Synthesis-Properties-Applications" Kluwer Press, Dordrecht, 1994.
3. G. M. Whitesides, J. P. Mathias, and C. T. Seto, Science, **254**, 1312-1319, (1991).
4. G. D. Stucky and J. E. MacDougall, Science, **247**, 669-678, (1990).
5. H. Gleiter, Nanostructured Materials, **6**, 3-14 (1995).
6. D. Vollath and D. V. Szabo, J. of Nanoparticle Research, **1**, 235-242, (1999).
7. W.J. van Ooij, S. Eufinger, W.J. van Ooij, and T.H. Ridgway, Journal of Appl. Pol. Sci., **61**, 1503 (1996),
8. W.J. van Ooij, S. Eufinger and T.H. Ridgway, Plasma and Polymers, **1**, 231 (1996).
9. S. Eufinger, W. J. van Ooij, and T. H. Ridgway, *Journal of Appl. Pol. Sci.*, **61**, 1503 (1996).
10. W. J. van Ooij, S. Eufinger, and T. H. Ridgway, *Plasma and Polymers*, **1**, 231 (1996).
11. D. Shi, Shixin Wang, Lumin Wang, W. J. van Ooij, Zhou Yu, and J. G. Zhao, *Appl. Phys. Lett.* (2000), in press.

Transport Properties of Bi-related Nanowire Systems

Y. M. Lin,[1] S. B. Cronin,[2] J. Y. Ying,[3] J. Heremans,[4] and M. S. Dresselhaus[1,2,*]
[1]Department of Electrical Engineering and Computer Science, [2]Department of Physics,
[3]Department of Chemical Engineering, Massachusetts Institute of Technology, Cambridge, MA 02139
[4]Delphi Research Labs, Delphi Automotive Systems, Warren, MI 48090
[*]On leave from the Massachusetts Institute of Technology, Cambridge, MA 02139

ABSTRACT

We present here an electrical transport property study of Te-doped Bi nanowires, and $Bi_{1-x}Sb_x$ alloy nanowires embedded in a dielectric matrix. The crystal structure of the nanowires were characterized by X-ray diffraction measurements, indicating that the nanowires possess the same lattice structure as bulk Bi in the presence of a small amount of Te or Sb atoms. The resistance measurements of 40-nm Te-doped Bi nanowires were performed over a wide range of temperature ($2 K \leq T \leq 300 K$), and the results are consistent with theoretical predictions. The 1D-to-3D localization transition and the boundary scattering effect are both observed in magneto-resistance measurements of $Bi_{1-x}Sb_x$ alloy nanowires at low temperatures ($T < 4 K$).

INTRODUCTION

Nanostructured materials have received much attention in the last decade because of their importance in fundamental studies and potential applications in diverse fields, such as chemistry, biology, optics, microelectronics, materials science, and thermoelectrics [1]. Various unusual phenomena and properties have been predicted and observed in nanoscaled materials. Among existing nanostructures, nanowires represent one of the most interesting systems because they exhibit stronger quantum confinement effects than 2D nanostructures such as superlattices, and they maintain structural continuity in one dimension, which allows for transport phenomena and they may serve as interconnections in future microelectronics applications.

Bismuth (Bi) is a very attractive material for the study of low-dimensional systems. Bi is a group V semimetal, in which the electrons are distributed in three highly anisotropic carrier pockets at the L points of the Brillouin zone, and the holes are contained in one pocket at the T point. The small energy overlap (38 meV at 77 K) in bulk Bi between the L-point conduction band and the T-point valence band is predicted to vanish in Bi nanowires when the diameter is smaller than ~50 nm, thus causing a semimetal-to-semiconductor transition [2]. Experimental results for this quantum-confinement-induced semimetal-semiconductor transition in Bi nanowires have been previously reported [3-4]. Since Bi has very small electron effective masses (~0.001 m_0 along the binary direction), quantum confinement effects can be observed at a larger scale (~50 nm), compared to less than 10 nm for most metals or semiconductors.

In addition to band shifts due to quantum confinement effects, it is also possible to controllably alter the energy-band structure and transport properties of Bi by alloying with another Group V element, Sb [5-6]. $Bi_{1-x}Sb_x$ alloys form substitutional solid solutions over the whole range of concentrations x. As x increases, the band structure of these alloys gradually transforms from that of Bi to that of Sb. Figure 1 shows a schematic representation of the band

structure of $Bi_{1-x}Sb_x$ as a function of x for $x < 0.3$. It is interesting to note that for $0.07 < x < 0.22$, the alloys are semiconductors with a direct or indirect band gap [7]. Therefore, $Bi_{1-x}Sb_x$ alloy nanowires constitute a promising 1D system in which the desired band structure and many other related properties can be achieved by combining the quantum confinement effect and the Sb alloying effect. Thus, many ideas that are central to the carrier pocket engineering concept [8] can be readily applied to this unique 1D system. Another important factor in optimizing electronic systems is the placement of the Fermi energy level in Bi nanowires. One possible approach to vary the Fermi energy is by doping with Group VI elements (e.g. Te), which serve as electron donors in $Bi_{1-x}Sb_x$ alloys, or Group IV elements (e.g. Pb, or Sn), which serve as electron acceptors.
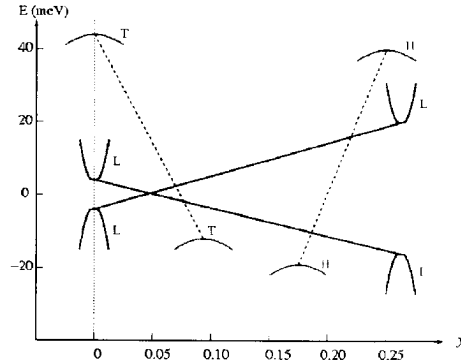
Figure 1. The schematic diagram of the band structure of bulk $Bi_{1-x}Sb_x$ alloys as a function

In the present work, the effects of adding Te or Sb to Bi nanowires are studied, both experimentally and theoretically. Bi nanowires for this study are synthesized by pressure injecting molten liquid metals into porous anodic alumina templates. In this fabrication method, it is straightforward to incorporate Te and Sb atoms in Bi nanowires by replacing the pure metal to be filled by the alloys of the desired composition. X-ray diffraction analysis of these nanowire arrays indicates that the lattice structures of the Bi-rich nanowires with a small amount of Te and Sb do not show significant differences from the undoped Bi nanowires. Temperature-dependent resistance $R(T)$ measurements are performed for $2 \text{ K} \leq T \leq 300 \text{ K}$ for the nanowire arrays using a two-point contact method. The experimental results exhibit good agreement with the theoretical calculations. The longitudinal magnetoresistance (MR) was studied as a function of applied magnetic field ($0 \text{ T} \leq B \leq 6 \text{ T}$) at various temperatures, and the localization effects are observed. For temperatures below 2 K, a 1D to 3D transition effect is noted. The non-monotonic behaviors in $MR(B)$ for larger-diameter nanowires are attributed to wire-boundary scattering effects, suggesting a high carrier mobility in these nanowires.

EXPERIMENTAL DETAILS

Bi, Te-doped Bi and $Bi_{1-x}Sb_x$ nanowire arrays were fabricated by a template-assisted approach, in which alumina templates consisting of hexagonally-packed arrays of nanopores

were used as the host material. The synthesis details and conditions to control the geometry of these nanopores have been described elsewhere [9-10]. The metal alloys used for the pressure injection were prepared by mixing high purity Bi (99.9999%, Alfa Aesar) and Te (99.9999 %, Alfa Aesar) or Sb (99.9999 %, Alfa Aesar) in a quartz tube, which was then evacuated and sealed. The sealed tube was heated to 650°C for 8 hours with constant agitation to facilitate homogenizing the melt. The melt is then quenched in cold water. Bi-rich nanowires were produced by pressure injecting molten metals into the nanopores of the alumina templates, following similar procedures described in Ref. [11]. After the pressure injection, the underlying aluminum substrate and the barrier layer in the as-prepared nanowire templates are dissolved in a saturated $HgCl_2$ solution and a weak acid solution, respectively, so that the nanowires were exposed on both sides of the template and electrical contacts could be made to the nanowires.

Prior to the transport measurements, the as-prepared nanowire arrays were annealed at 250°C for 8 hours to relieve the high pressure within the nanowires. Resistance and magnetoresistance measurements of the nanowire arrays were performed using a two-point contact method, in which gold wires were attached to both ends of the nanowires with silver paste. Typical resistances of the nanowire arrays range from tens of ohms to several thousand ohms. Since the number of wires connected to the contact electrodes in each set of samples would vary, the temperature dependence of the resistance of the various nanowire arrays were compared by normalizing the resistances to their respective values at 270 K.
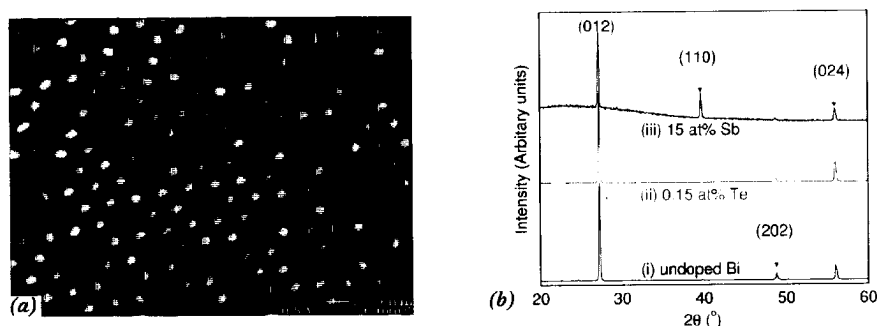
Figure 2. (a) A SEM image of the bottom surface of an alumina template after the pressure injection filling process, showing arrays of Bi nanowires (white spots). (b) The XRD patterns of 40-nm Bi-rich nanowire arrays with different metal compositions.

RESULTS AND DISCUSSION

Figure 2(a) shows a typical scanning electron microscopy (SEM) image of a bottom surface of the alumina template after the pressure injection filling process. The white spots represent pores filled by Bi or Bi alloys, and the dark spots are empty pore that have not been filled completely to the end of the pore. Figure 2(b) shows the x-ray diffraction (XRD) patterns for 40-nm nanowires arrays with different metal compositions. The XRD peaks of these nanowire arrays are assigned to the peaks of a Bi standard, showing that the lattice structures of Bi nanowires are not affected by the addition of Te (≤ 0.15 at%) and Sb (≤ 15 at%). The intensity

distributions of the peaks indicate that these nanowires possess a preferred crystal orientation perpendicular to the (012) lattice plane along the wire axes. The results are consistent with previous XRD studies on Bi nanowire arrays of various diameters [4], which show that there is a wire-diameter-dependent preferred crystal orientation along the wire axes for nanowires produced by pressure injection.

Figure 3(a) shows the measured $R(T)/R(270$ K) of 40-nm Bi nanowires with nominal Te concentrations based on the Bi/Te atomic ratio that was introduced in the melt to form the alloy. The actual Te concentration in the Bi nanowires is smaller than the nominal concentration due to the likely segregation of some Te atoms to the wire boundary during alloy solidification. Since the results are mainly dependent on the relative Te concentrations for the following discussions, we assume that 10% of the Te dopant in the alloy melt is present in the final nanowire product. With this assumption, 0.025 at%, 0.075 at%, and 0.15 at% Te-doped Bi alloys give rise to donor concentrations N_d of 6.67×10^{17}, 2.0×10^{18}, and 4.0×10^{18} cm^{-3} in the respective resulting nanowires. Based on the measured $R(T)$ in Fig. 3(a) and the calculated T-dependent carrier density, the T dependence of the average mobility μ_{avg} of these Te-doped Bi nanowires is obtained, shown as $\mu_{avg}^{-1}(T)/\mu_{avg}^{-1}(270$ K) in Fig. 3(b). μ_{avg}^{-1} of Te-doped Bi nanowires can be related to the various scattering processes using Matthiessen's rule by

$$\mu_{doped}^{-1}(T) = \mu_{undoped}^{-1}(T) + \mu_{imp}^{-1}(T) + \mu_{defect}^{-1}, \tag{1}$$

where $\mu_{undoped}$ is the average mobility of the undoped Bi nanowires of the same diameter, and μ_{imp} and μ_{defect} are associated with the increased ionized impurity scattering and the expected higher defect level in Te-doped Bi nanowires, respectively. The average mobility of undoped Bi nanowires can be well fitted by a $\mu_{undoped} \sim T^{-2.9}$ dependence for $T > 100$ K, as shown by the dashed line in Fig. 3(b), consistent with the predominant electron-phonon scattering at high T. The solid curves in Fig. 3(b) are the fitted results calculated from the transport models [2,4], showing good agreement with experimental results.

Figure 4(a) shows the longitudinal magnetoresistance of 40-nm $Bi_{0.85}Sb_{0.15}$ alloy nanowires as a function of magnetic field B at different temperatures. 40-nm nanowire samples with different Sb concentrations ($x = 0.05$ and 0.10) are also measured, and the results are similar to the ones shown in Fig. 4(a). At low fields, the magnetoresistance (MR) of most samples can be described by a parabolic relation

$$MR \equiv [R(B) - R(B = 0)] / R(B = 0) = A_0 B^2 \tag{2}$$
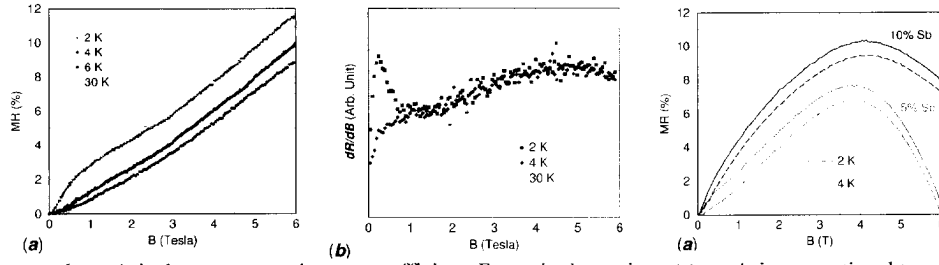
where A_0 is the magnetoresistance coefficient. For a single carrier (c) A_0 is proportional to

Figure 4. (a) Measured longitudinal magnetoresistance of 40-nm $Bi_{0.85}Sb_{0.15}$ alloy nanowires as a function of magnetic field B at different temperatures. (b) The first derivative with respect to the magnetic field B of the longitudinal magnetoresistance shown in (a). (c) Longitudinal magnetoresistance as a function of B for larger-diameter (d_w ~65 nm) $Bi_{1-x}Sb_x$ nanowire arrays. The maximum in the MR is attributed to boundary scattering effects.

the carrier mobility, while for a multiple carrier pocket system, A_0 is a complicated function of the mobility tensor elements. In Fig. 4(a), A_0 increases with decreasing temperature, consistent with a decreasing phonon scattering contribution as T decreases. It is noted that for $T < 4$ K, a plateau in the magnetoresistance is observed around $B = 0.7$ T. This abnormal feature can be more readily seen in the first derivative of the magnetoresistance, as shown in Fig. 4(b). The same behavior was also observed for other 40-nm nanowires with different Sb concentrations. This plateau feature is attributed to the 1D-to-3D localization effect at which the magnetic length equals the wire diameter, as described in Ref. [12].

Figure 4(c) shows the magnetoresistance as a function of magnetic field for larger-diameter ($d_w = 65$ nm) $Bi_{1-x}Sb_x$ nanowire arrays. The 1D-to-3D localization effect, although weaker than that in the 40-nm nanowires, can also be observed at a lower magnetic field. Another interesting feature is the non-monotonic $MR(B)$ and a maximum in the longitudinal MR, which are attributed to boundary scattering effects [13]. In the presence of magnetic fields, the trajectory of the carriers will be deflected, which increases the probability of boundary scattering. However, as the magnetic fields increase beyond a critical field such that the cyclotron orbits of the carriers lie within the wires, the frequency of the boundary scattering events will be reduced, resulting in a decrease in the longitudinal MR. We note that this maximum in the magnetic field due to the boundary scattering mainly depends on the wire diameter, as indicated by the curves shown in Fig. 4(c) for two different Sb concentrations. We also note that $Bi_{0.9}Sb_{0.1}$ nanowires have a larger magnetoresistance maximum than $Bi_{0.95}Sb_{0.05}$ nanowires. One major reason for the difference in the MR maximum in 65-nm nanowires of different Sb concentrations may be due to the increased boundary scattering with increasing Sb concentrations. It is expected that the introduced Sb atoms in Bi nanowires will migrate to the wire surface during the alloy solidification and subsequent annealing processes. Thus, nanowires with a higher Sb concentration tend to exhibit higher neutral impurity and defect densities near the wire boundary. Therefore, for a moderate magnetic field lower than the critical field, carriers traveling along the wire will experience more scattering events, resulting in a larger increase in the MR. However, it should be noted that in addition to the increased neutral impurity scattering, the introduction of Sb varies the relative population of different carrier pockets in Bi nanowires, which may also contribute to the change in the average carrier mobility and to the different

curvatures shown in Fig 4(c). Efforts are being made to acquire a more accurate determination of the Sb concentration and spatial distributions of the dopants in the nanowires in order to obtain a quantitative and more detailed understanding of the effect of Sb alloying in Bi nanowires.

CONCLUSIONS

We have synthesized Bi, Te-doped Bi, and $Bi_{1-x}Sb_x$ alloy nanowire arrays in anodic alumina templates, and studied their transport properties over a wide range of temperatures and magnetic fields. The XRD patterns of the nanowire arrays indicate that the Bi lattice structure is not altered by the Te or Sb atoms introduced. The T-dependent resistance measurements of Te-doped nanowires are consistent with theoretical calculations. The 1D-to-3D localization effect and the boundary scattering effect are observed in $Bi_{1-x}Sb_x$ alloy nanowires at low temperatures ($T < 4$ K), suggesting a high carrier mobility in the nanowires.

ACKNOWLEDGMENTS

REFERENCES

1. L. D. Hicks and M. S. Dresselhaus, Phys. Rev. B **47**, 12727 (1993).
2. Y.-M. Lin, X. Sun and M. S. Dresselhaus, Phys. Rev. B **62**, 4610 (2000).
3. J. Heremans, C. M. Thrush, Yu-Ming Lin, S. Cronin, Z. Zhang, M. S. Dresselhaus and J. F. Mansfield, Phys. Rev. B **61**, 2921 (2000).
4. Y.-M. Lin, S. B. Cronin, J. Y. Ying, M. S. Dresselhaus, and J. P. Heremans, Appl. Phys. Lett. **76**, 3944 (2000).
5. H. J. Goldsmid, Phys. Stat. Sol. (a) **1**, 7 (1970).
6. B. Lenoir, A. Dauscher, X. Devaux, R. Martin-Lopez, Yu. I. Ravich, H. Scherrer and S. Scherrer, in *Proceedings of the 15th International Conference on Thermoelectrics* (IEEE, 1996), pp. 1.
7. M. S. Dresselhaus, J. Phys. Chem. Sol. **32**, Suppl. 1, 3 (1971).
8. T. Koga, X. Sun, S. B. Cronin and M. S. Dresselhaus, Appl. Phys. Lett. **73**, 2950 (1998).
9. F. Keller, M. S. Hunter, D. L. Robinson, J. Electrochem. Soc. **100**, 411 (1953).
10. F. Y. Li, L. Zhang, R. M. Metzger, Chem. Mater. **10**, 2470 (1998).
11. Z. Zhang, J. Y. Ying and M. S. Dresselhaus, J. Mater. Res. **13**, 1745 (1998).
12. J. Heremans, C. M. Thrush, Z. Zhang, X. Sun, M. S. Dresselhaus, J. Y. Ying and D. T. Morelli, Phys. Rev. B, **58**, R10091 (1998).
13. Z. Zhang, X. Sun, M. S. Dresselhaus, J. Y. Ying and J. Heremans, Phys. Rev. B **61**, 4850 (2000).

Studies of the Dielectric Constant of Thin Film Bismuth Nanowire Samples Using Optical Reflectometry

M. R. Black[a,e], Y.-M. Lin[a], S. B. Cronin[b]. O. Rabin[c]. M. Padi[b], M. S. Dresselhaus[a,b,d]

[a]Department of EECS, Massachusetts Institute of Technology, Cambridge, MA
[b]Department of Physics, Massachusetts Institute of Technology. Cambridge. MA
[c]Department of Chemistry, Massachusetts Institute of Technology, Cambridge, MA
[d]Currently on leave from MIT
[e]Electronic mail: mrb@mgm.mit.edu

ABSTRACT

Arrays of 10 to 120 nm diameter single crystalline bismuth nanowires have been formed inside amorphous alumina templates. Since bismuth has a small effective mass compared to other materials, significant quantum mechanical confinement is expected to occur in wires with diameter less than 50nm. The subbands formed by quantum confinement cause interesting modifications to the dielectric function of bismuth. This study measures the dielectric function of bismuth nanowires in an energy range where the effects of quantum confinement are predicted (0.05 to 0.5 eV). Using Fourier transform infrared reflectometry, the dielectric constant as a function of energy is obtained for the alumina/bismuth composite system. Effective medium theory is used to subtract the effect of the alumina template from the measurement of the composite material, thus yielding the dielectric function of bismuth nanowires. A strong absorption peak is observed at $\sim 1000\,\mathrm{cm}^{-1}$ in the frequency dependent dielectric function in the photon energy range measured. The dependence of the frequency and intensity of this oscillator on incident light polarization and wire diameter are reviewed. In addition, the dependence of the optical absorption on antimony and tellurium doping of the nanowires are reported.

Introduction

Scientists and engineers use the effects of low dimensions as another means of tailoring a material to a desired application [1, 2, 3, 4]. In order for the design of a material to be optimized, the key parameters of the low dimensionality need to be measured and compared to theoretical calculations. This paper expands on previous work of looking at quantum confinement in bismuth nanowires by optical reflection.

Bismuth is an ideal material for quantum confinement studies. First of all, when a material's size approaches the de Broglie wavelength of its free carriers, the carriers become quantum confined. The electron and hole energy bands then split into subbands characteristic of a low dimensional material. For a given sample size, the energy separation of these subbands increase as the carriers' effective mass decreases. Since bismuth has small electron and hole effective mass tensors at the L-point (the mass components m^* vary from 0.001 m_0 to 0.26 m_0 depending on the crystalline direction), the separation between subbands is significant even at sample dimensions as large as $\sim$10 nm. Bismuth also has a large mean free path, $\sim$ 250 nm at 300 K[5], which in addition to the small effective mass is required for quantum confinement. As a result of the small effective mass and the large carrier mean free path, bismuth exhibits quantum confinement at manufacturable dimensions. Furthermore, bismuth has a low melting point ($\sim$271°C), which enables the fabrication of nanowires using

ε_1 and ε_2 Dependence on Wire Diameter
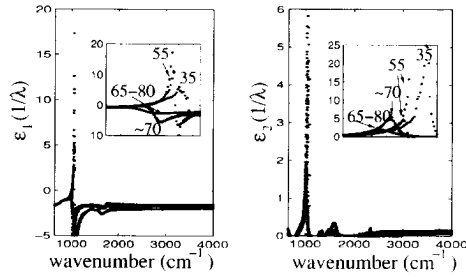
Figure 1: The wire diameter dependence of the dielectric function ($\epsilon_1 + i\epsilon_2$) of bismuth nanowires vs. wavenumber ($1/\lambda\,\mathrm{cm}^{-1}$) obtained from analysis of reflectivity measurements as reported in reference [7]. Results for samples 1-4 are shown.

a pressure injection technique. Lastly, bismuth nanowires are especially interesting because they exhibit a transition from a semi-metal with a small band overlap (38 meV at 0 K) to a narrow gap semiconductor as the wire diameter decreases and the quantum confinement energy increases [6]. This transition occurs in Bi nanowires at relatively large wire diameters because of its small band overlap and small effective mass tensor. For example, theoretical calculations predict this transition at a wire diameter of 48 nm for wires in the growth direction of our nanowires (< 202 >). The transistion from a semimetal to a semiconductor has significant effects on the electronic, thermoelectric, and optical properties of bismuth, particulary at low temperatures.

In a material that is quantum confined in two dimensions (quantum wires), the electronic joint density of states has a singularity at each energy corresponding to an intersubband transition. If the transition is allowed, incident light at this energy may be strongly absorbed. In a previous study, a strong narrow absorption peak is observed at $\sim$1000 cm^{-1} in bismuth nanowires [7]. In this previous study, the absorption energy is shown to increase as the wire diameter is decreased [7]. These results are reshown in Fig. 1. Since the energy separation of the electronic bands increases with decreasing wire diameter, the observed trend is qualitatively consistent with theory for intersubband transitions. In addition, the polarization dependence of the reflection is presented in this previous study and is also shown in Fig. 2. The features in the reflection at $\sim$1000 cm^{-1} disappear as the electric field is polarized along the direction of the wires. This paper further studies the strong absorption at $\sim$1000 cm^{-1} in bismuth nanowires by investigating the effect of antimony and tellurium doping.

Experimental Details

The bismuth nanowires in this study are fabricated by filling porous alumina with molten bismuth under a high pressure atmosphere [8, 9]. Since the alumina is a wide-bandgap semiconductor, the wires are isolated from each other and the free carriers are confined inside the wire. Porous anodic aluminum oxide templates are fabricated by anodizing aluminum sheets in an oxalic acid solution [8]. During this process, cylindrical pores 7-200 nm in
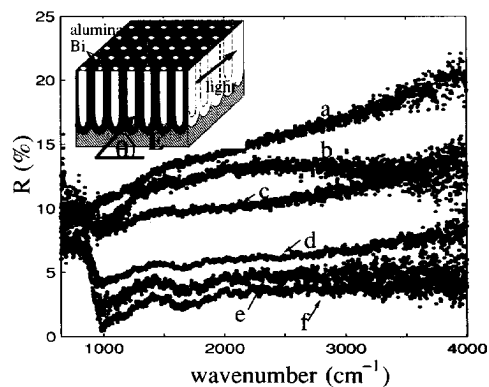
Figure 2: The polarization dependence of the reflection spectra of bismuth nanowires as a function of wavenumber $(1/\lambda\,\mathrm{cm}^{-1})$ as reported in reference [7]. Results for sample 1 is shown.

Table 1: Sample processing conditions

sample	voltage (volts)	temperature (K)	wire diameter (nm)	purity of Bi used to fill template(%)	dopant type	%in melt
1	60	273	65-80	99.99	none	0
2	60	275	~70	99.999	none	0
3	40	290	55	99.999	none	0
4	35	273	35	99.999	none	0
5	45	273	55	99.9999	Sb	15
6	45	273	55	99.9999	Te	0.0189
7	45	273	55	99.9999	Te	0.044
8	45	273	55	99.9999	Te	0.090

diameter are self-assembled into a hexagonal array, as previously reported [8, 9]. The process conditions used in this study are listed in Table 1.

The optical reflection $R(\omega)$ and transmission $T(\omega)$ are measured as a function of frequency at room temperature using a Nicolet Magna-IR 860 spectrometer and the Nic-Plan IR Microscope. Reflection data are taken in the infrared region from $650 < 1/\lambda < 4000\,\mathrm{cm}^{-1}$ at 293 K using a gold film as a comparison standard. The wavenumber resolution is $4\,\mathrm{cm}^{-1}$. Kramers Kronig relations are used to obtain the frequency dependence of the dielectric function of the composite material. Then from the dielectric function of the composite material and using effective medium theory, the dielectric function of the bismuth nanowires is obtained. Effective medium theory is required to separate the bismuth nanowire and alumina host contributions of the total dielectric function since in the frequency range of our experiments, the wavelength of light is more than 50 times greater than the wire diameter and the optical properties of the template and bismuth nanowires are measured simultaneously [10, 11, 12, 13].

Antimony Doping Dependence

Alloying crystalline bismuth with antimony adjusts the L-point bandgap. As the antimony concentration is increased from 0% to 4%, the bandgap decreases from $10meV$ to $0meV$. As the doping is increased further, the band gap continuously increases until pure antimony is reached and the bandgap is $200meV$ [14, 15]. A bismuth - antimony alloy wire was formed by introducing antimony into the melt and then using the same high pressure injection technique as for the pure bismuth wires to inject the alloyed metal into the alumina. The melt contained 15% antimony and 85% bismuth. Since the antimony concentration in the melt is not necessarily the same concentration as inside the nanowires, and furthermore since the nanowires may not have uniform doping along the wire axis, the ratio of antimony to bismuth must be measured after nanowire formation. Electron Dispersive Spectroscopy(EDS) was used to try to measure the concentration of antimony in the as grown sample. However, no antimony was detected. Therefore the concentration and distribution of antimony in the sample is currently unknown.

Although the exact antimony - bismuth ratio inside the nanowires is not known, the absorption peak behaves as expected with the addition of antimony. Fig. 3 shows that the nanowires formed from the 15% antimony melt have an absorption peak with higher energy than either the $35nm$ or $55nm$ undoped bismuth wires. If the sample were pure bismuth, the absorption would be expected to occur close to the $55nm$ undoped peak and below the $35nm$ undoped peak.

Tellurium Doping Dependence

Tellurium impurities are incorporated into our nanowires during the melt process. Concentrations of 0.090, 0.044, 0.018, and 0 weight percent are used. Again EDS is unable to measure impurity concentrations in the final sample. The samples are therefore referred to as heavily doped, lightly doped, very lightly doped, and undoped respectively.

Tellurium impurities in crystalline bismuth act as electron donors, and increase the Fermi energy to account for the increase in electron concentration. Tellurium dopants may also

Measured ε₂ Dependence on Sb doping
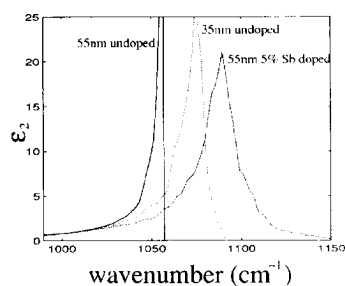
Figure 3: The effect of antimony doping on the absorption peak observed in the dielectric function $(\epsilon_1 + i\epsilon_2)$ of bismuth nanowires vs. wavenumber $(1/\lambda \ cm^{-1})$ obtained from analysis of reflectivity measurements. Without doping, the 55nm wires are expected to have an absorption peak close to the 55nm undoped wires and below the 35nm undoped wires. However, the doped sample has a peak above both the undoped 35nm and undoped 55nm, demonstrating an increase in bandgap with addition of antimony. Results for samples 3,4, and 5 are shown.

Absorption Dependence on Tellurium Doping
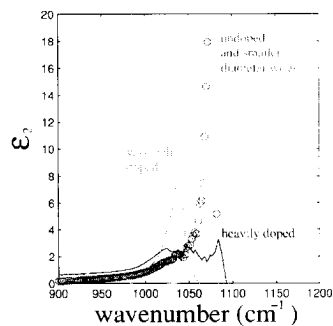
Figure 4: The effect of tellurium doping on the absorption peak observed in the dielectric function $(\epsilon_1 + i\epsilon_2)$ of bismuth nanowires vs. wavenumber $(1/\lambda \ cm^{-1})$ obtained from analysis of reflectivity measurements. Results for samples 3, 6, 7, and 8 are shown.

decrease τ the average time between scattering events, hence decreasing the coherence length, and thereby decreasing the quantum effects. Only considering the increase in Fermi energy, we expect that at higher doping levels the lower conduction subbands will become more occupied with electrons. When the conduction band is completely filled with electrons, an optical transition from the valence band to the conduction band is forbidden by the Pauli exclusion principal. Therefore, as the doping increases, the higher energy bands dominate the optical spectra. Since bismuth has a strongly coupled valence and conduction band at the L-point, the bands are highly non-parabolic. The intersubband transition is therefore expected to decrease and then increase as the Fermi energy is increased (at $0K$). This is approximately what is observed in Fig. 4. However since the doping is unknown at this time, it is premature to conclude as to the cause of the shift in absorption peak due to the tellurium doping.

Summary

This study reports the effect of tellurium and antimony doping on the absorption peak observed in bismuth nanowires at $\sim 1000\,\mathrm{cm}^{-1}$. The change in the absorption upon doping with either antimony or tellurium confirm that this absorption is from the bismuth nanowires and furthermore show that dopant is incorporated into the nanowires. When antimony is incorporated into the nanowires, the energy of the peak absorption increases. This increase is consistent with the increase in the bandgap of bulk bismuth - antimony alloys with increasing antimony doping. The peak energy changes non-monotonically with increasing doping of tellurium. More work is needed to determine the cause of this non-monotonic increase.

Acknowledgements

References

[1] N. Kouklin, S. Bandyopadhyay, S. Tereshin, A. Varfolomeev, and D. Zaretsky, Applied Physics Letters **76**, 460 519 (2000).

[2] D. E. Aspnes, A. Heller, and J. D. Porter, J. Appl. Phys. **60**, 3028 3034 (1986).

[3] M. S. Dresselhaus, T. Koga, X. Sun, S. B. Cronin, K. L. Wang, and G. Chen. In *Sixteenth International Conference on Thermoelectrics: Proceedings, ICT'97; Dresden, Germany*, edited by Armin Heinrich and Joachim Schumann, pages 12 20, Institute of Electrical and Electronics Engineers, Inc., Piscataway, NJ 09955-1331, 1997. IEEE Catalog Number 97TH8291; ISSN 1094-2734.

[4] L. D. Hicks and M. S. Dresselhaus, Phys. Rev. B **47**, 12727 12731 (1993).

[5] V. Damodara Das and N. Soundararajan. Phys. Rev. B. **35**, 5990 5996 (1987).

[6] Y. M. Lin, X. Sun, and M. S. Dresselhaus, Phys. Rev. B **62**, 4610–4623 (2000).

[7]

[8] M. R. Black, M. Padi, S. Cronin, Y.-M. Lin, O. Rabin, T. McClure, G. Dresselhaus, P. L. Hagelstein, and M. S. Dresselhaus, Appl. Phys. Lett.**75** (2000).

[9] Z. Zhang, J. Ying, and M. Dresselhaus, J. Mater. Res. **13**, 1745 1748 (1998).

[10] J. Heremans, C. M. Thrush, Y. Lin, S. Cronin, Z. Zhang, M. S. Dresselhaus, and J. F. Mansfield, Physical Review B **61**, 2921–2930 (2000).

[11] G. L. Hornyak, C. J. Patrissi, and C. R. Martin. J. Phys. Chem. B. **101**, 1548 1555 (1997).

[12] C. A. Foss, Jr. G. L. Hornyak, J. A. Stockert, and C. R. Martin, J. Phys. Chem. B. **98**, 2963 2971 (1994).

[13] D. E. Aspnes, Thin Solid Films **89**, 249 262 (1982).

[14] N. L. Cherkas, Opt. Spectrosc. **81**, 906 912 (1996).

[15] B. Lenoir, A. Dauscher, X. Devaux, R. Martin-Lopez, Yu.I.Ravich, H. Scherrer, and S. Scherrer. In *Fifteenth International Conference on Thermoelectrics: Proceedings, ICT '96*, pages 1 13, Institute of Electrical and Electronics Engineers. Inc., Piscataway, NJ 09955-1331, 1996.

[16] H. J. Goldsmid, Phys. Stat. Sol. **1**, 7 28 (1970).

High Spatial Resolution Assessment of the Structure, Composition, and Electronic Properties of Nanowire Arrays

M.S. Sander[1], A.L. Prieto[1], Y.M. Lin[2], R. Gronsky[3], A.M. Stacy[1], T.D. Sands[3], M.S. Dresselhaus[4]

[1]Department of Chemistry, University of California, Berkeley, CA 94720
[2]Department of Electrical Engineering and Computer Science, Massachusetts Institute of Technology, Cambridge, MA, 02139
[3]Department of Materials Science & Engineering, University of California, Berkeley, CA 94720
[4]On leave from Departments of Physics and Electrical Engineering and Computer Science, Massachusetts Institute of Technology, Cambridge, MA, 02139

ABSTRACT

We have employed transmission electron microscopy (TEM) and analytical electron microscopy to perform preliminary assessment of the structure, composition and electronic properties of nanowire arrays at high spatial resolution. The two systems studied were bismuth and bismuth telluride nanowire arrays in alumina (wire diameters ~40nm), both of which are promising for thermoelectric applications. Imaging coupled with diffraction in the TEM was employed to determine the grain size in electrodeposited Bi_2Te_3 nanowires. In addition, a composition gradient was identified along the wires in a short region near the electrode by energy-dispersive x-ray spectroscopy. Electron energy loss spectroscopy combined with energy-filtered imaging in the TEM revealed the excitation energy and spatial variation of plasmons in bismuth nanowire arrays.

INTRODUCTION

Nanowire arrays consisting of an ordered distribution of uniform diameter wires within a supporting matrix have attracted considerable recent interest.[1] These arrays can potentially be used to harness the properties of nanowires for robust applications in areas such as thermoelectrics, information storage, and photonics. Because transport in nanowires is confined to one dimension and the arrays have a large interfacial area, the array properties are particularly sensitive to even slight variations in structure and composition in the wires and at the wire-matrix interfaces. Therefore, to obtain an understanding of the relationship between the array characteristics and the array properties, it is necessary to assess the nanowires and wire-matrix interfaces at high spatial resolution.

In this work, we have focused on assessing the local characteristics in nanowire arrays of bismuth and bismuth telluride in alumina. These nanocomposite materials have potentially good thermoelectric properties.[2,3] Thermoelectric materials are currently not in widespread use for cooling and power generation applications due to their relatively low efficiency. A promising approach to increase thermoelectric efficiency is through confinement of the charge carriers in low-dimensional structures, as demonstrated recently in quantum well systems,[4] and this approach may be possible in two-dimensionally confined nanowires. The bismuth-alumina nanowire array system is also a good model system for understanding the relationship between

wire and interface characteristics and local electronic properties in arrays; this system is relatively simple and bismuth has interesting electronic properties due to its unique band structure. Bismuth telluride has good thermoelectric efficiency in bulk, and the bismuth telluride nanowire array system offers the possibility through manipulation of the wire composition to produce significant changes in the array properties.

In order to assess the local characteristics in these nanocomposite materials, characterization at high spatial resolution is required. Transmission electron microscopy allows for determination of the structure in the arrays with resolution of ~2Å, and TEM coupled with analytical detection systems allows for determination of the composition and electronic properties in ~1nm diameter regions of the specimen. Energy dispersive x-ray spectroscopy (EDS) in the TEM provides elemental composition information from the probed region. Electron energy loss spectroscopy (EELS) in the TEM in the low-energy loss region (0-40eV) is useful for studying valence excitations within the specimen, particularly collective electron excitations (plasmons). The goal of this work is to perform a preliminary assessment of the structure and composition in bismuth telluride nanowire arrays, as well as the electronic properties in bismuth nanowire arrays.

EXPERIMENTAL METHODS

The arrays were fabricated by deposition of the wire material into porous templates. Alumina templates were prepared by anodization of aluminum using a well-established process.[5] Bismuth nanowire arrays were fabricated by pressure injection of molten bismuth into the pores of the template; this process has been described in detail elsewhere.[6] Bismuth telluride nanowire arrays were prepared by electrodeposition into the templates. The procedure and more detailed characterization of the resulting arrays will be described in future work; here we give a brief overview of the process and a preliminary assessment of the wire structure. To deposit the wire material, an Ag film was sputter-deposited onto the top of the alumina template to serve as the electrode. The remaining aluminum was then chemically removed using a saturated $HgCl_2$ solution. The barrier layer created during anodization was removed from the pores by etching with KOH saturated in ethylene glycol. Bi_2Te_3 wires were formed by electrodeposition using a three-electrode set-up, with the Ag-backed porous alumina as the working electrode, Pt gauze as the counter electrode, and Hg/Hg_2SO_4 (in sat. K_2SO_4) as the reference electrode. Bismuth telluride was deposited in an ice bath from a solution of 0.0075M BiO^+ and 0.01M TeO_2^+ in 1M HNO_3. The deposition potential was -0.60V relative to the reference electrode, which was chosen to be within the deposition range employed in previous Bi_2Te_3 film depositions.[7]

Samples were prepared for characterization in the TEM in two ways. To assess the structure and composition in individual nanowires, the wires were released from the alumina template by selective etching using a CrO_3/phosphoric acid solution and then diluted through several replacements with water followed by ethanol. The nanowires were dispersed onto a holey carbon grid from the wire solution. To assess the electronic properties of the bismuth nanowire arrays, cross-sectional array specimens were prepared by dimpling followed by ion millling.

Assessment of the bismuth telluride nanowire structure, including imaging and diffraction, was performed using a JEOL 200CX TEM. The composition along individual nanowires was determined using a Philips CM200 TEM with a probe size of ~1nm and an Emispec™ x-ray detection system for EDS. EELS studies were performed in the CM200 using a Gatan PEELS detection system.

Figure 1. Bright-field (left) and dark field images of an individual Bi_2Te_3 nanowire.

RESULTS AND DISCUSSION

Bi_2Te_3 nanowire arrays

We have studied the structure and composition in the electrodeposited bismuth telluride nanowires. The average grain size in the wires was assessed using imaging combined with diffraction in the TEM. In figure 1, a bright-field image and corresponding dark-field image of an individual nanowire are shown. In the wires studied, the average grain size is smaller than the wire diameter, as illustrated in these images. The deposition parameters employed to produce these wires resulted in very fast pore filling. By varying the deposition conditions, including the deposition potential and temperature, it may be possible to vary the grain size. In addition, post-deposition annealing may be employed to increase the grain size. Such control is desirable because grain size has been shown to be an important factor governing the thermoelectric properties of bulk Bi_2Te_3[8,9]and is expected to also play an important role in nanowire array properties.

In addition to wire structure, wire composition may also critically affect array properties. X-ray diffraction of the array structures indicates that the wires are Bi_2Te_3, and EDS in the scanning electron microscope (SEM) shows a 2:3 Bi:Te ratio. In order to determine the composition of the individual wires, it is necessary to probe the wire composition at high spatial resolution. Therefore, EDS in the TEM has been employed to determine the composition in ~1nm regions of the wire. Across the wire diameter and along most of the wire length, the composition is constant 40:60 Bi:Te within the error of the technique, which is approximately a few percent. However, near the electrode, there is a compositional gradient along the wire length, as indicated in Table 1. This gradient may result from the electrochemical deposition process. Further study is required to determine the origin of the gradient and to assess how well the composition can be controlled in this region. Such a gradient may have a significant effect on the array properties because transport in the wires is confined to the direction of the wire axis, and the properties of bulk Bi_2Te_3 are known to vary with even slight changes in stoichiometry.[10]

Probe position (relative to electrode)	Bi (%)	Te (%)
Near electrode	35.0	65.0
+ ~.6μm	35.7	64.3
+ ~1μm	35.6	64.4
+ ~1.3μm	36.3	63.7
+ ~1.6μm	36.6	63.4
+ ~2μm	37.7	62.3

Table 1. Percentage of Bi and Te in ~1nm regions of the wire relative to the electrode.
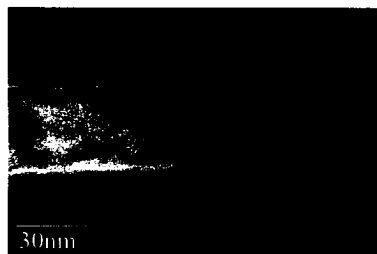
Figure 2. Energy-filtered image (above) created using electrons undergoing energy losses from ~10-20eV, as indicated in the EEL spectra at right.
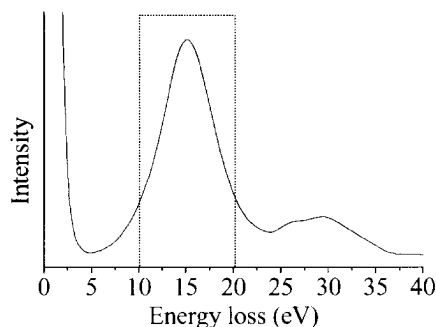
Bi nanowire arrays

In previous work, the characteristics of the wires and wire-matrix interfaces in pressure-injected bismuth nanowire arrays were described.[11] Here we report a preliminary assessment of the local electronic properties of the arrays as studied by EELS in the TEM. EEL spectra have been obtained with an ~1nm probe size. The low-loss spectrum from the center of an individual bismuth nanowire is shown in Figure 2. The strong peak at ~15eV is attributed to the bismuth volume plasmon. The two smaller peaks at higher energy loss (~26 and 29eV) are due to the bismuth $O_{4,5}$ ionization edges.[12] The energy-filtered image in Figure 2 was created using a 10eV energy filter to select the electrons that suffered an energy loss due to excitation of the 15eV volume plasmon, as indicated by the highlighted region of the spectrum. Along the bismuth wire, variations in contrast are apparent. These variations result from diffraction contrast, which is preserved in the energy-filtered image due to the large signal-to-noise ratio present in low energy images.[13] This image indicates that plasmon-loss images may provide additional useful information to help identify local strain fields within the wires. Identification of strain fields within nanoparticles is experimentally challenging using BF and DF imaging because such work involves extensive tilting of the specimen to align the particle in various zone axes, which is difficult to do with extremely small area particles.

In addition to studying the energy losses within the wires, EELS was also employed to assess the energy losses within the composite arrays. Spectra from the alumina template revealed an energy loss peak corresponding to the alumina bulk plasmon at ~26eV, while spectra from the wires revealed the peaks described above. Using a ~1nm probe at the wire-matrix interface, the spectrum shown in Figure 3 was obtained. Contributions from the bismuth and alumina bulk plasmons are apparent at ~15eV and 26eV, respectively. In addition, a lower energy peak (~5eV) is also present. This energy loss is attributed to excitation of an interfacial plasmon.[14]
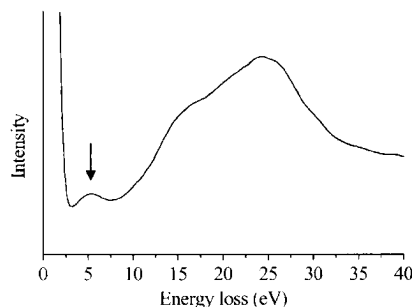
Figure 3. EEL spectrum obtained using an ~1nm probe centered directly on the Bi-Al_2O_3 interface in an array.

CONCLUSIONS

TEM and analytical electron microscopy were employed to study the local characteristics of arrays of bismuth and bismuth telluride nanowires in alumina. Imaging in the TEM revealed that the average grain size in electrodeposited BiTe nanowires is smaller than the wire diameter (~40nm). EDS of ~1nm regions along the wire length indicated that the composition is constant except in a short region (<5µm) near the electrode at the wire base. These results indicate that the local structure and composition in nanowire arrays may have a significant impact on the array properties.

Electron energy loss spectroscopy coupled with energy-filtered imaging was employed to assess the excitation energy and spatial variation of plasmons in individual bismuth nanowires as well as in a bismuth nanowire array. Energy filtered images of the bulk bismuth plasmon excitation in individual wires show a variation in intensity along the wire length due to diffraction contrast, which may provide useful information to identify regions of local strain within nanoparticles. In addition, a plasmon was identified at ~5.5eV at the wire-matrix interface. These results demonstrate the usefulness of employing EELS in the TEM to assess the local electronic properties in nanocomposite materials.

ACKNOWLEDGMENTS

REFERENCES

1   D. Routkevitch, A. A. Tager, J. Haruyama, D. Almawlawi, M. Moskovits, and J. M. Xu, IEEE Trans. **43,** 1646-58 (1996).

2   L. D. Hicks and M. S. Dresselhaus, Phys. Rev. B **47,** 16631-4 (1993).

3   Y.-M. Lin, X. Sun, and M. S. Dresselhaus, Phys. Rev. B **62,** 4610-23 (2000).

4   T. Koga, S. B. Cronin, M. S. Dresselhaus, J. L. Liu, and K. L. Wang, App. Phys. Lett. **77,** 1490-2 (2000).

5   S. Shingubara, O. Okino, Y. Sayama, H. Sakaue, and T. Takahagi, Jpn. J. Appl. Phys. **36,** 7791-7795 (1997).

6   Z. B. Zhang, D. Gekhtman, M. S. Dresselhaus, and J. Y. Ying, Chem. Mat. **11,** 1659-1665 (1999).

7   J.-P. Fleurial, A. Borshchevsky, M. A. Ryan, and W. Phillips, in *Proc. of the* 16th *International Conference on Thermoelectrics,* Dresden, Germany, 1997 (IEEE), p. 641-5.

8   A. Boulouz, A. Giani, F. Pascal-Delannoy, M. Boulouz, A. Foucaran, and A. Boyer, J.Crystal Growth **194,** 336-41 (1998).

9   S. Kikuchi, Y. Iwata, E. Hatta, J. Nagao, and K. Mukasa, in *Proc. of the* 16th *International Conference on Thermoelectrics,* Dresden, Germany, 1997 (IEEE), p. 97-100.

10   P. Magri, C. Boulanger, and J. M. Lecuire, J. Mat. Chem. **6,** 773-779 (1996).

11 M. S. Sander, Y. M. Lin, M. S. Dresselhaus, and R. Gronsky, in *Materials Research Society Symposium Proceedings vol. 581*, Boston, MA, USA, 2000 (Mater. Res. Soc.), pp. 213-217.

12 C. Wehenkel and B. Gauthe, Sol. St. Comm. **15**, 555-8 (1974).

13 Z. L. Wang and A. J. Shapiro, Ultramicroscopy **60**, 115-35 (1995).

14 H. Raether, *Excitation of plasmons and interband transitions by electrons* (Springer-Verlag, Berlin ; New York, 1980).

Crystallographic Description for Nanoparticle Asemblies – Application to Cadmium Selenide Clusters.

A L Vasiliev[1], M Aindow[1], J Lee[2], F Papadimitrakopoulos[2] and F Jain[3]

1. Institute of Material Science, Department of Metallurgy and Materials Engineering, University of Connecticut, Storrs CT 06269-3136
2. Nanomaterials Optoelectronics Laboratory (NOEL), Polymer Program, Department of Chemistry, University of Connecticut, Storrs CT 06269-3136
3. Nanomaterials Optoelectronics Laboratory (NOEL), Department of Electrical and Systems Engineering, University of Connecticut, Storrs CT 06269-3136

ABSTRACT: The stacking sequence of several layers of self-assembled semiconducting CdSe nanoparticles has been investigated using transmission electron microscopy. FCC, HCP, saddle sites occupation and ring structures were found coexisting in the supercrystals formed by CdSe nanoparticles.

1. INTRODUCTION

The wide variety of applications of semiconducting, metal and isolating nanoparticles has motivated many studies of their structure and properties. Sample uniformity makes it possible to manipulate nanocrystals into glassy or ordered nanocrystal assemblies. Ordered metallic, insulating, or semiconducting nanoparticles represent an exiting new class of materials [1]. These self-assembled mono-modal size-selected nanoparticles frequently adopt close-packed three-dimensional arrangements. The resemblance of these arrangements to the face-centered cubic or hexagonal close-packed crystal structures exhibited by many elements has to led to the widespread adoption of these crystallographic terms to describe the assemblies. Self-assembling of passivated gold nanoparticles was described recently in [2]. Semiconductor nanostructures have attracted tremendous interest in the past few years because of their special physical properties and their potential for applications in micro- and optoelectronic devices [3]. Recently the possibility of the synthesis of CdSe nanocrystals highly regular in size and shape was shown [4]. The CdSe nanocrystals, which are coated with surfactant organic molecules can self-organize into highly ordered microstructures. The goal of the work was the study of self-assembling arrangements of CdSe nanocrystals.

2. EXPERIMENT

CdSe nanoparticles were produced by solution pyrolysis of organometallic precursors in trioctylphosphine. Details of the synthesis was described in [4]. The nanoparticles are organically coated. The CdSe clusters were dissolved in a toluene solution. The solution were deposited on a standard Cu grid covered with a thin

amorphous carbon film. Different amounts of solution were dropped to the grid to change the number of layers formed by the nanoparticles. The samples were studied in a Philips EM 420 TEM operated at 100kV.

3. RESULTS AND DISCUSSION

A TEM image of non-ordered, glassy CdSe nanoparticles two-dimensional assembly is shown in fig.1. The random distribution of the CdSe particles was caused by the quick drying of the solution on the carbon substrate and difference in the particle sizes.

An ordered CdSe assembly formed at a lower solvent evaporation rate with different numbers of layers is presented in fig. 2. Steps with one CdSe layer in height were associated with difference in contrast. The tentative number of layers derived from contrast variations are shown. Subsequent images were obtained from *this or* similar *stepped* areas where the number of layers was unambiguous, and from regions exhibiting chain and ring stacking.
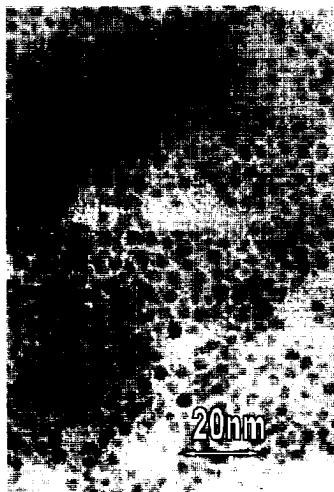
Fig. 1. TEM image of non-ordered CdSe particles.
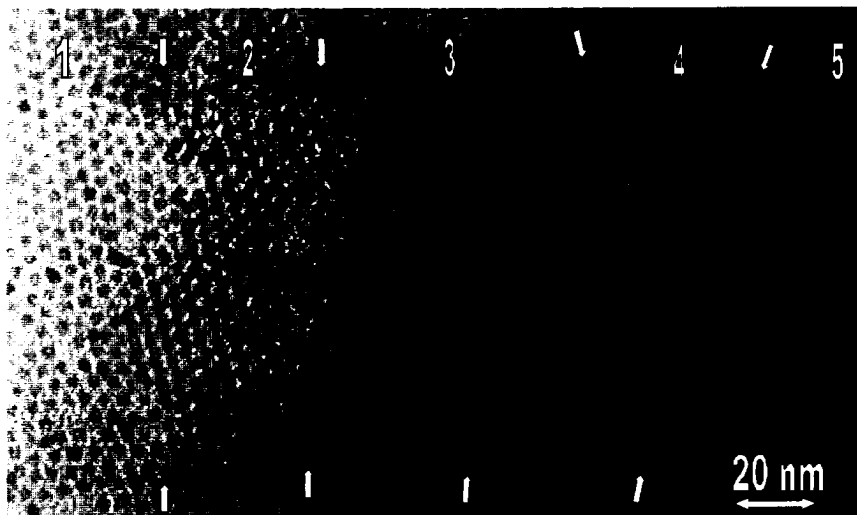
Fig. 2. TEM image of ordered CdSe nanoparticles with different number of layers (indicated by numbers). Arrows show the steps one CdSe nanoparticles layer in height.
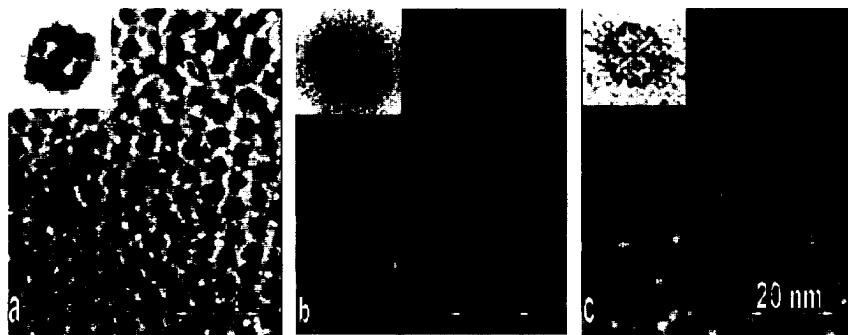
Fig.3. Single-(a), double-(b) and triple layers of CdSe nanoparticles. Correspondent FFT power spectra are in the inset.

The single layer of the CdSe nanoparticles (fig. 3a) shows hexagonal symmetry (note the FFT power spectrum). The nanoparticles in the second layer mostly occupied three-fold hollow sites (see fig. 3b). Correspondent FFT power spectrum from two layers more often demonstrated six-fold symmetry. However, in some areas the nanoparticles in the second layer occupied two-fold saddle sites (fig.4 a-c). The TEM images of such stacking demonstrate characteristic chains or lines. Similar arrangement were recently found experimentally by Wellner et al. [2] for gold nanoparticles. It was suggested that this type of ordering could be dependant on nanoparticle shape. The shape of the CdSe nanoparticles in our investigations was not perfectly spherical and that could cause
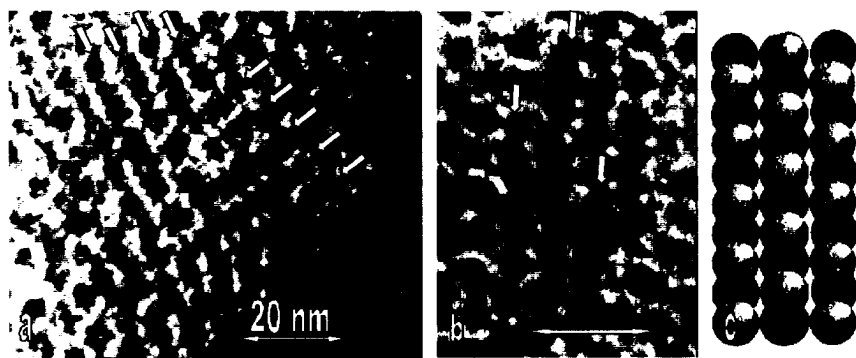
Fig. 4. Image of two layered part of the sample from fig.1 where second layer of CdSe nanoparticles occupied saddle sites (arrowed)-a). The enlarged image of the two-layer island with chains (arrowed) formed by particles in the saddle sites -b) and schematic representation of the twofold saddle sites occupation in the second layer -c).
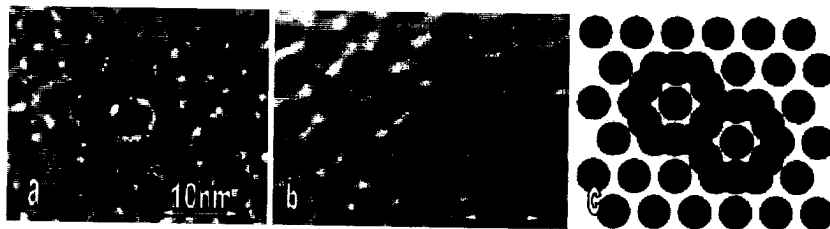
Fig.5. An image of ring structure –a). Two closely spaced parts of rings -c) and a schematic representation of ring structure –c).

the high density of chain-like structures in the sample. The chain-like structures were found as bi-layered islands (fig.4 b). We can not rule out the possibility of three and more layers formation of CdSe particles in the saddle sites in these areas. This corresponds to a disordered form of the C11$_h$ MoSi$_2$ structure [5]. There was one more stacking configuration of second layer. It looks like ring or semi-ring structure (fig.5 a-c). The ring arrangement of nanoparticles was recently shown in [6] when second layer was rotated and contracted leading to the energy minimization.

The contrast from the third layer was slightly different even in adjacent areas (fig. 2 and fig. 3c). The two-fold symmetry of the FFT power spectrum indicated the presence of hexagonal stacking or hcp structure (see fig. 3c, insert). However, close examination of other areas associated with the presence of a third layer pointed to the three-fold symmetry and fcc type of structure. The stacking of third and fourth layers near chain-like structures more often look like lines and may be due to further occupation of two-fold sites above the second layer which corresponds to a disorder form of the C11$_h$ MoSi$_2$ structure.

4. CONCLUSION

Three-dimensional arrangements of semiconducting CdSe nanoparticles can be fcc or hcp –type. Nanoparticle in the saddle sites or ring stacking of second layer can also coexist with these. Third and forth layers deposited on the top of saddle site stacking can form the C11$_h$ MoSi$_2$ structure.

REFERENCES

1. A.P. Alivisatos, *J.Phys.Chem.*.**100**, (31), 13226 (1996).

2. A. Wellner, P. Brown, M. Aindow, C.J.Kiely, and J.P. Wilcoxon, *Inst. Phys. Conf. Ser.* **161**, 561 (1999).

3. I.M. Goldby, L. Kuipers, B. von Assendorf, P.E. Palmer, *Appl. Phys. Lett.* **69**, 2819 (1996).

4. C.B. Murray, D.J. Norris, M.G. Bawendi, *J. Am. Chem. Soc.* **115**, (19), 8706 (1993).

5. M. Aindow, S.N. Williams, R.E. Palmer, J. Fink, C.J. Kiely, *Phil. Mag. Lett.* **79**, 569. (1999).

6. D. Zanchet, M.S. Moreno, D. Urgante, *Phys. Rev.Lett.* **82**, 5227. (1999).

Optical Response of Gold Nanoparticles in Dielectric Materials

Akira Ueda, Elana M. Bryant, Carlton B. Maxwell, Charline M. Blake, Richard R. Mu, Marvin H. Wu, Andrey I. Zavalin, Alkiviathes Meldrum[1] and Don O. Henderson
Chemical Physics Laboratory, Department of Physics, Fisk University, Nashville, TN 37208, USA
[1]Department of Physics, University of Alberta, Edmonton, Alberta, Canada

ABSTRACT

The fundamental studies of metallic nanoparticles embedded in various host materials have been made. The host-guest interaction causes the shapes of embedded nanoparticles, and the surface plasmon resonances of the metallic nanoparticles are affected by the host materials. The control of the surface plasmon resonance condition is a challenging question. We will discuss the interface effect of the systems where gold nanoparticles were fabricated between materials of MgO and SiO_2.

INTRODUCTION

Surface plasmon resonance (SPR) of small metallic particles has been studied since Mie's calculation of 1908 about the study [1] of optical properties of gold particles, and in the past three decades the new field of cluster science has been developed with many potential applications. Although many studies have been published, there are still new interesting systems and there are fundamental questions to be answered. In our laboratory, we have studied the systems of several insulating materials implanted with gold ions (Al_2O_3:Au, CaF_2:Au, Silica SiO_2:Au, MgO:Au, Muscovite Mica:Au, and Vycor Glass:Au) and of the porous materials impregnated with gold (Vycor Glass: Au)[2-5].

In the systems of SiO_2:Au and MgO:Au fabricated by ion implantation, we have previously seen the growth of gold nanocrystals and found the SPR positions to be 530 nm and 560 nm, respectively, after a suitable thermal annealing in $5\%O_2+95\%Ar$ atmosphere. These SPR positions agree with the Mie's theory using a dipole approximation (Flölich approximation) for spherical particles, that satisfies the following equation:

$$\varepsilon(\omega_{SP}) + 2\varepsilon_m = 0, \qquad (1)$$

where $\varepsilon(\omega)$ is the dielectric function of gold, ε_m is the dielectric function of host material, and ω_{SP} is the surface plasmon frequency.

As shown in Fig. 1, from our previous experiments, the gold nanocrystals in MgO have rounded cubic shape with a side-length of 10 nm or less, that aligns along the crystal axis of MgO (100), while the gold nanocrystals in silica glass (SiO_2) are spherical. (The detail of this result will be discussed elsewhere.) If only the surface energy of gold particles plays the dominant role for the nanocrystal growth, the shape should be spherical. The host MgO crystal, therefore, must contribute to this result of cubic gold particles because MgO single crystal has a cubic crystal structure. Fuchs has investigated the optical absorption of small ionic crystalline cubes in infrared region by calculating the normal modes of the surface polarization charges [6]. For cubes, he found that several surface polariton mode conditions for the dielectric function ranges $-3.68\varepsilon_m \le \varepsilon(\omega_{SP})$ $\le -0.42\varepsilon_m$, instead of the sphere condition of Eq.(1): $\varepsilon(\omega_{SP}) = -2\varepsilon_m$. The strongest mode satisfies the condition: $\varepsilon(\omega_{SP}) = -3.68\varepsilon_m$. It is expected that metallic cubes follow the similar conditions, and this corresponding strongest mode for a gold cube embedded in MgO is approximately located

at 680 nm. The shape of observed gold particles is rounded cube, so that the resonance condition for SPR might be $-3.68\varepsilon_m \leq \varepsilon(\omega_{SP}) \leq -2\varepsilon_m$.

On the other hand, if the distance between gold particles is short enough, gold particles are no longer regarded as isolated particles and the induced dipole-dipole interaction may result in an absorption band at longer wavelength.

In this paper, we will discuss the interfacial interaction between gold nanocrystals and the dielectric hosts mainly by observing the SPR band of the systems.
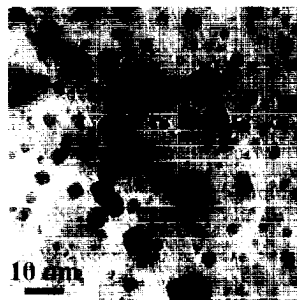
EXPERIMENTAL

MgO substrates were single crystal plates (1" x 1" x 0.5 mm) with polished (100) surface obtained from Princeton Scientific Corporation. Gold was deposited onto the substrates by electron beam

Figure 1 TEM image of Gold nanocrystals fabricated in MgO single crystal by ion implantation with a post annealing. The shape of the gold nanocrystals is rounded cubic and they align along the crystal axis of host MgO (100).

evaporation in a vacuum with the pressure of ~ 10^{-7} torr. Overcoating with MgO and SiO_2 was carried out also by electron beam evaporation with thickness of 100 nm and a deposition rate of 0.5 Å/sec for both Au and MgO. UV-VIS spectra of the samples were taken before and after every thermal annealing with a spectrophotometer (Hitachi, U-3501). Thermal annealing was carried out with a tube furnace with Ar gas (99.995%) flow.

In order to see the matrix dependence, we fabricated the following three systems: (1)Au deposition of 50 Å on MgO substrate with a MgO overcoat [MA50M] , (2) Au deposition of 25 Å on MgO substrate with a MgO overcoat [MA25M]], and (3) Au deposition of 50 Å on MgO substrate with a SiO_2 overcoat [MA50S]. Hereafter, the abbreviations for the systems MA50M, MA25M, and MA50S will be used for simplicity: the each letter in the abbreviations from left to right represents the substrate material, gold deposition with the thickness in Å, and the overcoat materials, respectively. For reference purpose, we have made samples without overcoating and an Atomic Force Microscope (AFM) was used to image gold nanoparticles as well as surface of coating.

RESULTS AND DISCUSSIONS

Fig. 2 shows the annealing temperature dependence of the UV-VIS transmission spectra for two systems (a)MA50S and (b)MA50M. Each spectrum was taken from the same samples for (a)MA50S and (b)MA50M annealed sequentially as indicated. For both cases, at low annealing temperatures, there are SPR absorption bands tailing into longer wavelength, probably because the prepared sample consists of an island-type gold film with effective thickness of 50 Å. The gold film may not be ruptured to form gold particles at low temperatures. At 800°C, the absorption tail at longer wavelength suddenly became weaker and the SPR became sharper as the annealing temperature increased. This indicates that the gold film had been ruptured and formed nano-meter size gold particles in the system. For the system with MgO overcoat (MA50M), the SPR band dramatically decreased at 1100°C, which indicated that gold atoms escaped from the system through the thin overcoat with thickness of 100 nm.
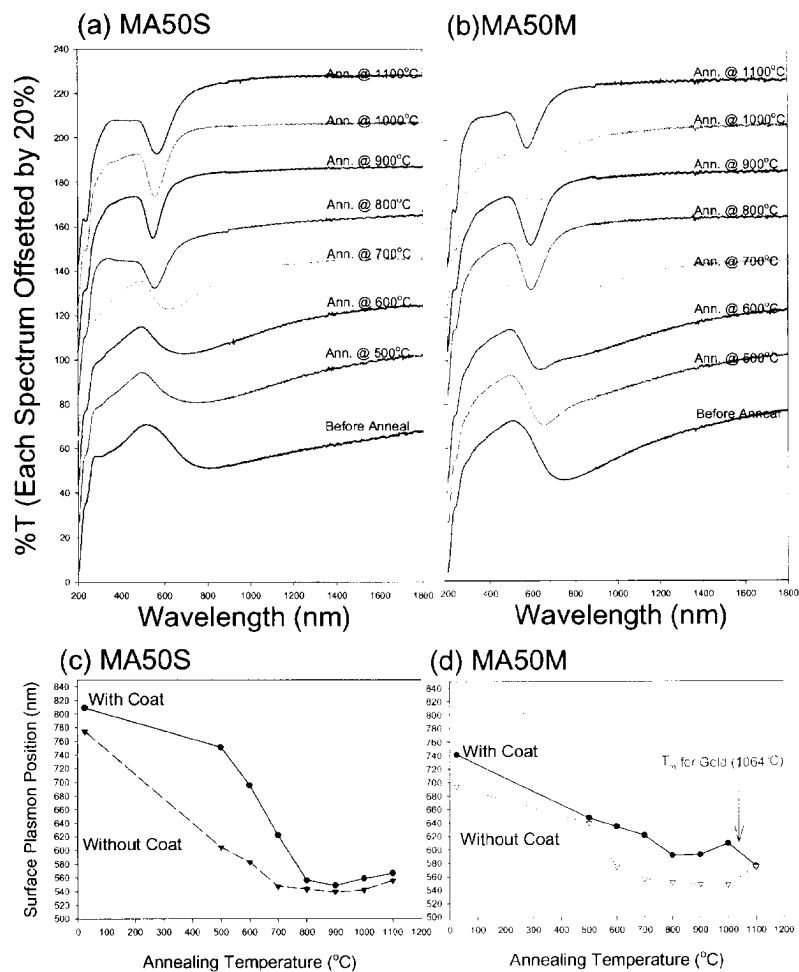
Figure 2 Annealing Temperature Dependence of UV-VIS Transmission Spectra for (a)MA50S and (b)MA50M and Surface Plasmon Position as a Function of Annealing Temperature for (c) MA50S and without Coating and (d) MA50M and without Coating.

The evolution of SPR position as a function of annealing temperature is plotted for each system of MA50S and MA50M accompanying un-coated samples as a reference, as shown in Fig. 2(c) and (d), respectively. For MA50S, the SPR positions became shorter as annealing temperature increased up to 800°C for both coated and un-coated system, and then it became nearly stable at 560 nm and 550 nm, for the coated and un-coated samples, respectively. Above 1000°C, the SPR positions slightly increased with the annealing temperature. For MA50M, the SPR positions gradually decreased as annealing temperature increased up to 800°C and then became stable. The SPR positions are 590 nm and 550 nm for coated and un-coated samples, respectively. At 1000°C, the coated sample increased SPR position slightly, and at 1100°C the positions merged together to 580 nm. Since the melting point of gold is 1064°C, gold could escape from the systems.

Similarly, Fig. 3(a) shows the annealing temperature dependence of the UV-VIS transmission spectra for system MA25M. Each spectrum was taken from the same sample of MA25M annealed sequentially as indicated. The evolution of SPR position as a function of annealing temperature is plotted for the system of MA25M accompanying un-coated sample as a reference, as shown in Fig. 3 (b). In this case, there is a weaker absorption tail at longer wavelength in comparison with systems MA50S and MA50M shown in Fig. 2. Since the starting effective thickness was 25 Å, the actual gold film was not uniform and probably a patched film that may contain nearly isolated gold particles. Thus the SPR position started from 645 nm and 625 nm for the coated and un-coated samples, respectively. However, the trend of evolution of spectra and SPR position are similar to those of system MA50M. The SPR positions in the stable region between 700°C and 900°C are 600 nm and 550 nm for the coated and un-coated samples, respectively. At 1000°C SPR position for the coated sample increased, and at 1100°C SPR positions for coated and un-coated samples merged together, as system MA50M behaved.
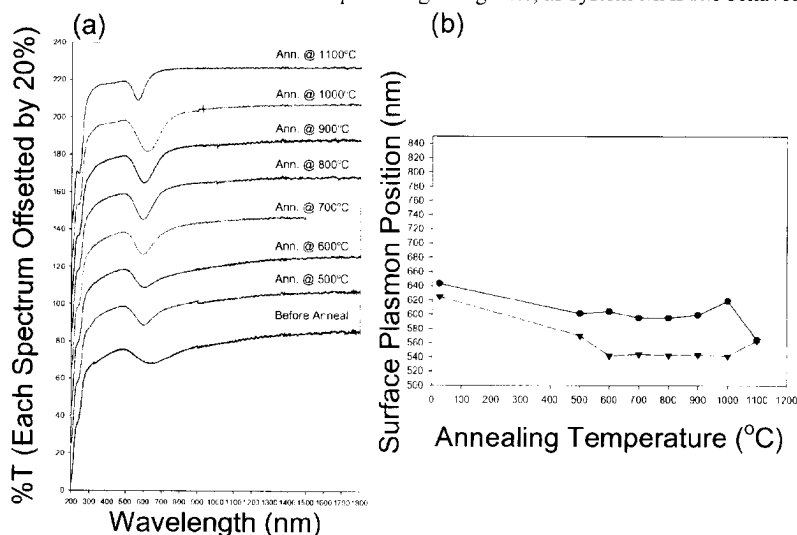
Figure 3 (a)Annealing Temperature Dependence of UV_VIS Transmission Spectra of the System MA25M and (b) SPR Position as a Function of Annealing Temperature.

Table 1 Summary of SPR Positions for Several Systems Obtained by Both Theoretical Calculation and Experiments.

	System	Particle Shape	SPR (nm)
Theoretical results	Au in MgO: $\varepsilon(\omega_S P)+2\varepsilon_{MgO}=0$	Sphere	550
	Au in SiO$_2$: $\varepsilon(\omega_S P)+2\varepsilon_{SiO2}=0$	Sphere	535
	Au in Vacuum: $\varepsilon(\omega_S P)+2\varepsilon_{Vac}=0$	Sphere	500
	Au in MgO: $\varepsilon(\omega_S P)+3.68\varepsilon_{MgO}=0$	Cube	680
Experimental results (After annealed up to 1000°C)	Au implanted in MgO	Cube	560 +3
	Au implanted in SiO$_2$	Sphere	532 ±3
	MA50S	N/A	560 ±5
	MA50 (fabricated with MA50S)	Oblate Spheroid	550 ±5
	MA50M	N/A	590 ±5
	MA50 (fabricated with MA50M)	Oblate Spheroid	550 ±5
	MA25M	N/A	600 ±5
	MA25 (fabricated with MA25M)	Oblate Spheroid	550 ±5

In Table 1, a summary of SPR positions for several systems obtained by both theoretical calculation and experiments. SPR for spherical Au particle in vacuum is the minimum value in the table because of its dielectric constant (the electric permittivity for vacuum). The uncoated samples, MA50 and MA25, were exposed to the air whose dielectric constant is close to vacuum and have SPR position at a relatively longer wavelength. This suggested that the shape of Au particles is not sphere. The systems, MA50M and MA25M, have SPR at longer wavelengths than that of the Au implanted in MgO. Since there is a possibility to have anisotropic shape of gold particles at the interface in the systems, especially MAu50M and MAu25M, those particles have more likely oblate spheroid type shape. As a reference, we have imaged gold particles of un-coated samples with an AFM. Fig. 4 shows the development of gold particles on the sample of M50: (a) as-deposited, (b) after annealed at 1000°C, and (c) after annealed at 1100°C. According to the AFM cross-section analysis, the gold particles are semispherical or oblate spheroid shaped. The aspect ratios (height to diameter) of gold particles are 0.05-0.11 for (a), 0.20-0.23 for (b), and 0.22-0.33 for (c). A model calculation for oblate spheroid with an aspect ratio of 0.01-0.3 in the air gave the SPR position around 500 nm (Oblate spheroids have an upper limit of SPR in a certain medium, as a longest SPR wavelength.), while the experimental results for un-coated samples (MA50 and MA25) are about 550 nm. Since the systems of un-coated samples are gold particles on MgO, the substrate effect should be considered.
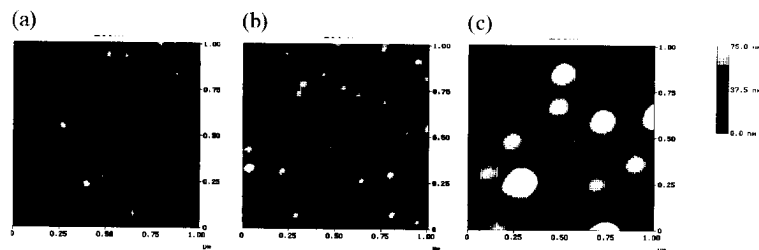
Figure 4 AFM Images of Gold Particles on an Un-coated Sample annealed at Different Temperatures: (a) as-deposited, (b) 1000°C, and (c) 1100°C. (The scan scales are all 1 μm x 1 μm.)

CONCLUSION

We have proposed the fabrication method of anisotropic gold particles. In order to manipulate the SPR position, we need to know the shape of gold particles in coated samples. At this stage, we did not obtain TEM images of the coated samples, and we need to know the crystal structure of coated MgO, as well. Furthermore, we need to take into account the interaction between gold particles.

REFERENCE

[1]G. Mie, Ann, Physik **25**, 377(1908). (German)

[2]D.O. Henderson, Y.-S. Tung, A. Ueda, R. Mu, Y. Xue, C. Hall, W.E. Collins, C.W. White, R.A. Zuhr, Jane G. Zhu, and P.W. Wang, J. of Vacuum Science and Technology **A 14**(3), 1199(1996); D.O. Henderson, Y.-S. Tung, R. Mu, A. Ueda, J. Chen, R. Gu, C.W. White, Jane G. Zhu, M. McKay, and O. Scott., International Conference of Defects in Insulating Materials, Wake Forest University, Winston-Salem, NC, USA, 1996. Materials Science Forum **239-241**, 695(1997).

[3]Z. Gu, R. Mu, A. Ueda, Y.-S. Tung, M.H. Wu, D.O. Henderson, A. Meldrum, C.W. White, and R.A. Zuhr, JVST **A16**,1409(1998).

[4]A. Ueda, D.O. Henderson, R. Mu, Y.-S. Tung, C.W. White, Jane G. Zhu, International Conference of Defects in Insulating Materials, Wake Forest University, Winston-Salem, NC, USA, 1996. Materials Science Forum **239-241**, 675(1997).

[5]D.O. Henderson, R. Mu, A. Ueda, Y.-S. Tung, C.W. White, R.A. Zuhr, and Jane G. Zhu, J. of Non-Crystalline Solids, **205/207**, 788(1996). The Ninth International Conference on Liquid and Amorphous Metal, Chicago, IL October 8-13, 1995, Proceedings; Y.-S. Tung, R. Mu, D.O. Henderson, A. Ueda, C.W. White, Jane G. Zhu, International Conference of Defects in Insulating Materials, Wake Forest University, Winston-Salem, NC, USA, 1996. Materials Science Forum **239-241**, 691(1997).

[6]Fuchs, Phys. Rev. **B11**, 1732 (1975); U. Kreibig and M. Vollmer, "Optical Properties of Metal Clusters," Springer Series in Materials Science 25 (Springer, New York, 1995).

Generalized Ellipsometry Using a Rotating Sample

Weiliang Xu[*], Lowell T. Wood, and Terry D. Golding[**]
Department of Physics, University of Houston, Houston, Texas 77204-5506, U.S.A.

ABSTRACT

We propose a generalized ellipsometric technique using a rotating sample. The ellipsometer consists of a polarizer, a rotatable sample holder, an analyzer, and a detector. Fourier coefficients are measured and used to extract the system's dielectric tensors and film thicknesses. The main advantage of the technique is that all parts of the ellipsometer are fixed except the sample, whose azimuth angle can be modulated. We show calculated responses to isotropic and anisotropic materials as well as superlattices. Potential applications for characterizations of anisotropic nanostructures are discussed.

I. INTRODUCTION

In a conventional rotating element ellipsometer, only one variable, i.e., the azimuth angle of the rotating element, is changed in the characterization of an isotropic material. In current generalized ellipsometers for characterizing anisotropic systems, however, either additional variables [1], e.g., the angle of incidence and the azimuth angles of the polarizer (or analyzer) and of the sample, are changed, or components not commonly found in a conventional rotating element ellipsometer are needed [2,3]. Even in the simplest case of uniaxial materials, two variables, i.e., the azimuth angles of the polarizer and analyzer, are required if sets of Ψ and Δ are measured to determine the dielectric tensors of the materials [4]. Optimization of ellipsometric setups with fewer variables involved in measurements is highly desirable in situations where measurements are remotely controlled, since the reliability of the controls and the accuracy of the measured data are improved. One such situation is the characterization of samples grown in space. In this paper we present a theoretical development and show that changing only the sample's azimuth angle is sufficient to determine dielectric tensors and film thicknesses of arbitrarily anisotropic systems. Instead of Ψ and Δ, the intensity dependence on the sample's azimuth angle is measured. Two approaches for analysis are proposed to determine the dielectric tensors and film thicknesses from the measured intensities. Popular conventional ellipsometer setups, e.g., polarizer-compensator-sample-analyzer (PCSA) or polarizer-sample-analyzer (PSA), can use this approach to characterize anisotropic systems by keeping all components fixed except the sample.

II. THEORY

In this section, we study the dependence of intensity on α_S, the sample's azimuth angle, to permit extraction of the dielectric tensors and film thicknesses. For an n-layer anisotropic

[*] Present address: DigiBot Inc., 4006 Beltline, Suite 234, Addison, TX 75001, wxu@digibotinc.com.
[**] Present address: Department of Physics, University of North Texas, TX 76203, golding@unt.edu

system, following the same procedure and coordinates setup as in Refs. [4,5], the Jones matrix (r) for reflection ellipsometry is

$$r_{pp} = \left(T_{31}T_{22} - T_{32}T_{21}\right)/\left(T_{11}T_{22} - T_{12}T_{21}\right),$$ (1)

$$r_{ps} = \left(T_{32}T_{11} - T_{31}T_{12}\right)/\left(T_{11}T_{22} - T_{12}T_{21}\right),$$ (2)

$$r_{sp} = \left(T_{41}T_{22} - T_{42}T_{21}\right)/\left(T_{11}T_{22} - T_{12}T_{21}\right),$$ (3)

$$r_{ss} = \left(T_{42}T_{11} - T_{41}T_{12}\right)/\left(T_{11}T_{22} - T_{12}T_{21}\right),$$ (4)

where (T) is the transfer matrix of the system. The formula for calculating (T) can be found elsewhere [6]. These expressions establish the relationships between the Jones matrix and the system's dielectric tensors and film thicknesses. For layer i, if we use the diagonal tensor $(\varepsilon_l)_i$, l=1, 2, 3, to represent the dielectric tensor with respect to its principal axes, Θ_i=(θ_{ri}, ϕ_{ri}, φ_{ri}, θ_{ii}, ϕ_{ii}, φ_{ii}) for the Euler angles of the frame of principal axes with respect to the laboratory frame for the real and imaginary parts of the dielectric tensor, and d_i for the thickness, (T) is completely determined by $(\varepsilon_l)_i$, Θ_i, and d_i, (i=1,...n).

If the PSA setup is used, the intensity after the analyzer is

$$I_d = I_p \left|\left(r_{pp}\cos\alpha_p + r_{sp}\sin\alpha_p\right)\cos\alpha_A + \left(r_{ps}\cos\alpha_p + r_{ss}\sin\alpha_p\right)\sin\alpha_A\right|^2,$$ (5)

where I_d is the intensity reaching the detector, I_p is a constant, and α_p and α_A are the azimuth angles of the polarizer and analyzer, respectively.

If α_p and α_A are fixed, changing α_S, i.e., rotating the sample, leads to the change of $\phi_i = (\phi_{ri}, \phi_{ii})$. Recall that the transfer matrix (T) depends on ϕ_i. Therefore, the Jones matrix changes with α_S and so does the intensity. However, the dielectric tensors on the principal axis frame and the Euler angles θ_i and φ_i remain the same. Substitution of Eqs. (1) – (4) into Eq. (5) gives I_d a function h of the dielectric tensors and film thicknesses. That is,

$$I_d(\alpha_S) = I_p h(\underline{(\varepsilon_l)_i}, \underline{\theta_{ri}}, \underline{\phi_{ri0}} + \alpha_S, \underline{\varphi_{ri}}, \underline{\theta_{ii}}, \underline{\phi_{ii0}} + \alpha_S, \underline{\varphi_{ii}}, \underline{d_i}),$$ (6)

where the underlined parameters do not change when the sample rotates, and ϕ_{ri0} and ϕ_{ii0} are the initial angles for ϕ_{ri} and ϕ_{ii}.

From Eq. (6), if the total number of $(\varepsilon_l)_i$, θ_{ri}, ϕ_{ri0}, φ_{ri}, θ_{ii}, ϕ_{ii0}, φ_{ii}, and d_i is k, and I_p is taken as unknown, they can, in principle, be determined by $k+1$ independent equations between I_d and I_p, $(\varepsilon_l)_i$, θ_{ri}, ϕ_{ri0}, φ_{ri}, θ_{ii}, ϕ_{ii0}, φ_{ii}, and d_i. In the rest of this section, we discuss two approaches of changing α_S to establish m ($m \geq k+1$) equations between I_d and I_p, $(\varepsilon_l)_i$, θ_{ri}, ϕ_{ri0}, φ_{ri}, θ_{ii}, ϕ_{ii0}, φ_{ii}, and d_i.

Approach one:

The intuitive way to establish m ($m \geq k+1$) equations between I_d and I_p, $(\varepsilon_l)_i$, θ_{ri}, ϕ_{ri0}, φ_{ri}, θ_{ii}, ϕ_{ii0}, φ_{ii}, and d_i is to set α_S to m different settings. If the intensities $I_d(\alpha_{S1})$, $I_d(\alpha_{S2})$, ..., $I_d(\alpha_{Sm})$ have been measured, m equations are set up. They are

$$I_p h(\underline{(\varepsilon_l)_i}, \underline{\theta_{ri}}, \underline{\phi_{ri0}} + \alpha_{S1}, \underline{\varphi_{ri}}, \underline{\theta_{ii}}, \underline{\phi_{ii0}} + \alpha_{S1}, \underline{\varphi_{ii}}, \underline{d_i}) = I_d(\alpha_{S1}),$$ (7)

$$I_p h((\underline{\varepsilon}_l)_i,\ \underline{\theta}_{ri},\ \underline{\phi}_{ri0}+\alpha_{S2},\ \underline{\varphi}_{ri},\ \underline{\theta}_{ii},\ \underline{\phi}_{ii0}+\alpha_{S2},\ \underline{\varphi}_{ii},\ \underline{d}_i)= I_d(\alpha_{S2}),$$ (8)

.....

$$I_p h((\underline{\varepsilon}_l)_i,\ \underline{\theta}_{ri},\ \underline{\phi}_{ri0}+\alpha_{Sm},\ \underline{\varphi}_{ri},\ \underline{\theta}_{ii},\ \underline{\phi}_{ii0}+\alpha_{Sm},\ \underline{\varphi}_{ii},\ \underline{d}_i)= I_d(\alpha_{Sm}).$$ (9)

To solve these equations for I_p, $(\varepsilon_l)_i$, θ_{ri}, ϕ_{ri0}, φ_{ri}, θ_{ii}, ϕ_{ii0}, φ_{ii}, and d_i, a test function is introduced:

$$Err = \sum_{j=1}^{m}\left[I_p h\left((\varepsilon_l)_i,\theta_{ri},\phi_{ri0}+\alpha_{Sj},\varphi_{ri},\theta_{ii},\phi_{ii0}+\alpha_{Sj},\varphi_{ii},d_i\right)-I_d(\alpha_{Sj})\right]^2 / \sigma_j^2 ,$$ (10)

where σ_j is the standard deviation for $I_d(\alpha_{Sj})$. Ideally, if there are no errors in the measurements of I_d, Eq. (10) reduces to Eqs. (7) – (9) if Err is minimized to zero. In practice, errors exist in I_d, but Err can be reduced to a minimum value. The I_p, $(\varepsilon_l)_i$, θ_{ri}, ϕ_{ri0}, φ_{ri}, θ_{ii}, ϕ_{ii0}, φ_{ii}, and d_i that minimize Err can be taken as the true values. We outline the algorithm for the minimization and discuss the error distribution in determining $(\varepsilon_l)_i$, θ_{ri}, ϕ_{ri0}, φ_{ri}, θ_{ii}, ϕ_{ii0}, φ_{ii}, and d_i.

For clarity of notation, we use x_l, $l = 1, 2, \ldots, k, k+1$ to represent the k variables of $(\varepsilon_l)_i$, θ_{ri}, ϕ_{ri0}, φ_{ri}, θ_{ii}, ϕ_{ii0}, φ_{ii}, d_i, and I_p, and define a vector $X^T=(x_1, x_2, \ldots, x_{k+1})$, where the superscript T denotes the transpose of the column vector X. When Err reaches its minimum,

$$\left(\partial Err/\partial x_l\right)_t = 0,\ l = 1, 2, \ldots, k+1,$$ (11)

where the subscript t means that x_l, i.e., $(\varepsilon_l)_i$, θ_{ri}, ϕ_{ri0}, φ_{ri}, θ_{ii}, ϕ_{ii0}, φ_{ii}, and d_i, assume the true values of the dielectric tensors and film thicknesses. Using matrix notation, Eq. (11) can be simply denoted as

$$\nabla Err = 2A^T H = 0 ,$$ (12)

where

$$H = (h_1, h_2, \ldots, h_m)^T ,$$ (13)

$$h_j = I_p h\left((\varepsilon_l)_i,\theta_{ri},\phi_{ri0}+\alpha_{Sj},\varphi_{ri},\theta_{ii},\phi_{ii0}+\alpha_{Sj},\varphi_{ii},d_t\right)-I_d(\alpha_{Sj}),\ j=1,2,\ldots,m,$$ (14)

$$A_{jl} = \left(\partial h_j/\partial x_l\right)_t / \sigma_j^2,\ j=1,2,\ldots,m;\ l=1,2,\ldots,k+1.$$ (15)

Near the minimum of Err, H can be linearized as $H = H_t + A\Delta X$, and substituting it into Eq. (12) obtains

$$\Delta X = -\left(A^T A\right)^{-1} A^T H_t = -MA^T H_t .$$ (16)

Eq. (16) gives an expression for changing X recursively to minimize Err. The standard deviation of x_l, $l=1, 2, \ldots, k, k+1$, determined with the above algorithm, is [8]

$$\sigma_{x_i}^2 = \mathbf{M}_{ii} . \tag{17}$$

Approach two:

Instead of setting a sample to different discrete angles, the sample can be rotated at a constant frequency ω. That is, $\alpha_S = \omega t$. In this case, Eq. (6) can be expressed as

$$I_d(\omega t) = I_p \sum_l (a_l \cos l\omega t + b_l \sin l\omega t), \tag{18}$$

where a_l and b_l are the Fourier coefficients.

If $m=2j+1$, $m \geq k+1$, Fourier coefficients a_0, a_1, b_1, ..., a_j, b_j, are measured, m equations of $(\varepsilon_l)_i$, θ_{ri}, ϕ_{ri0}, φ_{ri}, θ_{ii}, ϕ_{ii0}, φ_{ii}, and d_i can be established. They are

$$\frac{1}{t I_p} \int_0^t h\left((\varepsilon_l)_i, \theta_{ri}, \phi_{ri0} + \alpha, \varphi_{ri}, \theta_{ii}, \phi_{ii0} + \alpha, \varphi_{ii}, d_i\right) d\alpha = a_0, \tag{19}$$

....

$$\frac{2}{t I_p} \int_0^t h\left((\varepsilon_l)_i, \theta_{ri}, \phi_{ri0} + \alpha, \varphi_{ri}, \theta_{ii}, \phi_{ii0} + \alpha, \varphi_{ii}, d_i\right) \cos j\alpha d\alpha = a_j, \tag{20}$$

$$\frac{2}{t I_p} \int_0^t h\left((\varepsilon_l)_i, \theta_{ri}, \phi_{ri0} + \alpha, \varphi_{ri}, \theta_{ii}, \phi_{ii0} + \alpha, \varphi_{ii}, d_i\right) \sin j\alpha d\alpha = b_j, \tag{21}$$

where $t \leq 2\pi$ is the smallest period of function h.

To solve Eqs. (19) – (21), a test function

$$Err = \sum_{l=0}^{j} \left(\frac{2\int_0^t h \cos l\alpha d\alpha}{(1+\delta_{l0}) t I_p} - a_l\right)^2 \bigg/ \sigma_l^2 + \sum_{l=1}^{j} \left(\frac{2\int_0^t h \sin l\alpha d\alpha}{t I_p} - b_l\right)^2 \bigg/ \sigma_l^2 , \tag{22}$$

is introduced, where σ_l are the standard deviations for the Fourier coefficients.

The algorithm outlined in Approach one can be employed to solve Eqs. (19) – (21), if the intensities are replaced by the Fourier coefficients and the function h replaced by the Fourier integrals. Eq. (17) can also be used to estimate the error distributions of $(\varepsilon_l)_i$, θ_{ri}, ϕ_{ri0}, φ_{ri}, θ_{ii}, ϕ_{ii0}, φ_{ii}, and d_i.

If j is large, direct measurements of the Fourier coefficients may be inconvenient. In this situation, the intensity dependence on the sample's azimuth angle can be measured. With this relation, the Fourier coefficients can be obtained numerically. It should be noted that if $t<2\pi$, all α_S selected in Approach one should not be different by t. If $t=0$, i.e., I_d is constant, only a_0 is meaningful. In this case, this method fails.

III. MODELS CALCULATION

In this section, we prescribe the dielectric tensors and film thicknesses of some common structures and conduct forward calculation for the intensity dependence on sample's azimuth

angle. The purpose of the study is to show that different structures possess different relationships between intensity and sample's azimuth angle. Therefore, from a measured intensity dependence on sample's azimuth angle, a backward calculation can extract the dielectric tensors and film thicknesses by use of the two approaches described in the previous section.

In the study, we assume that the angle of incidence is $70°$, and the wavelength is 600nm. All materials are transparent for simplicity. A PSA setup is used and $\alpha_p = \alpha_A = 45°$. An isotropic material, two bulk anisotropic materials (uniaxial and biaxial) are studied. The isotropic and uniaxial materials are also used as the substrates of a superlattice structure, which is 20 periods of a two-layer structure on a substrate. They can be denoted as $ABAB...ABC$, where A and B are biaxial films, and C is substrate. The properties of these materials are listed in Table I. Relations between intensities and sample's azimuth are shown in Figure 1. Parts of the Fourier coefficients are listed in Tables II.

Figure 1 shows that the intensity relationships are different for different structures. Table II shows that except for isotropic materials, all other structures contain more non-zero Fourier coefficients than unknowns. Therefore, Eq. (22) can be used. For isotropic materials, Figure 1 shows that the intensity is a constant. As stated in the above section, this method fails in this case. One interesting observation is that in Figure 1, two superlattices show difference mainly near extremum positions. However, Table II shows that all Fourier coefficients have distinct difference. This fact implies that if Approach one is used, α_S has to be set near extremum positions so that the difference can be detected. However, Approach two does not have this limitation.

Table I. Refractive indices of different materials along their principal axes, Euler angles of the principal axes relative to the laboratory frame, thicknesses of the materials and number of parameters that can be determined.

	n_1	n_2	n_3	θ	ϕ_0	φ	d (nm)	k
Isotropic	1.8	1.8	1.8	any	any	any	∞	1
Uniaxial	1.8	1.8	2.0	20	60	any	∞	4
Biaxial	1.8	2.0	2.2	20	60	10	∞	6
Layer A	1.6	1.7	1.8	45	35	10	300	7
Layer B	1.5	1.6	1.7	30	20	30	600	7

Table II. Fourier coefficients a_l and b_l for the intensity $I_d(\omega t) = I_p \sum \left(a_l \cos l\omega t + b_l \sin l\omega t \right)$.

Lattice 1 (resp. 2) is a 40-layer periodic superlattice on an isotropic (resp. uniaxial) substrate.

|	a_0	a_1, b_1 (10^{-3})	a_2, b_2 (10^{-3})	a_3, b_3 (10^{-5})	a_4, b_4 (10^{-6})	a_5, b_5 (10^{-6})	a_6, b_6 (10^{-6})	a_7, b_7 (10^{-6})	a_8, b_8 (10^{-6})
Isotropic	.2665	0,0	0,0	0,0	0,0	0,0	0,0	0,0	0,0
Uniaxial	.2581	6.235 -10.80	2.045 3.542	3.500 0	-2.000 0	0,0	0,0	0,0	0,0
Biaxial	.2492	3.867 -4.329	17.89 16.44	9.900 -1.100	11.00 128.0	-1.000 -1.000	2.000 -2.000	0,0	0,0
Lattice 1	.2913	21.40 5.696	-22.87 16.50	914.0 4113	10290 5194	3050 10450	12930 -619.0	-35210 -29820	-16710 -5554
Lattice 2	.2936	23.38 12.77	-26.12 12.67	852.0 3941	11770 4137	3333 11640	10610 312	-34730 -29630	-17730 -4792
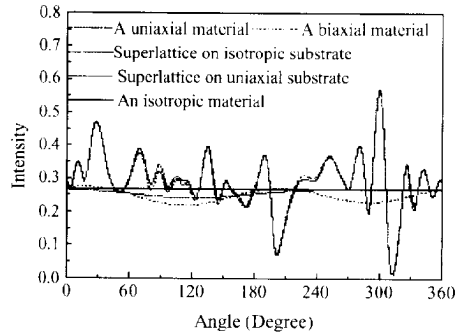
Figure 1. Intensity dependence on sample's azimuth angle for (1) an isotropic material, (2) a uniaxial material, (3) a biaxial material, (4) a 40-layer periodic superlattice on the isotropic substrate, and (5) a 40-layer periodic superlattice on the uniaxial substrate.

IV. SUMARY

In this paper, we present a theoretical development to optimize a generalized ellipsometer so that only the sample's azimuth angle needs to be changed in the determination of the dielectric tensors and film thicknesses of a arbitrarily anisotropic systems. Five models are calculated as examples.

ACKNOWLEDGEMENTS

REFERENCES

[1] D. W. Thompson, M. J. DeVries, T. E. Tiwald, and J. A. Woollam, *Thin Solid Films* **313-314**, 341 (1998).
[2] G. E. Jellison and L. A. Boatner, *Phys. Rev. B* **58**. 3586 (1998).
[3] R. W. Collins and J. Koh, *J. Opt. Soc. Am. A* **16**,1997 (1999).
[4] W. Xu, L. T. Wood, and T. D. Golding, *Thin Solid Films* (To be published).
[5] W. Xu, L. T. Wood, and T. D. Golding, *J.Opt. Soc. Am A* (Submitted for publication).
[6] W. Xu, L. T. Wood, and T. D. Golding, *Phys. Rev. B.* **61**, 1740 (2000).
[7] P. Yeh, *J. Opt. Soc. Am.* **69**, 742 (1979).
[8] P. R. Bevington, Data Reduction and Error Analysis for the Physical Sciences, Mc-Graw-Hill Book Company, New York. p. 242.

A 'Building Block' Approach To Mixed-Colloid Systems Through Electrostatic Self-Organization

Trent H. Galow, Andrew K. Boal and Vincent M. Rotello*
Department of Chemistry, University of Massachusetts, Amherst, Massachusetts 01003, USA.

ABSTRACT

We have developed a 'building block' approach to electrostatically-mediated construction of modular self-assembled colloid-colloid ensembles. Our strategy involves functionalization of one type of colloidal building block with a primary amine, and a counterpart building block with a carboxylic acid derivative (Scheme 1). By combining the two systems, acid-base chemistry followed by immediate charge-pairing resulted in the spontaneous formation of electrostatically-bound mixed-colloid constructs. The shape and size of these ensembles was controlled via variation of particle size for the two components and their stoichiometries.
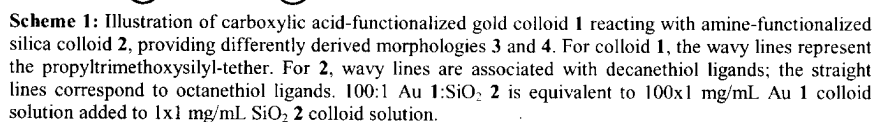
INTRODUCTION

Molecular self-assembly is the association of molecules into structurally well-defined, stable aggregates via thermodynamically-controlled non-covalent interactions. Application of self-organization to multi-scale ordering of colloidal nanoparticles provides a platform for the creation of macroscopic devices. The ability to finely control the spatial arrangement of nanoscopic entities in composite arrays allows for the creation of materials with interesting electronic [1], optical [2], optoelectronic [3], and magnetic properties [4].

For these applications to be realized, however, preparation of physically and chemically diverse nanocomposite materials is a major goal. Recent examples of these materials include biomolecule-colloid [5], colloid-colloid [6], polymer-colloid [7], dendrimer-colloid [8], and sol gel-colloid materials [9]. We report here a 'building block' approach to the construction of modular colloid-colloid ensembles through electrostatically-mediated self-organization.

EXPERIMENTAL DETAILS

Our methodology entailed functionalizing one type of colloidal building block with a primary amine, and a counterpart building block with a carboxylic acid derivative (Scheme 1). By combining the two systems, acid-base chemistry followed by immediate charge-pairing would result in the spontaneous formation of electrostatically-bound mixed-colloid constructs. These systems are easily discriminated both in size and properties, and can be synthesized in a straightforward manner.

Scheme 1: Illustration of carboxylic acid-functionalized gold colloid **1** reacting with amine-functionalized silica colloid **2**, providing differently derived morphologies **3** and **4**. For colloid **1**, the wavy lines represent the propyltrimethoxysilyl-tether. For **2**, wavy lines are associated with decanethiol ligands; the straight lines correspond to octanethiol ligands. 100:1 Au **1**:SiO$_2$ **2** is equivalent to 100x1 mg/mL Au **1** colloid solution added to 1x1 mg/mL SiO$_2$ **2** colloid solution.

Carboxylic acid-functionalized gold particles **1** were prepared by ligand exchange of commercially available 11-mercaptoundecanoic acid with octanethiol-functionalized gold colloids [10]. These were then dispersed in a THF/MeOH (3/1) medium to 0.5% w/v. Amine-derived colloids **2** were prepared by reacting 15 nm silica particles with 3-aminopropyltrimethoxysilane [11], and subsequently dispersed in a THF/MeOH (3/1) medium to 0.5% w/v. TEM analyses of **1** and **2** were performed to verify the structure of these colloidal systems. The resulting pictures show that the Au colloids **1** (Figure 1b) were about 2 nm in diameter, while the silica colloids **2** (Figure 1a) were 15 nm in diameter.
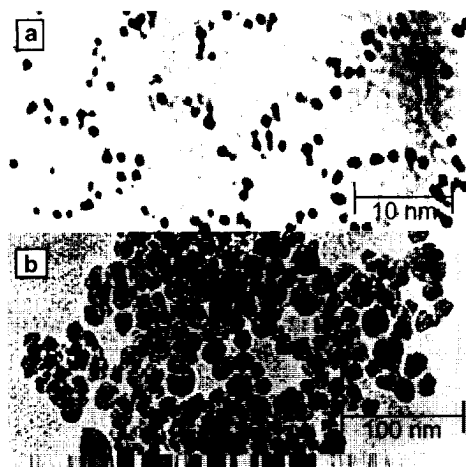
Figure 1: TEM micrographs of (a) Au **1** and (b) SiO₂ **2** colloid systems.

DISCUSSION

Initial studies focused on combining solutions **1** and **2** in a 1:1 ratio [12], where rapid aggregation of the gold colloid suspension was seen. The low magnification TEM (Figure 2a) shows the organized arrangement attained by this mixed-colloid system. The presence of giant 'fractal-like' superstructures ranging *ca.* 4-5 *micrometers* in size is clearly visible. Higher magnification TEM micrographs (Figure 2b) clearly shows that each silica particle is surrounded by a number of smaller Au nanoparticles. These Au colloids are themselves attached to additional silica colloids, affording giant mixed-colloid superstructures. Another interesting feature is the regular spacing of Au colloids on the surface of the silica particles, arising from the coulombic repulsions between charge-paired units. This observation is in line with other charged colloid systems where charged metallic nanoparticles are known to electrostatically repel each other and are typically well separated on substrate surfaces [13]. As a control study, we replaced **1** with an alkyl-functionalized derivative, removing any capacity to undergo acid-base chemistry. As expected no aggregation took place, indicating that the structural morphology observed in the **1.2** aggregates arises from electrostatic self-assembly.
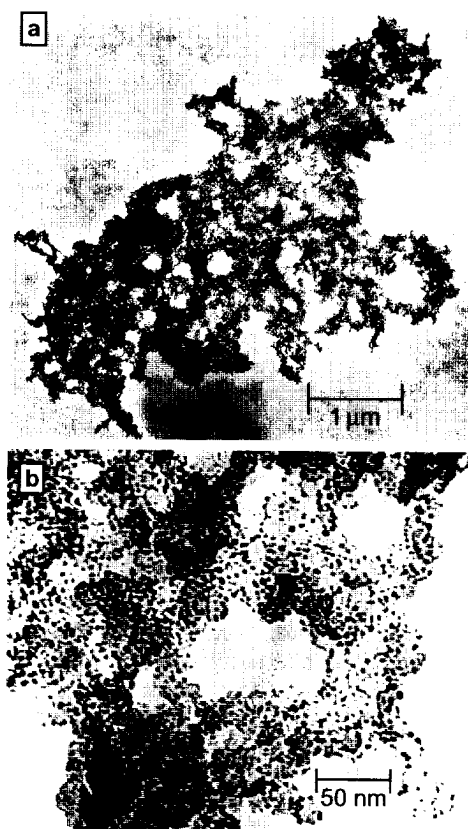
Figure 2: TEM micrographs of 1:1 Au 1:SiO$_2$ 2 system. Micrograph A is low magnification picture showing the giant fractal-like superstructure obtained. Micrograph B is high magnification image clearly showing the self-association present in 1:1 Au 1:SiO$_2$ 2 system. Au colloids appear dark, while silica nanoparticles appear light.

It has been demonstrated that controlling the Au density on silica colloid surfaces can lead to regulation of optical resonance [14]. We predicted we could manipulate the Au 1 colloid density and thus structural morphology of the mixed-colloid superstructure by increasing Au 1 equivalents. After combining solutions 1 and 2 at 20:1 and 100:1 respectively, and performing TEM studies, two distinct mixed-colloid morphologies were afforded. For the 20:1 system, the mixed-colloid assemblies obtained were 100-250 nm across, greatly reduced in size as compared to the giant superstructures attained for the 1:1 system. (Figure 3a). Also discernible was the increased density of Au colloids on the surface of the SiO$_2$ particles. As in the 1:1 system, the Au colloids were evenly spaced but the inter-gold colloid distance had decreased. For the 100:1 mixed-colloid system, the smallest colloidal clusters of all three systems were attained (Figure 3b). These constructs

consisted of only a small number of silica particles per cluster, ranging from 50-100 nm in size. Also visible is the complete surface coverage provided by the close packing of the Au colloids on the SiO_2 surface, with virtually no distance between the Au nanoparticles.
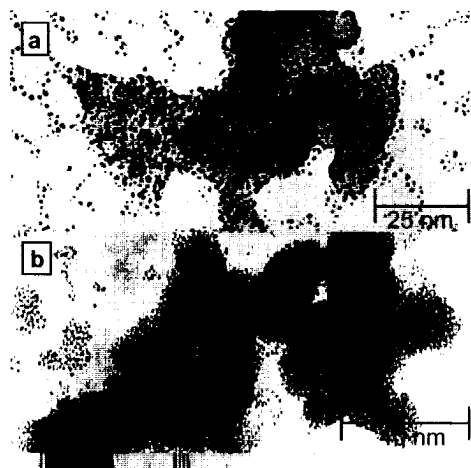

Figure 3: TEM micrographs of 20:1 and 100:1 Au 1:SiO$_2$ 2 mixed-colloid systems. Micrograph a corresponds to 20/1 system. Higher density of Au colloids. which remain evenly spaced, is seen. Micrograph b is associated with 100/1 system. and shows densely packed monolayer of Au 1 colloids electrostatically bound to the surface of 2.

CONCLUSION

In summary, a facile methodology for constructing diverse mixed-colloid ensembles was established. It was demonstrated that the mixed-colloid architecture was controlled by both electrostatic-self assembly and concentration changes, regardless of the nature of the core.

ACKNOWLEDGEMENTS

1.   A. K. Boal, V. M. Rotello *J. Am. Chem. Soc.* **121**, 4914 (1999). M. A. C. Templeton, D. E. Cliffel, R. W. Murray *J. Am. Chem. Soc.* **121**, 7081 (1999).

2. B. A. Korgel, D. Fitzmaurice *Adv. Mater.* **10** (9), 661 (1998). J. Schmitt, P. Machtle, D. Eck, H. Mohwald, C. A. Helm *Langmuir* **15**, 3256 (1999).

3. T. Cassagneau, J. H. Fendler, T. E. Mallouk *Langmuir*, ASAP Article.

4. T. Prozorov, R. Prozorov, A. Gedanken *Adv. Mater.* **10** (18), 1529 (1998). F. Caruso, A. S. Susha, M. Giersig, H. Möhwald *Adv. Mater.* **11** (11), 950 (1999).

5. C. J. Loweth, W. B. Caldwell, X. G. Peng, A. P. Alivisatos, P. G. Schultz *Angew. Chem. Int. Ed.* **38**, 1808 (1999). A. P. Alivisatos, K. P. Johnsson, X. G. Peng, T. E. Wilson, C. J. Loweth, M. P. Bruchez, P. G. Schultz *Nature*, 382, 607 (1996).

6. P. Jiang, J. Cizeron, J. F. Bertone, V. L. Colvin, *J. Am. Chem. Soc.* **121**, 7957 (1999).

7. D. L. Feldheim, K. C. Grabar, M. J. Natan, T. E. Mallouk *J. Am. Chem. Soc.* **118**, 7640 (1996). S. M. Marinakos, J. P. Novak, L. C. Brosseau III, A. B. House, E. M. Edeki, J. C. Feldhaus, D. L. Feldheim *J. Am. Chem. Soc.* **121**, 8518 (1999).

8. V. Chechik, R. M. Crooks *Langmuir* **121**, 6364 (1999). M. Zhao, L. Sun, R. M. Crooks *J. Am. Chem. Soc.* **120**, 4877 (1998).

9. S. Barathi, O. Lev *Chem. Commun.* 2303 (1997). T. Ung, L. M. Liz-Marzán, P. Mulvaney *Langmuir* **14**, 3740 (1998).

10. P. S. Russo, B. Fong *Langmuir*, **15**, 4421 (1999).

11. M. Brust, M. Walker, D. Bethell, D. J. Schiffrin, R. Whyman *Chem. Commun.* 801 (1994). R. S. Ingram, M. J. Hostetler, R. W. Murray *J. Am. Chem. Soc.* **119**, 9175 (1997).

12. A 1:1 Au **1**:SiO$_2$ **2** is equivalent to 1 mL 1 mg/mL Au **1** colloid solution added to 1 mL 1 mg/mL SiO$_2$ **2** colloid solution.

13. R. G. Freeman, K. C. Grabar, K. J. Allison, R. M. Bright, J. A. Davis, A. P. Guthrie, M. B. Hommer, M. A. Jackson, P. C. Smith, D. G. Walter, M. J. Natan *Science* **267**, 1629 (1995).

14. S. J. Oldenburg, R. D. Averitt, S. L. Westcott, N. J. Halas *Chem. Phys. Lett.* **288**, 243 (1998).

Convenient Molecular Approach of Size and Shape Controlled ZnSe and ZnTe Nanocrystals

Young-wook Jun, Jong-Il Park and Jinwoo Cheon*
Department of Chemistry and School of Molecular Science   BK21,
Korea Advanced Institute of Science and Technology (KAIST),
Taejon 305-701, Korea

ABSTRACT

Our study describes a convenient one-step synthesis of ZnSe and ZnTe nanocrystals (NC) whose sizes and shapes are precisely tuned by varing the growth temperature or stabilizing surfactants. We utilized molecular precursors, bis(phenylselenolate or phenyltellurolato)zinc -N,N,N',N'-tetramethylethylenediamine (TMEDA), which effectively produce 0-dimensional sphere or 1-dimensional nanorods of ZnSe or ZnTe, respectively. Nanocrystals are highly monodispersed and luminescent; the emission wavelength varies over a wide range depending on the particle size. This study constitutes a nice demonstration of direct size and shape controlled synthesis of semiconductor nanocrystals and this method can be extended to the synthesis of nanocrystals of other materials.

INTRODUCTION

Controlled synthesis of inorganic nanocrystals is one of the most important issues in nanocommunity because their size and shape act as important parameters for optical and electronic properties. Especially, 1-dimensional nanocrystals have drawn special attention because of novel properties due to their anisotropic crystal structure [1, 2].

Shape control of nanocrystals can be achieved in gas phase by several methods. One of the methods is template-assisted or strain-assisted synthesis in gas phase. For example, crystal growth inside a nanoporous solid, such as silica ball template, MCM-41, leads to the formation of nanorods, nanowires, and nanoballs [3, 4]. Pyramidal dots or nanowires can be obtained using strain-assisted epitaxial growth [5]. Lieber et al. reported that a solid rod can be obtained using vapor-liquid-solid growth [6] and Buhro et al. demonstrated solid rods also obtained by solution-liquid-solid growth [7].

The other means of controlling nanocrystals is colloidal synthesis using micelle templates. Mann et al. show that prismatic $BaCrO_4$ nanocrystals can be obtained by introducing Ba^{2-} and CrO^{4+} ion in AOT microemulsion using structured AOT micelles [8]. Nanorods were prepared by electrochemical reduction method [9], hydrazine reduction method [10], and simple ionic reactions [11]. Recently, a nonhydrolytic synthesis of CdSe nanorods in hot mixture of trioctylphosphine oxide and hexylphosphonic acid was reported [1].

In this paper, we demonstrate size and shape controlled ZnE (E=Se, Te) nanocrystals with quantum confinement effects. Shape of zinc chalcogenide nanocrystals is controllable either spherical or rod-like structure depending on the choice of stabilizing surfactants. Furthermore, the size of spherical nanocrystals is controlled by the growth temperature.

EXPERIMENTS

Trioctylphosphine (Aldrich) was used as received, while trioctylamine, and dimethylhexylamine were distilled before use. Trioctylphosphine oxide (TOPO) dodecylamine (Aldrich) were dried and degassed before use in the reaction vessel by heating ~200°C at ~1 Torr for ~2hr with argon gas bubbling. Zn(SePh)$_2$(TMEDA) [12] and (Zn(TePh)$_2$)(TMEDA) [13] were prepared following a literature method.

Low resolution transmission electron microscope image, energy dispersive X-ray analysis (EDAX), and selected area electron diffraction (SAED) were performed on an EM 912 Omega electron microscope operating at 120 kV. High resolution transmission electron microscope (HRTEM) images were obtained on a Hitachi H9000-NAR high resolution TEM operating at 300 kV. The UV-Vis absorption spectra of ZnTe anocrystals were obtained with a Shimadzu UV-3100S spectrophotometer and photoluminescence spectra were obtained with a Perkin-Elmer LS50 Luminescence spectrometer. X-ray powder diffraction patterns were measured on a Rigaku Miniflex instrument (0.5 kW) operating with a Cu K$_\alpha$(λ=0.1541 nm) X-ray source.

ZnSe Nanocrystals. Zn(SePh)$_2$(TMEDA) (0.5 g, 0.101 mmole) was dissolved in trioctylphosphine (10 ml) and the resulting solution was injected into hot trioctylphosphine oxide (3.92 g, 10.1 mmol). The latter solution was kept at one of four different temperatures: 320, 340, 367, or 385 °C. After 1 hr, the resulting yellow solution was cooled to 80 °C and treated with an excess of methanol to generate a yellow flocculate, which was separated by centrifugation and washed with methanol. The resulting pale yellow powder was readily redispersed in toluene.

ZnTe Nanocrystals. Zn(TePh)$_2$(TMEDA) (0.50 g, 0.88 mmol) was dissolved in 5ml of trioctylphosphine and the resulting solution was injected into hot trioctylamine (8.17 g, 44.1 mmol) solvent. The reaction mixture was kept at two different temperatures: 180 or 240 °C. After 2 hr, the resulting yellow solution was cooled to 40 °C and treated with an excess of anhydrous butanol to generate a yellow flocculate, which was separated by centrifugation and washed with buthanol. The resulting a pale yellow powder was dispersed in organic solvents such as toluene.

ZnTe Nanorods. Zn(TePh)$_2$(TMEDA) (0.50 g, 0.88 mmol) was dissolved in 5ml of pyridine and the resulting solution was injected into hot mixture of trioctylamine (20 ml) and dimethylhexylamine (5 ml). The reaction mixture was kept at 180 °C. After 2 hr, the resulting yellow solution was treated with an excess of anhydrous butanol to generate a gray flocculate, which was separated by centrifugation and washed with butanol. The resulting nanocrystals are obtained as a gray powder.

RESULTS AND DISCUSSION

Zinc chalcogenide nanocrystals were obtained by the thermolysis of $[Zn(EPh)_2][TMEDA]$. According to thermal gravimetric analysis (TGA), it is observed that the thermolysis of $[Zn(EPh)_2][TMEDA]$ begins with the dissociation of the TMEDA donor ligand and then ZnE and Ph_2E are produced in the following thermolysis step at higher temperatures.

Obtained spherical ZnSe nanocrystals are highly monodispersed with sizes that depend on the growth temperature. Relative to the position of the 480 nm (2.58 eV) absorption band edge for bulk ZnSe, the absorption band edges of the ZnSe QDs are blue-shifted. The absorption band shifts are 1.07, 0.49, 0.41 and 0.29 eV for QDs grown at 385, 367, 340 and 320 °C, respectively. The band maxima in photoluminescent spectra are 387 nm (3.20 eV), 429 nm (2.89 eV), 443 (2.80 eV) and 451 nm (2.75 eV) for samples grown at 380, 367, 340 and 320 °C, respectively (Fig. 1A). In case of spherical ZnTe nanocrystals, similar behaviors were observed. Relative to the position of the 548 nm (2.26 eV) absorption band edge of bulk ZnTe, blue shifts are 0.53 and 1.31 eV for the nanocrystals grown at 180 and 240 °C, respectively. The band maxima in photoluminescent spetra are 451 and 377 nm for samples grown at 180 and 240 °C (Figure 2A). Larger shifts are seen for samples grown at higher growth temperature in both cases. These results suggest that smaller nanocrystals are produced at higher growth temperatures where more nucleation sites exist and relatively less available zinc chalcogenide precursor molecules are present for each nucleus during the growth process.
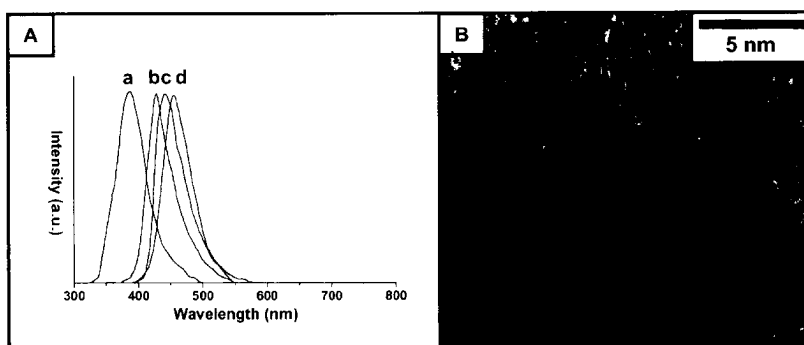

Figure 1. *Spherical ZnSe nanocrystals (A) PL spectra ZnSe NCs grown at (a) 385, (b) 367, (c) 340, and (d) 320 °C. (B) HRTEM image of 4.9 nm ZnSe NCs*
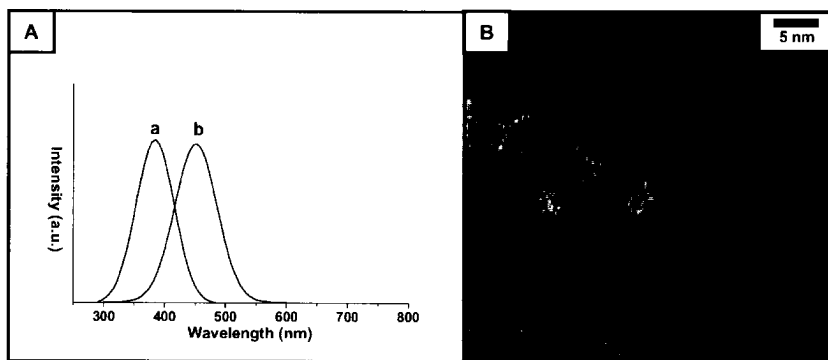
Figure 2. *Spherical ZnTe nanocrystals (A) PL spectra ZnTe NCs grown at (a) 240 and (b) 180 °C, (B) HRTEM image of 4.2 nm ZnTe NCs*

High resolution transmission electron micrographs show that the zinc chalcogenide nanocrystals are roughly spherical and that the particles within a single sample have relatively uniform sizes. The average sizes of the ZnSe QDs are 2.7 ($\pm$ 0.2) nm, 4.0 ($\pm$ 0.35) nm, 4.4 ($\pm$ 0.35) and 4.9 ($\pm$ 0.29) nm for samples grown at 385, 367, 340, 320 °C (Figure 1A) and ZnTe nanocrystals have average sizes of 4.2 ($\pm$ 1.1) and 5.4 ($\pm$ 0.9) nm for samples grown at 240 and 180 °C, respectively (Figure 2B). Powder X-ray diffractometry (XRD) and selected area diffractometry (SAED) reveal patterns corresponding to (111), (220) and (311) of the cubic phase of ZnTe nanocrystals.

With the same conditions and procedures, the injection of the precursor [Zn(TePh)$_2$][TMEDA] into the mixed surfactant solvents of trioctylamine (20 ml) and dimethylhexylamine (5 ml) leads to the shape change of the nanocrystals from spherical to rod-like shape and after 2 hr gray precipitates of ZnTe nanocrystals are obtained from initially pale yellow solution at 180 °C. It is believed that the combination of two different surfactants provides rod micelles during one-dimensional crystal growth process.

TEM image of rod-like ZnTe nanocrystals show that the nanocrystals have relatively larger size than spherical nanocrystals (Figure 3A). The diameters of the rod-like nanocrystals are uniform with ~25 nm and the lengths are several hundred nanometers (200 ~ 700 nm) with aspect ratio from 8 to 30. Figure 3B, C show SAED patterns of single ZnTe nanorod. Our rod-like ZnTe nanocrystals have well defined single crystallinity with cubic phase according to the electron diffraction study. The intensity of diffraction patterns varies depending on the crystallographic directions; the intensity of electron diffraction spots is increasingly stronger from 002 to 220 plane, which indicates that the ZnTe crystals are formed in unidirectional crystal growth pattern of ZnTe 110 face.
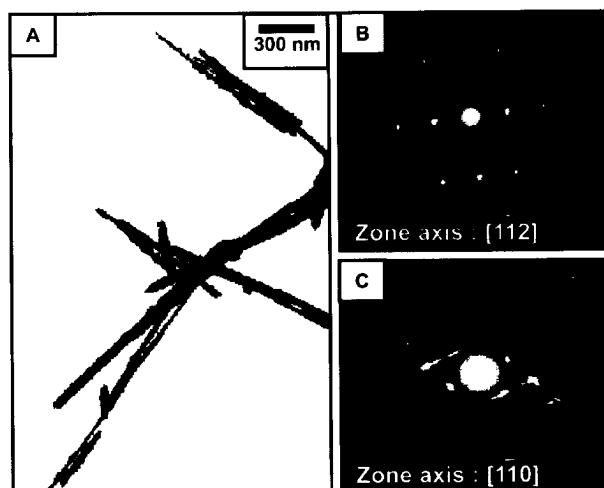
Figure 3. ZnTe nanorods (A) HRTEM image. (B) and (C) SAED pattern with zone axis

CONCLUSION

The results in this paper constitute a simple and convenient one-pot synthesis of size and shape controlled zinc chalcogenide nanocrystals using a monomeric molecular precursor, [Zn(EPh)$_2$][TMEDA]. By varying the growth temperature or the choice of the templating surfactants, the size and shape of the nanocrystals are controllable and quantum size effects are observed.

ACKNOWLEGMENTS

REFERENCES

1. X. G. Peng, L. Manna, W. D. Yang, J. Wickham, E. Scher, A. Kadavanich and A. P. Alivisatos, *Nature,* **404**, 59 (2000).
2. S. J. Park, S. Kim, S. Lee, Z. G. Khim, K. Char and T. Hyeon, *J. Am. Chem. Soc.*, **122**, 8581 (2000).
3. Z. Liu, Y. Sakamoto, T. Ohsuna, K. Hiraga, O. Terasaki, C. H. Ko, H. J. Shin and R. Ryoo, *Angew. Chem. Int. Ed.* **39**,3107 (2000).
4. H. K. Kang, Y. -W. Jun, J. -I. Park, K. -B. Lee and J. Cheon, *Chem. Mater.*, in press.
5. R. Leon, P. M. Petroff, D. Leonard and S. Fafard, *Science*, **267**, 1966 (1995).
6. J. Hu, T. W. Odom and C. M. Lieber, *Acc. Chem. Res.*, **32**, 435 (1999).
7. T. J. Trentler, K. M. Hickmann, S. C. Goel, A. M. Viano, P. C. Gibbons and W. E. Buhro, *Science,* **270,** 1791 (1995).
8. M. Li, H. Schnablegger and S. Mann, *Nature,* **402**, 393 (1999).
9. Y. -Y. Yu, S. -S. Chang, C. -L. Lee and C. R. C. Wang, *J. Phys. Chem. B,* **101**, 6661 (1997).
10. I. Lisiecki, F. Billoudet and M. P. Pileni, *J. Phys. Chem.*, **100**, 4160 (1996).
11. C. -C. Chen, C. -Y. Chao and Z. -H. Lang, *Chem. Mater.* **12**, 1516 (2000).
12. Y. -W. Jun, J, -E. Koo and J. Cheon, *Chem. Commun*, 1243 (2000).
13. Y. -W. Jun, C, -S. Choi and J. Cheon, *Chem. Commun*, in press.

Nanowires and Nanotubes

4-Point Resistance Measurements of Individual Bi Nanowires

Stephen B. Cronin[a], Yu-Ming Lin[b], Pratibha L. Gai[f], Oded Rabin[c], Marcie R. Black[b], Gene Dresselhaus[d], and Mildred S. Dresselhaus[e]
[a]Department of Physics, [b]Department of Electrical Engineering and Computer Science, [c]Department of Chemistry, [d]Francis Bitter Magnet Laboratory, and [e]on leave from the Massachusetts Institute of Technology, Cambridge, MA 02139
[f]DuPont Central Research and Development, Wilmington, DE 19880

ABSTRACT

We have synthesized single crystal bismuth nanowires by pressure injecting molten Bi into anodic alumina templates. By varying the template fabrication conditions, nanowires with diameters ranging from 10 to 200nm and lengths of ~50μm can be produced. We present a scheme for measuring the resistance of a single Bi nanowire using a 4-point measurement technique. The nanowires are found to have a 7nm thick oxide layer which causes very high contact resistance when electrodes are patterned on top of the nanowires. The oxide is found to be resilient to acid etching, but can be successfully reduced in high temperature hydrogen and ammonia environments. The reformation time of the oxide in air is found to be less than 1 minute. Focused ion beam milling is attempted as an alternate solution to oxide removal.

INTRODUCTION

The motivation for studying Bi nanowires is based on the unique properties of bulk Bi. First, Bi has very small effective masses, with mass components as small as $0.001m_e$ [1]. The small effective masses of Bi cause the effects of quantum confinement to be more pronounced since the energy of a quantized bound state is inversely proportional to the effective mass. Therefore, the effects of quantum confinement can be observed for nanowires of relatively large wire diameter. Second, bulk Bi has a very long mean free path, ~0.4mm at 4K and ~100nm at 300K [2]. Since the diameters of the nanowires are much smaller than the mean free path of the electrons, we expect the wires to exhibit 1D ballistic transport. Third, the low melting point of Bi (271°C) allows us to prepare the wires by pressure injection of molten Bi into a porous alumina template. It will be shown that this fabrication method yields extremely high quality crystalline nanowires. Finally, calculations of the transport properties predict that the Bi nanowires should have a very high thermoelectric efficiency [3].

As mentioned above, the effects of quantum confinement are pronounced in Bi because of its small effective masses. The change in band structure due to quantum confinement is shown schematically in figure 1. The dashed curves depict the band structure of bulk Bi, in which the T-point valence band overlaps with the L-point conduction band by 38meV [4], making bulk Bi a semimetal. Due to quantum confinement effects, the band edges split into subbands as shown by the solid curves. As the diameter decreases, the separation of the subbands gets larger, and eventually the lowest conduction subband and the highest valence

subband no longer overlap and the material becomes an indirect-gap semiconductor. This is referred to as the semimetal-to-semiconductor transition.

Detailed calculations of the energies of the subbands as a function of wire diameter have been carried out by solving Schrödinger's equation numerically for Bi nanowires with a circular cross section [3]. The semimetal-to-semiconductor transition was found to occur at a critical diameter of ~50nm. For most other materials. where $m^*\sim m_e$, the effects of quantum confinement in a 50nm diameter wire would be negligible. However, because of the extremely small effective masses in Bi, the quantum effects are so pronounced that we expect to observe dramatic changes in the electronic properties of the nanowires due to this semimetal-to-semiconductor transition at relatively large wire diameters.
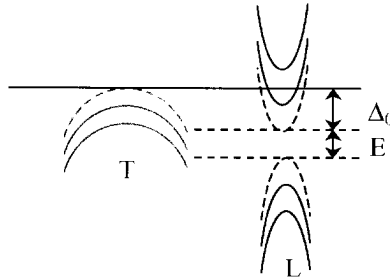

Figure 1. *The quantized band structure of a Bi nanowire depicted schematically.*

The Bi nanowires used in this study were prepared by a pressure injection method, whereby molten Bi is injected into a porous alumina template at a high pressure. Details of this fabrication process are published elsewhere [5]. We then dissolve the alumina template in a solution of 45 g/l CrO_3 and 5 vol. % H_3PO_4, leaving a solution of free standing wires.

Initial attempts were made to pattern 4-point electrodes on top of a single Bi nanowire using electron-beam lithography [6,7]. However, due to the very high contact resistances observed, reliable data could not be attained below room temperature. An oxide layer was suspected to be the cause of the high contact resistance observed.

Figure 2 shows a high resolution transmission electron microscope (HRTEM) image of a single Bi nanowire. As expected, we found a very thick amorphous oxide layer surrounding the crystalline Bi nanowire. For the wire in figure 2, the initial diameter was 40nm. However, after oxidation, the crystalline Bi part of the nanowire is reduced to 25nm and is surrounded by a 7nm thick oxide layer. The lattice fringes in this image indicate that the Bi nanowire has excellent single crystallinity.

The thick oxide observed in the HRTEM imaging explains the high contact resistance previously observed in the electrical measurements. Efforts were made to remove the oxide and pattern 4-point electrodes on a single Bi nanowire with low contact resistance.
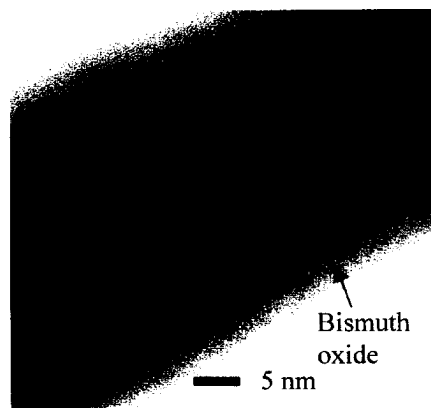
Figure 2. High resolution transmission electron microscope (HRTEM) image of a 40nm diameter Bi nanowire.

OXIDE REMOVAL: Acid Etch

As a first attempt, we tried to remove the oxide layer from the nanowire using a dilute acid. Samples were prepared for the HRTEM by putting a drop of solution containing free standing wires on a TEM grid. The grid with nanowires was then dipped in HCl diluted 10:1 in water for 3 seconds expecting the acid to dissolve the oxide and leave the Bi intact. However, we found that the acid dissolved the Bi, while leaving the oxide shell intact, the opposite of our intention. Figure 3 shows the HRTEM image of the resulting bismuth-oxide nanotube after this process. Several other acids were tried, such as HF. H_2SO_4 and H_3PO_4, but all yielded similar results. Despite the fact that this is an interesting result, it is not the desired result for achieving good contacts for the 4-point resistance measurement.

OXIDE REMOVAL: Hydrogen Annealing

As a second attempt to remove the oxide from the Bi nanowires we used an environmental-HRTEM (environmental-high resolution transmission electron microscope) in the DuPont Research and Development Center developed by Dr. Pratibha Gai, to study chemical reactions between gas molecules and solids directly on the atomic scale [8,9]. This Environmental-HRTEM system allows one to flow hydrogen gas through the sample chamber at elevated temperatures, while imaging the reaction on an atomic scale. We found that after flowing hydrogen through the sample space at 130°C for 6 hours, we were able to completely reduce the oxide. Figure 4 shows the HRTEM images before and after the hydrogen annealing. The top part of figure 4 a shows crystalline bismuth, below which appears the amorphous oxide layer, as indicated next to the figure. After hydrogen annealing, shown in figure 4 b, the oxide has been successfully removed and there is a clean crystalline interface at the surface of the nanowire.
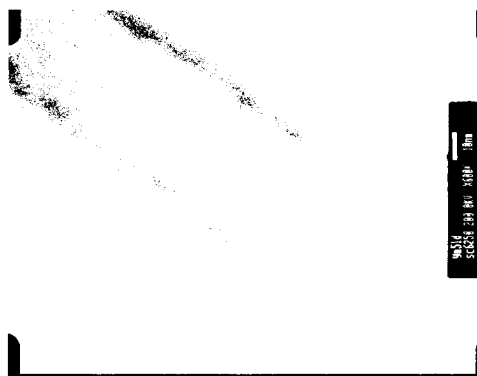
Figure 3. *High resolution transmission electron microscope (HRTEM) image of an empty bismuth-oxide shell, remaining after the HCl acid dip.*

The same result was also achieved when we repeated the experiment with ammonia gas instead of hydrogen gas.

Although we have successfully removed the oxide from the Bi nanowires, the oxide was found to reform in air in less than one minute. Therefore, in order for this technique to be applied to the 4-point resistance measurement it must be done *in situ*, together with the metal deposition of the 4-point electrode pattern. That is, the 6 hour hydrogen (or ammonia) anneal must be done right before the deposition of metal electrodes, while maintaining a high vacuum to prevent the oxide from reforming on the nanowire. Because of the dangers associated with hydrogen (and ammonia), this *in situ* oxide reduction was not performed.
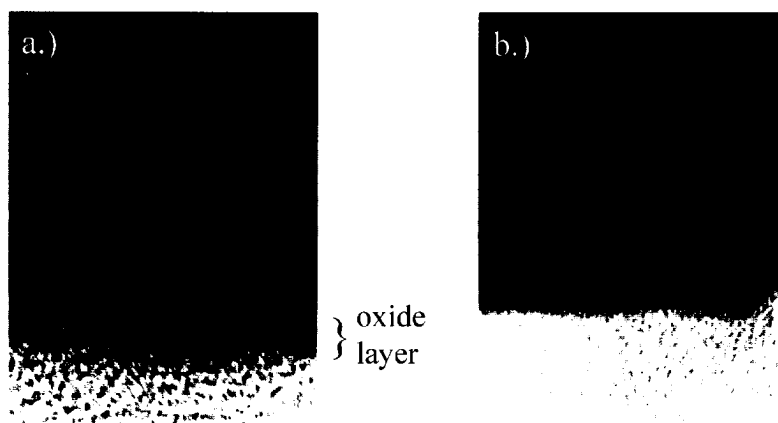

Figure 4. *High resolution transmission electron microscope (HRTEM) image of a Bi nanowire a.) before and b.) after annealing in hydrogen gas at 130°C for 6 hours.*

OXIDE REMOVAL: Focused Ion Beam (FIB) Milling

As a third attempt to remove the oxide from the Bi nanowire, focused ion beam (FIB) milling was employed as a strategy to first mill away the oxide layer and then deposit platinum electrodes on the nanowire. This work was done at Harvard University in collaboration with Dr. Thomas Rueckes and Prof. Charles Lieber. The strategy is depicted schematically on the right side of figure 5. On the left side of figure 5 the scanning electron microscope (SEM) image shows a 40nm diameter Bi nanowire with four platinum electrodes as deposited by a focused ion beam. First the nanowire was milled with a gallium ion beam in the selected areas of the 4-point electrode pattern. Then platinum was deposited to form the 4-point electrode pattern.

Since bismuth is known to be a very soft material and the bismuth-oxide is expected to be very hard, the amount a gallium ion milling is critical. If the ion beam mills beyond the surface oxide, the inner bismuth core will start to mill extremely fast, potentially depleting the entire wire. However, if the wire is insufficiently milled, the oxide will not be depleted enough to reduce the contact resistance. The contact resistance of the sample shown in figure 5 was on the order of 1MΩ, indicating that there was insufficient milling of the oxide to significantly reduce the contact resistance. In the future, a more systematic study of the different milling dosages will be carried out.
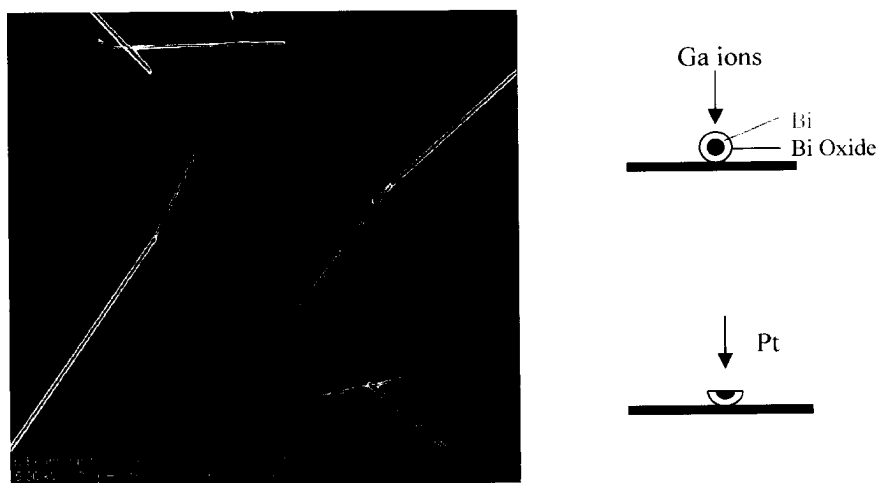

Figure 5. *Right: schematic diagram depicting the two step process of gallium ion milling and platinum deposition. Left: scanning electron microscope (SEM) image of a 40 nm Bi nanowire with 4-point Pt electrodes, prepared by first ion milling selectively the areas underneath the four electrodes.*

CONCLUSION

We have prepared single crystal Bi nanowires in the diameter range 10 to 200nm. HRTEM (high resolution transmission electron microscopy) imaging shows that a 7nm thick oxide is formed on the Bi nanowires that causes very high contact resistance when electrodes are patterned on the nanowires. Further HRTEM studies show that acids dissolve the crystalline bismuth faster than the oxide, leaving an oxide nanotube. High temperature hydrogen and ammonia environments were found to reduce the oxide after a sufficient amount of time. However, this method must be used *in situ* with the deposition of metal because of the extremely rapid formation of the oxide in air. The focused ion beam is a promising technique for removing the oxide, however the critical milling dosage must be precisely calibrated to ensure complete sputtering of the oxide without damaging the nanowire.

ACKNOWLEDGEMENTS

REFERENCES

1. R.T. Isaacson and G.A. Williams, Phys. Rev. **185**, 682 (1969).
2. R. Hartman, Phys. Rev. **181**, 1070 (1969).
3. Y.-M. Lin, X. Sun, M.S. Dresselhaus, Phys. Rev. B, **62**, 4610 (2000).
4. C.F. Gallo, B.S. Chandrasekhar, and P.H. Sutter, J. Appl. Phys. **34**, 144 (1963).
5. Z.Zhang, D. Gekhtman, M.S. Dresselhaus, and J.Y. Ying, Chem. Mater. **11**, 1659 (1999).
6. S.B. Cronin, S. B. Cronin, Y.-M. Lin, T. Koga, J. Y. Ying, and M. S. Dresselhaus, "Transport Measurements of Individual Bismuth Nanowires", in *Molecular Electronics: MRS Symposium,* edited by S.T. Pantelides, *et. al.,* Materials Research Society Press, Pittsburgh, PA, December, 1999.
7. S. Cronin, Y.-M. Lin, T. Koga, X. Sun, J. Y. Ying, and M. S. Dresselhaus, "Thermoelectric Investigation of Bismuth Nanowires", in *The 18th International Conference on Thermoelectrics: Symposium Proceedings,* Baltimore, MD, 1999.
8. P.L. Gai: Direct Probing of Gas Molecules-Solid Catalyst Interactions On the Atomic Scale; *Adv. Materials.,* **10**, 1259 (1998).
9. P.L. Gai: Environmental-HREM of Gas-Catalyst Reactions, *Topics in Catalysis,* **8**, 97 (1999).

Direct Synthesis of Silicon Nanowires, Silica Nanospheres, Wire-Like Nanosphere Agglomerates, and Silica-Based Nanotubes and Nanofiber Arrays

J. L. Gole,[1] J. D. Stout,[1] Z. R. Dai,[2] and Z. L. Wang[2]

Schools of Physics,[1] and Material Science[2]

Georgia Institute of Technology, Atlanta, Georgia 30332-0430

(ph294jg@prism.gatech.edu, 404-894-4029)

For several decades, the vapor-liquid-solid (VLS) process,[1,2] where gold particles act as a mediating solvent on a silicon substrate, forming a molten alloy, has been applied to the generation of silicon whiskers. The diameter of the whisker is established by the diameter of the liquid alloy droplet at its tip. The VLS reaction generally leads to the growth of silicon whiskers epitaxially in the <111> direction on single crystal silicon <111> substrates.[1-3] Recently, Lieber,[4] Lee,[5] Yu,[6] and coworkers have extrapolated on the ideas entailed in the VLS technique to develop laser ablation of metal containing silicon targets, obtaining bulk quantities of silicon nanowires. More recently, Lee et al.[5,7] have shown that oxides play a dominant role in the nucleation and growth of semiconductor nanowires be it by laser ablation, thermal evaporation, or chemical vapor deposition. Lee et al.[5] have suggested a new growth mechanism, referred to as oxide assisted nanowire growth, which represents a new approach to nanowire synthesis. Our initial approach[8-10] to this problem has involved the application of the techniques of high temperature synthesis to modify the approach of Lee et al. and generate virtually defect free SiO_2 sheathed crystalline silicon nanowires and silica (SiO_2) nanospheres which can be agglomerated to wire-like configurations impregnated with crystalline silicon nanoclusters. Further controlled condensation can extend this agglomeration to produce nanotubes and nanofiber arrays.

Figures 1 correspond to Transmission Electron Micrographs of exemplary virtually uniform and straight nanowires which we have generated from a 50/50 Si/SiO_2 equimolar mixture heated to a temperature of 1400°C at a total pressure of 225 Torr for 12 hours. The central crystalline silicon core is ι 30 nm in diameter whereas the outer SiO_2 sheathing is ι 15 nm in thickness. The HRTEM views in Figures 1(b) and (c) demonstrate a number of distinguishing characteristics. Figure 1(c) demonstrates that the axes of the SiO_2 clad crystalline silicon nanowires are parallel to <111>. This is distinct from the results obtained by Lee et al.[5]
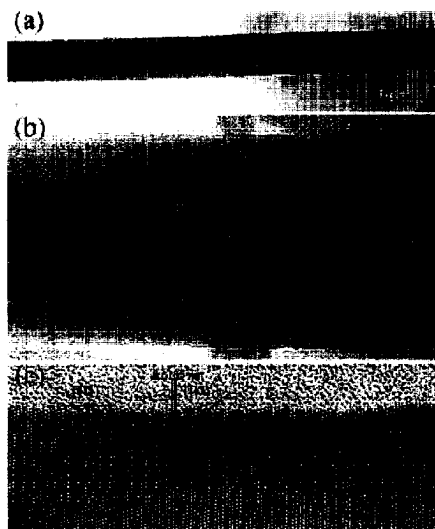
Fig 1

TEM of (a) SiO2 sheathed crystalline nanowire, (b) closer view showing(1) slight undulations and stress patterns which are apparent in a virtually defect free nanowire, and (c) closer view showing crystalline core axes parallel to <111> direction. Synthesized @ 1400C from 50/50 Si/SiO2 mix (Ptotal−225 Torr, flow rate 100 sccm of UHP argon).
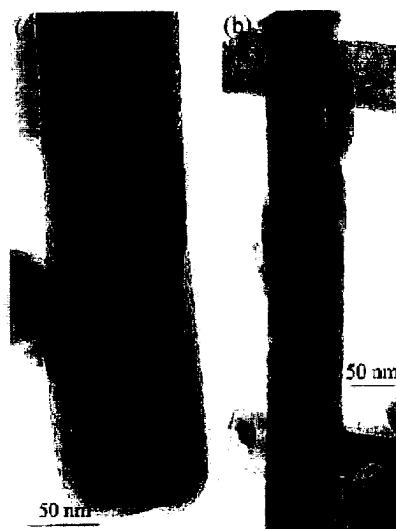
Fig 2

TEM closeup view of (a) end of SiO2 sheathed crystalline silicon nanowire showing pinch off of inner crystalline core at the end of the formation process and (b) opposite end of SiO2 sheathed crystalline silicon wire showing strength of SiO2 sheath. Conditions as in Fig 1.

whose wires have their axes parallel to <112> as they display twinning, high order grain boundaries, and stacking faults. At the Si-SiO$_2$ interface, (Fig. 1(c)), the crystal planes are best described as {211}. The wire which is depicted in Figures 1 appears virtually defect free. As figure 1(b) suggests, the inner crystalline silicon core undulates slightly. However, the fluctuations in the shading that are apparent in the HRTEM micrograph indicate that the wires are of sufficient quality that the detailed strain due to slight bending above the TEM mount can be readily observed in the micrograph.

Figures 2(a) and 2(b) demonstrate further distinguishing characteristics of the nanowires which we have generated. Figure 2(a) demonstrates the pinch off of the crystalline silicon core at the beginning of the wire growth, suggesting a distinctly different formation mechanism than that suggested by Lee et al.[5] for their wires generated using a similar source and by Morales and Lieber[2] for their iron catalyzed wire formation from Fe/Si mixtures generated using laser ablation. While Lee et al.[5] find evidence for a growth mechanism along <112> with which they associate a complex process involving Si$_x$O formation, the observed structure in Figure 2(a) would suggest at least a close analogy to the VLS mechanism, albeit with an apparent self assembly of the silicon in the absence of a metal catalyst. Further, the data in Figure 2(b), which shows the opposite end of the same nanowire suggests a significant strength for the outer SiO$_2$ sheath. Finally, a comparison to the TEM micrographs of Lieber et al.,[4] which show the clear termination of their nanowires at larger - nearly spherical FeSi$_2$ nanoclusters, offers yet an additional contrast, suggesting that there are a number of potential approaches to nanowire synthesis.

Figure 3 corresponds to an exemplary TEM micrograph of dispersed silica (SiO$_2$) nanospheres of diameter ι 30 nm which can be generated in gram quantities (Figure 4) on a cold plate placed in the gas flow field of our high temperature synthesis source. As a function of slightly modified experimental conditions,[11] these nanospheres have a nearly monodisperse particle size distribution and vary in size from ι 45 to 8 nm in diameter. Transmission Electron Microscopy, TEM,[8] X-ray diffraction,[8] and ESR[12] measurements now demonstrate that the nanospheres are amorphous and absent of dangling bonds. They have been used to sequester active copper sites for the selective conversion of ethanol to acetaldehyde[13] in a process that is at least three times more effective than that using fumed silica produced from the flame hydrolysis of silicon tetrachloride.[14] Further, it has been possible to reduce a Ni(III) solution in an
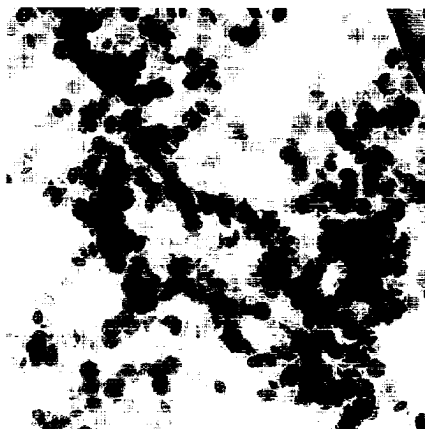
Fig 3
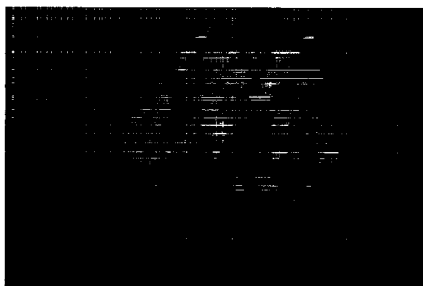TEM of virtually "monodisperse" SiO2 nanospheres 30nm in diameter.
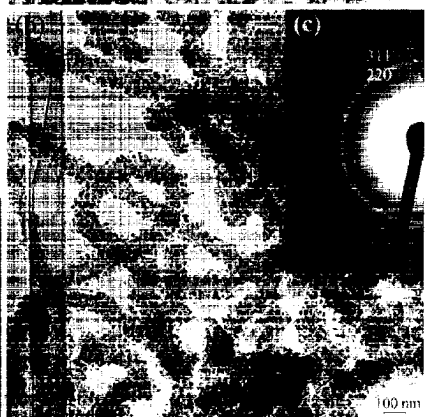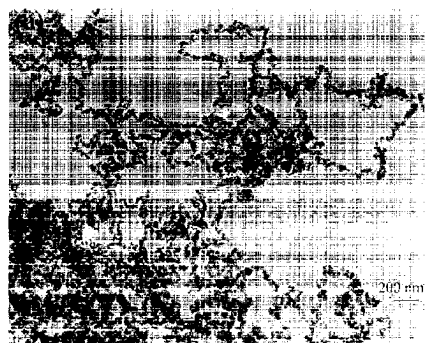

Fig 4

Fig 5
TEM micrographs of (a) SiO2 nanospheres agglomerating into wire-like groupings and (b) closer view showing crystalline silicon nanoclusters (see diffraction pattern insert) impregnating the SiO2 wire-like agglomeration.

electroless process on the surface of the nanospheres, producing a ferromagnetic crystalline nickel coating[12] of variable thickness.

With additional adjustments of flow rates and temperature gradients, it is possible to agglomerate the nanospheres into the wire-like configurations depicted in Figure 5 (a) which, on closer view, correspond to wire-like SiO_2 nanosphere agglomerates impregnated by crystalline silicon nanoclusters (Figure 5 (b) and inset). This agglomeration can be extended in a controlled manner to produce the variety of silica nanotubes and nanofiber arrays depicted in Figures 6
and 7.

The initiation of nanotube growth appears to involve seeding by crystalline silicon particles along the growth direction. Figure 6(a) depicts the growth of the silica nanotubes between crystalline silicon particles which may also impregnate the tubes. The image displayed in Figure 6(b) suggests that a silicon particle is located at the area that links aligned nanofiber arrays, similar to those also depicted in Figure 7, and a silica nanotube. The outer diameter of the tubes is
ι 70-80 nm, and the wall thickness is ι 20 nm. Thus, with their 30 nm inner-tube diameter, they would appear to be ideally suited for catalysis of high molecular weight hydrocarbons. It appears that the crystalline silicon particle blocks and hence terminates the growth of the silica nanofibers located inside the bundle, while the outermost fibers continuously grow in an oxidation process forming a continuous shell, which constitutes the nanotube. This process is also suggested by the structure shown in Figure 6(c), where the formation of a crystalline silicon particle at the end of a silica fiber agglomeration again appears to play a key role in the formation of the nanotube. In Figure 6(d) we demonstrate that the silica tubular structure can also display a "necklace-like" internal chain structure. This chain-like structure represents an intermediate between densely packed and aligned nanofibers and the continuous nanotube.

Figure 7 demonstrates an intriguing coalescence of silica nanowires to form a variety of unique three-dimensional structures. Shown in Figures 7(a-d) are typical cage structures composed of aligned silica nanofibers. The nanofibers grow into bundles, while paralleling a structure that has near cylindrical symmetry.[9] The width of the cage is 0.3 - 1 μm much larger than the diameter of the silica nanofibers (ex. ι 20 nm). These arrays clearly demonstrate a significant versatility to those silica nanostructures which can be synthesized. In fact, Figure
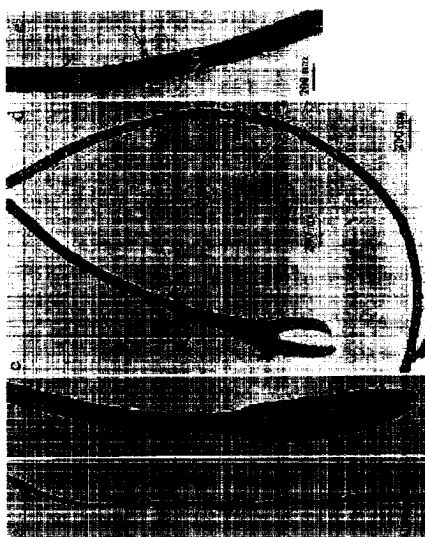
Fig 6
TEM images of synthesized silica nanotube structures
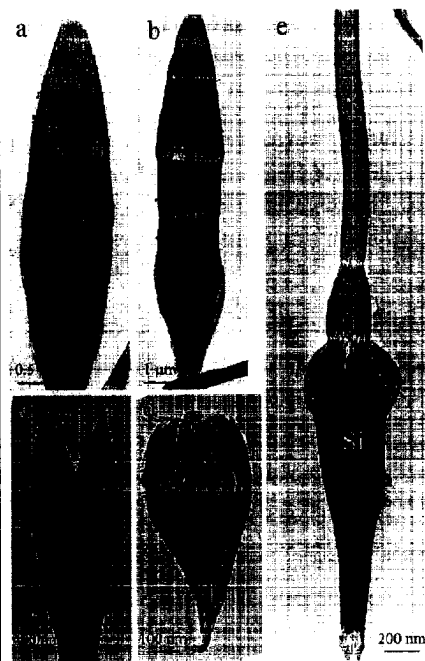usually formed following the trapping of nanocrystals.

Fig 7
TEM images of silica "bundled" arrays and cages.

7(e) takes the shape of a "Chinese lantern" structure composed of silicon and SiO_x, where an SiO_x nanotube extends from the top of a silica wire bundle.

The direct synthesis results which we have obtained in concert with the results of Lee et al.[5] and Lieber et al.[4] would suggest that there are several exciting possibilities for the synthesis of useful silicon and silica based nanowires and nanostructures. Within our approach, we have modified and extended a configuration similar to that reported by Lee et al.[5] to generate the SiO_2 passivated (sheathed) crystalline silicon nanowires using an Si-SiO_2 mix with further extensions to form nanotubes and nanofiber arrays. While Lee et al.[9] have noted that their approach produces silicon nanoparticles which they suggest subsequently form passivated nanowires via the combined steps

$$Si_xO \delta Si_{x-1} + SiO \ (x > 1)$$

$$2SiO \delta Si + SiO_2 ,$$
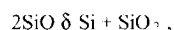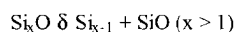
our results indicate that the judicious manipulation of this high temperature system including mixture stoichemistry, flow conditions (kinetics), and temperature range, yields more than would have been previously anticipated. In fact we have also used a carbon/SiO mixture to synthesize biaxial and coaxial SiC/SiO_2 nanowires.[10] The current results would seem to suggest that additional mechanisms may be operative which are analogs not only of a nanoscale VLS mechanism[1-3] but also involve a form of crystalline silicon as well as silica self assembly.

References

1.   G. A. Boostma and H. J. Gassen, J. Cryst. Growth 10, 223 (1971).

1.A. M. Morales and C. M. Lieber, Science 279, 208 (1998).

2.Y. F. Zhang, Y. H. Zhang, N. Wang, D. P. Yu, C. S. Lee, I. Bello, and S. T. Lee, Appl. Phys. Lett. 72, 1835 (1998).

3.See for example, J. Hu, T. W. Odom, and C. M. Lieber, Acc. Chem. Res. 32, 435 (1999) and references therein.

4.See for example, S. T. Lee, N. Wang, Y. F. Zhang, and Y. H. Tang, "Semiconductor Nanowires from Oxide", MRS Bulletin, August 1999, pg. 36, and references therein.

1.D. P. Yu, Z. G. Bai, Y. Ding, Q. L. Hang, H. Z. Zhang, J. J. Wang, Y. H. Zou, W. Qian, G. C. Xiong, H. T. Zhou, and S. Q. Feng, Appl. Phys. Lett. 72, 3458 (1998).

1.N. Wang, Y. H. Tang, Y. F. Zhang, C. S. Lee, I. Bello, and S. T. Lee, Chem. Phys. Lett. 299, 237 (1999).

1.J. L. Gole, J. D. Stout, W. L. Rauch, and Z. L. Wang, Appl. Phys. Lett. 76, 2346 (2000).

2.R. P. Gao, Z. L. Wang, J. D. Stout, and J. L. Gole, Advanced Materials 12, 1938 (2000).

3.Z. L. Wang, Z. R. Dai, Z. G. Bai, R. P. Gao, and J. L. Gole, Appl. Phys. Lett. 77, 3349 (2000).

4.J. L. Gole, J. D. Stout, and Z. L. Wang, to be published.

5.S. M. Prokes, W. E. Carlos, Lenward Seals, Stephen Lewis, and James L. Gole, "Ferromagnetic Nickel Coated Silica Nanospheres from Electroless Solution", in preparation.

6.J. L. Gole and M. G. White, "New Cu/SiO$_2$ Based Catalyst for Selective Ethanol - Acetaldehyde Conversions", Georgia Tech invention disclosure, March 2000. "Nanocatalysis: Selective Conversion of Ethanol to Acetaldehyde Using Monoatomically Dispersed Copper on Silica Nanospheres", Journal of Catalysis, submitted.

7.Sales literature, Cabot Corporation.

Nanoparticles in Biology

DNA-Directed Assembly of Anisotropic Nanoparticles on Lithographically Defined Surfaces and in Solution

Brian D. Reiss, Jeremiah N. K. Mbindyo, Benjamin R. Martin, Sheila R. Nicewarner, Thomas E. Mallouk, Michael J. Natan, and Christine D. Keating*
Department of Chemistry, The Pennsylvania State University
University Park, PA 16802, USA
*Author to whom correspondence should be addressed at keating@chem.psu.edu

Abstract

Anisotropic, noble metal nanoparticles have been synthesized using a template synthesis strategy. In short, metallic salts are reduced in the nanometer scale pores of either an alumina or polycarbonate membrane. The particles can then been released from the template to form suspensions of anisotropic nanoparticles. These nanoparticles have been modified with deoxyribonucleic acid (DNA) oligomers of varying length using several different attachment chemistries. The thermodynamics and kinetics of modifying these particles with DNA has been explored. DNA has also been used to assemble the particles on planar Au surfaces as well as lithographically defined Au pads on Si wafers. In addition to surface assembly, DNA has been used to assemble the nanowires into simple, yet deterministic structures in solution.
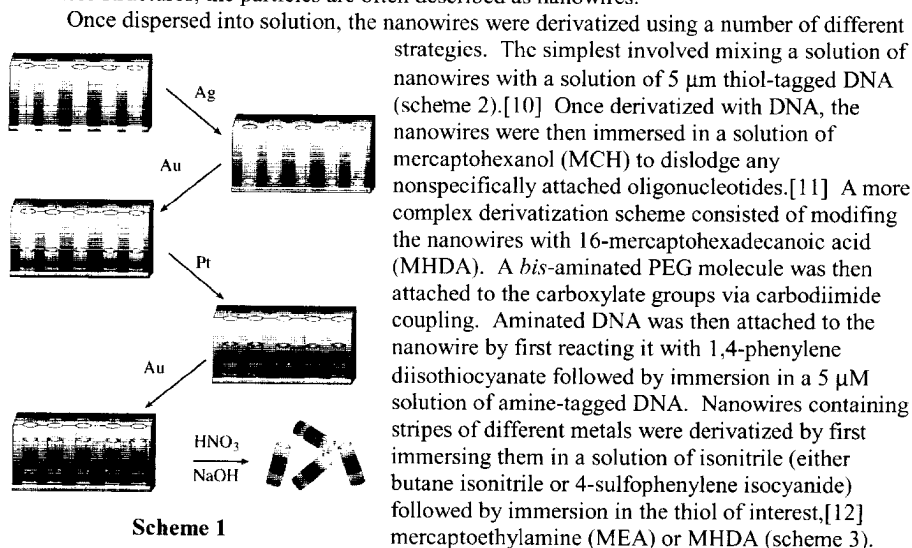
Introduction

Since the mid twentieth century there has been a great deal of interest in the miniaturization of electronic devices. Currently state of the art photoloithographic technology can fabricate devices in the 100 nm size range, but there is an economic motivation to reduce the dimensions of electronic circuitry even further. Due to scientific constraints, there are limitations in the extent to which devices can be fabricated using photolithography.[1] For this reason, there has been a great deal of interest in the development of novel technologies for fabricating smaller devices than can be prepared using photolithography. One such alternative is the "bottom up" approach where devices are self-assembled from very small building blocks as opposed to being etched out of larger pieces of material (a "top down" strategy).[2] Such an approach offers two key advantages. First of all, since devices can be fabricated from nanoparticles or even individual molecules, it is feasible to fabricate much smaller devices than can be prepared using photolithography. The second key advantage is cost. Modern fabrication facilities for photolithography cost over a billion dollars to build, but one can start self assembling devices for a fraction of that cost.
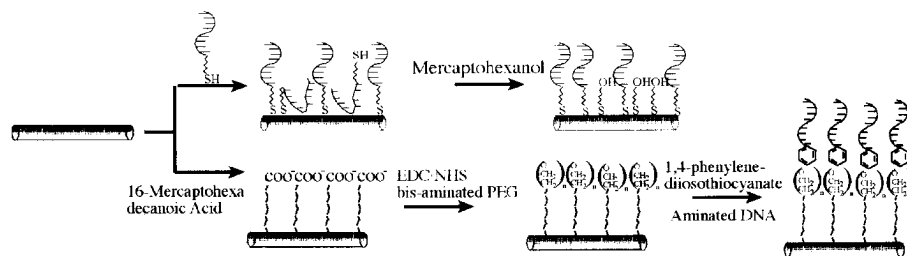
The goal of this research is to assemble anisotropic nanoparticles into functional electronic devices, including memory devices, logic gates, etc. To accomplish this task, two things are necessary: the anisotropic nanoparticles and a "smart glue" to make the particles self assemble into desirable geometries. DNA was chosen as a glue because it offers several unique advantages. [3-5] The primary advantage is selectivity, which results from the specificity an oligonucleotide has for its complementary oligonucleotide. Oligonucleotides have been shown to bind selectively in the presence of hundreds of thousands incorrect sequences.[6] This selectivity allows the user to design systems using different attachment chemistries that are all based on the same fundamental chemistry. For example, if oligonucleotides n bases long are used, 4^n different attachment chemistries could be designed that all work at similar pHs, ionic

strengths, and temperature. The second main advantage of DNA is reversibility. If two oligonucleotides hybridize to form an incorrect structure, they can be dehybridized by raising the temperature, changing the ionic strength, or adjusting the pH, which introduces the possibility of annealing the system to get the desired structure.
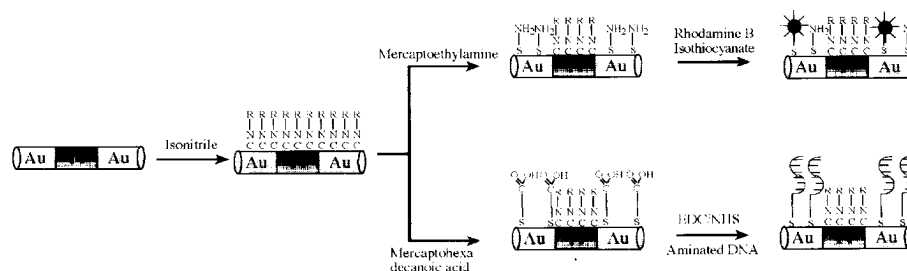
Experimental Details

To prepare the anisotropic nanoparticles a template synthesis technique was chosen in which metallic salts are electrochemically reduced into the pores of either an alumina or polycarbonate membrane (scheme 1).[7, 8] To accomplish this, Ag is thermally evaporated onto the backside of the membrane where it acts as a macroscopic electrode. Metallic salts are then reduced into the pores of the membrane using a three electrode electrodeposition technique. Once the particles are grown, the Ag is dissolved in HNO_3, and the membrane can then be dissolved in NaOH, yielding a colloidal sol of anisotropic particles that are nanometers in diameter and several microns long.[9] These particles can be made of different metals, including Au, Ag, Pt, Ni, Pd, and Cu, or they can be composed of semiconducting or polymeric materials. By controlling the amount of material reduced into the pores of the template, particles can be grown of any desired length up to approximately ten microns. Furthermore, by varying the pore size, particles can be grown at any desired diameter, ranging from 12 nm to 300 nm, so there is complete control over the dimensions of the resulting particles as well as their composition. This synthetic strategy was modified so that stripes of different materials could even be included along the length of the nanoparticles. Since the ultimate goal of this work is to fabricate devices from these structures, the particles are often described as nanowires.

Once dispersed into solution, the nanowires were derivatized using a number of different strategies. The simplest involved mixing a solution of nanowires with a solution of 5 μm thiol-tagged DNA (scheme 2).[10] Once derivatized with DNA, the nanowires were then immersed in a solution of mercaptohexanol (MCH) to dislodge any nonspecifically attached oligonucleotides.[11] A more complex derivatization scheme consisted of modifing the nanowires with 16-mercaptohexadecanoic acid (MHDA). A bis-aminated PEG molecule was then attached to the carboxylate groups via carbodiimide coupling. Aminated DNA was then attached to the nanowire by first reacting it with 1,4-phenylene diisothiocyanate followed by immersion in a 5 μM solution of amine-tagged DNA. Nanowires containing stripes of different metals were derivatized by first immersing them in a solution of isonitrile (either butane isonitrile or 4-sulfophenylene isocyanide) followed by immersion in the thiol of interest,[12] mercaptoethylamine (MEA) or MHDA (scheme 3).

Scheme 1

Scheme 2

Scheme 3

The molecule of interest could then be attached to the Au stripes. Aminated DNA was attached to MHDA derivatized nanowires using carbodiimide couple, and rhodamine B was attached to MEA derivatived nanowires using isothiocyanate chemistry.

The surfaces used in these experiments consisted of Au films that could be derivatized with DNA using any of the attachment chemistries described above. For certain experiments, surfaces containing Au pads lithographically defined on Si wafers were used. In these experiments the surfaces were treated with 3-(triethoxysilyl)propyl succinic anhydride and then soaked in H_2O to hydrate the anhydride group, leaving the Si sections of the surface coated with carboxylate groups.

To assemble nanowires in solution, Au and Pt striped nanowires were derivatized as described above. The Au stripes were derivatized with DNA that was twelve bases in length, and different oligonucleotides were attached to different batches of nanowires. They would then be mixed together along with a twentyfour base oligonucleotide that contained two twelve base sections, one that was complementary to the oligonucleotide on each batch of nanowires. The solutions would then be allowed to stir overnight.

Figure 1: Optical micrograph of striped, Au, Pt, Au nanowires that are 200 nm in diameter and 5 microns long.

Discussion

A batch of nanowires is shown in Figure 1. These nanowires are 200 nm in diameter and five microns long, and they consist of stripes of Au, Pt and Au. Figure 2 shows three optical microscope images of Au nanowires immobilized on Au films through selective DNA hybridization. Figure 2A illustrates nanowires that are 200 nm in diameter and 3 microns long that have been selectively immobilized on Au films using DNA chemistry. In figure 2A nanowires that were derivatized with DNA complementary to the oligonucleotides immobilized on the Au film. Figure 2B contains nanowires that were modified with DNA that was noncomplementary to the oligonucleotides the Au film. Typical surface coverages for these systems are on the order of 1.5×10^6 particles/cm^2 for the complementary experiment and 5×10^5 particles/cm^2 for the noncomplementary experiment. This striking difference in surface coverage indicates that the DNA is preferentially attaching the nanowires to the complementary surface. Even though the complementary surfaces have much higher coverages than the noncomplementary surface, there is still a noticeable coverage of nanowires on the noncomplementary surface. A number of experimental parameters are being investigated to alleviate this trend including, varying the temperature of the reaction, adjusting the components of the buffer used in the reaction, reducing the dimensions of the nanowires, and altering the length and sequence of the DNA used.

Since the ultimate goal of this work is to assemble nanowires into functional devices, the nanowires need to be assembled on a patterned surface that can orient them as they adhere to it. Such an experiment is illustrated in Figure 2C. In this particular case, a Si wafer with Au pads lithographically defined on the surface was substituted for the Au film. The Si sections of the surface were modified with carboxylate groups as described above to reduce the number of nanowires attached to the Si. In this experiment, the Au nanowires (200 nm x 3 μm) can clearly be seen selectively assembling on the Au pads, but again, nonspecific adsorption of nanowires is a problem.

All the experiments discussed thus far consisted of solid Au nanowires. However, nanowires containing stripes of different materials are desirable because the stripes can be derivatized orthogonally allowing more complex assembly schemes. Nanowires derivatized in such a way are illustrated in Figure 3. These particular nanowires are 200 nm in diameter and 3 microns long, and they consist of stripes of Au, Pt, and Au. They were derivatized with butane isonitrile, followed by mercaptoethylamine, followed by rhodamine B isothiocyanate as described above. The left image is a simple bright field optical microscope image to show the psoitions of the nanowires. The right image is a fluorescence image. The nanowires are clearly fluorescing on the Au tips and not in the central portions of the nanowires. This trend results from the orthogonal derivatization that isolates the rhodamine selectively on the Au stripes.

A similar derivatization scheme was then used to assemble in solution. To create assemblies of nanowires, particles were grown that were composed of stripes of Pt, Au, and Pt.
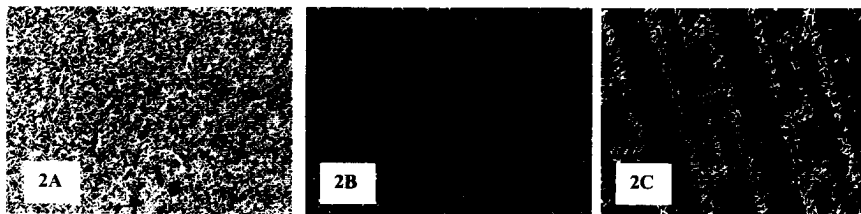

Figure 2: DNA directed assembly of nanowires that are 200 nm in diameter and 3 mm long on Au films modified with complementary oligonucleotides (A), noncomplementary oligonucleotides (B), and on lithographically defined Au pads on a Si wafer(C).
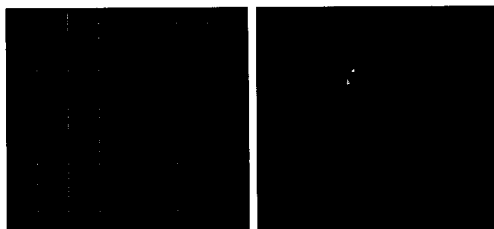
Figure 3: Au, Pt, Au striped nanorods imaged using optical microscopy (left) and fluorescence microscopy (right).

The Pt stripes were derivatized with a sulfonated isonitrile while the Au stripes were derivatized with DNA. The nanowires then self assemble into cross structures (Figure 4A) due to the hybridization of DNA and due to the coulombic repulsion of the sulfonate groups. Currently crosses can be fabricated in a 50 percent yield compared to 20 percent in controls. We are currently trying to optimize this process to get a higher yield of crosses. Cross structures are of interest due to their potential applications in the fabrication of memory devices and logic gates.

A second interesting structure to attempt to assemble is a triangle. To fabricate these structures, nanowires that are 70 nm in diameter and containing stripes of Pt, Au, Pt, and Au were fabricated and derivatized as described above. Two batches of such nanowires were assembled into crosses. These crosses differ from the previous crosses because they have Au tips that are modified with DNA. A third DNA-derivatized nanowire can then be introduced into the system. It can hybridize to these two sticky Au ends to complete the triangle. Figure 4B is a SEM micrograph of such a structure. Currently the yield of such structures is very low (around 5%), but we are attempting to improve it by varying the temperature at which the assembly is performed, adjusting the buffer composition, altering the length and sequence of the oligonucleotides, and reducing the dimensions of the nanowires.

Conclusions

In conclusion, nanowires have been fabricated using a template synthesis technique. These nanowires can be monometallic, or they may contain stripes of different materials. Nanowires can be freed from their template and modified with DNA oligonucleotides. Once modified, they can be assembled on Au films or on Au pads that have been lithographically defined on Si wafers. The nanowires can also be assembled into simple structures in solution, including crosses and triangles. These simple structures may potentially form individual devices, or they may be assembled into more complicated devices. In the future we hope to optimize this assembly methodology and assemble functional devices.
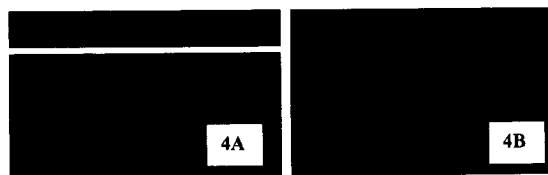

Figure 4: SEM micrograph of two Pt, Au, Pt nanowires that are 70 nm in diameter and 3 microns long assembled into a cross structure via selective DNA chemistry (A). SEM micrograph three nanowires assembled into a triangular structure using similar chemistry

References

1. T. Ito and S. Okazaki, *Nature,* **406**, 1027 (2000).
2. J. J. Storhoff, R. C. Mucic and C. A. Mirkin, *J. Clust. Sci.,* **8**, 179 (1997).
3. N. C. Seeman, *Acc. Chem. Res.,* **30**, 357 (1997).
4. C. A. Mirkin, R. L. Letsinger, R. C. Mucic and J. J. Storhoff, *Nature,* **382**, 607 (1996).
5. A. P. Alivisatos, K. P. Johnsson, X. Peng, T. E. Wilson, C. J. Loweth, M. P. Bruchez and P. G. Schultz, *Nature,* **382**, 609 (1996).
6. M. B. Eisen and P. O. Brown, *Methods. Enzym.,* **303**, 179 (1999).
7. D. AlMawlawi, C. Z. Liu and M. Moskovits, *J. Mater. Res.,* **9**, 1014 (1994).
8. C. R. Martin, *J. Mater. Res.,* **266**, 1961 (1994).
9. B. R. Martin, D. L. Dermoddy, B. D. Reiss, M. Fang, L. A. Lyon, M. J. Natan and T. E. Mallouk, *Adv. Mater.,* **11**, 1021 (1999).
10. J. K. N. Mbindyo, B. D. Reiss, B. R. Martin, D. J. Dermoddy, M. J. Natan and T. E. Mallouk, *Adv. Mater.,* **in press**, (2000).
11. T. M. Herne and M. J. Tarlov, *J. Am. Chem. Soc.,* **119**, 8916 (1997).
12. J. J. Hickman, P. E. Laibinis, D. I. Auerbach, C. Zou, T. J. Gardner, G. M. Whitesides and M. S. Wrighton, *Langmuir,* **8**, 357 (1992).

Nanosphere Lithography: Synthesis and Application of Nanoparticles with Inherently Anisotropic Structures and Surface Chemistry

Christy L. Haynes, Amanda J. Haes, and Richard P. Van Duyne
Department of Chemistry, Northwestern University
Evanston, IL 60208-3113, U.S.A.

ABSTRACT

Early work with size-tunable periodic particle arrays (PPAs) fabricated by nanosphere lithography (NSL) demonstrated that the localized surface plasmon resonance (LSPR) could be tuned throughout the visible region of the spectrum. The LSPR is sensitive to changes in nanoparticle aspect ratio and local dielectric environment. This property has recently been exploited to develop a novel method of measuring surface-enhanced Raman scattering (SERS) excitation profiles. Single layer PPAs consist of size-tunable anisotropic nanoparticles that can be modified to exhibit anisotropic surface chemistry. This work demonstrates multiple schemes for PPA modification using self-assembled monolayers and colloid decoration. Nanoparticle anisotropy can be further exploited with the recent combination of NSL and reactive ion etching (RIE); this extends the two-dimensional PPA structure into the third dimension

INTRODUCTION

In recent years, it has become possible to investigate the size dependent nature of chemical and physical properties in the nanoscale regime. While "top-down" nanoarchitecture techniques are the natural extension from previous capabilities, "bottom-up" approaches are gaining popularity.[1] This paper discusses the application of the "bottom-up" nanofabrication strategy nanosphere lithography (NSL) to create structurally anisotropic nanoparticles. Deckman et al pioneered the NSL technique wherein the natural self assembly of a monolayer of nanospheres forms a hexagonally close-packed crystal.[2] Deposition of material through this colloidal crystal mask, with subsequent removal of the nanospheres, results in an array of evenly spaced, homogeneous nanoparticles known as a periodic particle array (PPA) (Figure 1).[3] The dimension of these truncated tetrahedral nanoparticles can be tuned by choice of nanosphere diameter and deposition thickness (b). While it is possible to study the behavior of any chemical
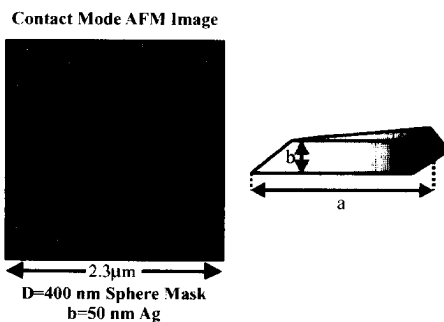
Contact Mode AFM Image

2.3μm
D=400 nm Sphere Mask
b=50 nm Ag

Figure 1. AFM image of Ag PPA and graphical illustration of a single nanoparticle.

or physical property as a function of material size regime, the optical properties of metallic nanoparticles hold special significance in the field of surface-enhanced Raman scattering (SERS), and thus, are the focus of this work.

SERS was first witnessed in 1974 by Fleishmann et al.[4] However, the true significance of the amplified Raman signals was not understood until 1977 when Jeanmaire and Van Duyne attributed the large signals to an electromagnetic enhancement.[5] Until recently, most experimental work in SERS was devoted to determining how the 10^6 SERS enhancement is divided between the chemical (CHEM) and the electromagnetic (EM) enhancement mechanisms. The CHEM is based on the concept of site-specific adsorption and is therefore a short-range effect.[6] While the CHEM enhancement mechanism is important, the EM enhancement mechanism contributes the majority of the total SERS enhancement. The EM enhancement mechanism is based on the concept that electrons in a roughened metal surface will oscillate collectively when the plasma of electrons is excited by an incoming photon of a characteristic frequency. The collective oscillation has two consequences: 1) the resonant photons are selectively absorbed and 2) electromagnetic fields are generated around the nanoparticle roughness feature. This collective electron oscillation is known as the localized surface plasmon resonance (LSPR) and is easily monitored by standard UV-vis absorption spectroscopy. When a Raman active molecule is positioned within the generated electromagnetic fields, the Raman signal increases by up to eight orders of magnitude.[7] Both chemical and conformational information can be elucidated from SERS data, but because the enhancement mechanisms are not fully understood, it is difficult to optimize SERS experiments.

In effort to understand the fundamental principles of SERS, the size dependence of the LSPR has been investigated. Previous attempts to optimize SERS experiments utilize a technique known as a wavelength-scanned excitation profiles.[8] In these experiments, one roughened metal substrate is dosed with a non-resonant Raman-active molecule, and Raman spectra are captured with multiple excitation wavelengths. This technique is undesirable because the experiment is limited by the number of available irradiation wavelengths and the changing Raman bands. By combining LSPR control with the topographic, optical, and spectroscopic measurements, a more flexible approach for excitation profiling is possible.

Intensive study has shown that nanoparticle optical properties depend on nanoparticle material, size, shape, substrate, and dielectric environment. Recent extensions of NSL explore nanoparticle templating to create anisotropic surface chemistry and embedding of the nanoparticles into the substrate material.

EXPERIMENTAL DETAILS

Materials. Ag (99.99%, 0.50 mm diameter) was purchased from D. F. Goldsmith (Evanston, IL). Borosilicate glass substrates were Fisher brand No. 2 cover slips from Fisher Scientific. Tungsten vapor deposition boats were acquired from R. D. Mathis (Long Beach, CA). Polystyrene nanospheres of various diameters were purchased from Interfacial Dynamics Corporation (Portland, OR). 1-Hexanedithiol (1-HDT) and trans-1,2-bis(4-pyridyl)ethylene were purchased from Aldrich Chemical Company (Milwaukee, WI). Silver and gold colloid solutions were prepared according the preparation by Lee and Meisel.[9] For all steps of substrate preparation, water purified with cartridges from Millipore (Marlborough, MA) to a resistivity of 18 MΩ was used.

Substrate Preparation. Glass substrates were cleaned by immersion in 3:1 concentrated H_2SO_4:30% H_2O_2 at 80°C for one hour. After cooling, the substrates were rinsed repeatedly with millipure water and then sonicated for 60 minutes in 5:1:1 H_2O:NH_4OH:30%H_2O_2 solution. Following sonication, the substrates were again rinsed repeatedly with water and then used immediately or stored in water for no longer than one week.

Periodic Particle Array Preparation. Single-layer periodic particle arrays (SL PPAs) were prepared using NSL. Nanospheres used to form deposition masks on glass substrates were used as received without any further dilution with a surfactant solution. Once the 2D colloidal crystal deposition mask was formed, the substrates were mounted into the chamber of a Consolidated Vacuum Corporation vapor deposition system. Ag films of various thicknesses were then deposited over the nanosphere mask. The mass thickness for each film was measured using a Leybold Inficon XTM/2 deposition monitor quartz crystal microbalance (East Syracuse, NY). After the Ag deposition, the nanosphere mask was removed by sonicating the entire substrate in either CH_2Cl_2 or absolute ethanol for 2 minutes. An array of nanoparticles with P_{6mm} symmetry remains on the substrate. In general, domain sizes of 35 μm^2 are achieved with low defect density. The negligible effect of defect sites has been previously addressed.[10]

AFM and UV-vis Extinction Spectroscopy Measurements. AFM images were collected under ambient conditions using a Digital Instruments Nanoscope III microscope operating in either contact mode or tapping mode. Etched Si nanoprobe tips (Digital Instruments, Santa Barbara, CA) with spring constants of approximately 0.15 N m^{-1} were used. These conical shaped tips had a cone angle of 20° and an effective radius of curvature of 10 nm. The resonance frequency of the Tapping mode cantilevers was measured to be between 280-330 KHz. The AFM images presented here represent raw, unfiltered data. Extinction spectra were recorded in standard transmission geometry using an Ocean Optics SD2000.

SERS Measurements. The probe laser was the 514.5 nm output of the Spectra-Physics Beamlok 2060 Ar$^+$ laser. The light was sent through a holographic notch plus filter (Kaiser Optical Systems, Ann Arbor, MI) that eliminates the reflected laser light and the Rayleigh scattered light. The laser spot size, approximately 2 μm in diameter, is much smaller than the typical PPA domain size. The remainder of the light was focused with a 43X objective into a 200 μm core diameter multi-mode optical fiber (Ensign-Bickford, Simsbury, CT) that carried the light to the spectrometer. Light exiting this fiber was collimated with a home-built expanding 4X telescope. The collimated light was then focused into the entrance of a single grating 0.5 meter monochromator (VM-505, Acton, Acton, MA) and measured with a LN$_2$-cooled CCD detector (PM-512, Photometrics, Tucson, AZ).

RIE Apparatus. The 2D colloidal crystal deposition masks were mounted into the chamber of a home-built RIE chamber. The substrate was then etched with 20 mTorr CF_4 at 2.2 W/cm^2 for varied lengths of time.

DISCUSSION

Anisotropic Structure – SERS Excitation Profiles. The location of the LSPR is dependent on the size, shape, and dielectric environment of the sample. Independent control of each of these factors allows tunablility of the LSPR to any wavelength in the visible, near infrared, or mid infrared regions of the spectrum.[11] With this capability realized, the opportunity exists to correlate structural, optical, and spectroscopic data in order to better understand the SERS phenomena. In this investigation, the power of these tunable, anisotropic

nanoparticles is exploited in an innovative new method to probe the SERS excitation profile in a way that is significantly simpler to implement experimentally than the traditional excitation wavelength-scanned approach. Control of particle shape and size allows use of this novel height-scanned excitation profile rather than the standard wavelength-tuned excitation profile, allowing optimization of the SERS enhancement by tuning the particle geometry and laser excitation wavelength.

The general method for performing a height-scanned excitation profile has three steps: 1) fabricate several PPA samples, maintaining equivalent structural parameters with the exception of deposition height, 2) adsorb the Raman active molecule and measure the LSPR by UV-vis extinction spectroscopy, and 3) measure the SERS spectrum from each sample with the same Raman excitation wavelength (λ_{ex}). A plot of the LSPR versus the SERS intensity of any vibrational band will show the correlation between the roughened metal surface's physical characteristics and the resulting SERS enhancement.

A sample data set with six PPA samples is shown in Figure 2. Silver PPAs were fabricated on glass with in-plane widths of approximately 80 nm and out-of-plane heights ranging from 13 nm to 63 nm. Each sample was incubated in a 5 mM solution of *trans*-1,2-bis(4-pyridyl)ethylene (BPE) before extinction spectra were measured. The LSPR wavelengths of these samples ranged from 519 nm to 707 nm. While the pyridine aromatic ring stretch (1608 cm^{-1}) and the trans alkene stretch (1640 cm^{-1}) peaks were discernable in all six λ_{ex}=514.5 nm spectra, the intensity differences were vast. The maximum signal measured for the 1640 cm^{-1} peak was almost two orders of magnitude larger than the minimum signal. When plotting the wavelength of the LSPR versus the Raman intensity of the 1640 cm^{-1} peak, the resulting curve shows a maximum at 535 nm, red-shifted 20 nm from the excitation wavelength (Figure 2).

Anisotropic Surface Chemistry. While exploring the size dependent properties of PPAs, a myriad of novel nanostructures have been developed. Two classes of nanostructures with anisotropic surface chemistry have been among those generated: 1) nanoparticle templates and 2) nanowells.

One extension of the basic NSL technique utilizes the standard noble metal SL PPA as a template for molecular patterning. In a proof-of-concept experiment, a Ag SL PPA was used as a template for dithiol molecules. Metal colloids were then bound to the free end of the dithiol molecule to prove templating capability quantitatively by AFM. By modifying the order of
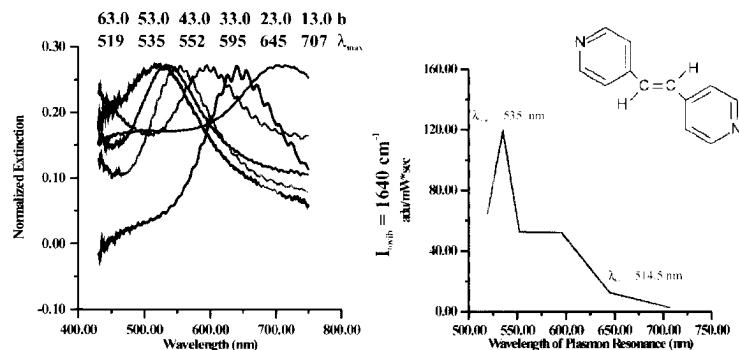

Figure 2. *Extinction spectra and height-scanned excitation profile for trans-alkene stretch of BPE of Ag PPA surface.*

nanosphere mask removal and dithiol dosing, it is possible to deposit dithiol molecules only on the top face of the nanoparticles or to surround the nanoparticles on four sides by dithiol molecules. In both decoration schemes, one must first self-assemble the colloidal crystal mask and deposit gold or silver through the mask holes. In order to deposit colloidal particles only on the top face of the nanoparticles, incubation in the dithiol solution must occur before removing the sphere mask. In this case, the linker molecule will only bind on the top of the nanoparticles, and soaking the sample in gold or silver colloid solution yields a PPA with colloids bound only to the top surface of the nanoparticles (Figure 3B). If fully colloid-coated nanoparticles are desired, the sphere mask must be removed before soaking the PPA sample in the dithiol solution. Because linker molecules can access the entire nanoparticle, colloids will surround the nanoparticles as well (Figure 3C).
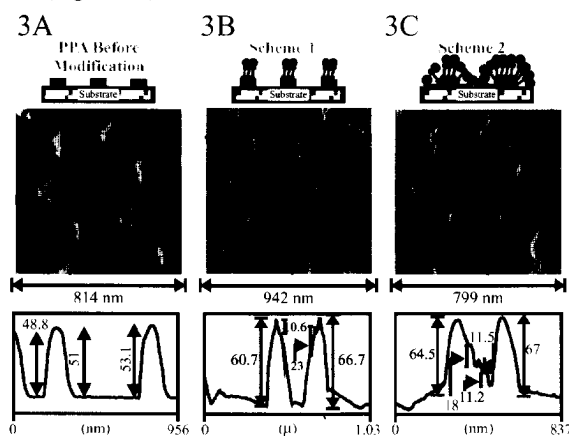
Figure 3. *Ag single layer PPAs as templates for colloidal patterning*

Anisotropic labeling of the template nanoparticles is possible with this NSL technique. AFM evidence proves that the molecular diffusion through the nanosphere mask is directional. Consequently, it should be possible to label the top and the sides of the template nanoparticle with different molecules. Surface-enhanced spectroscopic studies of these bifunctionalized nanoparticles will yield information about enhancement as a function of topography.

The second new nanoarchitecture promoting anisotropic surface chemistry implements the polystyrene nanosphere mask as a reactive ion etching (RIE) mask. When CF_4 plasma strikes the polystyrene nanospheres, the hydrocarbons are fluorinated. This non-volatile product is not etched away, so the spheres act as an etch stop. Meanwhile, as the CF_4 plasma penetrates the holes in the sphere mask, volatile SiF_2 radicals and SiF_x products are etched away.[12] The resulting structures are PPA-shaped nanowells.

Deposition of material through the nanosphere mask after etching embeds nanoparticles within the substrate. The LSPR has been measured from silver nanoparticles embedded in Si(111) and SiO_2 substrates. Future studies will explore applications of nanowell, nanorod, layered nanoparticles in nanowell, and fully embedded nanoparticle systems.

CONCLUSION

The presented excitation profile results clearly demonstrate the power of understanding the role of the LSPR in the SERS enhancement mechanism, and this work would not be possible without the predictable, tunable anisotropic nanoparticles fabricated with the NSL technique. The most important consequence of this work is that there is a SERS-active substrate that is fully characterized. Future correlation of experimental results with electrodynamic modeling[10] will advance the goal of understanding the relationship between the surface topography, the location of the LSPR, and the enhancement mechanism of SERS

The extension of NSL to the fabrication of nanoparticles with anisotropic surface chemistry holds much future promise. The ability to selectively label varying nanoparticle faces will contribute to sensing and barcoding applications. The powerful combination of NSL and RIE not only presents nanoparticles with anisotropic dielectric environments, but also suggests that very high aspect ratio nanoparticles can be fabricated by this flexible synthesis technique.

ACKNOWLEDGEMENTS

REFERENCES

1. M. B. Mohamed, K. Z. Ismail, S. Link, M. A. El-Sayed, *Journal of Physical Chemistry B.*, **102**, 9370-9374 (1998).
2. H. W. Deckman, J. H. Dunsmuir, *Applied Physics Letters*, **41**, 377-379 (1982).
3. J. C. Hulteen, R. P. Van Duyne, *Journal of Vacuum Science and Technology A*, **13**, 1553-1558 (1995).
4. M. Fleischmann, P. J. Hendra, A. J. McQuillan, *Chemical Physics Letters*, **26**, 163-166 (1974).
5. D. L. Jeanmaire, R. P. Van Duyne, *Journal of Electroanalytical Chemistry*, **84**, 1-20 (1977).
6. M. Moskovits, *Reviews of Modern Physics*, **57**, 783-826 (1985).
7. G. C. Schatz, The Image Field Effect: How Important Is It?, *Surface Enhanced Raman Scattering*, eds. R. K. Chang, T. E. Furtak (Plenum Press, 1982) pp. 35-50.
8. P. F. Liao, J. G. Bergman, D. S. Chemla, A. Wokaun, J. Melngailis, A. M. Hawryluk, N. P. Economou, *Chemical Physics Letters*, **81**, 355-359 (1981).
9. P. C. Lee, D. Meisel, *Journal of Physical Chemistry*, **86**, 3391-3395 (1982).
10. T. R. Jensen, M. L. Duval, L. Kelly, A. Lazarides, G. C. Schatz, R. P. Van Duyne, *Journal of Physical Chemistry B*, **103**, 9846-9853 (1999).
11. T. R. Jensen, M. D. Malinksy, C. L. Haynes, R. P. Van Duyne, *Journal of Physical Chemistry B*, **104**, 10549-10556 (2000).
12. G. Cunge, P. Chabert, J. Booth, *Plasma Sources Science and Technology*, **6**, 349-360 (1997).

Effective Medium Theory of DNA-linked Gold Nanoparticle Aggregates: Effect of Aggregate Shape

Anne A. Lazarides, K. Lance Kelly, and George C. Schatz
Department of Chemistry, Northwestern University
Evanston, IL 60208-3113

ABSTRACT

We present a dynamical effective medium theory (EMT) of the dielectric properties of nanoparticle aggregates formed from DNA-linked gold nanoparticles. Experimental measurements show that such aggregates have reduced UV extinction and plasmon bands that are considerably red-shifted and broadened relative to the plasmon absorption feature observed in spectra of dispersed colloid. The EMT, which can be used to reproduce the observed spectral changes, is tested by comparing aggregate spectra calculated using the EMT dielectric function with spectra from explicit coupled particle calculations, and good agreement is found. The EMT dielectric function is used as well in discrete dipole calculations to calculate extinction spectra for a variety of aggregate shapes not amenable to analytic solution, and the sensitivity of the spectra to aggregate shape is examined. We find that the spectra are only weakly sensitive to aggregate shape, and conclude that, when calculating extinction of the DNA-linked aggregates for comparison with experiment, spherical shapes can be assumed.

INTRODUCTION

Recently, a DNA detection method has been developed that is based upon the distance-dependent optical properties of gold nanoparticle aggregates that form in the presence of DNA linker molecules.[1-4] Gold particles are functionalized with alkane-thiol-capped oligonucleotides (single-stranded DNA); complementary linker oligonucleotide (DNA) strands direct the assembly of nanoparticle networks through the forces of sequence-specific hybridization (DNA duplex formation). The optical properties of the linked nanoparticles have been shown to be a function of the size of the nanoparticles, the length of the linking duplex DNA, and the size of the nanoparticle aggregates. When nanoparticles of a size between 12 and 16 nm are linked with DNA duplexes composed of 24 oligonucleotide base pairs, aggregate formation is accompanied by a color change from red to purplish-blue (Figure 1).
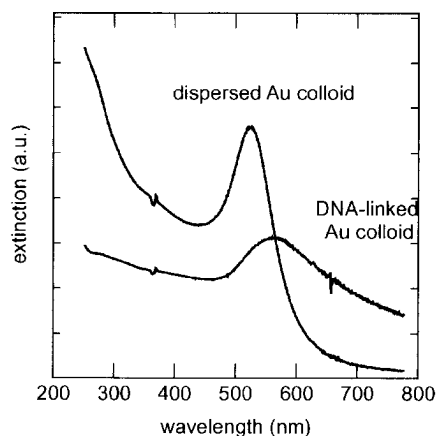
Figure 1. *Extinction spectra for dispersed and DNA-linked Au nanoparticles, courtesy of the authors of ref. 3. The 13 nm particles are capped with 3'- and 5'-(alkanethiol) 12-base oligonucleotides. The aggregated colloid is formed in the presence of a 24-base oligonucleotide, each half of which is complementary to the one of the two nanoparticle-capping oligonucleotides.*

In earlier work, two of us demonstrated that aggregates composed of thousands of particles may be described accurately using a coupled dipole approach in which the particles are located on a cubic lattice, and the induced polarizations are determined using complex conjugate gradient solutions of the dipole interaction equations, with Fourier methods used to evaluate dipole-dipole interactions.[5,6] The dipole polarizability of each particle is determined exactly using Mie theory. Since the lattice does not represent a solid object, lattice sites may be unoccupied. This does not cause trouble with evaluating the dipole sums by Fourier transforms, but the method is restricted to aggregates wherein the particles are located on cubic lattices (sc, bcc, fcc or lattice gases). We find the lattice representation of the aggregates to be quite effective for the DNA/gold aggregates. We have tested this coupled dipole theory against more complete theories that include converged multipole expansions, and we find that, for the particle sizes and interparticle spacings that are characteristic of the DNA-linked nanoparticle aggregates, the coupled dipole results are accurate.

Another approach to describing the optical properties of nonmagnetic nanoparticle aggregates is to derive a dielectric function that characterizes the electric susceptibility of bulk aggregate. This effective medium approach takes advantage of the fact that optical wavelengths are much larger than either the particle size or the mean distance between particles. In this circumstance, a homogeneous description may provide an accurate representation of the heterogeneous material. In this paper we examine the properties of a recently developed dynamical effective medium theory (EMT) that was designed to treat aggregate structures similar to the DNA-linked nanoparticle aggregates.[7,8] These aggregates are typically hundreds of nanometers or microns in size and are composed of nanoparticles of a size between 10 and 30 nm. Typically, the metal fraction of the aggregates is less than 20% by volume. We will show by comparison with coupled dipole theory that the low volume fractions and small nanoparticle sizes make it relatively easy to develop an EMT that is accurate. However, because the

aggregate sizes are comparable to the wavelength of light, extinction spectra are difficult to determine unless the aggregates are spherical. Nonspherical aggregates, however, can be treated using a finite element based approach, the discrete dipole approximation (DDA),[9] with the EMT dielectric function as input. We present DDA results for a variety of nonspherical aggregates and compare them with spectra calculated for spherical aggregates to determine the sensitivity of aggregate extinction to aggregate shape.

THEORY

The simplest approach to constructing an EMT is to assume that the particles are non-interacting. Under this assumption, the polarization of a small spherical aggregate can be evaluated by summing the response of all the spheres of which an aggregate is composed. For each sphere, the polarizability (in the long wavelength limit) is

$$\alpha_o = \frac{\varepsilon - 1}{\varepsilon + 2} a^3$$

where a is the sphere radius and ϵ is the metal dielectric function. The polarizability of a small sphere of aggregate material of radius R (R<< λ) is given by a similar expression:

$$\alpha_{agg} = \frac{\varepsilon_{eff} - 1}{\varepsilon_{eff} + 2} R^3$$

where the effective aggregate dielectric function is ϵ_{eff}. Alternatively, invoking the additivity that follows from the assumption of a non-interacting response, $\alpha_{agg} = N\alpha_o$, where N is the number of spheres in the sphere of aggregate material. Substituting the expressions above, we obtain the following relation between ϵ and ϵ_{eff}:

$$\frac{\varepsilon_{eff} - 1}{\varepsilon_{eff} + 2} = f \frac{\varepsilon - 1}{\varepsilon + 2}$$

where f is the volume fraction of metal spheres (f = Na^3/R^3). This formula defines the well known Maxwell-Garnett effective medium dielectric constant, and it is actually much better than this trivial derivation would imply. However, it does not describe electrodynamic effects.

To describe electrodynamic effects, we use a result from a theory of Draine and Goodman[9] that is at the heart of their important improvement to the DDA method. Draine and Goodman demonstrated that the optical response of a lattice of dipoles can be made to match that of bulk continuum by an appropriate choice of the wavevector-dependent dipole polarizability, α, provided that the lattice parameter is sufficiently small. The expression that relates the polarizability to the bulk dielectric function is referred to as the "lattice dispersion relationship". In our approach,[7] the relationship is inverted (at each wavelength) to determine the value of the dielectric function, ϵ_{eff}, from the known nanosphere polarizability. The relevant formula is:

$$\alpha = \cfrac{\alpha_o}{1 + \cfrac{\alpha_o}{d^3}\cfrac{3}{4\pi}\left[(b_1 + \varepsilon_{\text{eff}}b_2 + \varepsilon_{\text{eff}}b_3 S)(kd) - \cfrac{2}{3}i(kd)^3\right]}$$

where

$$\alpha_o = \frac{\varepsilon_{\text{eff}} - 1}{\varepsilon_{\text{eff}} + 2}a^3$$

In this expression, d is the lattice spacing, k is the magnitude of the wavevector, b_1, b_2, and b_3 are constants, and S is a geometric factor that depends on the direction of the wavevector relative to that of the lattice. In our implementation of the lattice dispersion relationship, α is the exact nanosphere dipole polarizability as obtained from Mie theory. Further details, along with comparisons between Maxwell-Garnett theory and the new dynamical effective medium approximation are given in Ref. 7. In the next section, we demonstrate the accuracy of the theory and use it to examine the sensitivity of aggregate UV-vis extinction spectra to aggregate shape.

RESULTS

A. EMT Dielectric Functions

The dielectric function for a material composed of 13 nm Au spheres in water is illustrated in Fig. 2a, for frequencies that correspond to UV and visible radiation. The metal fraction, f, of the nanoparticle material is 0.155 by volume, which is the inclusion fraction of a simple cubic array of spheres separated by a distance equal to a particle radius, r, i.e. an sc lattice with lattice parameter equal to 1.5r. The function is complex, indicating that the material is absorptive as well as refractive. The index of refraction (square root of the dielectric function) is illustrated in Fig. 2b.
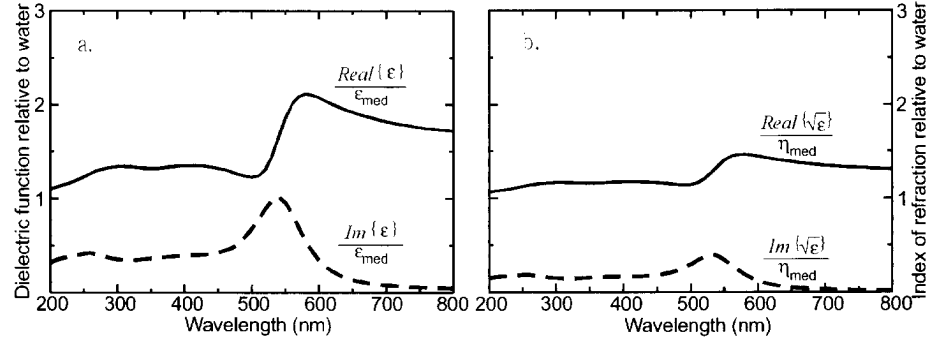
Figure 2. *(a) Complex dielectric function, ϵ, and (b) complex index of refraction, η, for a material composed of 13 nm Au nanoparticles (metal fraction 0.155) in water. The effective dielectric function and index of refraction are shown relative to ϵ and η of the medium, 1.77 and 1.33 respectively.*

The peak absorption of the nanoparticle material occurs at the frequency at which the imaginary part of the index of refraction is a maximum, which, for this material, is at a wavelength of 532 nm. From the real part of the index it can be seen that the material refracts light primarily at frequencies lower than that of peak absorption, i.e. at wavelengths corresponding to red or IR light.

B. Optical Response of a Nanoparticle Aggregate: Comparison with Coupled-Dipole Results

At each frequency for which the dielectric properties of a material are known, an electrodynamic problem can be posed for a given sample size and shape whose solution yields the extinction of that sample. Using the nanoparticle dielectric function described above, we have calculated the extinction spectrum of a spherical aggregate of 13 nm Au nanoparticles in water that is 234 nm in diameter. We have chosen an aggregate that is spherical in shape so that the calculation is a simple application of Mie theory, a rigorous theory for spherical objects. To test the accuracy of our dielectric function, we perform another more involved calculation that treats the heterogeneity of the nanoparticle material directly and models each of the 912 particles explicitly. We use a level of theory (coupled dipole theory) that we have tested against higher order theories[5] and have shown to be accurate for nanoparticles of this size that are separated by distances greater than or equal to a nanoparticle radius, as is the case here. Extinction spectra calculated by the two methods are shown together for comparison in Figure 3. Extinction is
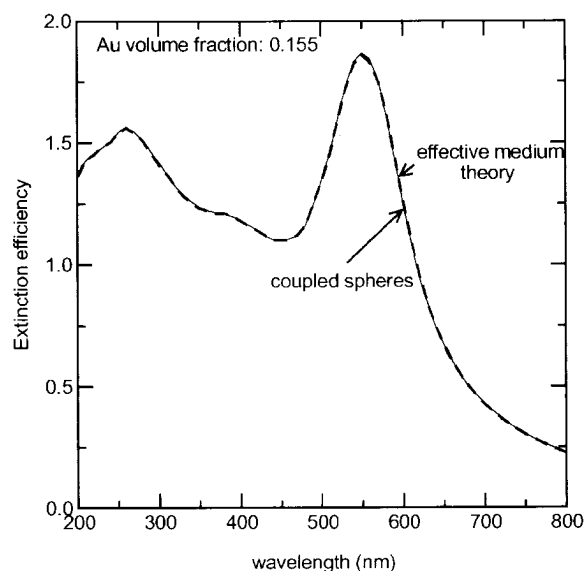
Figure 3. *Extinction spectra of a 234 nm spherical aggregate of 13 nm spheres in water, arranged on a simple cubic lattice. The aggregate is 15.5% Au by volume. The solid line is the extinction as calculated with each nanoparticle modeled explicitly; the dashed line is extinction as calculated with Mie theory using the effective dielectric function of the nanoparticle material as input.*

plotted as an efficiency, i.e. the extinction cross section relative to the geometric cross section. The perfect agreement of the two results validates the use of a homogeneous description of the nanoparticle material and, in particular, the dynamical effective medium theory.

C. DDA Method for Calculating Extinction Spectra

Having demonstrated the ability of our dielectric function to accurately represent nanoparticle material dielectric response, we seek to use it to predict optical spectra of aggregates that are not spherical and, therefore, not addressable with Mie theory. To accomplish this, we adopt a method of solution known as the Discrete Dipole Approximation[9] (DDA) that is most widely applied to solid scatterers. The DDA approach involves a discretization of the interior of the scatterer (or 'target') into a lattice of polarizable dipoles, whose polarizabilities are derived from the dielectric function of the target material. The approach is fully flexible with respect to aggregate shape. The method is described in detail in Ref. 9, and a previous application is presented in Ref. 10. Because of the dielectric nature of the nanoparticle material, the lattice spacing of the DDA grid that discretizes the aggregate interior can be quite large relative to that required to obtain converged results when applying the method to a metallic target. Note that, for these calculations, the grid used for computation is unrelated to the actual spacing between nanoparticles.

To test the DDA approach, we use the method first to calculate the extinction spectrum of an aggregate whose dielectric function and spectrum are known. In Figure 4 we display the DDA result for our 234 nm spherical aggregate of 13 nm Au spheres in water (0.155 Au by volume) and compare it to the extinction spectrum computed previously using Mie theory. In both cases, our derived nanomaterial dielectric function, illustrated in Fig. 2a, is used as input. From the nearly exact match of the two spectra, we conclude that the discrete dipole approximation is accurate for materials of this type and can be used with confidence to calculate spectra for arbitrarily shaped aggregates, as desired. Also shown in Fig. 4 are contributions to the extinction spectrum from absorption and scattering and, for comparison with the aggregate spectrum, a spectrum of dispersed ($f = 0.155 \times 10^{-3}$) 13 nm Au spheres. (The dispersed particle extinction has been scaled by a factor of 100 to compensate for the larger size of the geometric cross section used to normalize the extinction cross section when calculating efficiencies, $Q_{ext} = C_{ext}/ C_{geom}$, for the dispersed case relative to C_{geom} of the aggregate.) Clearly, both the absorption and scattering maxima are red shifted from the absorption maximum of the dispersed spheres. (The dispersed 13 nm particles are too small to scatter visible light; hence, their extinction spectrum is essentially an absorption spectrum.) The aggregate absorption maximum occurs at approximately the same wavelength as the maximum in the imaginary part of the nanoparticle material index of refraction (Fig. 2b). Scattering occurs primarily at longer wavelengths, as expected given the nonrefractive nature of the material at shorter wavelengths. While larger aggregates would scatter light at longer wavelengths as well, significant scattering for these smaller aggregates is limited to wavelengths less than 700 nm, consistent with the notion that the phase variation, kD, across a target of size D must be greater than 1 for significant scattering to occur.
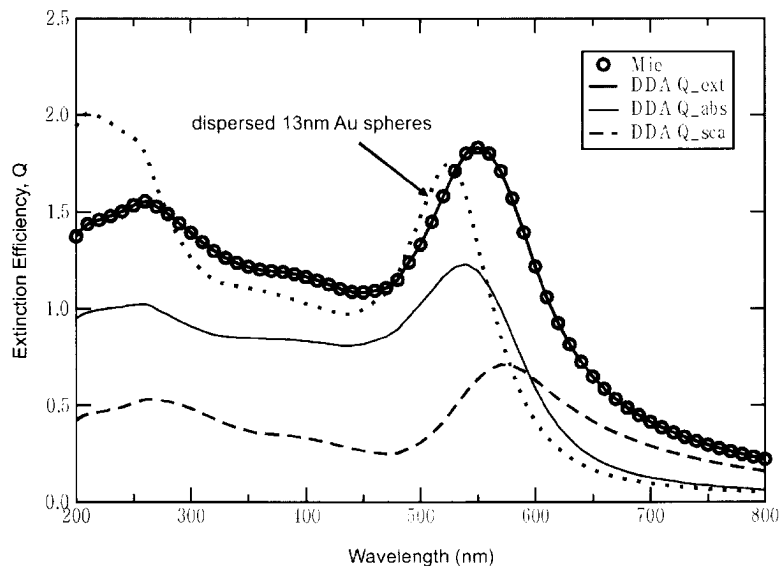
Figure 4. *Extinction spectra of the 234 nm DNA-linked gold aggregate (metal fraction 0.155) in water: comparison of spectrum calculated using the Discrete Dipole Approximation and spectrum (from Fig. 3) calculated using Mie theory. The similarity of the two spectra validates the use of the DDA in subsequent calculations. The spectrum of dispersed 13 nm Au particles (of which the aggregate is composed) in water is shown as well, as are the absorption and scattering contributions to the aggregate extinction.*

D. EMT Spectra of Nonspherical Aggregates

The DDA method was used to calculate spectra of other aggregates of 13 nm Au particles (Au fraction 0.155) from the same dielectric function. Spectra of a 5:1 oblate aggregate equal in volume to a spherical aggregate of diameter 234 nm are illustrated in Figure 5. The spectra depend upon the orientation of the polarization and propagation axes of the incident light relative to the principle axes of the ellipsoidal aggregate. Two spectra are shown, one for polarization along one of the major axes of the aggregate and one for polarization along the minor axis. In both cases, the propagation direction is along a major axis. Both spectra display peaks at wavelengths significantly shorter than that of the spectrum of a spherical aggregate: for the case of polarization along the minor axis, the spectrum has a plasmon peak that is closer to that of dispersed Au colloid than to a spherical aggregate of the same volume. In the UV, however, all spectra are quite similar, indicating insensitivity of the extinction in this wavelength region to aggregate shape. Similar calculations were done for 5:1 prolate ellipsoids of equal volume. In the visible, these spectra are closer to that of a spherical aggregate than are the spectra of oblate ellipsoidal aggregates, and in the UV, they are again similar.
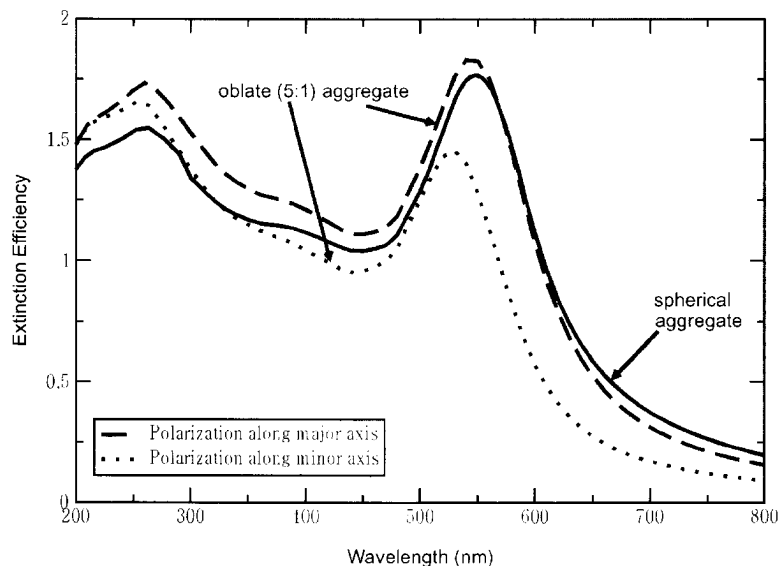
Figure 5. *Extinction spectra of DNA-linked gold nanoparticle aggregates: comparison of a 234 nm spherical aggregate and an equivolume 5:1 oblate aggregate. In the UV, the spectra are similar. In the visible, when the polarization direction is aligned relative to the aggregate, spectra are polarization- and aggregate shape-dependent.*

Since, in solution, where the DNA-linking takes place and the aggregate spectra are collected, aggregates assume random orientations relative to a light source, we calculated as well orientationally-averaged extinction spectra for both oblate and prolate (5:1) aggregates of 13 nm Au spheres, metal fraction 0.155. The results are shown in Figure 6 along with the spectrum of the equal volume spherical aggregate. It is clear from the figure that, while the ellipsoidal aggregates are slightly more extinctive in the UV than spherical ones and have plasmon bands that are slightly less red-shifted and less broadened, the spectra are remarkably similar. From this we conclude that spherical aggregates provide a reasonable model for extinction calculations of DNA-linked gold nanoparticle aggregates even though the latter presumably assume a variety of shapes.

C6.5.8
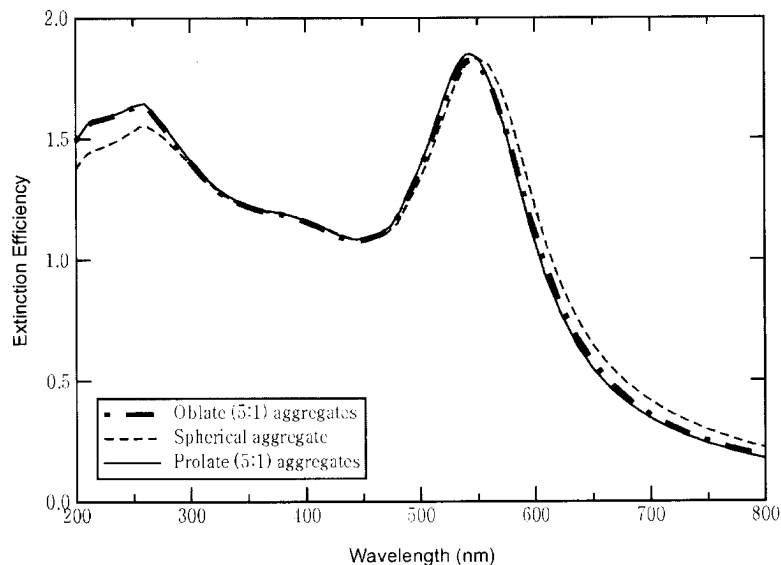
Figure 6. *Extinction spectra of DNA-linked gold nanoparticle aggregates in water: orientational averages of spectra of ellipsoidal aggregates. The spectra are similar, indicating that spectra of ensembles of randomly-oriented equivolume ellipsoidal aggregates are aggregate shape independent.*

CONCLUSIONS

We have developed a dynamical effective medium theory for the dielectric permittivity, ϵ_{eff}, of a class of nanoparticle materials composed of inclusions embedded in a dielectric medium. The theory is applicable to systems in which uniformly sized nanoparticles are separated by distances greater than or equal to a particle radius and are exposed to radiation at energies such that the wavelengths are long relative to the nanoparticle size. We have applied the theory to materials composed of DNA-linked gold nanospheres in an aqueous medium. In these materials, interparticle separations are controlled by the number of base pairs in the duplex DNA interconnects and are sizable enough to satisfy the conditions for accuracy of the theory. Using the dynamical EMT dielectric function, we are able to calculate linear optical properties of nanoparticle aggregates of various shapes and sizes using electrodynamic methods appropriate for the specific aggregate shapes.

We have tested the dynamical EMT by comparing aggregate extinction spectra calculated using the derived dielectric function, ϵ_{eff}, with spectra calculated using explicit particle models and accurate electrodynamic methods that are converged with respect to the order of interaction between the particles. By virtue of the indistinguishability of the EMT spectra and spectra calculated using exact methods, we conclude that the homogeneous representation provided by the effective dielectric function is accurate. We have also adopted an electrodynamic computational scheme based upon the DDA[9] for calculating optical properties of arbitrarily

shaped targets and have used it to calculate the extinction spectra of aggregates that are ellipsoidal (oblate and prolate) in shape and have eccentricities as large as 5:1. For these latter calculations we again used the EMT dielectric function.

Spectra were calculated for individual aggregates oriented with respect to the incident light and also for populations of randomly oriented aggregates, such as would be present in the aqueous environment where DNA-directed assembly takes place. The calculations show that, for nanoparticle aggregates that are ellipsoidal in shape and oriented with respect to the polarization and propagation directions of the incident light, the location of the plasmon band is a function of both shape and orientation. However, the spectra calculated for orientationally averaged populations of ellipsoidal aggregates display very little sensitivity to aggregate shape, as long as the aggregate volumes are held constant. From this we conclude that, when calculating extinction for DNA-linked nanoparticle aggregates, one can assume that the aggregates are spherical even though the aggregates formed in the laboratory may assume a variety of shapes.

The spectra displayed here for the purpose of illustrating the accuracy of the dynamical effective medium theory have plasmon bands that are only modestly red-shifted and broadened relative to the plasmon band of dispersed particles. Elsewhere[8] we have shown that the more substantial aggregation-induced spectral changes that are observed experimentally (Fig. 1) can be reproduced in calculated spectra if the nanoparticle aggregate sizes are chosen to be larger than the sizes used here to illustrate the theory.

ACKNOWLEDGEMENTS

REFERENCES

1. R. C. Mucic, J. J. Storhoff, R. L. Letsinger and C. A. Mirkin, Nature 382, 607 (1996).
2. R. Elghanian, J. J. Storhoff, R. C. Mucic, R. L. Letsinger, and C. A. Mirkin, Science 277, 1078 (1997).
3. J. J. Storhoff, R. Elghanian, R. C. Mucic, C. A. Mirkin, and R. L. Letsinger, J. Am. Chem. Soc. 120, 1959 (1998).
4. J. J. Storhoff, A. A. Lazarides, C. A. Mirkin, R. L. Letsinger, R. C. Mucic and G. C. Schatz, J. Am. Chem. Soc. 122, 4640 (2000).
5. A. A. Lazarides and G. C. Schatz, J. Phys. Chem. 104, 460-7 (2000).
6. A. A. Lazarides and G. C. Schatz, J. Chem. Phys. 112, 2987 (2000).
7. A. A. Lazarides and G. C. Schatz, J. Chem. Phys., to be submitted.
8. A. A. Lazarides, K. L. Kelly, T. R. Jensen, and G. C. Schatz, Theochem, 529, 59 (2000).
9. B. T. Draine, P. J. Flatau. J. Opt. Soc. Am. A. 11 1491 (1994); B.T. Draine, J. J. Goodman. Astrophys. J. 405, 685 (1993); Program DDSCAT, by B. T. Draine, P. J. Flatau. University of California, San Diego, Scripps Institute of Oceanography, 8605 La Jolla Dr., La Jolla, CA 92093.
10. W. H. Yang, G. C. Schatz and R. P. Van Duyne, J. Chem. Phys. 103, 869 (1995); T. Jensen, L. Kelly, A. Lazarides and G. C. Schatz, J. Cluster Science 10, 295 (1999).

Microstructural and Magnetic Properties of Core-Shell Ni-Ce Nanocomposite Particles Assemblies

Xiang-Cheng Sun[1*], J. A. Toledo[1] and M. Jose Yacaman[2]

[1]Prog. Simulación Molecular, Instituto Mexicano del Petróleo, Lázaro Cárdenas 152[#], 07730, D.F. México, México
[2]ININ, Amsterdam No.46-202, Col. Condesa 06100, D. F. México, México
*E-mail: sunxiangcheng@yahoo.com

ABSTRACT

Novel magnetic core-shell Ni-Ce nanocomposite particles (15-50 nm) are presented. SEM observation indicates a strongly ferromagnetic interacting order with chain-like features among Ni-Ce nanocomposite particle assemblies. Typical HREM image demonstrates that many planar defects (i. e. stacking faults) exist in large Ni core zone (10-45 nm); the innermost NiCe alloy and outermost NiO oxide exist in the thin shell layers (3-5 nm) . Nano-diffraction patterns show an indication of well-defined spots characteristic and confirm the nature of this core-shell nanocomposite particles. Superparamagnetic relaxation behavior above average blocking temperature (T_B =170K) for Ni-Ce nanocomposite particles assemblies have been exhibited, this superparamagnetic behavior is found to be modified by interparticle interactions, which depending on the applied field; size distribution and coupling with the strong interparticle interaction. In addition, an antiferromagnetic order occurs with a Neél temperature T_N of about 11K due to Ce ion magnetic order fuction. A spin-flop transition is also observed below T_N at a certain applied field and low temperature.

INTRODUCTION

Magnetic nanoparticles have been an active subject of intense research due to their unique magnetic properties that are appealing from both scientific and technological points of view [1-3]. Specifically, metallic (Fe, Co, Ni, etc) [3-6] and oxide (γ-Fe_2O_3, etc) [4] magnetic nanoparticles have attracted considerable attention as high-density magnetic storage media because a high coercive force and a high saturation magnetization can be achieved. Recently, experimental evidences for low temperature superparamagnetism relaxation [7] and the ordering of spin-glass like behavior [4, 8] in some single domain magnetic particles (i.e. γ-Fe_2O_3) had also been of significant interest. In this study, novel Ni-Ce nanocomposite particles coated with NiCe alloy and NiO oxide shell layers were prepared. Their unique microstructure features and superparamagnetic order properties will be reported here.

EXPERIMENTAL

The Ni-Ce particle nanocomposite were prepared by the plasma-metal reaction technique [9]. A JEOL-4000EX high-resolution transmission electron microscope (*HRTEM*) was used to determine the detailed core-shell phase and average grain size of the particle. It also allows recording selected area electron nano-diffraction patterns. A Phillips XL30 scanning electron microscope (*SEM*) equipped with X-ray energy-dispersive analysis (*EDX*) system, was employed to provide the morphology of particles and chemical analysis. The magnetization measurements were performed by using SQUID magnetometer in the temperature range from 2 to 300K at different applied magnetic fields. Measurements were performed by the zero-field-cooling (ZFC) and the field-cooling (FC) methods. From the curves of M *vs* T (ZFC and FC cases) . The average blocking temperature (T_B) was obtained, which is defined as the maximum of the ZFC curve.

RESULTS AND DISCUSSION

Figure 1. *SEM morphology of Ni-Ce nanocomposie particles*

SEM image (figure 1) clearly indicates that these particles exhibit strong a tendency of forming chain-like features with negligible shape anisotropy. This chain-like behavior can be attributed to a strong ferromagnetic interaction, and the tendency of reducing the specific surface energy of the system among Ni-Ce nanocomposite particle assemblies.

From the typical HREM image (figure 2) of this Ni-Ce nanocomposite particle, very clear lattice images of core-shell type structure are observed. Each particle consists of a large core and a thin outer shell. In addition, many structural defects are observed, such as stacking faults. Most particles are covered with *ca.* 3-5nm thick crystalline phase, which has some discontinuities (as shown by the arrow of figure 2). This indicates that the shell phases are polycrystalline. The outermost layer spacing is 0.24nm, this value corresponds with that of NiO (111) plane, and in the innermost layers spacing of 0.278nm and 0.219nm have been indicated, which correspond to

NiCe (111) and Ni₂Ce (311) planes, respectively. Nano-diffraction patterns (figure 3) show well-defined rings and spots characteristic of nanocomposite grained materials, where some crystal relationships among orthorhombic [111] of NiCe and cubic [311] of Ni₂Ce, face-center crystal [222] of NiO, cubic [111] of nickel can be identified. These features are due to the core-shell nature of the particles. It is worth noticing that, stacking faults exists in the nickel core region give rise to distortions in the particle crystal surface that lead to the diffuse scattering in the Nano-diffraction patterns.
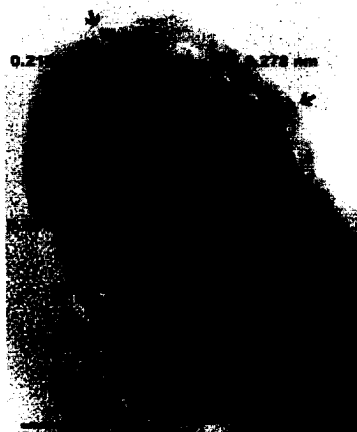
Figure 2. HREM image of Ni-Ce nanocomposite particles with innermost CeNi compounds (lattice spacing, 0.278nm and 0.219nm, for CeNi and CeNi₂, respectively) and outermost NiO layer (lattice spacing, 0.24nm) shell structures. Also planar defects, i.e. stacking faults, as showed in arrows.
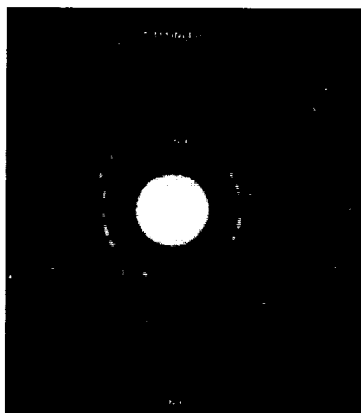
Figure 3. *Nano-diffraction patterns of Ni-Ce nanocomposite particles, indicating the crystal relationship among orthorhombic [111] of NiCe and cubic [311] of Ni₂Ce, face-center crystal [222] of NiO, cubic [111] of nickel.*

The variations of zero-field-cooled (*ZFC*) and field-cooled (*FC*) magnetization with temperature at different applied magnetic field (from 500Gs to 1Tesla) between 2 and 300K are shown in figure 4 (a, b, c, d).
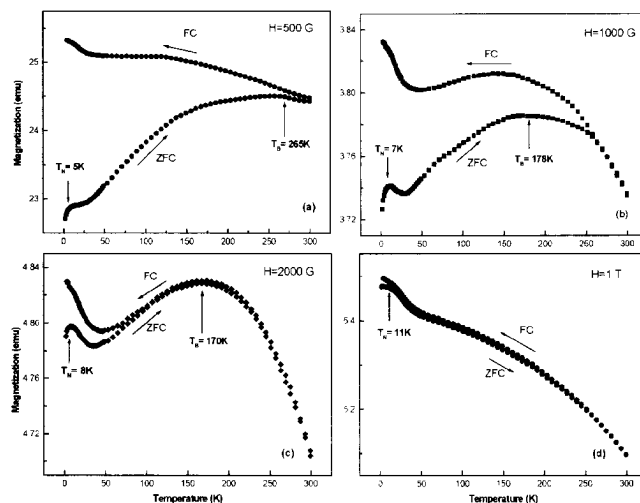
Figure 4 (a, b, c, d). *Magnetization as function of temperature for Ni-Ce nanoparticles*

Figure 4 (a, b, c, d) shows the typical blocking behavior of superparamagnetic nanoparticles, the Ni-Ce nanoparticles show a different magnetizatization process when the sample is cooled below the blocking temperature with an applied magnetic field [10]. The ZFC magnetization curves have a broad maximum at about 170K, such a maximum is also a characteristic feature of superparamagnetic relaxation and blocking behavior. Actually, the broad maximum of $\chi_{ZFC}(T)$ suggests a broad distribution of grain sizes of the particle assemblies. The most prominent feature is that the blocking temperature varies as the strength of applied magnetic field changes. This indicates that, such superparamagnetic behavior can be modified by the applied field and the size distribution [11]. SEM images also indicates a strong interparticle interaction among those particle assemblies, and as we know, superparamgnetic properties could be modified by such like dipole-dipole interaction effect [12]. Those effects suggest that our Ni-Ce nanocomposite particles could be considered interaction dominated rather than being pure superparamagnetic ensembles according to the Néel-Brown model.

On the other hand, as shown in the figure 4, the magnetization for Ni-Ce nanoparticles exhibit a sharp maximum around Neél temperature $T_N = 5$-11K suggesting an antiferromagnetic transition. This can be attributed to the appearence of magnetic ordering of Ce ions [13] in the thin shell layer of Ni-Ce nanocomposite particles. At low temperature, the magnetization of Ni-Ce nanocomposite particles exhibits complicated hehavior (see figure 4 (a, b, c, d), which

suggests that a spin-flip occurs below T_N in the antiferromagnetic state of this Ni-Ce nanocomposite particle assemblies

CONCLUSION

A new type of magnetic core-shell Ni-Ce nanocomposite particle (15-50 nm) have been prepared. SEM morphology and HREM image indicate these are typical large cores and thin shell nanocomposite particles with many microstructure defects. Nano-diffraction patterns confirm the nature of these core-shell nanocomposite particles. Modified superparamagnetic behavior above average blocking temperature (T_B =170K) for Ni-Ce nanocomposite particles assemblies have been exhibited, this superparamagnetic behavior is affected by the strong interparticle interaction. In particular, a spin-flip transition and the antiferromagnetically order with a Neél temperature T_N of about 11K was observed at low temperature for Ni-Ce nanocomposite particle assemblies.

ACKNOWLEDGMENTS

REFERENCES

1. *Magnetic properties of fine particles*, J. L. Dorman and D. Fiorani Eds. (North-Holland, Amsterdam, 1991).
2. C. L. Chien,   *J. Appl. Phys.*, **69**, 5267 (1991).
3. R. D. Shull and L. H. Bennett, *Nanostruct. Mater.*, **1**, 83 (1992).
4. B. Martinez, X. Obrador, Li. Balcells, A. Rouanot, and C. Monty, *Phys. Rev. Lett.*, **80**, 181 (1998).
5. M. M. Ibrahim, S. Darwish and M. S. Seehra, *Phys. Rev. B*, **51**, 2955(1995).
6. M. E. McHerry, S. A. Majetich and E. M. Kirkpatrick, *Mater. Sci. Eng.*, **A204**, 19 (1995).
7. X.X. Zhang, J. Tejeda, J.M. Hernandez and R.F. Ziolo, *Nanostruct. Mater.*, **9**, 301 (1997).
8. S. Morup, F. B.odker, P. V. Hendriksen, and S. Linderoth, *Phys. Rev. B* **52**, 287 (1995).
9. Z. L. Cui, L. F. Dong and Z. K. Zhang, *Nanostruct. Mater.*, **5 (7/8)**, 829 (1995).
10. Q. Chen and Z. J. Zhang, *Appl. Phys. Lett.*, **73**, 3165 (1998).
11. M. Hanson, C. Johansson, M. S. Pederson and S. Morup, *J. Phys: Conden. Matter.*, **7**, 9269 (1995).
12. D. Fiorani, J. L. Dorman, R. Cherkaoui, E. Tronc, F. Lucari, F. D'Orazio, L. Spinu, M. Nogues, A. Garcia and A. M. Testa, *J. Magn. Magn. Mater.*, **196-197**, 143 (1999).
13. F. Fourgerot, B. Chevalier and J. Etourneau, *Physica B*, **230/232**, 256 (1997).

Nanoparticles of Polypyrrole and Their Effect on Mediating Li Ion Transport from Liquid Electrolyte to Cathode

Yong Pang, Ningpine Chen, and Liang Hong
Department of Chemical & Environmental Engineering
National University of Singapore
Singapore 119260

ABSCTRACT

Nano-scale particles of polypyrrole (PPy) have been synthesized by polymerizing the respect monomer in the presence of its substituted homologue with oxyethylene (POE) oligomers as the substitute groups. The polymerization was carried out by introducing an aqueous solution of oxidant into the tetrahydrofurane (THF) solution of the monomers. The particles obtained possess brush-like architectures in the dispersing medium, and their sizes in dry state fall into the range of 10 to 40 nm according to TEM analysis. When dispersed by a low content (< 0.1 wt %) in an aprotic organic solvent, the nanoparticles synthesized have been found to affect the conduction of lithium ion. The effect is interpreted as a significant reduction in the electrical resistance at the electrode/electrolyte interface according to gain-phase impedance measurement. This has been attributed to the mediating role of the graft POE chains on the colloidal particles.

INTRODUCTION

The conventional procedures of the preparation of conducting polymer colloids rely on emulsion polymerization by using water-soluble polymers, such as poly(vinyl alcohol-*co*-vinyl acetate), PEO, and cellulosic derivatives etc., as steric stabilizers [1]. In this way, the stabilizer is physically adsorbed onto the surface of the PPy particles. The average particle diameter of the colloidal particles varies over the range 66~300 nm. Recently, Simmons et al. have reported a "reactive stabilizer" route leading to colloidal PPy [2]. By this method, water-soluble monomers such as N-vinylpyrrolidone was copolymerised with various vinylic (bi)thiophene comonomers to obtain water-soluble statistical copolymers. After the *in situ* polymerization of the pyrrole monomer, resulting PPy particles were typically 100~150 nm in diameter. The present paper proposes an alternative approach that results in even smaller PPy nanoparticles. By this method, large organic molecules containing polyoxyethylene (PEO) moiety are bound to pyrrole or aniline molecule via a spacer, tolylene diisocyanate (TDI). Besides the synthesis of the PPy nanoparticles, their application for improving ionic conductivity of liquid electrolyte of lithium is also explored in this study.

EXPERIMENTAL DETAILS

Preparation of the grafted polypyrrole nanoparticles

THF 40ml, pyrrole (0.70ml, 10.1 mmol), TDI (1.45ml, 10.1mmol) were added into a 100ml conical flask. The mixture was stirred for 36h at room temperature. Then oxyethyl-containing oligomer (11 mmol) and dibutyl tin dilauriate (DBTDL, ca. 0.3 ml) were added into the solution. After that, the reaction was allowed to extend for 24 more hours at room temperature. An aqueous solution consisting of $(NH_4)_2S_2O_8$ (2.77g, 12.1 mmol) and deionized water (DIW) 40ml was introduced into the organic solution, and the two-liquid-phase mixture was stirred for 8

h at room temperature for carrying out the oxidation polymerization of the pyrrole and its derivatives as shown in Scheme 1.

The resulting PPy colloids were subjected to a high-speed centrifugation (11,000 rpm for 2h on Jouan M14.11) to sediment the PPy colloids. The clear supernatant was decanted off, and the sediment was dispersed into THF/DIW (1:1 vol) mixture by mechanical agitation; the dispersion was then subjected to the centrifugation. The cycle of centrifugation and dispersion was repeated twice for purifying the colloids.

Preparation of the colloidal dispersions in aprotic organic solvents

In a typical procedure, the colloids of PPy derivatives obtained after purification was dried at 60°C overnight, the solid was then dispersed into DMSO by mechanical agitation and followed by ultrasonication. Consequently, a very stable colloidal dispersion of PPy derivatives in DMSO (~0.2 wt%) was prepared.
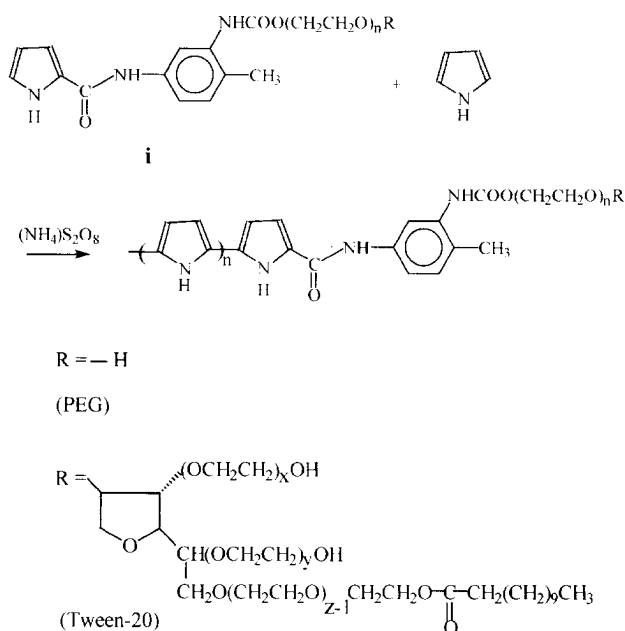
Scheme 1. Grafting the oxyethyl oligomer chain to PPy nanoparticles

TEM measurement

The colloids of the PPy derivatives were diluted with DIW to 200 ppm. Dip a carbon-coated copper grid in the dispersion once and let it dry at room temperature. The TEM measurements were conducted on a Philips CM300 FEG.

Dispersing the colloidal particles into LiBr-DMSO solution

In the DMSO colloidal dispersion, the maximum concentration is about 0.2wt%. A slightly over load of solid poly(Py-*co*-Py-TDI-PEG600) would cause difficulty in dispersing the colloid uniformly in DMSO. In most cases, the 0.1wt% dispersion was used as the medium for dissolving LiBr to make a liquid electrolyte.

Evaluation of the electrical properties of the colloidal dispersion

AC impedance measurements were conducted on a Solarton SI 1260 Impedance/Gain-Phase Analyzer. The amplitude of the sinusoidal excitation signal was 10 mV. DC conductivities were measured with a Hioki 3540mΩ HiTester. For both AC and DC measurements liquid samples are placed in a rectangular shape cell with two parallel brass sheets as electrodes.

DISCUSSION

It is known that pyrrole units in polypyrrole (PPy) are linked through their α-carbons [3]. As such, when the reaction mixture is subjected to oxidizing polymerization, the bare pyrrole molecules would polymerize first to form PPy nuclei and the growth of the nuclei would be terminated upon the participation of the α-substituted pyrrole molecules i. Accordingly, the poly(ethylene glycol) chains are attached chemically to the surface of PPy particles, leading to brush-like PPy colloidal particles as illustrated in *Scheme 1*. Table 1 summarizes three types of PPy nanoparticles synthesized, which differ in the structure of the surface-grafted oxyethylene oligomer.

Table 1. Identification of the various nanoparticles synthesized

Oligomer branch	Polypyrrole
PEG600	poly(Py-*co*-Py-TDI-PEG600)
PEG1000	poly(Py-*co*-Py-TDI-PEG1000)
Tween 20	poly(Py-*co*-Py-TDI-Tween20)

Studies based on TEM observation

TEM images of poly(Py-*co*-Py-TDI-PEG600) (Fig. 1a) and poly(Py-*co*-Py-TDI-PEG1000) (Fig. 1b) show quite different mean particle sizes between the two, the former having an average diameter around 30nm whereas the latter an average diameter smaller than 10nm. As the TEM sample of poly(Py-*co*-Py-TDI-PEG600) was prepared after separation and re-dispersion processes, it is likely that the elementary particles underwent agglomeration in the separation step. The resulting agglomeration could not be broken down any more. On the contrary, the TEM sample of poly(Py-*co*-Py-TDI-PEG1000) was prepared without being separated from the polymerization system as it could not form sediment by centrifugation.

The DC measurement of the colloidal dispersion in DMSO containing soluble LiBr

As dimethyl sulfoxide (DMSO) is an aprotic polar organic solvent, it is therefore a suitable liquid medium for studying Li ion conduction. DMSO itself has a conductivity (S/cm) of minus nine power of order (Table 2). When 0.42 wt % of LiBr is dissolved in it, the conductivity of the solution is boosted by one thousand times owing to a large degree of dissociation of LiBr via the co-ordination of DMSO molecules to Li^+ ions. Similarly, when poly(Py-*co*-Py-TDI-PEG600) colloid (~0.1 wt%) is dispersed in pure DMSO, the conductivity of the dispersion also inflates by one thousand times because the number of colloidal particles per unit of volume is considerably large.
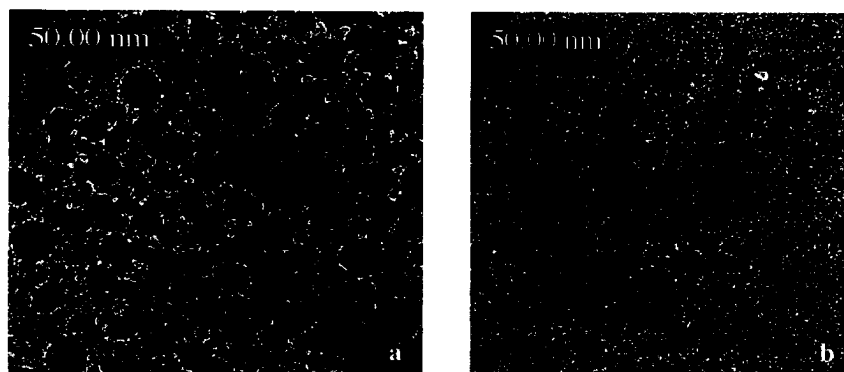
Fig. 1   TEM of (a) poly(Py-*co*-Py-TDI-PEG600) and (b) poly(Py-*co*-Py-TDI-PEG1000)

Table 2. *Effect of the PPy colloids on the conductivity of the electrolyte**

Solid content of the DMSO dispersion		LiBr		
(wt%)		0	0.42wt%	0.88wt%
Poly(Py-*co*-Py-TDI-PEG600)	0	2.0E-09	3.4E-06	1.1E-05
	0.096%	2.7E-06	2.5E-05	2.2E-05
Poly(Py-*co*-Py-TDI-Tween20)	0	2.0E-09	3.4E-06	1.1E-05
	0.094%	2.6E-06	8.2E-05	7.3E-05

* The unit of the data in the table is S/cm.

A simple estimation can give the picture of how it is. Assume that the particles have spherical shape with the average diameter of 70 nm. If the mass density of poly(Py-*co*-Py-TDI-PEG600) is taken as 1, 0.1 wt % of poly(Py-*co*-Py-TDI-PEG600) particles dispersing in DMSO means that there are about 6×10^{12} particles in 1 ml of dispersion. Frequent collisions among the particles allow electrons to be transferred throughout the DMSO medium.

Apparently, only conducting polymer colloids can offer this function. It is interesting to note that as poly(Py-*co*-Py-TDI-PEG600) (~0.1 wt%) is dispersed into the solution of LiBr in DMSO, the conductivity of the resulting liquid system is seven times greater than that of the LiBr solution (0.42 wt %). However, when the LiBr concentration is doubled, the enhancing effect of the colloid becomes less obvious (Table 2). The enhancement effect of the colloid becomes more evident when poly(Py-*co*-Py-TDI-Tween20) was used.

It has been verified that the conductivity enhancement effect of the PPy colloidal particles does not come from their PEO pendant coils alone. Instead, the PPy core is an active component that improves the ionic conduction of the DMSO-LiBr electrolyte system. This particular behaviour of PPy particles may relate to the electrically positive surface on them due to the existence of protonic sites as well as cationic (doped) sites, anions (SO_4^{2-} in the present case that are from the oxidant) surrounding the positively charged core. In the resulting double layer, the negatively charged out-layer may contain not only SO_4^{2-} but also Br^- ions. The migration of Br^- ions toward the surface of colloidal particles is driven by the surplus positive charge, which is likely due to incomplete shielding of the positive charge by SO_4^{2-} diffusion layer. Accordingly, incoming of Br^- into the diffusion layer will enhance the dissociation of LiBr in DMSO. Following this logic, the larger extent of the enhancement of Li conductivity when the particle bearing Tween20 was used can be attributed to the bulky sorbitan unit and the hydrophobic dodecyl segment of Tween20 as shown in Scheme 1. These two structural features may lead to a more expanding anion diffusion layer, which favours the participation of Br^- ions into the diffusion layer and thus enhancing the ionic conductivity in the solution.

AC impedance measurement

As the DC measurement does not cause swift perturbation in the diffusion double layer of PPy colloidal particles, the method allows one to assess the involvement of Br^- ions into the diffusion layer. However, DC measurement cannot be employed to detect the charge transfer at the interface between the electrode and the solution. Frequency scanning in the AC
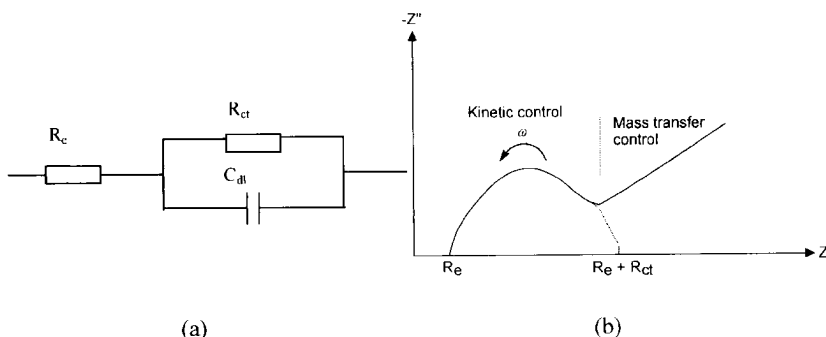
Fig. 2 (a) The simplified equivalent circuit; (b) The plot of impedance in the complex plane of a simple electrochemical system.

impedance spectroscopy ($0.1 \sim 10^5$ Hz) can screen the diffusion layer's effect of PPy particles and study the mass transport of Li^+ ions at the interface between liquid electrolyte and cathode. Approximately, an electrolyte between two electrodes can be simulated by a RC

equivalent circuit (Fig. 2a), where R_e stands for the resistance of the electrolyte between the two electrodes, R_{ct} the resistance of charge transfer between electrolyte and electrodes, and C_{dl} the capacitor of the double layer formed between electrolyte and the electrodes. The experimental impedance plot is always obtained as the plot shown in Fig. 2b. According to the impedance plot, one is able to work out the values of the resistance of the electrolyte (R_e) and the overall low frequency resistance ($R_e + R_{ct}$). Table 3 shows that the AC conductivity (admittance) of electrolyte are almost the same in all the cases, while the conductivity based on ($R_e + R_{ct}$) are apparently greater in the presence of the PPy colloids than in the absence of them. The results suggest that poly(Py-*co*-Py-TDI-PEG600) colloidal particles can facilitate the charge transfer in the double layer between electrodes and the electrolyte. This inference is actually similar as the report by Lindfors et al. [4], where a small amount of PAn could improve significantly the charge transfer at the substrate-membrane interface in a single-piece all-solid-state lithium-selective electrode.

Table 3 Effect of poly(Py-*co*-Py-TDI-PEG600) colloidal particles on the low frequency AC admittance for LiBr/DMSO electrochemical cell system

LiBr (wt %)	Colloid content (wt %)	Admittance of electrolyte[a] (S/cm)	Overall low frequency admittance[b] (S/cm)
0	0.1	1.6×10^{-5}	8.3×10^{-6}
0.42	0	1.3×10^{-3}	1.6×10^{-5}
	0.1	1.6×10^{-3}	7.2×10^{-5}
0.88	0	2.2×10^{-3}	1.6×10^{-5}
	0.1	2.3×10^{-3}	8.9×10^{-5}

a. Calculation based on R_e; *b.* Calculation based on $R_e + R_{ct}$

CONCLUSIONS

Nanoparticles of polypyrrole with grafted oxyethylene oligmer chains have been synthesized via an in-situ seed-blocked method. They are able to enhance Li ion transport in polar aprotic organic liquid and at the interface between the electrolyte and cathode as well.

REFERENCES

1. S. P. Armes, and M. Aldissi, Synthesis of polymeric surfactants for the preparation of sterically-stabilized polyaniline colloids, *Polymeric Materials Science and Engineering*, (ACS, 1989), **60**, pp.751-756.
2. M. R. Simmons, P. A. Chaloner, and S. P. Armes, *Langmuir*, **11**, 4222-4224 (1995).
3. K. Schofield, Hetero-aromatic nitrogen compounds, *Pyrroles and Pyridines* (Plenum Press, 1967) pp. 60-66.
4. T. Lindfors, P. Sjoberg, J. Bobacka, A. Lewenstam, and A. Ivaska, *Anal. Chim. Acta*, **385**, 163-173 (1999).

Semiconductor Nanoparticles

Purpose-Built Anisotropic Metal Oxide Nanomaterials

Lionel Vayssieres, Jinghua Guo and Joseph Nordgren
Department of Physics, Uppsala University, Box 530, SE-75121 Uppsala, Sweden

ABSTRACT

Large arrays of perpendicularly oriented anisotropic nanoparticles of ferric oxyhydroxide (Akaganeite, β-FeOOH) and oxide (Hematite, α-Fe$_2$O$_3$) of typically 3-5 nm in diameter, self-assembled as bundles of about 50 nm in diameter and of up to 1 μm in length have been successfully grown onto polycrystalline substrates without template and/or surfactant by heteronucleation from an aqueous solution of ferric salts and their optical and electronic properties investigated.

INTRODUCTION

Iron compounds are essential materials in chemistry, biology and geology due to their large occurrence in nature [1], for instance, in water [2], plants [3], minerals [4] and clay minerals [5], sediments [6], and sedimentary rocks [7]. The molten core of the Earth is primarily elemental iron, which is the fourth most abundant element in the Earth's crust and is found in significant amount in Martian soil [8]. The oxides of iron play a central role in geochemistry of soil [9], in planetary science [10], and contribute for instance, to the oxidation of sedimentary organic matter [11]. In its various allotropic forms, iron oxides and oxyhydroxides represent important basic and raw materials [12]. Their large abundance, non-toxicity, low-cost, high refractivity, and various colors, contribute to their popularity as polishing agents, and for colorants (red and yellow ochre) for the pigment and paint industry. Indeed, iron oxides are the most commonly used colored pigments in the paints and coatings market [13]. It is also widely studied for the alloys and steel industry [14], in metallurgy [15], as catalysts [16-18] and photocatalysts [19], for magnetic storage devices, cathodes for primary and secondary batteries [20], chemical flame suppressant [21] and for the crucial industrial, economical and environmental issue of corrosion [22]. The thermodynamically stable crystallographic phase of ferric oxides is hematite (α-Fe$_2$O$_3$) which represents the most important ore of iron considering its high iron content and its natural abundance. Therefore, designing iron(III) oxides with a novel, anisotropic and highly oriented morphology is of great fundamental importance for basic physical, earth and life sciences and of relevance for various fields of industrial applications. Numerous vacuum deposition techniques have been used to generate thin films of iron oxides (e.g. molecular beam epitaxy [23], chemical vapor deposition [24], cathodic sputtering [25], and metal deposition and subsequent oxidation [26]). Our strategy is a chemical approach and a general concept named "*purpose-built materials*" [27], well-sustained by a thermodynamic monitoring of the nucleation, growth and ageing processes [28] and well-illustrated on the nanoparticle size control of magnetite (Fe$_3$O$_4$) over an order of magnitude [29]. This concept and synthetic method allows to design and create novel metal oxide nanomaterials with the proper morphology, texture and orientation in order to probe, tune, and optimize their physical properties. Thin films materials are obtained by direct growth onto various substrates from aqueous precursors at low temperature. Such approach to material synthesis offers the ability to generate anisotropic nanoparticles as well as the competence to control their orientation on substrates.

EXPERIMENTAL

The general concept [27] and synthetic procedure is performed according to the general template-less thin film processing technique developed by Vayssieres et al. [30] and has been successfully applied for the growth of large arrays of highly oriented anisotropic metal oxides [31, 32]. Iron(III) oxides thin films (akaganeite and hematite) are grown directly onto a substrate from aqueous ferric chloride salt at 95°C in such conditions that the thermodynamic stabilization of the oxyhydroxide structure (akaganeite) is obtained [31]. A subsequent heat treatment in air is performed to obtain monodisperse nanorod-array of hematite. The solid phase transition was followed by thermal analysis (i.e. differential scanning calorimetry (DSC) and thermogravimetric analysis (TGA) performed in air at a heating rate of 10°C/min. The electronic structure was investigated by soft x-ray absorption spectroscopy (XAS) at synchrotron facilities (Advanced Light Source, Lawrence Berkeley National Laboratory, BL 7.0.1).

RESULTS AND DISCUSSION

β-FeOOH occurs in nature as the mineral akaganeite and crystallizes in the tetragonal system (space group I4/m $\equiv$ C_{4h}^5, a = 10.44, c = 3.01 Å). The structure is described as a tunnel structure (similar to α-MnO$_2$) hosting H$_2$O or Cl$^-$ and based on a defect close packed oxygen lattice with three different kinds of oxygen layers. Every third layer is only two-third occupied with rows of oxygens missing along the c-axis. The cation occupation of octahedral sites between the other anion layers is in double rows, but separated by single rows of empty sites along c. The octahedral cation sites remain between the third anion layer and its neighbor layer are completely filled. This topology produces di-octahedral chains, which are arranged about the four-fold symmetry c-axis (figure 1). The chains share vertices along their edges, forming square-cross section tunnels, some 5 Å on edge. Although, the tunnel seems large it must be noted that only a single row of oxygens is missing. Hence, only species with sizes similar to O$_2^-$ ions can be readily accommodated. The crystals are rod shaped grouping of 5*5*n unit cells where n refers to replication down the c-axis. These crystals have empty cores, that is, 3*3*n cell hole runs down the center of the crystal, producing a square channel about 3 nm on a side. The anisotropic crystals form a bundle called a somatoid. Dehydration of β-FeOOH at high temperature leads to the thermodynamically stable α-Fe$_2$O$_3$ phase.
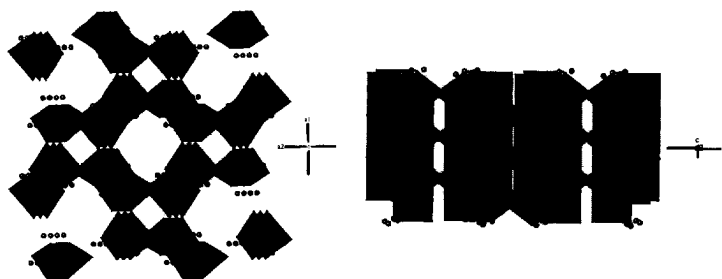
Figure 1. *Crystal structure of β-FeOOH (akaganeite). The spheres represent hydrogen atoms.*
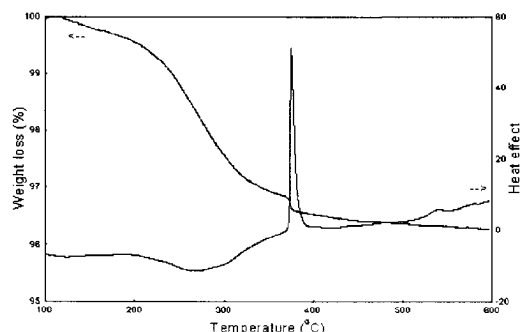
Figure 2. *TGA (left scale) and DSC (right scale) analysis of β-FeOOH nanorod powder.*

Thermal analysis of β-FeOOH nanorods (figure 2) shows a low overall weight loss of 3.75% within the range of 100-600° C. A 0.5% loss due weakly bonded water molecules occurs until 200°C. Most of the weight loss (3%) is occurring between 200 and 300°C accompanied by a broad endothermic shoulder which corresponds to the evaporation of structural water. A very sharp exothermic peak occurs at 385°C with a concomitant 0.2% loss of water corresponding to the crystal phase transition to hematite. A continuous slow decay of the TGA curve is observed until 600°C corresponding to the slow process of diffusion and evaporation of surface/bulk OH groups as H_2O with a very small exothermic peak at 540°C.

Hematite crystallizes in the trigonal crystal system, space group $R\bar{3}c \equiv D_{3d}^6$, and is isostructural with corundum (α-Al_2O_3). The unit cell can be described as rhombohedral with three equal axes a = 5.43 Å and an angle between edges $\alpha = 55°18'$ containing two formula unit (Z = 2), or hexagonal with a = 5.03Å and c = 13.75 Å (Z = 6). The lattice is built on a hexagonal close packed (HCP) array of oxygen with four of every six available octahedral sites around O atoms occupied with Fe (figure 3). The octahedral and tetrahedral sites are above and below one another in a HCP lattice, the tetrahedral sites remaining empty. Octahedra are sharing faces along a threefold axis and are distorted to trigonal antiprisms because of the Fe-Fe repulsion occurring across one shared face and not the others. This yields to a very dense structure (i.e. high oxygen packing index), showing a high polarisability and a high refractive index.
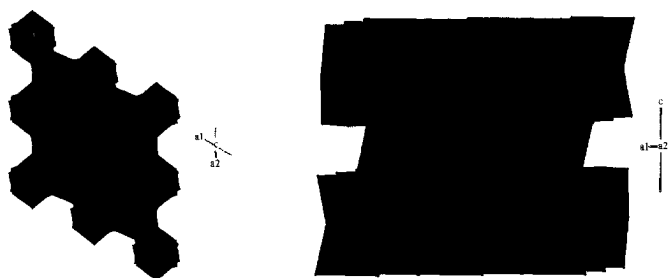
Figure 3. *Crystal structure of α-Fe_2O_3 (hematite).*

Figure 4. *(left) TEM of α-Fe₂O₃ somatoid and (right) SEM of α-Fe₂O₃ oriented nanorod-array.*

The purpose-built nanorod-array, consisting in a somatoid of about 50 nm in diameter with single-crystalline nanorods of 3-5 nm in diameter, perpendicularly oriented onto the substrate is shown on figure 4. Figure 5 shows the x-ray absorption spectra (XAS) of hematite nanorod-array at Fe L-edge and O K-edge. The Fe L-edge ($2p \rightarrow 3d$) spectrum shows the spin orbit splitting of the $2p$ core level, i.e. $2p_{3/2}$ (L_3-edge) and $2p_{1/2}$ (L_2-edge) and the p-d and d-d coulomb and exchange interactions that create multiplet feature within the edge. The ligand field splitting of 3d transition metals being in the same order of magnitude than p-d and d-d interactions, the energy splitting between t_{2g} and e_g orbitals of the Fe^{3+} ion (d^5) in distorted octahedral symmetry is found to be of 1.4 eV. The oxygen K-edge spectrum ($1s \rightarrow 2p$) shows two regions corresponding to oxygen 2p orbitals hybridized respectively, with Fe 3d orbitals (530-535 eV) and with Fe 4s,4p orbitals (535-550 eV).

The UV visible properties of the hematite nanorod-array are shown on figure 6. A strong optical absorption in the UV and visible (blue) region (350-550 nm) is found, which spread out, to a lower extent, into the entire visible region. This broad absorption and good stability against photocorrosion (Eg ≈ 2.2 eV) has driven much efforts in the past to produce photovoltaic cells from n-type hematite materials but very unsuccessfully, due to a high and fast rate of recombination of photogenerated carriers and a low carrier mobility. Thin films of nanostructured hematite based on spherical nanoparticles of 50 nm have been synthesized in an attempt to reduce the charge recombination but the efficiency remained very low [33].
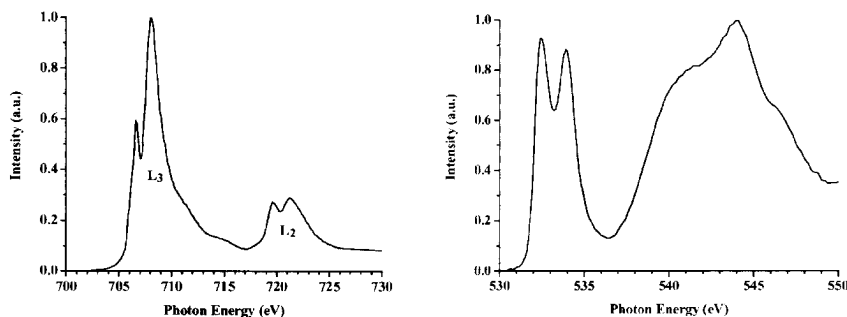
Figure 5. *XAS spectra at Fe L-edge (left) and O K-edge (right) of α-Fe₂O₃ nanorod-array.*
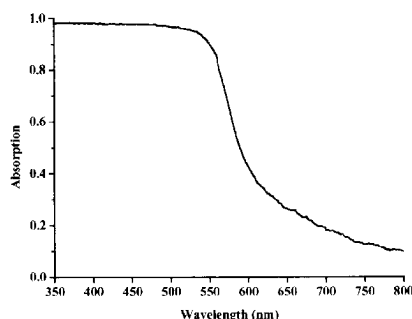
Figure 6. *UV-Visible optical absorption spectrum of hematite nanorod-array.*

Recently, such *purpose-built* perpendicularly oriented nanorod-arrays of hematite have been used to develop photovoltaic cells. Indeed, the diameter of the nanorods allows a perfect match with the minority carrier diffusion length of hematite [34]. Accordingly, a very efficient photogenerated charge separation was obtained as well as a high incident photon to electron conversion efficiency of ca. 60% at 350 nm, which led to the creation of a 2-electrode hematite photovoltaic cells [35]. Besides the well-designed direct, grain boundary-free, electron pathway and the excellent structural match with the hole diffusion length, a 2D quantum confinement has also been suggested from resonant inelastic x-ray scattering (RIXS) of synchrotron radiation [36] to account for the unusual high efficiency of the hematite nanorod-array photoanode.

Such design is suitable for other oxides and allowed, for instance, the creation of highly oriented arrays of ZnO [32] to study the photoelectrochemical, electron transport, and luminescence properties as well as to probe and demonstrate the character and symmetry of ZnO conduction band orbitals by polarization-dependent x-ray absorption spectroscopy and quantum calculation study [37].

CONCLUSION

The ability to produce, at low cost, anisotropic nanoparticles and to control their orientation onto a substrate in order to generate well-controlled 3D nanostructures, will contribute to create a novel generation of smart and functional nanomaterials, built for the purpose of their applications: the materials of the future. Simultaneously, it should contribute to reach a better fundamental understanding of their fascinating physical properties and therefore, bring the competence to optimize existing devices and, most probably, developing new ones.

ACKNOWLEDGEMENTS

REFERENCES

1. J. L. Jambor and J. E. Dutrizac, *Chem. Rev.* **98**, 2549-2585 (1998).

2. W. Stumn and J.J. Morgan, *Aquatic Chemistry* (Wiley, 1996).
3. G. Winklemann, F. Van der helm and J. B. Neidlans, *Iron transport in Microbes, Plants and Animals* (VCH, 1987).
4. L. A. J. Garvie and P. R. Buseck, *Nature* **396**, 667-670 (1998).
5. J. E. Kostka, E. Haefele, R. Viehweger and J.W. Stuck, *Environ. Sci. Technol.* **33**, 3127-3133 (1999).
6. H. M. Bao, P. L. Koch and R. P. Hepple, *J. Sediment. Res.* **68(5)**, 727-738 (1998).
7. B. B. Ellwood, K. M. Petruso, F. B. Harrold and D. Schuldenrein, *J. Archeological Sci.* **24**, 569-573 (1997).
8. R.V. Morris, D.C. Golden, T.D. Shelter and H.V. Lauer, *Meteorit. Planet. Sci.* **33(4)**, 743-751 (1998).
9. W. Stumm and B. Sulzberger, *Geochim. Cosmochim. Acta* **56(8)**, 3233-3257 (1992).
10. G. Kletetschka, P. Wasilewski and P. Taylor, *Phys. Earth Planet. In.* **119**, 259-267 (2000).
11. D. R. Lovley, *Microbiol. Rev.* **55(2)**, 259-287 (1991).
12. R. M. Cornell and U. Schwertmann, *The Iron Oxides* (VCH, 1996).
13. P. G. Morse, *Chem. Eng. News* **76(41)**, 42-62 (1998).
14. K. Tano, E. Öberg, P. O. Samskog, T. Monredon and A. Broussaud, *Powder Technol.* **105**, 443-450 (1999).
15. A. Von Ropenack, in J.E. Dutrizac and A.J. Monhemius Eds. *Iron control in Hydrometallurgy* (Ellis Horwood, 1986) pp. 730-741.
16. R. Pestman, R.M. Koster, E. Boellaard, A.M. Van der Kraan and V. Ponec, *J. Catal.* **174**, 142-152 (1998).
17. S-S. Lin and M. D. Gurol, *Environ. Sci. Technol.* **32**, 1417-1423 (1998).
18. Y. Zhang, J. E. Ellison and J.C. Cannon, *Ind. Eng. Chem. Res.* **36(5)**, 1948-1952 (1997).
19. Y. Matsumoto, *J. Solid State Chem.* **126**, 227-234 (1996).
20. S. Licht, B. Wang and S. Ghosh, *Science* **285**, 139-1042 (1999).
21. C. B. Kellog, K. K. Irikura, *J. Phys. Chem. A* **103(8)**, 1150-1159 (1999).
22. S. E. Oh, D.C. Cook and H.E. Townsend, *Corrosion Sci.* **41**, 1687-1702 (1999).
23. T. Fujii, et al *Surf. Sci.* **366(3)**, 579-586 (1996).
24. A. Martinez, J. Pena, M. Labeau, J.M. Gonzalez-Calbet and M. Vallet-Regi, *J. Mater. Res.* **10(5)**, 1307-1311 (1995).
25. K. Siroky, J. Jiresova and L. Hudec, *Thin Solid Films* **245(1-2)**, 211-214 (1994).
26. W. Weiss, *Surf. Sci.* **377(1-3)**, 943-947 (1997).
27. L. Vayssieres, A. Hagfeldt and S.-E. Lindquist, *Pure Appl. Chem.* **72(1-2)**, 47-52 (2000).
28. L. Vayssieres, Ph.D. Dissertation, Université Pierre et Marie Curie, Paris 1995.
29. L. Vayssieres, C. Chaneac, E. Tronc and J.-P. Jolivet, *J. Colloid Interface Sci.* **205(2)**, 205-212 (1998).
30. L. Vayssieres, A. Hagfeldt, S.-E. Lindquist, patent pending.
31. L. Vayssieres, N. Beermann, S.-E. Lindquist and A. Hagfeldt, *Chem. Mater.* (in press).
32. L. Vayssieres, K. Keis, S.-E. Lindquist and A. Hagfeldt, submitted.
33. U. Björksten, J. Moser and M. Grätzel, *Chem. Mater.* **6**, 858-863 (1994).
34. J. H. Kennedy and K. W. Frese, *J. Electrochem. Soc.* **125**, 709 (1978).
35. N. Beermann, L. Vayssieres, S.-E. Lindquist and A. Hagfeldt, *J. Electrochem. Soc.* **147(7)**, 2456-2461 (2000).
36. J.-H. Guo, L. Vayssieres, C. Såthe, S. Butorin and J. Nordgren to be published.
37. J.-H. Guo, L. Vayssieres, C. Persson, R. Ahuja, and J. Nordgren to be published.

AUTHOR INDEX

SUBJECT INDEX